FOG

Freiberg Online Geology

FOG is an electronic journal registered under **ISSN 1434-7512**

2014, VOL 36

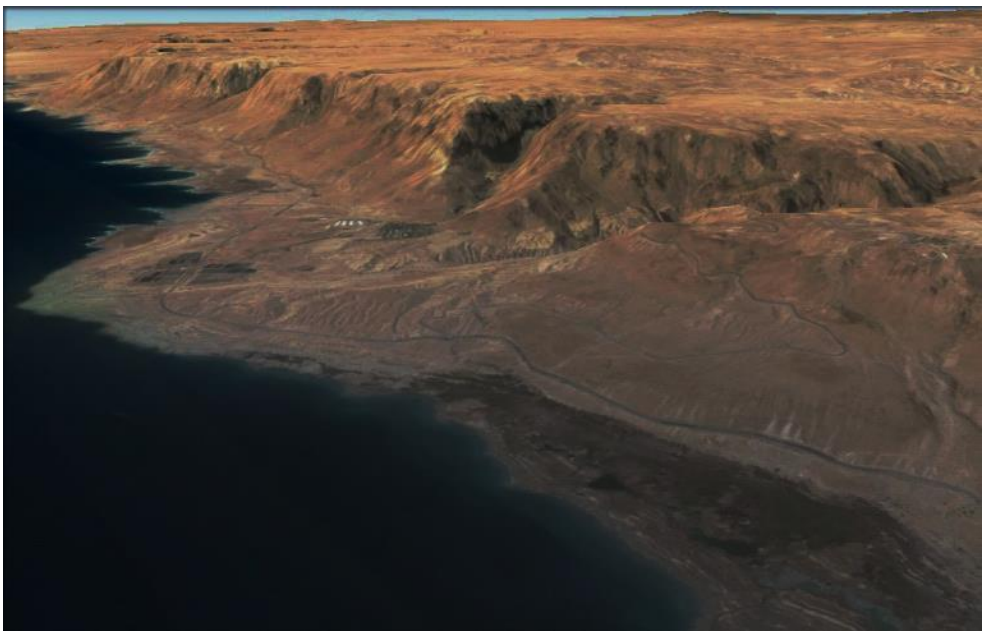

Matthias Strey

2-D numerical flow and density modeling in Dead Sea Group sediments (Darga, Israel)

134 pages, 64 figures, 21 tables, 111 references

„…judgement is selection of a fact. There are, in a sense, no facts in nature; or if you like, there are an infinite number of potential facts in nature, out of which the judgement selects a few which become truly facts by that act of selection." – Immanuel Kant, Critique of Judgement

Acknowledgement

The assistance of Tino Rödiger and Christian Siebert, UFZ Halle, I gratefully acknowledge. Tino helped in transferring the structural model into ArcGIS, in modeling with FEFLOW, keeping me on track of the work focus and the necessary facts. Christian spent his local experience and geological comprehension from the Dead Sea region. Ulf Mallast from UFZ Halle provided geological maps and remote sensing data for localizing the sublacustrine discharges.

Professor Broder Merkel promoted the work with gainful recommendations.

Agnes Sachse, UFZ Halle, supported my findings about the hydraulic connection between the Cretaceous hard rock and the Quaternary sediments. Yoseph Yechieli, GSI Jerusalem, assisted with borehole drillings and his enormous paper work about the Dead Sea hydrogeology.

Birgit Gaitzsch, TU Freiberg, refreshed my knowledge of fan-delta environment sedimentology. Ahmed Gharaibeh, TU Freiberg, introduced me to analogies in the Jordan geology and aquifer properties. Special thanks to Raghid Sabri, TU Freiberg, who contributed via everyday support in the office, delivered Palestinian well data, gave contact to the GSI, helped with Hebraic translations and enlightened the background of Hebraic and Arabic scientists in Germany. Omed Mustafa, TU Freiberg, told me about the productivity of local aquifers in the Levant. Ramadan Abdelaziz, TU Freiberg, makes me sensitive for the regional comparability of aquifers along the Middle East Mediterranean Sea shoreline and for parameter settings during the model development. Thank you to the entire hydrogeological staff of TU Freiberg for support.

Special thanks to Björn Kaiser and the FEFLOW Support team in Berlin who contributed with technical advice.

My family is an indispensable counseling at any time and place.

Statement of authorship

I hereby certify:

that I authored this master thesis independently, did not use other than the specified references and did not make use of other unauthorized assistance.

that I did not submit this master topic for assessment in any way as an examination paper neither in Germany nor abroad.

that this master thesis agrees with the supervisor's assessed thesis.

_____ _____

Summary

On the western side of the Dead Sea (DS) a mesoscale structural and 2D numerical flow and transport model has been created to quantify and investigate mechanisms of groundwater discharge for the Quaternary Dead Sea Group (DSG) sediment between the hard rocks of the Judean Mountains and the DS. The environment around the Wadi Darga outlet was chosen as focus area.

The conceptual model was developed from geological drilling logs and field observations along the shoreline of the DS. The software package FEFLOW 6.1 was successfully applied for realizing the steady-state finite element subsurface flow and density modeling in the DSG sediments. The used scale of the model exhibited that the introduction of discrete elements (DE) as conduit (solution tube) network is suitable for a regional multilayer aquifer with dissolution voids.

Surface and subsurface spring locations on the shoreline of the Wadi Darga outlet provided the most important constraint in the development and improvement of the applied finite element model scenarios.

The system is driven by gravitational forces, i.e. the high topographic gradient of the Judean Mountains contract the groundwater heads in the Cretaceous hard rocks and the subhorizontal surface towards the DS flattens the hydraulic gradient within the DSG sediment towards the DS. Groundwater migrates from the Judean Mountains through the DSG sediment to the DS, where dense saltwater forces freshwater to rise. The resulting springs are dominantly controlled by the gravitation potential of the groundwater. Fresh-salt water interaction influences the location of the discharge points.

The lowest groundwater flow velocities were determined through the Judean Mountains (several years with 0.02 to 0.26 m/d). Residence times within the first 300 m of the DSG sediment are rather large (0.3 to 30 m/d), reducing considerably within the conduit/conduits along 1 km of the DSG (350 to 3,500 m/d) and prolonging slightly to the outlet of the DSG sediment (30 to 350 m/d).

Mass concentration patterns indicate a depth-dependent orientation of the fresh-salt water interface that obviously obeys a push-pull salinity mechanism and is governed by lithological permeability heterogeneities. That means, in different depths there are different steps of the fresh-salt water interface. Highly conductive conduits produce large groundwater head gradients in their vicinity. The fresh-salt water interface above is turned forwards in the direction of the DS (push mechanism). The more impermeable layers preserve the subvertical interface or favor the intrusion of saline water (pull mechanism).

Hydraulic conductivity variations within the DSG sediment can easily be triggered by salt karst features that add permeability to the matrix. The application of DE on the assumed high conductivity layers reflects the structural observations in the field. The sum of matrix and discrete conduit flow resulted in complex density-dependent flow patterns. These become obvious in diffuse fresh-salt water interfaces with an inhomogeneous distribution of salinity gradient zones.

The applied DE schemes revealed that within a realistic range of hydraulic aperture values from tested minimum 1 mm to 1 m water flow is not sensitive to increasing hydraulic apertures with

increasing depth, i.e. water flow in the deeper subsurface layers cannot be induced from increasing hydraulic aperture to the depth. The threshold value for the minimum DE cross-section area for which discharge to the DS can be realized was determined to $5*10^{-3}$ m² for a given hydraulic aperture of 0.001 m in the clay layers.

With respect to the frequency of applied DE, at least an area of 50 m from the limestone-DSG-border in the direction of the DS needs to be covered with DE to facilitate discharge to the DS. Such dissolution voids can be created by inflowing freshwater that dissolves lacustrine rock salt. To facilitate surface discharge as well, DE have to end not closer than 50 m away from the DS bottom/surface.

As proven by scenarios with horizontal and vertical inclined DE, discharge to the DS is not sensitive for these directions of additional permeability. This behavior can be explained by the applied confined conditions of the DSG sediment. A further scenario with an additional brine concentration on the conceptual two Judean faults was applied. It results in the repressing of freshwater within the Lower Judea Group aquifer. The increasing saltwater pressure does not facilitate water from the Lower Judea Group aquifer to rise along the Judean fault and to enter the DSG sediment. Discharge to the DS in the upper part of the DSG sediment is not considerably influenced by the additional salinity input due to the higher elevation level of the streamlines.

Observed large freshwater springs could be simulated in form of outlets that are controlled by a larger flow area of tubes. Springs only occur where saltwater pressure does not prevail over the freshwater pressure, according to the results not below -528 Meter above mean sea level (m msl). The discharge system is particularly susceptible if conduits are permanently developing in the upper part of the DSG sediment. DE Cross-section areas and hydraulic apertures within a range of 5 mm to 5 cm result in surface and subsurface springs. The observed different turbidities in the springs could not be explained conclusively. Larger simulated discharges with a larger amount of suspended clayey material are fed by higher hydraulic conductivity zones with larger flow velocities within a range of 0.001 to 0.01 m/s. But even the maximum simulated flow velocity does not exceed the critical velocity of 0.2 m/s for the erosion of unconsolidated dry clay. Groundwater velocities of smaller discharges are usually in the range of 10^{-4} to 10^{-6} m/s and are not effective for dry clay mineral erosion. However, the large pore water content within the DSG sediment may reduce intra-crystalline bonding forces of clay minerals due to enhanced H_2O-inclusion into the layer structure. This may effect easier erosion at lower velocities.

Concerning the rate budget, the median fluid input/output of the model domain was determined to 180 m³/d. The median mass input/output of the model was determined to 650 g/s. About 130 m³/d and 450 g/s enter the DSG sediment and escape without quantitative loss.

The models have been evaluated according to a constraint index. The optimum solution with the highest constraint index was aimed for a model with DE. The flow and mass rate budget is balanced. DE exhibit a constant aperture of 0.001 m and a constant cross-section area of 0.005 m² over the entire DSG sediment. Springs for this model occur at the surface, at shallow depth and at greater depth similar to the observed discharges.

Table of contents

Summary V

List of figures X

List of tables XII

Symbols and abbreviations XIII

1 Motivation 14

2 Introduction 15

3 Study area 16

3.1 Geography 16

3.2 Geology 19

3.3 Salt karst 30

3.4 Hydrogeology 32

4 Model design 38

4.1 Conceptual model 38

4.2 Hydrogeological concepts 45

4.2.1 Hydraulic conductivities 45

4.2.2 Interaction of saltwater and freshwater 46

4.2.3 Potential effects 47

4.2.4 Discrete element network 48

4.3 Model code and problem settings 49

4.3.1 Parameter references 50

4.3.2 Discrete elements 51

4.4 Model discretization 54

4.5 Boundaries 56

4.6 Model execution and calibration 57

4.6.1 From initial to standard model 58

4.6.2 DSG layering 59

4.6.3 Deduction of a DE network 60

4.7 Sensitivity analysis 61

4.7.1 Scenario: Matrix flow threshold 61

4.7.2 Scenario: Hydraulic aperture vs. depth 62

4.7.3 Scenario: Cross-section area threshold 64

4.7.4 Scenario: Cross-section area vs. depth 64

4.7.5 Scenario: Discrete element frequency 65
4.7.6 Scenario: Discrete element inclination 67
4.7.7 Scenario: Salinity pool for ascending deep waters 67
4.7.8 Scenario: Debris removal 68
4.8 Uncertainty analysis 70
4.8.1 Mesh quality 70
4.8.2 Reference concentration 70
4.8.3 Anisotropy of conductivity 70
4.8.4 Dispersivity and molecular diffusion 70
4.9 Constraint Index CI 71
5 Results 73
5.1 Model calibration 74
5.1.1 From initial to standard model 74
5.1.2 DSG layering 79
5.1.3 Deduction of a DE network 82
5.2 Sensitivity analysis 87
5.2.1 Scenario: Matrix flow threshold 87
5.2.2 Scenario: Hydraulic aperture vs. depth 88
5.2.3 Scenario: Cross-section area threshold 90
5.2.4 Scenario: Cross-section area vs. depth 92
5.2.5 Scenario: Discrete element frequency 94
5.2.6 Scenario: Discrete element inclination 96
5.2.7 Scenario: Salinity pool for ascending deep waters 97
5.2.8 Scenario: Debris removal 99
5.3 Uncertainty analysis 101
5.3.1 Mesh quality 101
5.3.2 Reference concentration 101
5.3.3 Anisotropy of conductivity 102
5.3.4 Dispersivity and molecular diffusion 103
5.4 Constraint Index CI 106
5.5 Rate budget 108
6 Conclusions 110
7 Discussion 113
8 References 117

9 Appendix 122

List of figures

Figure 1: Location map of Wadi Darga and spot image of the study area 16
Figure 2: Surface drainage basin (A) and subsurface drainage basin (B) 17
Figure 3: Average annual rainfall in the study area 18
Figure 4: DEM of the study area 19
Figure 5: Geological map of the study area 20
Figure 6: DS basin and regional aquifers 21
Figure 7: Stratigraphy of the Mizpe Shalem area 23
Figure 8: Location and depth of boreholes in the Mizpe Shalem site 24
Figure 9: Drilling records 25
Figure 10: Location of boreholes along the western DS shoreline 26
Figure 11: Schematic Gilbert fan-delta 27
Figure 12: Seismic cross-section DS 3677 (time migration section) 29
Figure 13: Derived geological cross-section from several seismic cross-sections 29
Figure 14: Preferential water pathways in the DSG sediment 30
Figure 16: Surface and sublacustrine discharges 32
Figure 17: Depth-depending surface and sublacustrine discharges 33
Figure 18: Groundwater flow direction from the Judean Mountains to the DS 35
Figure 19: Water table elevations 36
Figure 20: Hydrogeological settings of the Wadi Darga 39
Figure 21: Conceptual model for slice ML-2 41
Figure 22: Conceptual model for slice ML-4 41
Figure 23: Conceptual model for slice DR-4 42
Figure 24: 1D geometry type which is applied for discrete element modeling 52
Figure 25: Triangle mesh generator and scenario description of a steady-state model 55
Figure 26: Applied initial meshing density 55
Figure 27: Hydrogeological properties for the numerical modeling 58
Figure 28: Assigned hydraulic conductivities for the 4-layer DSG sediment 60
Figure 29: Discrete element network 61
Figure 30: Hydraulic aperture distribution for case 1 and case 2 63
Figure 31: Cross-section area distribution for case 1 and case 2 65
Figure 32: Applied DE frequency schemes 66
Figure 33: Applied DE inclination schemes 67
Figure 34: Streamlines (models with kf contrast from standard, x:z = 1:2) 79
Figure 35: Hydraulic heads (multilayer model, x:z = 1:2) 80
Figure 36: Streamlines (multilayer model, x:z = 1:2) 81
Figure 37: Mass concentration pattern (multilayer model, x:z = 1:1) 81
Figure 38: Push-pull-mechanism 82
Figure 39: Hydraulic heads (network model, x:z = 1:2) 83
Figure 40: Streamlines (network model, x:z = 1:5) 83
Figure 41: Mass concentration pattern (network model, x:z = 1:1) 84
Figure 42: Streamlines (network model with increased aperture, x:z = 1:2) 84

Figure 43: Mass concentration pattern (network model with increased aperture, x:z = 1:1) 85
Figure 44: Darcy flux in the DSG (network model with increased aperture, x:z = 1:5) 86
Figure 45: Streamlines (matrix flow threshold model, x:z = 1:5) 88
Figure 46: Streamlines (hydraulic aperture vs. depth, x:z = 1:5) 89
Figure 47: Mass concentration pattern (hydraulic aperture vs. depth, x:z = 1:1) 90
Figure 48: Streamlines (cross-section area threshold, 3,000 d) 91
Figure 49: Streamlines (cross-section area threshold, 5,000 d) 92
Figure 50: Streamlines (cross-section area vs. depth, x:z = 1:5) 93
Figure 51: Mass concentration pattern (cross-section area vs. depth, case 2, x:z = 1:1) 93
Figure 52: Streamlines (discrete element frequency, x:z = 1:5) 95
Figure 53: Mass concentration pattern (discrete element frequency, x:z = 1:1) 96
Figure 54: Streamlines (discrete element inclination, x:z = 1:5) 97
Figure 55: Streamlines (salinity pool, x:z = 1:5) 98
Figure 56: Mass concentration patterns (salinity pool, x:z = 1:1) 99
Figure 57: Streamline and mass concentration pattern (debris removal) 100
Figure 58: Reference and improved mesh quality 101
Figure 59: Streamline and mass concentration pattern for a minor change in C_S 102
Figure 60: Streamline and mass concentration pattern for anisotropic conductivity 103
Figure 61: Streamline and mass concentration patterns for different dispersivity ratios 104
Figure 62: Rate budget of applied dispersivity ratio cases 105
Figure 63: Streamline and mass concentration patterns for molecular diffusion ranges 105
Figure 64: Bar diagram for the CI calculation 106
Figure 65: Rate budgets of fluid flow and mass flow 109

List of tables

Table 1: List of boreholes 26
Table 2: Structural resolution of the conceptual model for the slice ML-2 43
Table 3: Structural resolution of the conceptual model for the slice ML-4 43
Table 4: Structural resolution of the conceptual model for the slice DR-4 44
Table 5: Hydraulic conductivity parameterization of ML-4 layers 46
Table 6: Problem class definition within FEFLOW 49
Table 7: Projection within FEFLOW 50
Table 8: Flow and mass boundary conditions within FEFLOW 50
Table 9: Flow and mass transport properties within FEFLOW 51
Table 10: 1D and 2D discrete feature elements that can be applied within FEFLOW 52
Table 11: Workflow for the application of discrete elements in 2D sections 53
Table 12: Flowchart for the development of the models and scenarios 57
Table 13: Other used material properties 58
Table 14: Hydraulic aperture increase with depth 63
Table 15: Cross-section area increase with depth 64
Table 16: Synopsis of the developed models 69
Table 17: Results for the initial to the standard model (hydraulic heads) 75
Table 18: Results for the initial to the standard model (streamlines) 76
Table 19: Results for the initial to the standard model (mass concentration patterns) 77
Table 20: Constraint Index CI 107
Table 21: Statistical parameters of the model rate budgets 109

Symbols and abbreviations

The displayed maps have been projected in WGS 1984 UTM Zone 36N.

Abbreviation	**Explanation**
DE	Discrete Elements
DS	Dead Sea
DSG	Dead Sea Group: Quaternary sediments of the Jordan Rift Valley
m msl	Meter above mean sea level
Sediment abbreviations according to DIN EN ISO 14688-1*:*	
Cl	Clay
Sa	Sand
Gr	Gravel
Mineral phase abbreviations according to Siivola and Schmid (2007)*:*	
Gp	Gypsum
Arg	Aragonite
Cal	Calcite
Hl	Halite

1 Motivation

According to the OpenGeoSys modeling results of Gräbe et al. (2013) groundwater recharged in the Judean Mountains (Israel and West Bank) should enter the Dead Sea (DS) without quantitative loss. In fact, there are only a few concentrated springs from the Quaternary aquifer in front of the mountains where freshwater discharges to the DS. In order to figure out the mechanism of outflow and the flow and mass budget, the sediment between the mountain outcrops and the seafloor was investigated during this research. Due to the lack of reliable geological and hydrogeological data along the study area of Wadi Darga numerous scenarios needed to be conducted during the sensitivity analysis to optimize the flow field of the focused sediment. The consideration of discrete elements (DE) as stochastic network geometry in dissolution-prone layers of the Dead Sea Group (DSG) was recommended by Saller et al. (2013) and was applied within a FEFLOW model domain.

2 Introduction

The arid and semi-arid regions of the world increasingly suffer from groundwater scarcity. The Middle East is one of these areas which are subjected to major groundwater depletion. Drinking water availability for future generations demands for stabilized groundwater heads and sustainable management of regional groundwater systems (Aeschbach-Hertig and Gleeson 2012).

The scope of the study was to create a transport model with FEFLOW® on a shoreline location at the western part of the DS to figure out the discharge to the DS. The major aspects of the investigation concern a

1. structural model of a fan-delta along a cross-section in the northern Wadi Darga outlet
2. numerical flow model with an integrated stochastic approach for the highly complex DSG sediment elucidating the interdependence between heterogeneous hydraulic conductivity distributions and spatially limited sublacustrine discharges to the DS
3. density model of the DSG sediment providing answers to the shape and the separation of the fresh/salt water interface

The numerical model should be capable of revealing the changes of hydraulic conductivity in the lake sediments (erosion) by changing geometry and chemical concentration properties. The model should reflect the pathways of inflowing recently recharged fresh groundwater that moves along Cretaceous limestone aquifers (Upper and Lower Judea Group) towards the outcropping lake sediments into the DS.

The western coast of the DS is currently a major area of hydrogeological research. Research institutes and companies deploy scientists from Israel, Jordan, Palestine and Germany that are involved in programs which have been intensively funded in the last decade. Especially, water movement in the Judean Mountain Range (Gräbe et al. 2013) and sinkhole development along the shoreline (Abelson et al. 2006; Yechieli et al. 2006) have been the focus of investigation. Having determined the qualitative and quantitative hydrogeological properties of the Judean Mountain Range, there is now a need to close the gap of discharge processes between the mountainous limestone aquifers and the DS.

In the long run, the research beyond this topic includes to understand the process of groundwater flow dynamics in the area of the DS and to get access to the water balance of the DS. The impact of decreasing heads of the DS and groundwater is immense for the drinking water supply in the region. This study should help to mitigate permanent damage that is caused by superficial balancing of potential drinking water resources in the DS region.

The aim of the model accompanies a visualization of the flow and transport in the DSG sediments as a statistical hydraulic 2D-flownet of primary and secondary flow paths (chaotic flow network). Assumptions include unidirectional flow, constant water inflow or constant concentration input. The mixing processes of fresh and salt water belong to the core interest of the density model. The investigation also focuses on the kind and the intensity of processes that are responsible for large differences in the output mass concentration to the DS. The study outlines the quantitative and qualitative share between terrestrial and sublacustrine discharge to the DS and its responsible transport mechanisms.

3 Study area

3.1 Geography

Wadi Darga is located on the western shoreline of the DS in the West Bank (Figure 1). It drains the eastern Judean Mountains to the DS. From the rift escarpment to the DS, the 4 x 2 km² large surface outlet of Wadi Darga includes the sediment fan and the study area, which is represented by the adjoining drainage area in the north. Wadi Darga belongs to the surface catchment of Daraja that comprises an area of 235 km² (Figure 2). Regarding the groundwater drainage, Wadi Darga is part of the subsurface catchment of the Kane-Samar basin with an area of 390 km² (Ben-Itzhak and Gvirtzman 2005). The elevation of the Judean Mountains ranges from 500 to 1,200 m msl whereas the deepest point of the western DS shoreline is marked by the current sea level of the DS with -425 Meter above mean sea level (m msl) (Dweik and Shuval 2007). The deepest point of the DS bathymetry is located at -730 m msl (Hall and Krasheninnikov 2005).

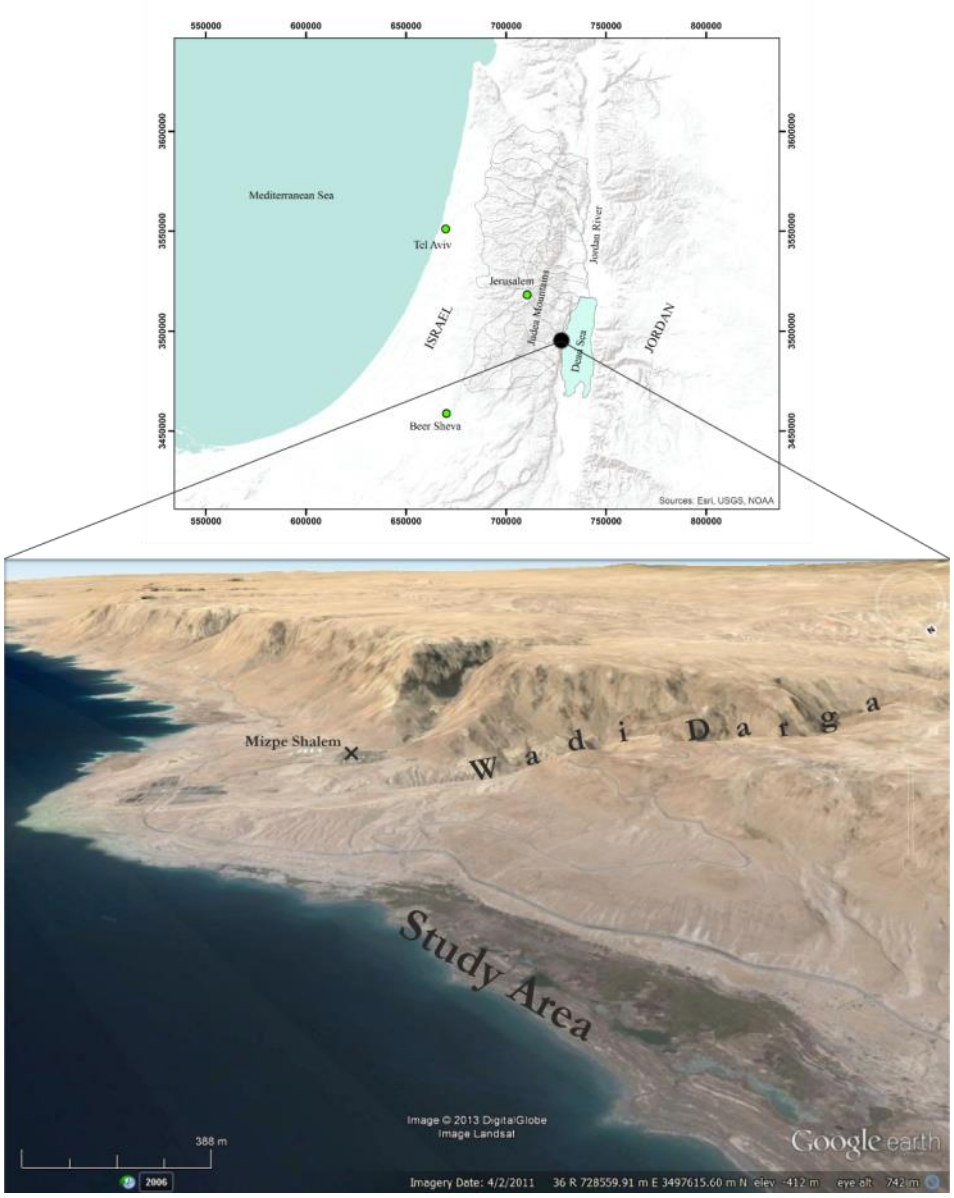

Figure 1: Location map of Wadi Darga and spot image of the study area

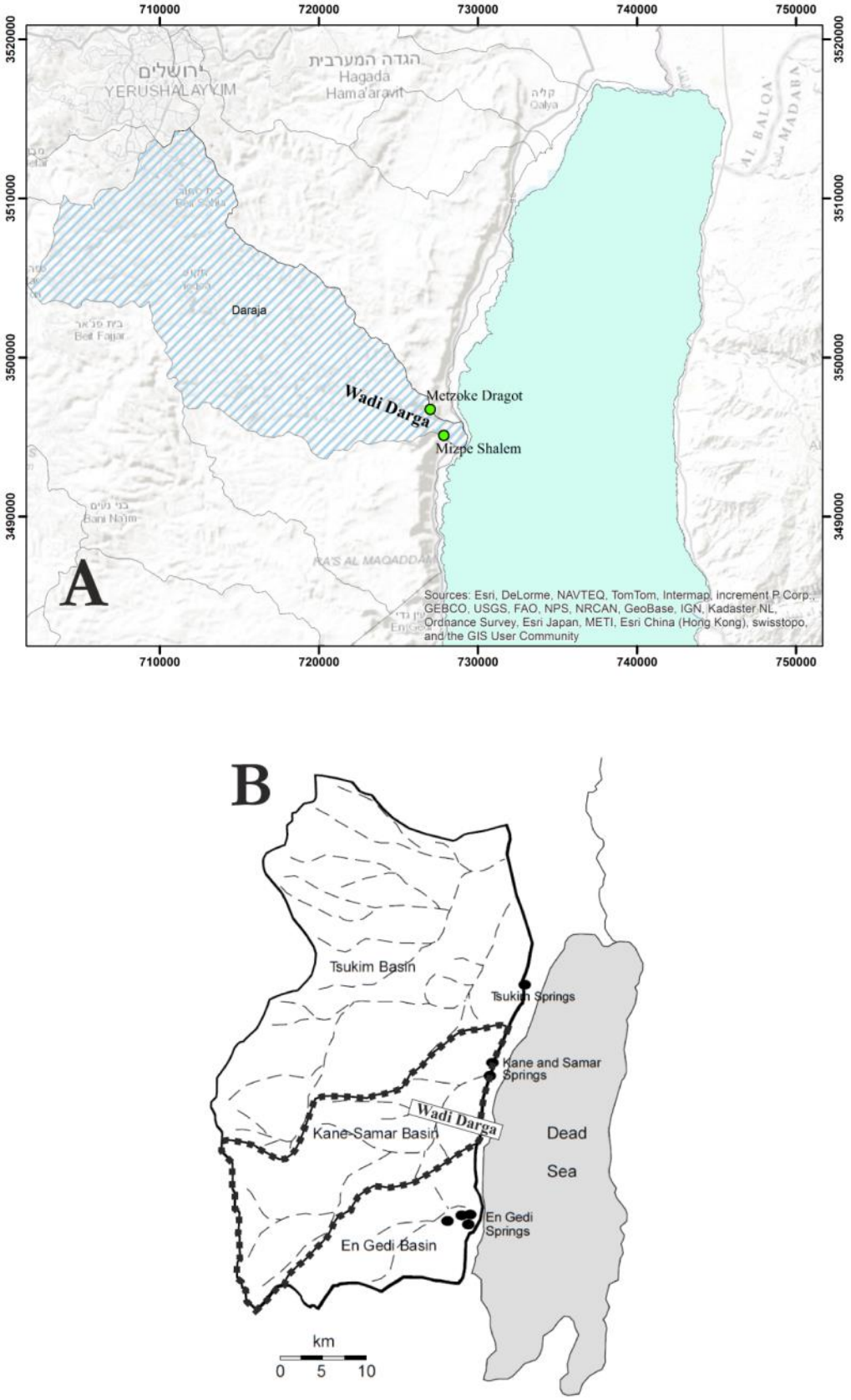

Figure 2: Surface drainage basin (A) and subsurface drainage basin (B) of the study area (after Ben-Itzhak and Gvirtzman 2005)

The extreme hydrological conditions of the study area strongly affect the water balance. Precipitation rates range from 600 to 800 mm/a on top of the Judean Mountains to less than 50 mm/a close to the DS (Figure 3). According to Blake and Goldschmidt 1947 and Yechieli and Ronen 1997 average precipitation amounts of 70 mm/a are attained in Wadi Darga. Due to the hydrological gradient the replenishments of the aquifer and surface runoff of the study area depend on the water supply from the Judean Mountains. The morphological appearance, geological structure and climate closely correlate along the descending slope of the Judean Mountains to the DS shore.

Hydrological parameters of rainfall intensity and duration are controlling flash flood runoff events in the rainy season from October to April, with January and February being the wettest months. Further important influence factors for water availability concern the size of the catchment area, as mentioned above, and rock types. The average annual temperature in the DS basin is 23 to 28°C with average daily means of 15°C in winter and 31°C in summer. The average relative humidity in the rift valley ranges from 20 to 30% with a minimum in June and maximum in January (Dweik and Shuval 2007; Flexer et al. 2009).

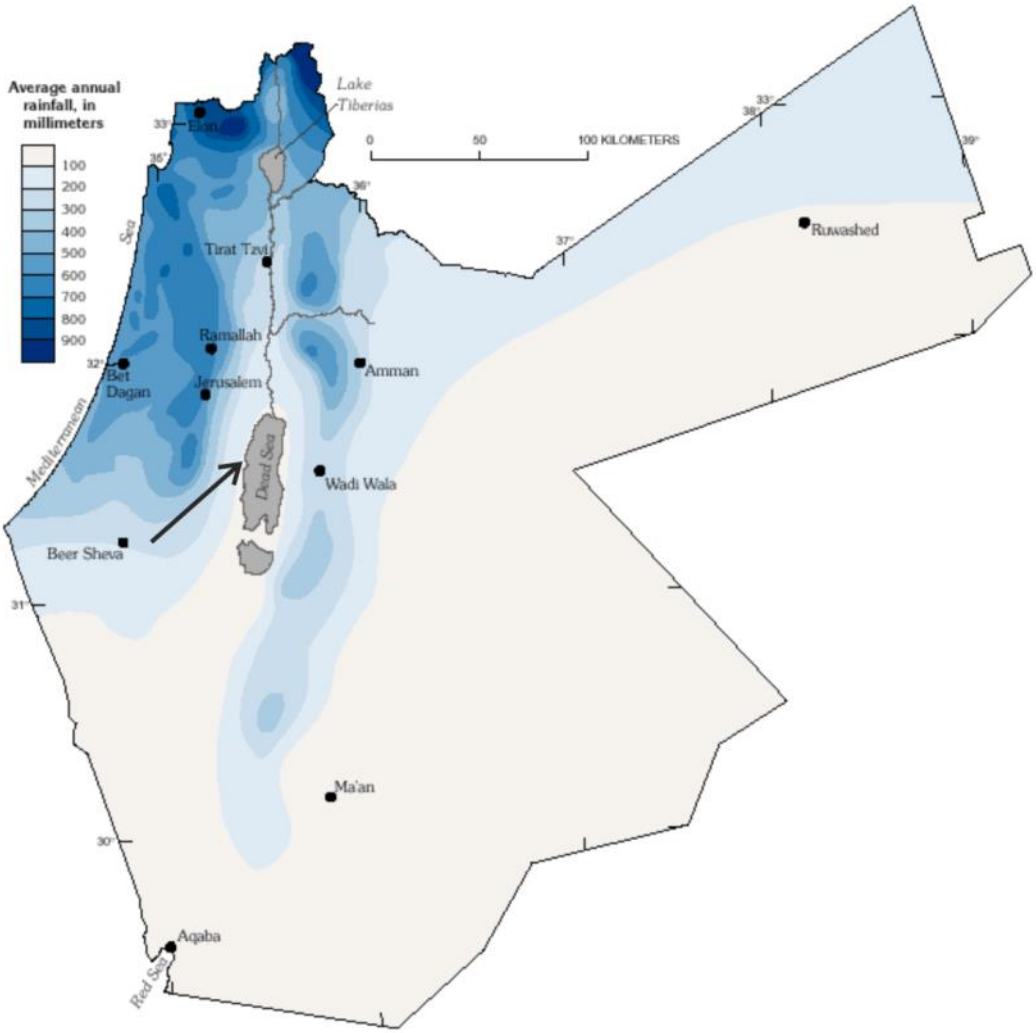

Figure 3: Average annual rainfall in the study area (Dweik and Shuval 2007)

3.2 Geology

In order to develop a schematic 2D cross-section along the specified study area available topographical, geological and hydrostratigraphic maps have been collected. Figure 4 and Figure 5 show the topological and geological setting of the study area.

- Geological maps:
  - Mizpe Shalem (Mor and Burg 2000)
  - En Gedi (Raz 1986)
  - Newe Zohar (Agnon and Sagy 2011)
  - Sedom (Agnon et al. 2006)
- DEM 5 m: UFZ (2011)
- GDEM 30 m: NASA and METI (2011)
- Dead Sea 2010: NASA (2010)
- Surface Catchment Areas: PWA (2005)

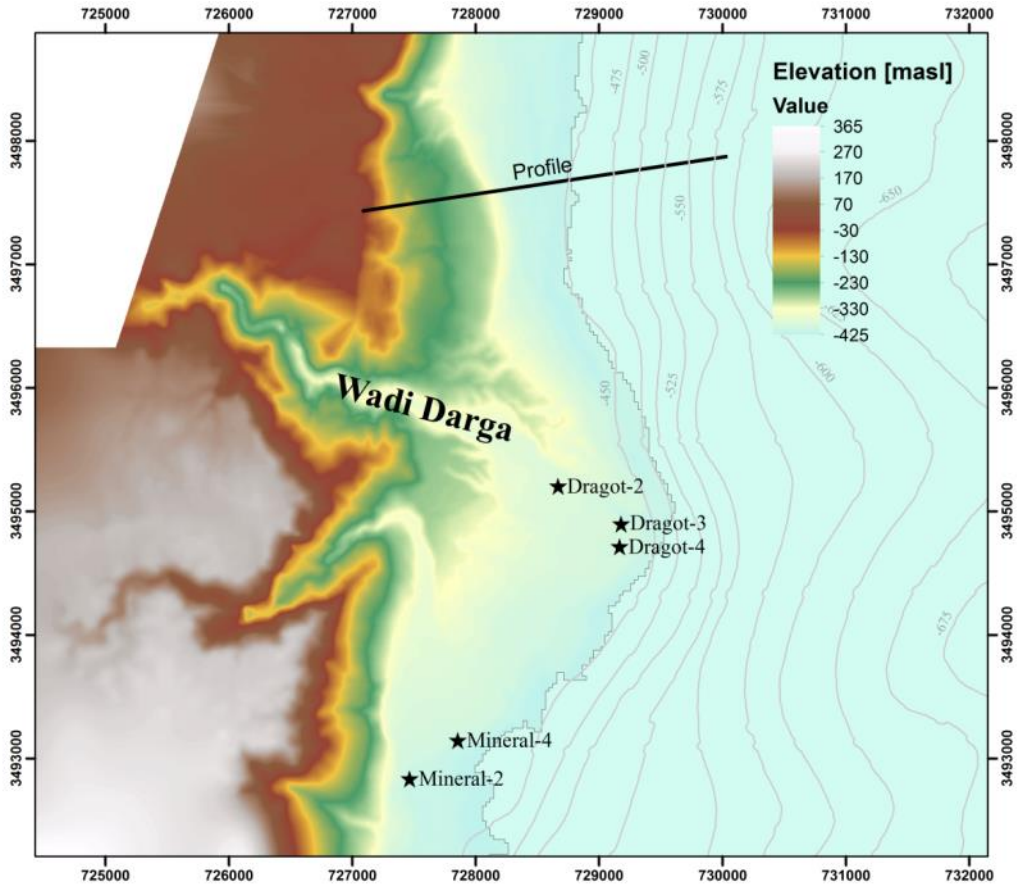

Figure 4: DEM of the study area. Borehole locations in the Darga region are displayed

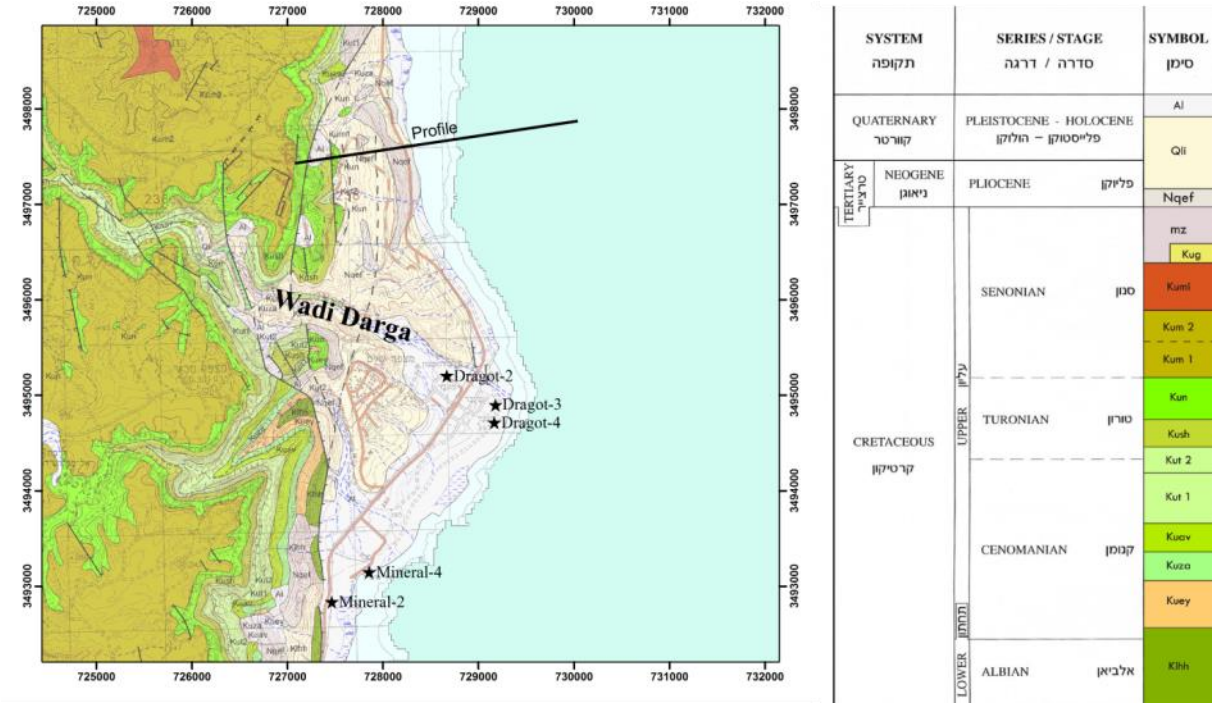

Figure 5: Geological map of the study area. The geological symbols are explained in Figure 7

The geological history of Wadi Darga as part of the DS region is comparably young. Together with the Jordan Graben the DS as water-filled part of a pull-apart basin encloses the strike-slip fault which is part of the East African Rift System. The DS basin has developed since 18 Ma when the 1,000 km large, still active DS transform fault was formed (Garfunkel and Ben-Avraham 1996). The tectonical setting of the fan-delta plays a major role in governing rock displacement and therefore water pathways and water type composition. The local fault pattern is determined by the normal faults of the Jordan – DS strike-slip system exposing 300 to 500 m high escarpments (Gardosh et al. 1990). Due to the lateral displacement of 105 km between the Arabian and African plate boundary the latitudinal continuation of outcropping aquifers on the western and eastern rift escarpment is different. The strike-slip segments of the pull-apart basin are arranged as step (en-echelon) faults which result in the graben structure as motion in the same sense (Ben-Avraham and Brink 1989). The structural geometry of the western escarpments is characterized by fault zones and folds with chiefly E-W and SW-NE orientations (Mallast et al. 2011). Sinkholes along the western DS shore occur along a lineament axis of 350° (Raz 2000; Abelson et al. 2002) and gain importance in the on-going text for the structural setup of the DSG sediment and physicochemical conclusions.

The western edges of the DS Basin are composed of Cretaceous and Eocene rocks, dominantly carbonates, and minor sandstones. The basin subsurface is made up of igneous rocks and post-Paleogene sediments. The western rift escarpment comprises four major aquifers (Figure 6): Kurnub Group (Lower Cretaceous), Judea Group (Upper Cretaceous), certain layers of the Mt. Scopus Group (Upper Cretaceous – Paleogene) and the DSG (Quaternary).

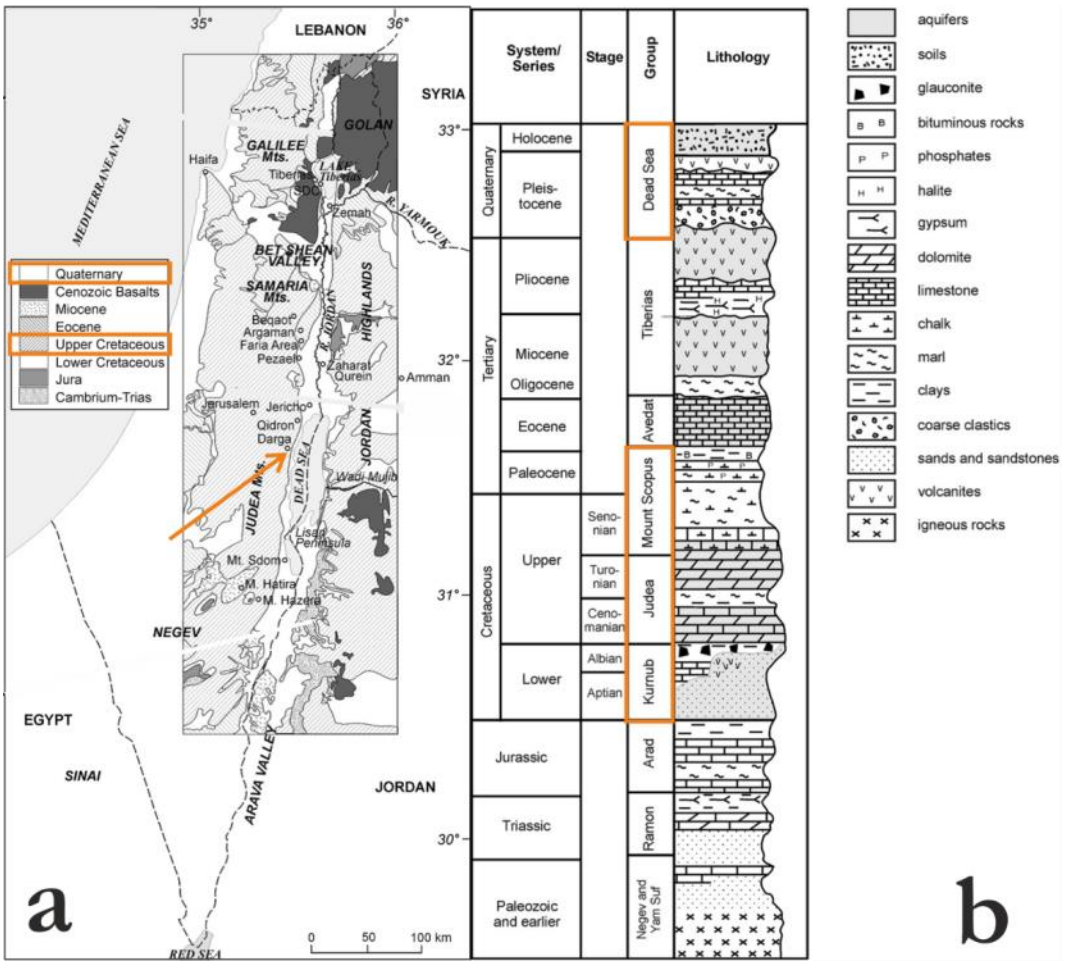

Figure 6: DS basin and regional aquifers (a) Outcropping geology in the Jordan valley area with emphasized study area (b) Important aquifers of the Jordan basin lithology and emphasized important groups for the western escarpment (after Möller et al. 2007)

Throughout the ages, the DS basin represents an epicontinental sea. During the Triassic, the epicontinental milieu issued from a post-rift subsidence resulting in carbonate and evaporite deposits of about 2,000 m thickness (Druckman and Kashai 1981). The reactivated Tethys rift was accompanied by basaltic volcanism in the carmel mountains during the Jurassic (Ben-Gai and Ben-Avraham 1995). Cretaceous age featured intensive erosion and karstification of Jurassic rocks. The uplift of the Arabo-Nubian Shield resulted in the sedimentation of terrigenic clastics and shallow-marine deposits of the Kurnub Group. Shallow-marine lagoon milieu favored the sedimentation of carbonates and anhydrite of the Judea Group (Buchbinder et al. 2000; Rosenthal et al. 2006). The limestones are intercalated with beds of chert, chalk, bituminous marls and chalks, phosphorite layers and clay. Their largest thickness can be observed in the central Judean Mountains (~ 900 m) reducing to a minimum of about 600 m along the DS coast. Further, corresponding to the synclines and anticlines of the Syrian Arc, the marly limestones of the Mt. Scopus group were formed (Flexer 2001).

At the beginning of the Palaeogene, transgression caused the deposition of marly-flinty carbonates of the Avedat Group (Michelson 1978; Hurwitz et al. 2000). Since the Early Miocene, alkali olivine basalts erupted in the northern and central Jordan basin (Garfunkel 1989). For instance, strongly fractured basalt outcrops near to Lake Kinneret in the northern part of the study

area. Due to the uplift of the graben shoulders, two accesses from the Mediterranean Sea to the DS dried out. The stratification of the Paleogene on the western DS shoreline represents an overlap of local and regional sedimentation patterns which results from interbedding of lacustrine and terrestrial sediments during the Paleogene. During the Eocene, shallow marine carbonates precipitated from the Mediterranean Sea, which at that time comprised the today's area of the DS. During the Early Miocene the initial graben system developed as result of decompression forces and the first sediment blocks have been detached. Clastic sediments dominated the depositional milieu during the Miocene. The marine influence from the open sea of the Mediterranean Sea stopped. Marine sediments from the Mediterranean transgression event deposited during the Lower Pliocene. Since the beginning of the Upper Pliocene the Mediterranean Sea finally receded and the Sedom lagoon covered the DS graben. The geochemistry of the DS basin is now controlled by the interaction of the brine and the inflowing freshwater (Katz et al. 1977; Stein 2001; Gavrieli and Stein 2006). During the Upper Pliocene the lake run dry partly and left behind thick layers of evaporites. Afterwards, again freshwater deposits from the wadi contributed most of the sediment. Additionally, Arava conglomerates were deposited along the study area as well. Concluded from the sedimentation patterns, the terrestrial sediments of the Tertiary prevail the marine deposits. Terrestrial sediments are assumed to be coarse gravel with a typical interbedding of clay.

In the Quaternary, the proceeding subsidence of the Jordan Graben resulted in seasonally waterfilled sedimentary basins (Horowitz 2001). The ablation of evaporites and flushing of brines constitutes the Lake Lisan whose progressive evaporation was the origin of the DS (Katz et al. 1977). Those processes made the geochemistry of the DS totally different to that of the Mediterranean Sea and even facilitate the density driven rise of saline waters along faults. Regarding the Quaternary stratigraphy, the postulated *Qli* section (cf. Mor and Burg 2000) is supposed to be divided into the Lisan Fm and the Samra Fm. Their deposits originate from the Lake Samra (~135 to 75 ka, Waldmann 2002) and the Lake Lisan (~75 to 15 ka, Torfstein et al. 2008) in the DS basin. The Lisan Fm consists of thin-bedded layers of aragonite, chalk, gypsum, clays, separating the Samra permeable layers and the alluvial clastic sediments. The Samra Fm consists of two sub-units built up of conglomerates, sandstone and siltstone with a lower unit of conglomerates and an upper unit of bigger portions of silt layers and Lisan Fm interfingering. The uppermost Quaternary section *Al* is supposed to represent clastic sediments that are imbedded on the Lisan sediments and in the Lisan layers as lobes of conglomerates (Begin 1974; Guttman 2009).

The focus of investigation is the coastal alluvial DSG sediment of Quaternary age. This lake sediment exhibits a total thickness 160 m (Chen et al. 2009) and is discordantly overlaying the limestone outcrops of the Judea Group. A geological columnar section of the Mizpe Shalem area with the DSG as uppermost unit is displayed in Figure 7.

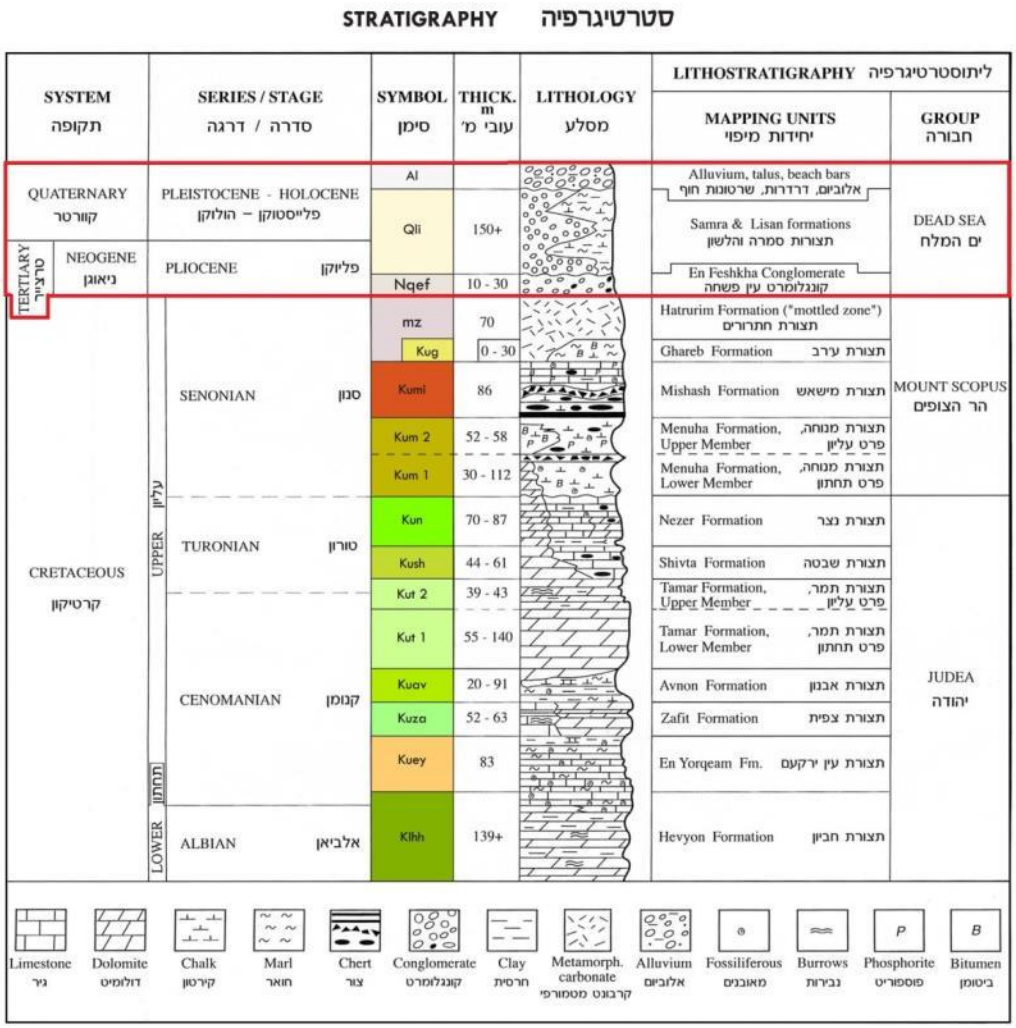

Figure 7: Stratigraphy of the Mizpe Shalem area (Mor and Burg 2000). The subdivision of the DSG is discussed in the on-going text

Used publications that helped to resolve the structure of the DSG sediment, particularly Wadi Darga, are Gardosh et al. (1990), Yechieli et al. (1990), Yechieli et al. (1993), Enzel et al. (2000), Mor and Burg (2000), Horowitz (2001), Yechieli et al. (2001), Eyal et al. (2002), Salameh (2002), Yechieli (2005), Abelson et al. (2006), Bartov et al. (2006), Gavrieli and Stein (2006), Migowski et al. (2006), Yechieli et al. (2006), Yechieli (2006), Waldmann et al. (2007), Torfstein et al. (2008), Wernicke (2010) and Haliva-Cohen et al. (2012).

Only a handful of information about the geological subsurface of the focus area is available. There are no boreholes which intersect the entire DSG sediment. Available drilling locations in the DSG sediment of the Wadi Darga outlet are for instance Mineral-1, Mineral-2 and Mineral-3 that are published in Yechieli et al. (2006) (Figure 8). Due to the scarcity of basic geological cross-sections only some rough sketches of the geological situation have been drawn, like in that Figure 8. Some drilling records of the DSG sediment are compiled in Figure 9.

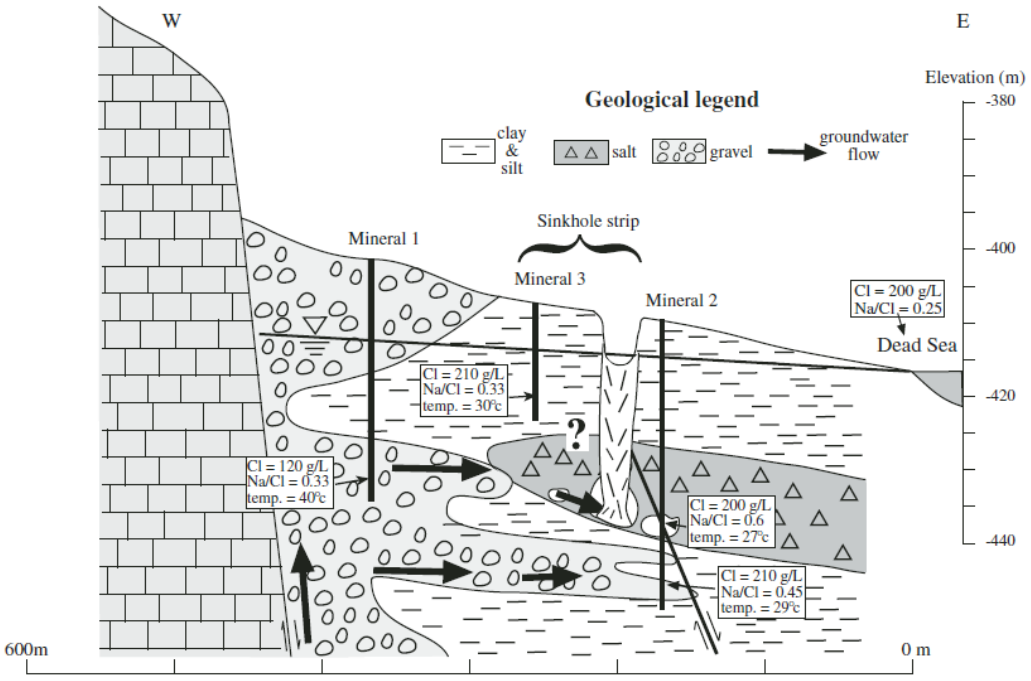

Figure 8: Location and depth of boreholes in the Mizpe Shalem site (Yechieli et al. 2006, for location of the Mineral beach drillings confer Figure 4)

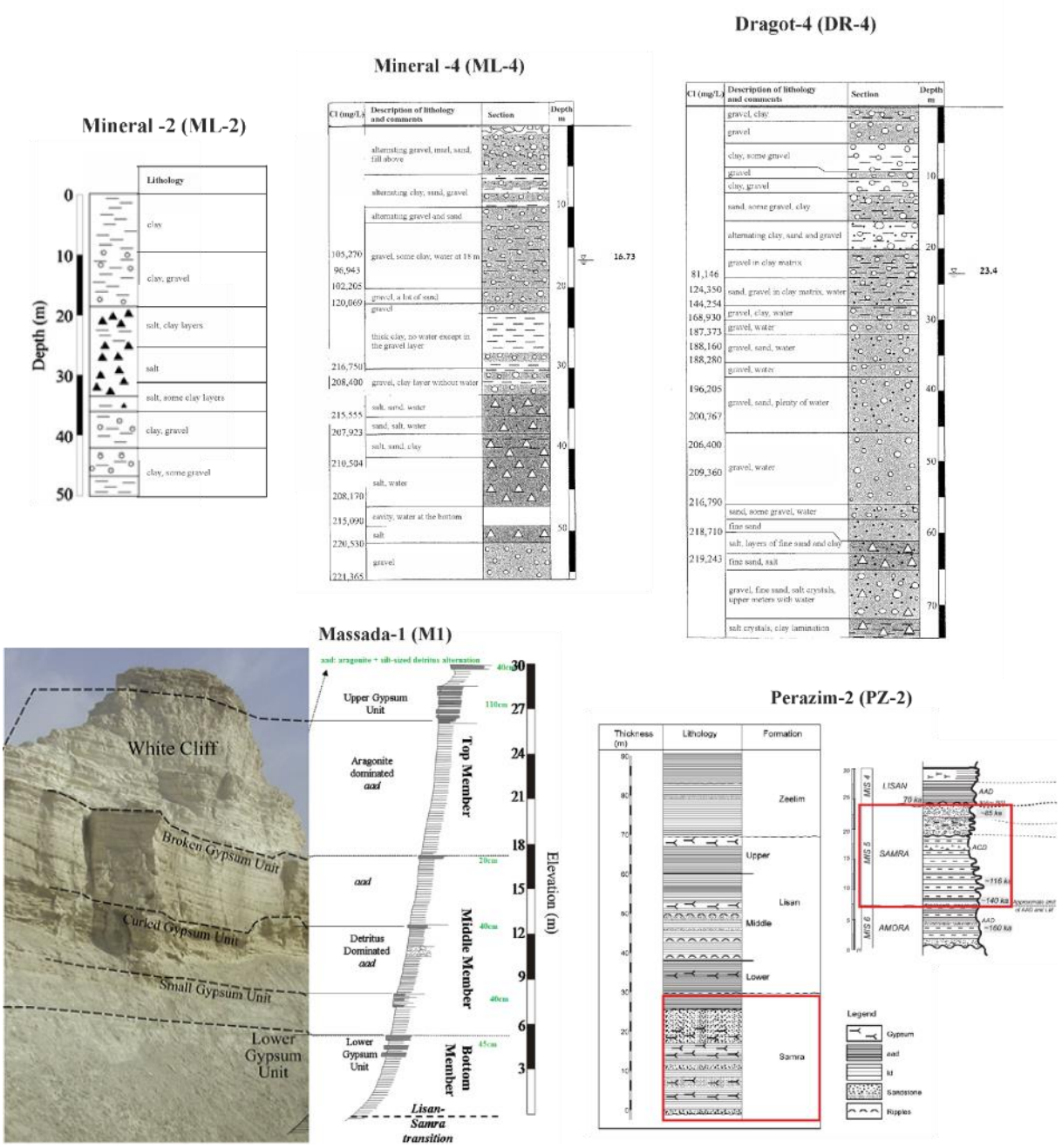

Figure 9: Drilling records of ML-2 (after Stein et al. 2010), ML-4 (after Yechieli 2005), DR-4 (after Yechieli 2005), M1 (after Torfstein et al. 2008 and Torfstein et al. 2013) and PZ-2 (after Waldmann et al. 2007 right and Haliva-Cohen et al. 2012 left)

During research additional borehole logs were found in old reports of the GSI library in Jerusalem which originate from Yechieli (2005). Borehole locations along the western DS, which intersect the DSG sediment are illustrated in Figure 10 and explained in Table 1. Available boreholes are exclusively situated in the Darga region or south of it, in particular in the En Gedi region and in the southern DS region.

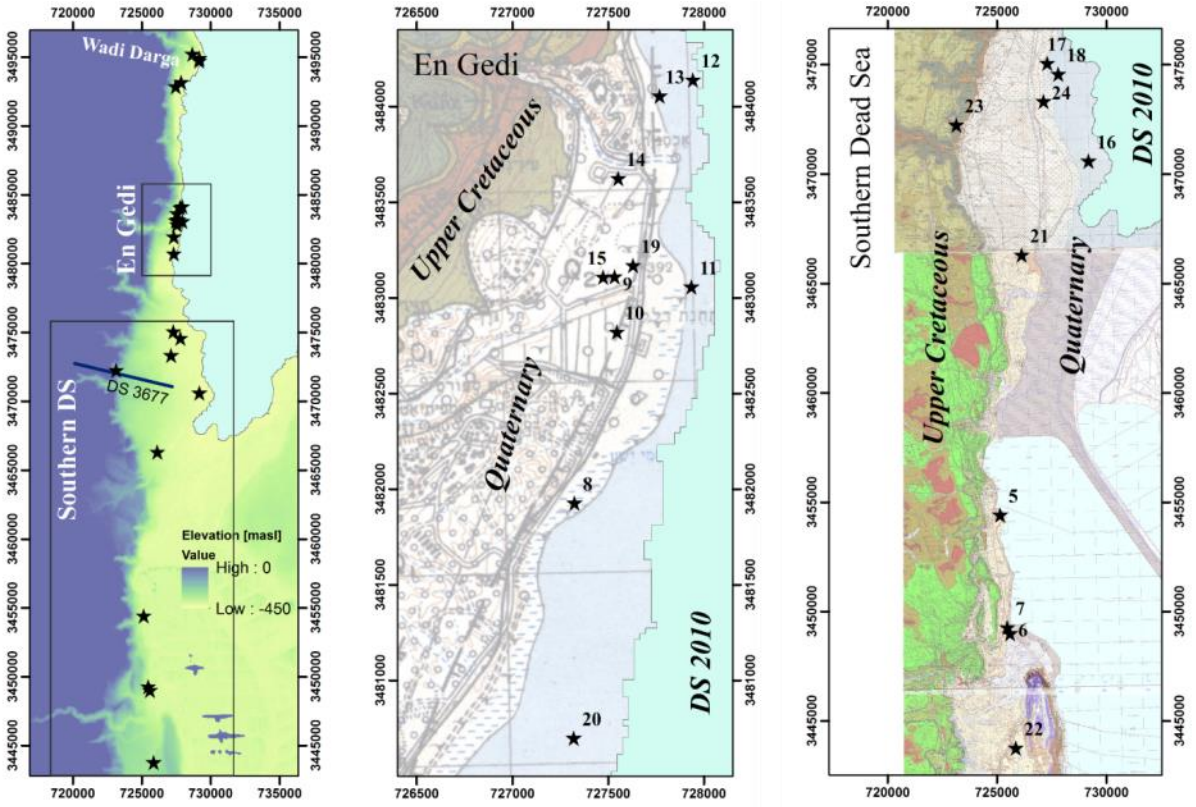

Figure 10: Location of boreholes along the western DS shoreline which intersect the Quaternary unit

Table 1: List of boreholes. Additionally, groundwater heads are designated: *1* Yechieli (2005), *2* Yechieli et al. (2006), *3* Yechieli et al. (2010)

ID	Borehole	Location	x_utm	y_utm	Elevation [masl]	Depth [m]	GW head [masl]	Year of measured GW head	ref. GW head
0	Dragot-2	Dragot	728669	3495202	-381.16	96	-413	2012	3
1	Dragot-3	Dragot	729180	3494896	-390.08	85	-413.12	2005	1
2	Dragot-4	Dragot	729168	3494713	-393.32	75	-416.72	2005	1
3	Mineral-2	Mineral Beach	727466	3492834	-406.18	50			
4	Mineral-4	Mineral Beach	727857	3493145	-401.17	56	-417.90	2005	1
5	EB-2	En-Boqeq	725147	3454414	-388.36	80	-393.20	2005	1
6	NZ-1	Neve Zohar	725594	3448992	-388.60	93			
7	NZ-3	Neve Zohar	725470	3449269	-386.94	77	-391.44	2005	1
8	YS-1	Yesha	727325	3481927	-399.25	55	-406.55	2005	1
9	EG-7	En Gedi	727534	3483110	-389.03	65	-415	2006	2
10	EG-13	En Gedi	727546	3482821	-388.20	67	-408	2006	2
11	EG-15	En Gedi	727935	3483057	-407.80	20	-417.80	2005	1
12	EG-16	En Gedi	727943	3484138	-414.70	12	-417.20	2005	1
13	EG-17	En Gedi	727769	3484054	-396.46	65	-416.39	2005	1
14	EG-18	En Gedi	727553	3483623	-385.99	80	-409.03	2005	1
15	EG-19	En Gedi	727475	3483108	-387.74	60	-418	2005	3
16	DSIF	Zeelim	729183	3470595	-394	35	-414	2006	2
17	HS-2	Hever South	727293	3475059	-393	78	-411	2006	2
18	HS-3	Hever South	727803	3474569	-393	40			
19	MAAZ1A	Mazor	727630	3483169	-391	80	-415	2006	2
20	MZ-1	Mazor	727321	3480699	-408.68	68			
21	M1	Massada	726133	3466304	-374	30			
22	PZ-2	Perazim	725864	3443764	-300	30			
23	DS3677west	En Gedi	723149	3472242					
24	DS3677east	En Gedi	727129	3473322					

With respect to the deposition geometry of the Wadi Darga fan-delta, similarities are largest to lacustrine fan-deltas postulated from Gilbert (1914). Gilbert deltas (Figure 11) are developed in tectonically active regions, as it is valid for the DS area. Recent examples are river outlets to Lake Malawi (Scholz et al. 1993) or receiving waters of Lake Wakatipu, New Zealand (Pickrill and Irwin 1982). The typical lake for a Gilbert-delta is a freshwater lake. However, saltwater can be

considered in a similar way: The density and therefore sedimentation velocity is the only distinguishing feature resulting in a larger horizontal transport within saltwater. The DS peculiarity is that the lateral extension of the delta is restricted to the interaction with the dynamic DS water level and the resulting thick deposition of fine sediments compared to the widespread tilted coarse-grained fore-set of a typical Gilbert delta.

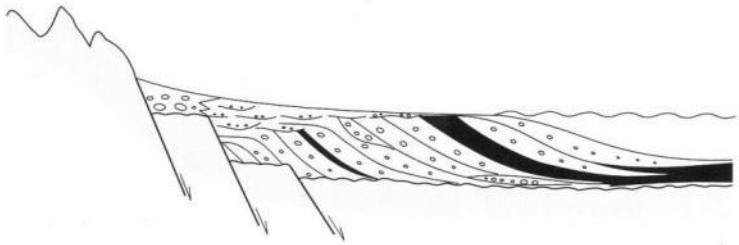

Figure 11: Schematic Gilbert fan-delta. Its geometry and lacustrine depositional milieu is comparable to the arid Wadi Darga fan-delta (Massari and Colella 1988; Schäfer 2005)

Sediments of Wadi Darga consist of poorly-consolidated material (Eyal et al. 2002). Fine sediments of clay and salt layers prevail coarse gravel layers with respect to the thickness of the sediments. Due to the decrease of transport energy in lateral direction sediments reveal finer grain size away from the mountains to the DS (Yechieli et al. 2006), in particular <500 m from the shore (Yechieli and Gat 1997).

According to the depositional environment, DSG sediments can be subdivided into fluviatile, lacustrine and aeolian sediments. Fluviatile sediments are clastic sediments that derive from the Jordan river and as well from wadi deposits which have been transported during flash floods in the rainy season. As suspensive material those fluviatile sediments are deposited on the lake bottom. Lacustrine sediments are considered as salt sediments precipitated from the DS. The differentiation between lacustrine and fluvial sediments is supported by Gardosh et al. (1990). Material deposited by air additionally contributes to the amount of fine-salty sediments.

The DSG sediments are built up of Holocene Post-Lisan Fm, the Pleistocene Lisan Fm and the Pleistocene Samra Fm. After Stein et al. (2010) a salt sequence and marly sediments unconformably overlie the laminated glacial Lisan aragonites. The uniform Pleistocene section below the Post-Lisan deposits is divided into the Lisan and Samra Formation of dominantly evaporites. The 50 m thick Lisan Formation consists of *aad* sediments embedded between gypsum units. According to Waldmann et al. (2007) *aad* sediments are characterized as layered calcitic marls (0.5 to 1 cm thick) that intercalate with aragonite and silty detritus. The upper part of the Lisan Formation exhibits aragonite dominated *aad* sediments, the lower is detritus dominated. Clay layers of 10 m maximum thickness intersect aragonite and gypsum deposits. The total interrupted thickness of the primary gypsum unit at the Massada M1 site was deposited with a calculated sedimentation rate of about 3 cm per 1 ka (after Torfstein et al. 2008). The Samra Formation below extends to a thickness of 40 m and is composed of clayey or sandy gypsum layers of several centimetres including thin *acd* sediments. Waldmann et al. (2007) described the *acd* sediments as layered calcitic marls (0.5 to 1 cm thick) that intercalate with laminated calcite and silty detritus.

The boreholes Mineral-2, Mineral-4 and Dragot-4 have been utilized for the setup of the DSG sediment. Their geology can be described as follows. The borehole Mineral-2 exposes clastic and salt deposits of the Holocene Post-Lisan Formation with a depth of 50 m. Cohesive material dominates the upper and the lower 15 m of the log with a larger share of gravel in the lower part. In between, pure halite precipitates occur, in the upper meters intersected by some clay layers.

The borehole Mineral-4 exposes clastic and salt deposits of the Holocene Post-Lisan Formation with a depth of 55 m. The first 25 m are composed of non-cohesive gravel and sand with some clay laminae or clay-dominating sections. A 10 m deep unit of thick clay and alternating gravel and clay layers underlies the upper coarse unit. Along the log meters 35 to 50 pure halite precipitates are deposited with the upper meters containing major sandy and clayey impurities. Several meters of the lower section are recorded as cavity. The salt unit is followed by homogeneous gravel.

The borehole Dragot-4 exposes clastic and salt deposits of the Holocene Post-Lisan Formation with a depth of 75 m. The first 30 m are dominated by cohesive clayey material with embedded gravel layers or inhomogeneous distributed gravels. From 30 m to 60 m thick gravel strata prevail layers of alternating gravel and sand. The intercalation of salt begins below 60 m. Pure halite precipitates and salt containing fine and coarse sediments (to meter 75) are underlain by the uniform layering which is described above.

The Massada M1 drilling was chosen to represent the Pleistocene Lisan Fm. The section is made up of layered calcitic marls of typically 0.5 to 1 cm thickness. The marls are intercalating with aragonite and silty detritus (*aad* facies). Top and bottom of the sequence exhibit homogenous gypsum deposits with a thickness up to 15 cm (Torfstein et al. 2008; Haliva-Cohen et al. 2012).

The Perazim PZ-2 geological section was chosen to represent the Pleistocene Samra Fm. This sequence consists of layered calcitic marls of typically 0.5 to 1 cm thickness. The marls are interbedded with sequences of laminated calcite and silty detritus (*acd* facies). The top and bottom of the section exposes gypsum and sand layers of several cm thickness (Waldmann et al. 2007; Haliva-Cohen et al. 2012).

Regarding the lateral continuation of the Cretaceous limestone towards the lake centre, there is only sparse information. The depth of the normal faulted blocks has been generally inferred from seismic cross-sections recorded at the location of En Gedi (Figure 12). According to the seismic cross-section the Cretaceous bedrock and the Pleistocene sediment fill can be verified. Block structures of the Cretaceous limestone exhibit displacement along faults. Within the outcropping Cretaceous rocks a conjugate fault system with inverse dipping compared to the normal faulted single block cannot be excluded at all. However, due to the lack of velocity information neither the depth of the normal faulted single block nor the location of the blocks relative to each other can be concluded. All the interpreted lineament angles are objected to the underlain velocity cross-section, i.e. true angles differ from the recorded time migration seismic cross-section. The geological cross-section of En Gedi is essentially deduced from that seismic information (Figure 13).

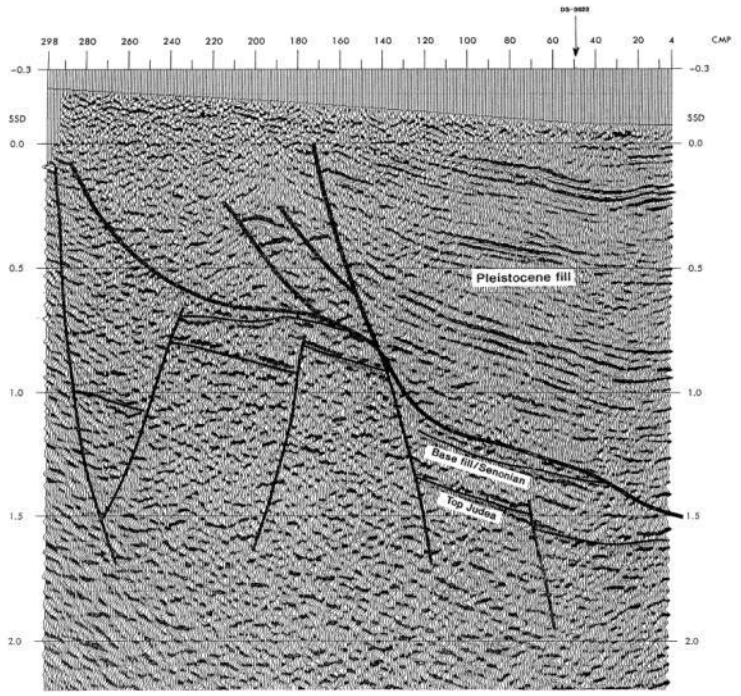

Figure 12: Seismic cross-section DS 3677 (time migration section), for the location cf. Figure 10 (I.O.C 1982)

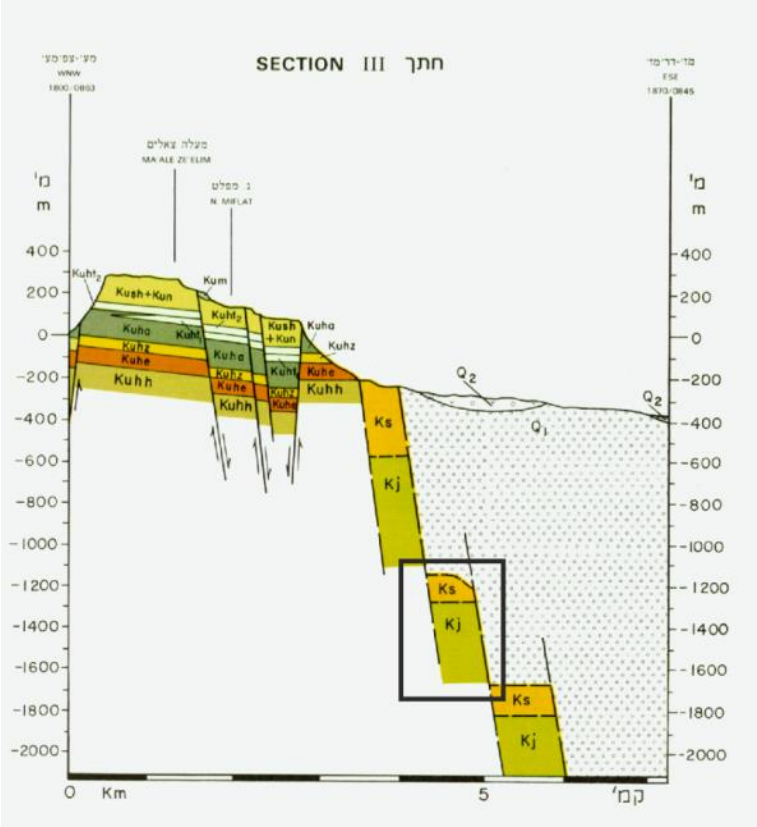

Figure 13: Derived geological cross-section from several seismic cross-sections which have been recorded in En Gedi. Note the depth and lateral extent of the single normal faulted block (Raz 1986)

3.3 Salt karst

The phenomenon of karstification in arid regions is not only common on carbonate rocks but also in rock salt, i.e. evaporites including gypsum and halite. According to Salameh (2001) within the Lisan Fm 3 to 6% of the total rock are salts. In terms of determining hydraulic flow patterns in the DSG sediment especially the resulting secondary porosity from karstification could potentially govern water movement along impermeable strata. The hydrochemical composition of the DSG sediment water represents the equilibrium to the outcropping host rock and represents a fingerprint of the study area with respect to inflowing, reacting and outflowing water constituents. The dissolution and precipitation of salt minerals and their concentration and dilution in a defined period of time play a major role in inducing conduit flow in the DSG sediment. Developed conduits (solution tubes) favor higher flow velocities and shorter residence times within the sediment. This behavior forces hydrogeological investigations in Quaternary aquifers to focus on discontinuous flow as well. The most recent imagination of conduits within the DSG sediment is displayed in Figure 14.

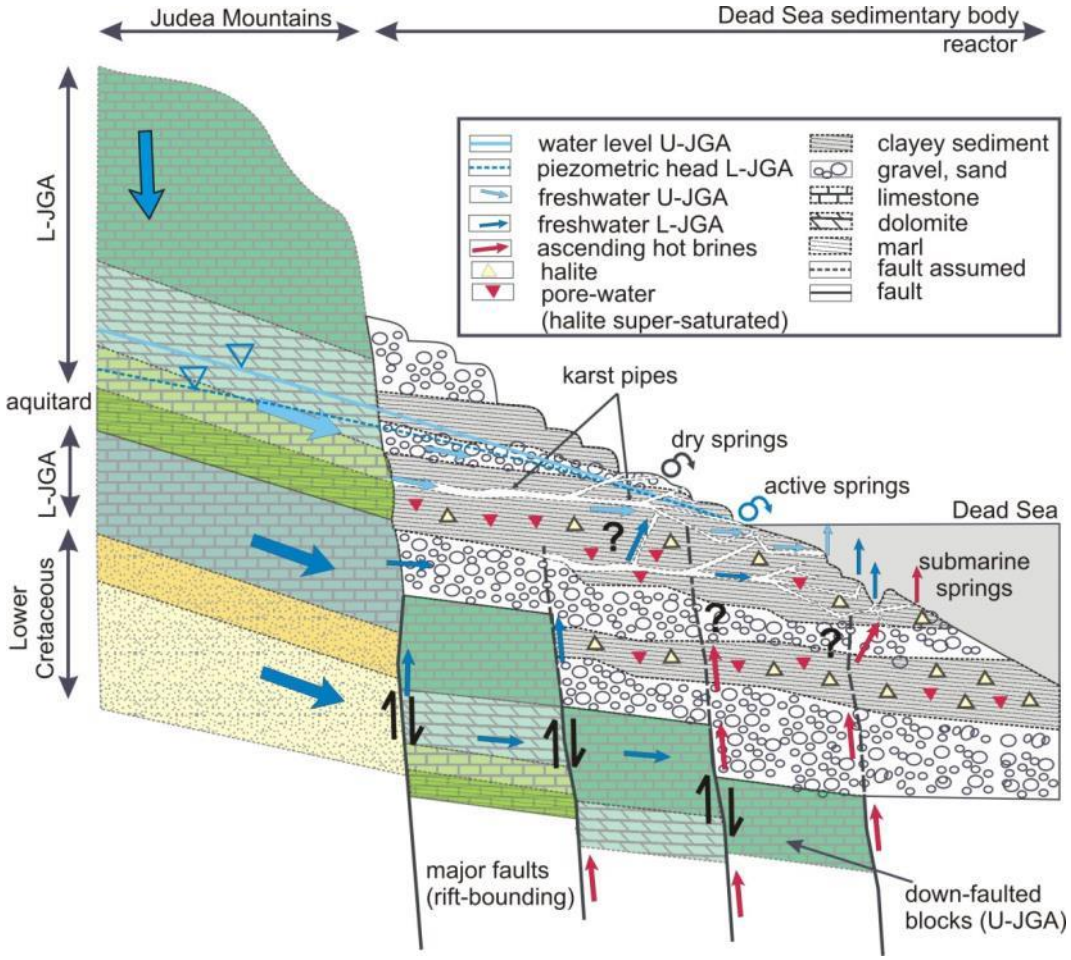

Figure 14: Preferential water pathways in the DSG sediment resulting in subaerial and sublacustrine discharges (Siebert 2013)

According to the geological drillings the lake sediments consist of salt clastics precipitated from the DS. Salt minerals with a solubility product lower than halite are precipitated. Due to permanent freshwater inflow undersaturated with respect to rock salt and subsequent subrosion halite is typically not able to attain the saturation concentration and therefore does not precipitate. Only,

at places where water flow is very low and crystal growth is not inhibited by varying water fluxes halite exceeds its solubility product and precipitates (Wernicke 2010). Distinctive halite layers containing salt crystals in a muddy matrix have been observed by Yechieli et al. (1993) in about 30 m depth in a drilling core near Zeelim. Upsalting towards the DS and other mechanisms that increase the concentration of the respective mineral phase promote precipitation.

Depending on the saturation index, halite is either still dissolved or was dissolved by changing inflow conditions and becomes karstified. The latter behavior can be intensively studied as phenomenon along the western DS coast where a huge number of sinkholes imply dissolution processes in the subsurface (Yechieli et al. 2006). The concerned salt layer is regarded as halite layer (opposed to the calcite, gypsum and aragonite laminae of the Lisan and Samra Fm, respectively) and occurs along the western DS shoreline. Its thickness varies from 2 to 26 m with its top ranging from -420 to -440 m msl to a depth of 20 to 50 m. The halite layer is characterized by low porosities and local horizons of high porosity and permeability (including cavities as well) (Yechieli et al. 2006). Frumkin et al. (2011) specified porosities in cavernous parts with 40%. Salt dissolution itself result in porosities up to tens of percent. Besides, this author proposed further porosity trends: Low porosity above the groundwater table, decreasing porosity in the gravel layers with greater depth and high porosity below the halite layer. According to Abelson et al. (2006) sinkhole occurrence is less where competent gravel and less weak or muddy sediments (silt, clay) exist. In fact, an increasing thickness of gravel layers above the salt layer can be recognized towards the alluvial fan centre. Beside the dissolution of halite layers, there is evidence for carbonate karst that is induced by sulfuric acid. Yechieli (2005) recognized H_2S smell in boreholes along the western DS coast. In fact, the Lisan and Samra Fm. contains meter thick gypsum deposits that indicate the origin for hydrogen sulfide. The conversion is intensively driven by microbial assimilation, inducing reducing redox conditions and subsequent sulfate reduction.

Observations of springs which dissolve Pliocene rock salt formations along Lake Kinneret are reported from Gvirtzman et al. (1997), Nativ (1997) and Flexer et al. (2000). Those saline springs are recharged by meteoric waters and discharge on active faults in and around the lake (Horowitz 2001). The dissolution of fossil rocksalt bodies from the Pliocene Mount Sedom Fm along the eastern DS shore has been observed by Belitzky and Mimran (1996).

3.4 Hydrogeology

Available data of the study area contain water table measurements of the DS and inflow areas, determination of spring horizons (although they are changing in very short time intervals), information about the boundary conditions (density measurements of the lake sediments, macrochemical analytics of pore water, groundwater level in Judean Mountains as constant head). A map with surface springs and sublacustrine discharges in the study area are displayed in Figure 15. Available hydrochemistry data is limited to samples from springs, sublacustrine discharges and sinkholes but not discussed in this study.

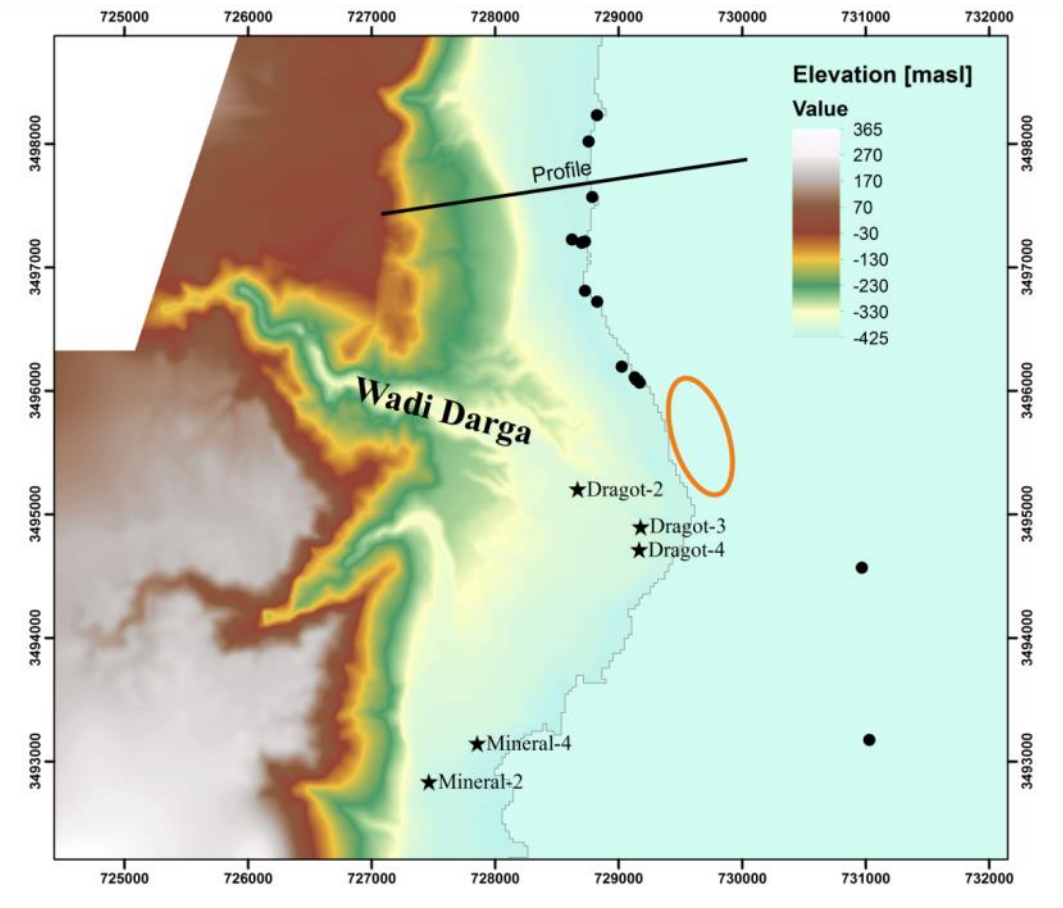

Figure 15: Surface and sublacustrine discharges which have been collected during field campaigns, conducted by C. Siebert, UFZ Halle. Encircled is the area with concentrated sublacustrine discharges inferred from thermal records

Surface and sublacustrine discharges have been recognized during diving campaigns from 2009 to 2012, conducted by C. Siebert, UFZ Halle. At a maximum depth of 30 m (-455 m msl) discharges have been proven. More frequently they have been found from -435 to -445 m msl. Density and oxygen measurements indicate discharges up to a depth of 50 m (-475 m msl). Regarding the spring discharge two kinds of sublacustrine discharges need to be considered. Springs of large extent are already discharging in the depth of some 5 to 20 m below sea level. The more passive springs can be observed along the shoreline to the shallow DS (e.g. -407 m msl, -412 m msl, -422 m msl, -425 m msl, according to Figure 15). With respect to the turbidity of the springs, the more passive and small outflows reveal clear water, the larger discharges contribute major amounts of suspended clayey material. According to thermal data (accessed by U. Mallast in

2011, UFZ Halle) especially the northern part of the Wadi Darga fan exposes sublacustrine outflows (Figure 15). Proven surface and subsurface discharges for the study area have been visualized in x-z view (Figure 16).

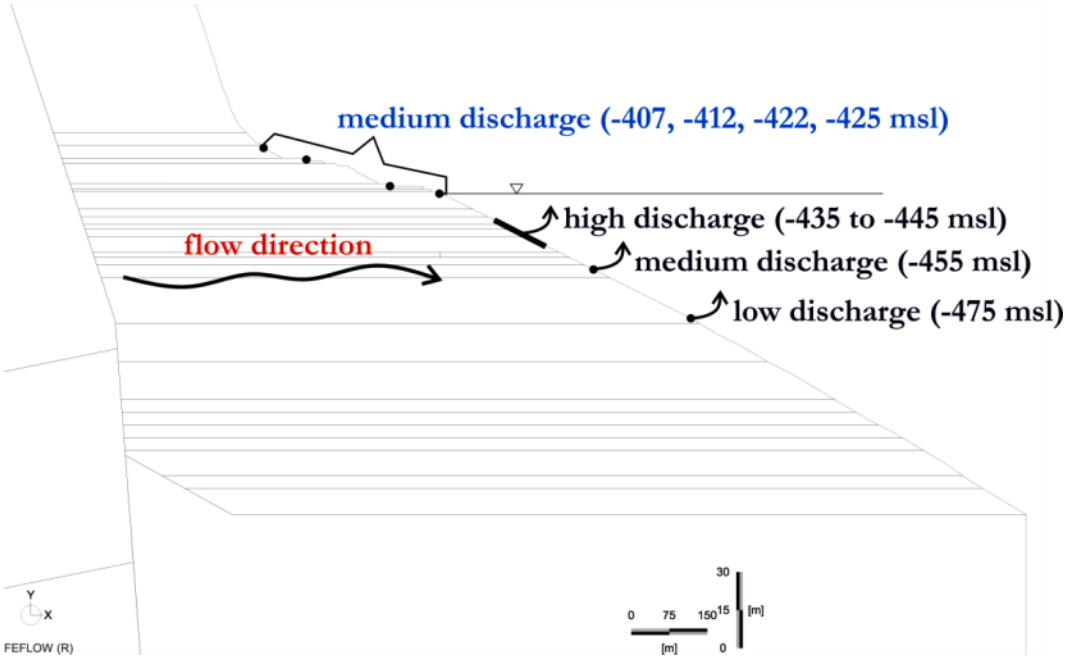

Figure 16: Depth-depending surface and sublacustrine discharges in the study area along the selected cross-section

Cretaceous limestones along the western shoulder of the DS reveal the high altitude gradient from the DS (-425 m msl) to the gentle plateau of the Judean Mountains. There, the watershed in N-S direction divides groundwater flow towards the Mediterranean Sea and the DS region. The groundwater network of the DS composes of two major aquifers systems: The Cretaceous carbonate rocks of the Judea Group and the coastal Quaternary alluvial aquifer (Arad and Michaeli 1967; Yechieli et al. 1995). The latter one is the focus of this investigation. The 2D-slice of the study area is located along the northern part of Wadi Darga. The graben shoulder contains the two aquifers Upper and Lower Judea group hydraulically divided by the En Yorqeam Fm (Figure 7). The Lower Judea Group exhibits phreatic conditions close to the watershed and becomes confined towards the DS. Regarding this property, the Judea Group is important for the hydraulic conductivity distribution along the DS shoreline and particularly determines the hydraulic potential for the adjacent DSG sediment. In order to gain some knowledge about adjoining water pathways, REY groundwater patterns give some indication as they coincide with respective groundwater recharge areas (Möller et al. 2009a). The several sublacustrine freshwater discharges do exhibit a significant aquifer signature from the Cretaceous Judea limestone. Due to overprinting within the DSG sediment the differentiation between the Upper and Lower Judea Group is not significant at all. Salt deposits such as gypsum and the duration of interaction with DSG minerals and interstitial brines change the REY signal (Ionescu et al. 2012). The hydraulic contact to the underlying aquiferous Lower Cretaceous Kurnub Group sandstones (Rosenthal et al. 2009) cannot be excluded. Eroded deposits and evaporative bodies below the DSG sediments (according to Gvirtzman et al. (1997) at least 5 km thick) are assumed to be not relevant for groundwater inflow into the DS due to the high compaction by overlying sediments. Furthermore, uprising

waters which are relevant for sublacustrine discharge (Gvirtzman et al. 1997) have to be taken into account.

Predominant direction of groundwater flow is from W to E towards the DS Basin (Figure 17). The structural geometry of the step faults is regarded as major controlling factor of groundwater flow in the study area, i.e. E-W and SW-NE (Mallast et al. 2011). The Holocene in fact exhibits structural elements that display ESE-WNW orientations with extensional directions of NNE-SSW (Gardosh et al. 1990; Enzel et al. 2000). Spring areas that are regarded to be structural controlled occur in En Feshka, Kane-Samar (including the study area), Qedem and En Gedi (Guttman 2000; Ben-Itzhak and Gvirtzman 2005; Mallast et al. 2011). Yechieli (2006) modeled the hydraulic conductivity with increased vertical hydraulic conductivity Kz and diminished horizontal hydraulic conductivity Kx values along faults.

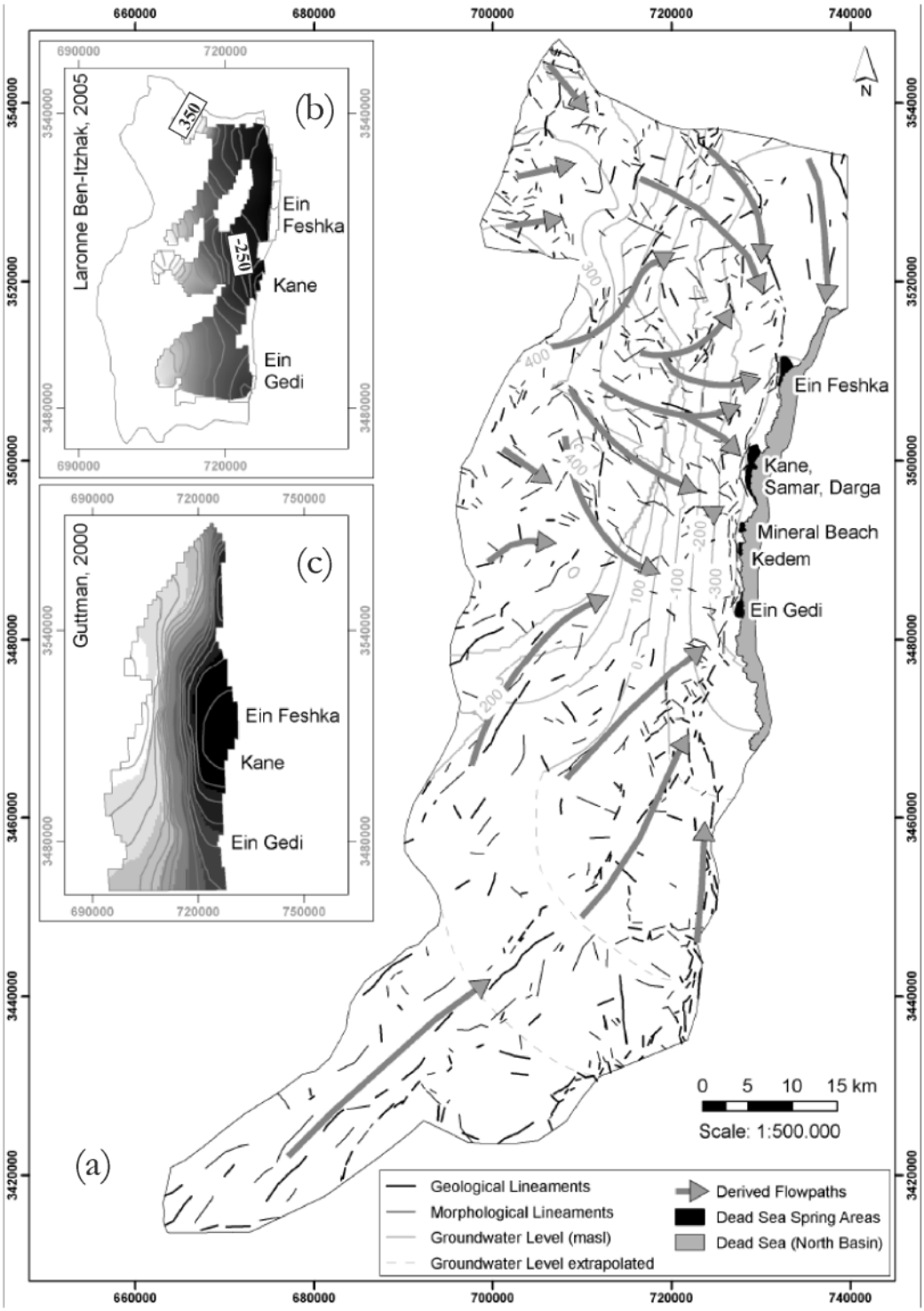

Figure 17: Groundwater flow direction from the Judean Mountains to the DS. (a) Concluded from lineament analysis in Mallast et al. (2011). (b) Water table elevations from Ben-Itzhak and Gvirtzman (2005) and from (c) Guttman et al. (2000)

Along the DS the perched Zafit Fm subaquifer is hosted within the Upper Judea Group aquifer and discharges on top of the En Yorqeam aquiclude in form of local springs within the cliffs (Wadi Arugot, Wadi David) (Figure 7). Secondly, the water discharges from the DSG sediments and results in hundreds of springs along the DS shoreline (En Feshka, Kane-Samar region, Mizpe Shalem, En Gedi). According to Ben-Itzhak and Gvirtzman (2005) springs from the west-

ern DS coast originate from both the Upper and Lower Judea Group. Water table elevations of both groups are displayed in Figure 18.

In a limited way the local groundwater flow reveals an inverse flow direction due to saltwater penetration. That behavior results from the tight lake sediments which cannot be compared to a porous medium of high hydraulic conductivity. The investigated DSG sediment itself exhibits GW potentials <5 m below surface in a distance <100 m from the shore and several 10s of m from 500-1,500 m away from the shore line (Yechieli and Gat 1997; Yechieli 2005) (Figure 10). However, field investigations near the DS shoreline spotted confined conditions with artesian groundwater as well (Christian Siebert, UFZ Halle, pers. communication). The DSG sediment is a double continuum characterized by less permeable layers and tubes of free water movement. The primary permeability of the sediments may be low but the secondary permeability in the dissolution conduits is high (cf. also the Quaternary sediments on the eastern DS shoreline in Jordan, in Salameh 2002). Inferred from the geological composition, the larger the distance from the shoreline the more permeable the deposited material. Field observation performed by C. Siebert from UFZ Halle confirmed, the coarse-grained upper part of the DSG sediment does not comprise water-bearing strata and therefore suggests a deeper hydraulic head.

Figure 18: Water table elevations for (a) Upper Judea Group and (b) Lower Judea Group (Ben-Itzhak and Gvirtzman 2005). The study area is denoted

The DS saltwater drain to the Judea aquifer might play only a minor role for the DSG sediment. The field observation of freshwater sublacustrine springs corroborates this thesis. However, the interaction between the coastal aquifer and the DS generates major discussions. The lateral continuation of a possible saltwater wedge within the DSG is not well researched. The interface in the easiest way can be calculated by the formula according to Ghyben-Herzberg. According to

that the depth of the interface in the DS with ρ (saltwater) = 1.23 g/cm³ is 4.35 times that of the groundwater head above sea level compared to 40 times in the ocean with ρ (saltwater) = 1.025 g/cm³ (Yechieli 2000). Yechieli (2000) reported the existence of this very shallow fresh-salt water interface along coarse-grained beds within the DSG sediment. Kiro (2007) promoted the understanding of the dynamic interface as response to the DS level drop in a temporal and spatial resolution with the help of the USGS SUTRA code (Voss 1984). The latest study of Yechieli et al. (2010) focused on the temporal development of the interface as response to simulated DS level drops. In that context, the potential of dewatering sediments of the DSG has to be taken into account, e.g. Yechieli and Gat (1997) discerned wet spots of low hydraulic conductivity and high saline pore water. The behavior of groundwater levels at different stations during long-term monitoring was therefore used to deduce possible sediment compositions of the respective study area. In detail, high-permeable alluvial fans such as the Darga site exhibit larger groundwater level drops and are more prone to groundwater level variations than low-permeable sites. With respect to grain size trends from the mountain outcrop to the DS, groundwater head variations are not only regarded as a function of the permeability of the aquifer but because of that should also be a function of the site distance from the DS.

The hydraulic connection between the DSG sediment and the DS results in within-days groundwater level changes as response to DS level variations (Yechieli et al. 1995). With increasing distance to the DS the water level drop decreases (Yechieli et al. 2009). Some locations exhibit a dynamic steady-state (Kiro et al. 2008), others show a smaller groundwater level drop compared to the DS (Yechieli et al. 1995). The nowadays decrease of the DS level maintains circulation of saline-waters to the coastal aquifer and results in continuous sediment flushing (Kiro et al. 2008).

Due to the occurrence of salt layers in the DSG sediment and low groundwater flow velocities towards the Quaternary layers the receiving freshwaters are subjected to salt enrichment resulting in increasing water densities. The impact of ascending thermohaline waters during that process have to be considered. Along the fresh-salt water interface both the density difference to the DS and the inherent brackish sediment pore water properties need to be focused when discussing flow and transport mechanisms.

Low precipitation and high evaporation rates in the direct environment around the DS result in less to not existent groundwater infiltration. The available groundwater originates from the Judean Mountains which are the recharge area. Therefore, the relative contribution of groundwater recharge on the DSG sediment from meteoric waters can be neglected.

4 Model design

4.1 Conceptual model

The important geological structures of the numerical model were designed in ArcGIS 10. Assumptions about the lateral extent and thicknesses of geological formations are based on literature references.

Different hydrogeological systems are available in the study area. To conceptualize the hydrogeological compartment interconnectivity of the DSG, per se two systems need to be distinguished. Both systems in common have the saline pore waters that are comparable to the DS salinity. The first is characterized as a passive hydrogeological system that dominantly preserves the surface-near salt layers of the DSG sediment and predominantly consists of clastic sediments and halite (Figure 19, A). The pore space of the salt environment is dominated by a fluid, which is supersaturated with respect to halite. Precipitating salt may clog possible pathways of groundwater towards the DS. Though, inflowing groundwater induces erosion that results in salt karst features of different extent and density and allows preferential flow and transport to the DS. The matrix of the surrounding sediments still represents the salty and clayey DSG sediment with a low interconnected porosity, exhibiting hydraulic conductivities lower than 10^{-9} m/s. Therefore, the concept is to manage the karst features in the way of a karst tube network within the low permeable DSG sediment.

The second system is formed by the deposition of terrestrial clastic material flushed into the lake by runoff events of Wadi Darga. That environment represents the area around the outlet of Wadi Darga and is deposited in form of a typical delta structure. The clastic environment favors hydrogeological active conditions with the salt layer being already dissolved by inflowing freshwater (Figure 19, B). The transport and accumulation of terrestrial clastic material by runoff from Wadi Darga are responsible for its delta-like structure. The observable absence of surface and sublacustrine discharges directly in front of the delta implies water-retaining strata in the fan that might prevent outflow. The resulting low bulk hydraulic conductivity of this structure may divert water to more permeable or karstified layers in the north of the fan-structure where the highest density of surface and sublacustrine discharges has been observed. Depending on the subsurface flow velocity and the extent of the permeable layers, or conduits, the input of suspended clayey material varies and contributes to the characteristic composition of discharging waters to the DS.

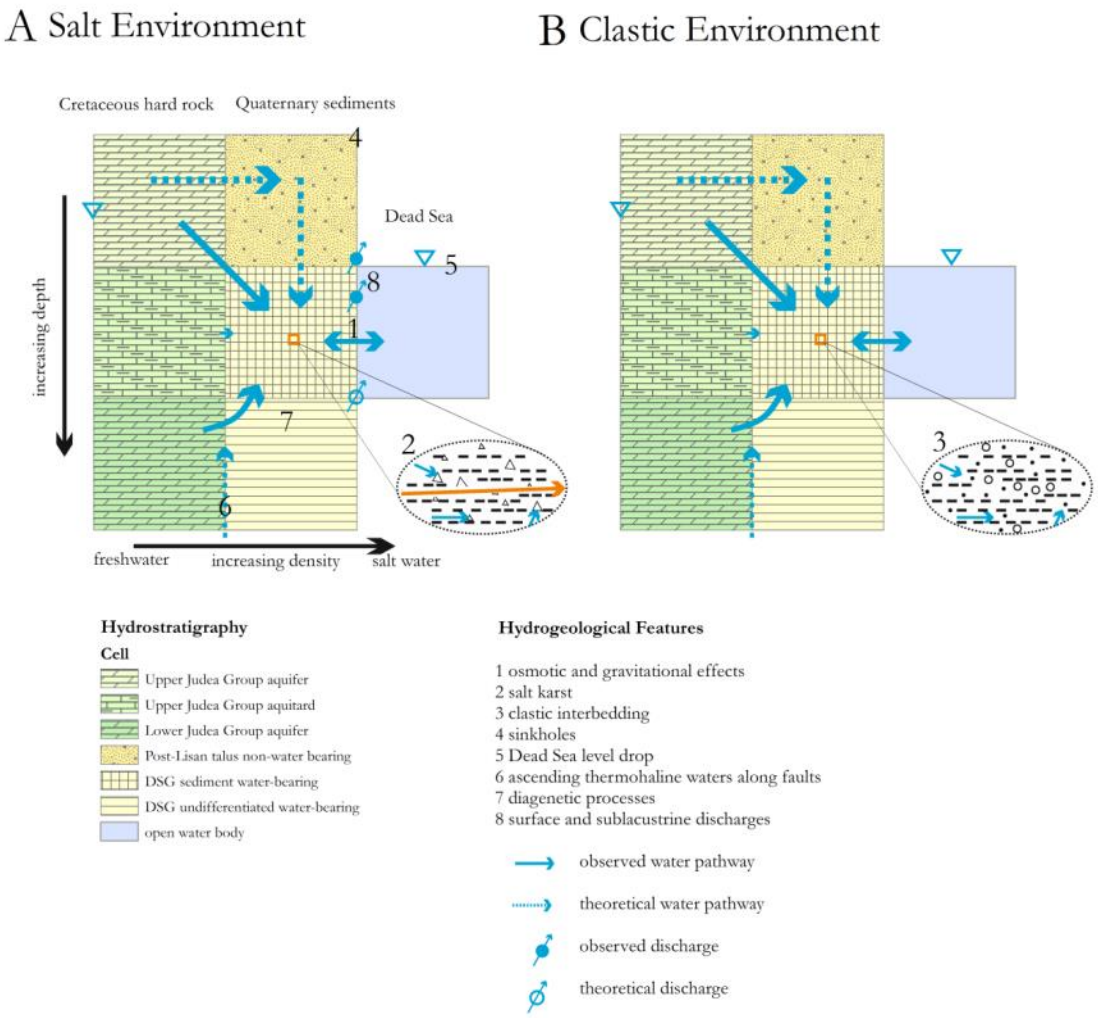

Figure 19: Hydrogeological settings of the Wadi Darga considering a flow behavior induced by (A) salt features and low sediment transport and (B) clastic mixing and high sediment transport. Vector length is as measure for the transferred water volume

The aim of this thesis was to understand the flow and transport processes in the first, the salty layer environment north of Wadi Darga. Therefore, a geological cross-section in the northern part of Wadi Darga was chosen. That area is also characterized by observable sublacustrine discharges (for location see Figure 4). The cross-section length is about 3,000 m with a direction of 81.5° which is perpendicular to the sinkhole occurrence direction of 350° (cf. chapter *Geology*). The DSG topography of the slice was rastered with a small interval of about 5 m along the subaerial curvature and with a larger interval of 50 m along the DS bathymetry (Hall 2000).

The slice geometry is visualized in Figure 20, Figure 21 and Figure 22. The maximum depth for the conceptual cross-section was determined to -1,400 m msl. The maximum displayed depth of the DS water is 125 m (-550 m msl) with a maximum lateral extent of 1,200 m. The DSG sediment referred from the drillings exposes a thickness of maximum 160 m with a final depth of -550 m msl and a maximum lateral extent of 1,900 m. The overlying terrestrial sediment cover is deposited eastwards from -210 m msl with an average thickness of 120 m. The Cretaceous lateral outcrop of about 450 m exposes an elevation difference of nearly 200 m starting at -10 m msl. The steep gradients of the Cretaceous (~20°) and coarse-grained sedimentary cover (from ~10°

to ~30° on the fore-slop to the DS) are opposed to the shallow gradients of the DSG sediment (~7°). The bottom morphology of the DS is flat with 7°. Horizontal depositions of the DSG sediments were assumed due to lacustrine sedimentation processes.

The vertical geological resolution is based on the surface curve and the projected thickness of geological formations according to Mor and Burg (2000). The intersection between geological layers and the morphology was deduced from the overlapping DEM 5 m map and the geological map. The projected DEM 5 m map revealed a small displacement error versus the correctly projected geological map. The displacement was corrected by a DEM-shift of -115 m in x and -65 m in y direction.

The setup of the Cretaceous aquifers was arranged in blocks with an assumed slope angle of about 70° in 1:1 x-z-projection and estimated outcropping width of approximately 500 m. The detached Cretaceous block was constructed at a depth of -1,100 m msl with a thickness of 150 m. Basically, these assumptions were deduced from Raz (1986) visualizing the spatial dependencies of the geological fault system units. The graben fill of the DS is summarized as undifferentiated DSG sediment (cf. Bender 1968). The compositions of these sediments are similar to that of the differentiated DSG sediments.

The top of the group of intercalated terrestrial and lake sediments within the differentiated DSG sediment was assumed to be not higher than -400±30 m msl as typical Holocene DS lake levels (Bookman et al. 2004; Migowski et al. 2006; Torfstein et al. 2008). The unit with subhorizontal terrestrial clastic sediment above the Lisan Formation is designated as Post-Lisan Formation (maximum thickness of 200 m).

To resolve the DSG sediment below the Post-Lisan Formation, the Lisan and Samra Fm layers with a structural resolution of about 10 m were inferred from the Massada M1 and the Perazim PZ-2 drilling (Table 2, Table 3, Table 4). The DSG sediment of the final conceptual models (Figure 20, Figure 21, Figure 22) reveals a total thickness of 160 m and was aligned with constant thicknesses and constant material distribution over the entire DSG sediment body.

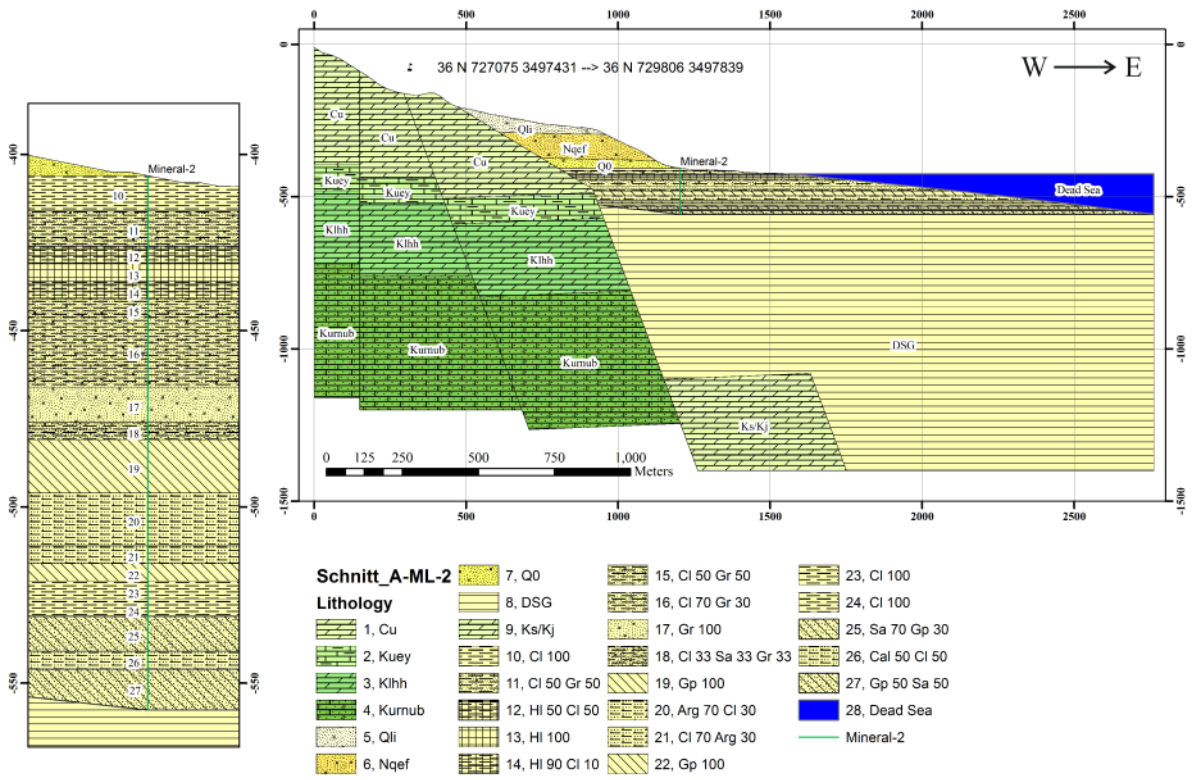

Figure 20: Conceptual model for slice ML-2

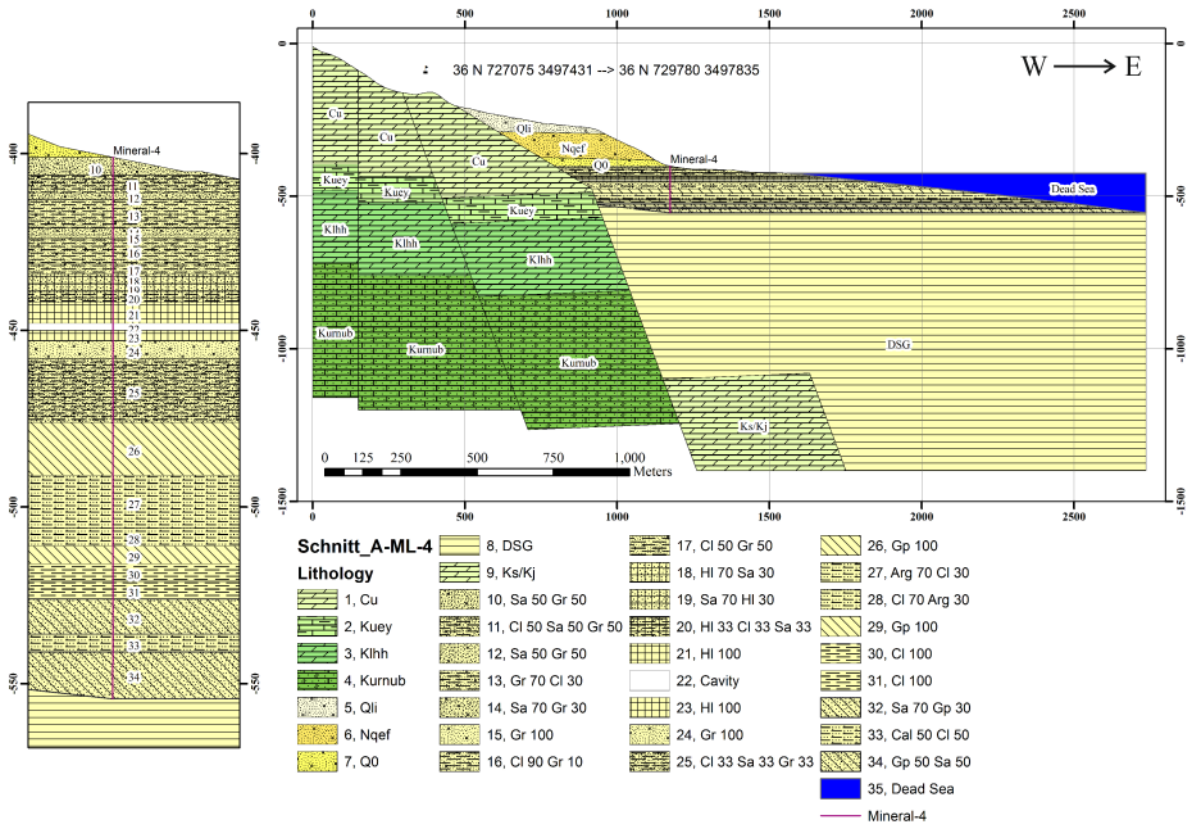

Figure 21: Conceptual model for slice ML-4

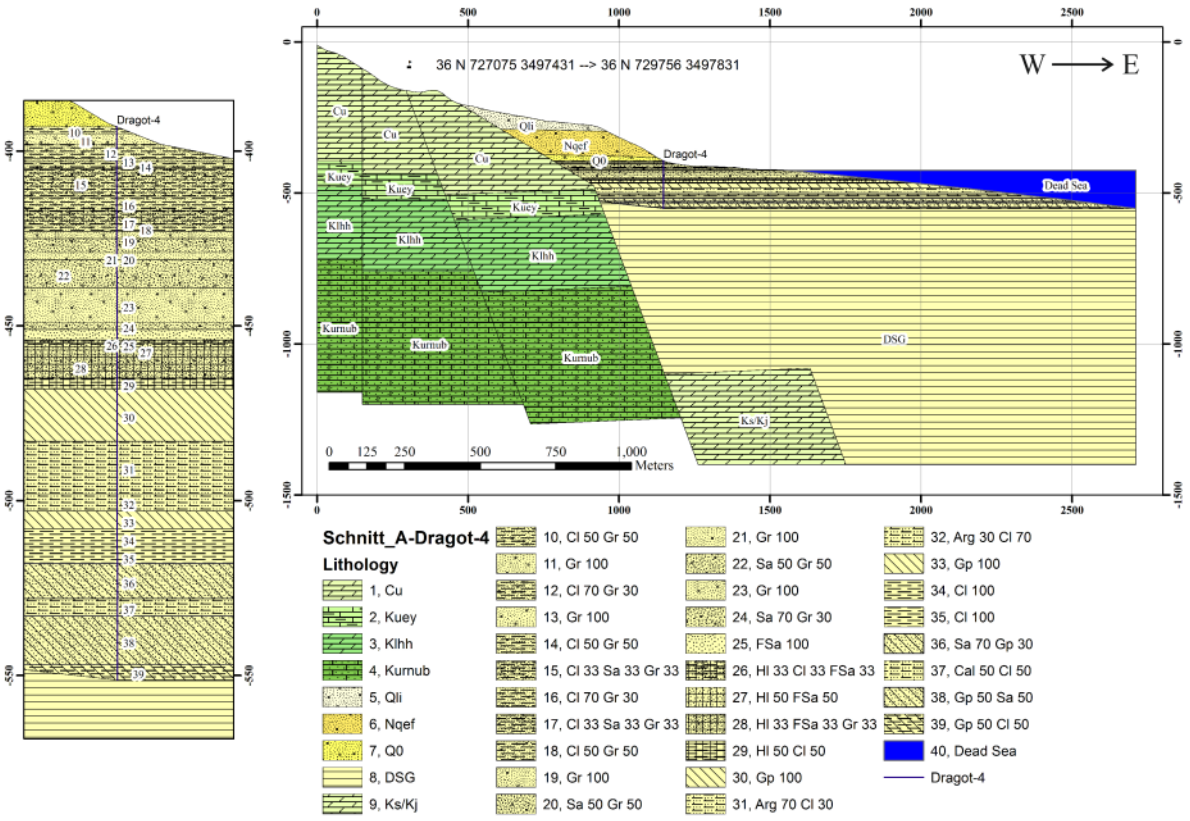

Figure 22: Conceptual model for slice DR-4

Table 2: Structural resolution of the conceptual model for the slice ML-2. According to Waldmann et al. (2007) the *aad* unit is regarded as layered calcitic marls (0.5-1 cm thick), intercalating with aragonite and silty detritus. The *acd* unit is regarded as layered calcitic marls (0.5-1 cm thick), intercalating with laminated calcite and silty detritus. References: No.1 - Bender (1968), ML-2 drilling: Yechieli (2005), HS-2 drilling: Ezersky et al. (2011), Massada drilling: Torfstein et al. (2008) and Haliva-Cohen et al. (2012), Perazim drilling: Haliva-Cohen et al. (2012) and Waldmann et al. (2007)

No.	Top level [masl]	Borehole profile [m]	Lithology	Share [%]	Remarks	Series	Fm	Group
1	-200	-	sand/gravel	30/70	Qli+Nqef+Q0: earliest Quaternary of recent alluvial clastic sediments, fluviatile deposits, eolian sands, not hydraulic active			
2	-406	0	clay	100				
3	-416	10	clay/gravel	50/50				
4	-426	20	halite/clay	50/50				
5	-431	25	halite	100	ML-2 drilling	Holocene	Post-Lisan	
6	-436	30	halite/clay	90/10				
7	-441	35	clay/gravel	50/50				
8	-446	40	clay/gravel	70/30				
9	-466	60	gravel	100	HS-2 drilling			DSG
10	-476	70	clay/sand/gravel	33/33/33				
11	-481	75	gypsum	100	Massada drilling			
12	-496	90	aragonite/clay	70/30	Massada drilling, aad aragonite dominated		Lisan	
13	-511	105	aragonite/clay	30/70				
14	-516	110	gypsum	100	Massada drilling, aad detritus dominated	Pleistocene		
15	-521	115	clay	100				
16	-526	120	clay	100	Perazim drilling		Samra	
17	-531	125	gypsum/sand	30/70				
18	-541	135	calcite/clay	50/50	Perazim drilling, acd			
19	-546	140	gypsum/sand	50/50	Perazim drilling			
20	-560	154			Perazim drilling, final depth			

Table 3: Structural resolution of the conceptual model for the slice ML-4. References: No.1 - Bender (1968), ML-4 drilling: Yechieli (2005), HS-2 drilling: Ezersky et al. (2011), Massada drilling: Torfstein et al. (2008) and Haliva-Cohen et al. (2012), Perazim drilling: Haliva-Cohen et al. (2012) and Waldmann et al. (2007)

No.	Top level [masl]	Borehole profile [m]	Lithology	Share [%]	Remarks	Series	Fm	Group
1	-200	-	sand/gravel	30/70	Qli+Nqef+Q0: earliest Quaternary of recent alluvial clastic sediments, fluviatile deposits, eolian sands, not hydraulic active			
2	-401	0	gravel/sand	50/50				
3	-406	5	clay/sand/gravel	33/33/33				
4	-411	10	gravel/sand	50/50				
5	-413	12	gravel/clay	70/30				
6	-421	20	sand/gravel	70/30				
7	-423	22	gravel	100				
8	-424	23	clay/gravel	90/10				
9	-431	30	gravel/clay	50/50	ML-4 drilling	Holocene	Post-Lisan	
10	-434	33	salt/sand	70/30				
11	-437	36	sand/salt	70/30				
12	-439	38	salt/sand/clay	33/33/33				
13	-442	41	salt	100				DSG
14	-448	47	cavity					
15	-450	49	salt	100				
16	-453	52	gravel	100				
17	-458	57	clay/sand/gravel	33/33/33	HS-2 drilling			
18	-476	75	gypsum	100	Massada drilling			
19	-491	90	aragonite/clay	70/30	Massada drilling, aad aragonite dominated		Lisan	
20	-506	105	aragonite/clay	30/70				
21	-511	110	gypsum	100	Massada drilling, aad detritus dominated	Pleistocene		
22	-516	115	clay	100				
23	-521	120	clay	100	Perazim drilling		Samra	
24	-526	125	gypsum/sand	30/70				
25	-536	135	calcite/clay	50/50	Perazim drilling, acd			
26	-541	140	gypsum/sand	50/50	Perazim drilling			
27	-555	154			Perazim drilling, final depth			

Table 4: Structural resolution of the conceptual model for the slice DR-4. References: No.1 - Bender (1968), DR-4 drilling: Yechieli (2005), Massada drilling: Torfstein et al. (2008) and Haliva-Cohen et al. (2012), Perazim drilling: Haliva-Cohen et al. (2012) and Waldmann et al. (2007)

No.	Top level [masl]	Borehole profile [m]	Lithology	Share [%]	Remarks	Series	Fm	Group
1	-200	-	sand/gravel	30/70	Qli+Nqef+Q0: earliest Quaternary of recent alluvial clastic sediments, fluviatile deposits, eolian sands, not hydraulic active			
2	-393	0	gravel/clay	50/50	Dragot-4 drilling	Holocene	Post-Lisan	DSG
3	-395	2	gravel	100				
4	-398	5	clay/gravel	70/30				
5	-402	9	gravel	100				
6	-403	10	clay/gravel	50/50				
7	-405	12	sand/gravel/clay	33/33/33				
8	-413	20	gravel/clay	30/70				
9	-417	24	sand/gravel/clay	33/33/33				
10	-421	28	gravel/clay	50/50				
11	-423	30	gravel	100				
12	-425	32	gravel/sand	50/50				
13	-429	36	gravel	100				
14	-431	38	gravel/sand	50/50				
15	-439	46	gravel	100				
16	-449	56	sand/gravel	70/30				
17	-451	58	fine sand	100				
18	-454	61	salt/fine sand/clay	33/33/33				
19	-456	63	fine sand/salt	50/50				
20	-458	65	gravel/fine sand/salt	33/33/33				
21	-465	72	salt/clay	50/50				
22	-468	75	gypsum	100	Massada drilling	Pleistocene	Lisan	
23	-483	90	aragonite/clay	70/30	Massada drilling, aad aragonite dominated			
24	-498	105	aragonite/clay	30/70	Massada drilling, aad detritus dominated			
25	-503	110	gypsum	100				
26	-508	115	clay	100				
27	-513	120	clay	100	Perazim drilling		Samra	
28	-518	125	gypsum/sand	30/70				
29	-528	135	calcite/clay	50/50	Perazim drilling, acd			
30	-533	140	gypsum/sand	50/50	Perazim drilling			
31	-547	154	gypsum/clay	50/50				
32	-553	160			Perazim drilling, final depth			

As consequence of the solution processes, the aquifer of the DSG sediment represents a double continuum. For the model approach the aquifer was splitted into two components: A predominant matrix system and conduit network.

4.2 Hydrogeological concepts

Due to numerical stability the produced 2D vertical models have been subjected to water-saturated, confined conditions and steady flow and steady transport.

4.2.1 Hydraulic conductivities

In the closer environment of the study area no information from hydraulic tests is available for a direct parameterization of present aquifers. Therefore, hydraulic conductivities (kf-values) have been assumed from literature (Domenico and Schwartz 1998). The used hydraulic conductivities of clay, sand, gravel and salt layers of the ML-4 drilling are shown in Table 5. Layers of heterogeneous composition are summarized and characterized by the lowest hydraulic conductivity in the composition. Table 5 also displays the assumed hydraulic conductivities for the 4-layer model and percentages of the respective hydraulic conductivities that have been used for specific scenarios.

Table 5: Hydraulic conductivity parameterization of ML-4 layers. Details of the lithology are depicted in Table 3. Model numbers refer to Table 16

No.	ML-4 lithology	kf [m/s]	kf [m/s]	0.9*kf [m/s]	0.8*kf [m/s]	0.7*kf [m/s]	0.6*kf [m/s]	0.5*kf [m/s]
		for multilayer DSG	for model 030	for models 047 to 052				
2	gravel/sand	1.0E-04	1.0E-06	9.0E-05	8.0E-05	7.0E-05	6.0E-05	5.0E-05
3	clay/sand/gravel	1.0E-09		9.0E-10	8.0E-10	7.0E-10	6.0E-10	5.0E-10
4	gravel/sand	1.0E-04		9.0E-05	8.0E-05	7.0E-05	6.0E-05	5.0E-05
5	gravel/clay	1.0E-09		9.0E-10	8.0E-10	7.0E-10	6.0E-10	5.0E-10
6	sand/gravel	1.0E-04		9.0E-05	8.0E-05	7.0E-05	6.0E-05	5.0E-05
7	gravel	1.0E-03		9.0E-04	8.0E-04	7.0E-04	6.0E-04	5.0E-04
8	clay/gravel	1.0E-09		9.0E-10	8.0E-10	7.0E-10	6.0E-10	5.0E-10
9	gravel/clay	1.0E-09		9.0E-10	8.0E-10	7.0E-10	6.0E-10	5.0E-10
10	salt/sand	3.0E-05	1.0E-10	2.7E-05	2.4E-05	2.1E-05	1.8E-05	1.5E-05
11	sand/salt	7.0E-05		6.3E-05	5.6E-05	4.9E-05	4.2E-05	3.5E-05
12	salt/sand/clay	3.3E-05		3.0E-05	2.7E-05	2.3E-05	2.0E-05	1.7E-05
13	salt	1.0E-11		9.0E-12	8.0E-12	7.0E-12	6.0E-12	5.0E-12
14	cavity							
15	salt	1.0E-11		9.0E-12	8.0E-12	7.0E-12	6.0E-12	5.0E-12
16	gravel	1.0E-03	5.0E-04	9.0E-04	8.0E-04	7.0E-04	6.0E-04	5.0E-04
17	clay/sand/gravel	3.7E-04		3.3E-04	2.9E-04	2.6E-04	2.2E-04	1.8E-04
18	gypsum	1.0E-11	1.0E-10	9.0E-12	8.0E-12	7.0E-12	6.0E-12	5.0E-12
19	aragonite/clay	3.1E-10		2.8E-10	2.5E-10	2.1E-10	1.8E-10	1.5E-10
20	aragonite/clay	7.0E-10		6.3E-10	5.6E-10	4.9E-10	4.2E-10	3.5E-10
21	gypsum	1.0E-11		9.0E-12	8.0E-12	7.0E-12	6.0E-12	5.0E-12
22	clay	1.0E-09		9.0E-10	8.0E-10	7.0E-10	6.0E-10	5.0E-10
23	clay	1.0E-09		9.0E-10	8.0E-10	7.0E-10	6.0E-10	5.0E-10
24	gypsum/sand	7.0E-05		6.3E-05	5.6E-05	4.9E-05	4.2E-05	3.5E-05
25	calcite/clay	5.1E-10		4.5E-10	4.0E-10	3.5E-10	3.0E-10	2.5E-10
26	gypsum/sand	5.0E-05		4.5E-05	4.0E-05	3.5E-05	3.0E-05	2.5E-05

4.2.2 Interaction of saltwater and freshwater

Inflowing freshwater from the Judean Mountains and saltwater from the DS are interacting. This results in saltwater intrusion in a confined aquifer and the development of a fresh-salt water interface. Investigations to the advance of the saltwater front are generally subsumed as *Henry's problem*. Henry (1964) presented analytical expressions for the steady-state solute distribution. His solutions are regarded as standard tests for models, which are capable of modeling variable density groundwater. In this context, the findings of Voss and Souza (1987) and Galeati et al. (1992) need to be mentioned as well. In fact, various different-dense fluids occur in the DSG and produce various saltwater intrusion patterns, which have been investigated during this study. The study does not answer questions related to the FEFLOW inherent definition of the dependency between solution density and salt content (Equation 1) but it is a prerequisite. The basic formulation for saltwater intrusion for steady-state flow shows Equation 2. The DS salinity, which is a density value, was assumed to be 340 g/L (Lensky et al. 2005). Density differences of groundwater are in the range of 0.18 g/cm³ with fresh to brackish water from 1.06 to 1.19 g/cm³ and lake water with 1.24 g/cm³ (Mallast et al. 2013).

$$\rho = \rho_0 \left(1 + \bar{\alpha} \frac{C}{C_s}\right)$$ **Equation 1**

where

ρ_0	fluid density where C = C_0 [kg/m³]
$\bar{\alpha}$	fluid density difference ratio []
C	contaminant concentration [kg/m³]
C_s	maximum concentration [kg/m³]

with

$$\bar{\alpha} = \frac{(\rho_{max} - \rho_0)}{\rho_0}$$

$$\nabla \vec{q} = Q_p - \frac{\bar{\alpha}}{C_s}\left(\varepsilon \frac{\partial C}{\partial t} + \vec{q} \nabla C\right)$$ **Equation 2**

where

$\vec{q}$	Darcy flux [m/d]
Q_p	specific sink/source rate of fluid [1/s]
$\bar{\alpha}$	fluid density difference ratio []
C_s	maximum concentration [kg/m³]
ε	kinematic porosity []
C	contaminant concentration [kg/m³]

4.2.3 Potential effects

One key observation need to be considered in a sensitive way: The various pressure potentials of the system freshwater/DSG-sediment-brine/DS-brine. They are driven by gravitational and diffusion forces remembering the steep topographic gradient and the density differences of the study area. Obviously, the pressure potentials of the

1. Upper Judea Group aquifer water
2. Lower Judea Group aquifer water
3. DS

are not the only governing forces of the groundwater movement in the DSG sediment. Mentioned earlier,

4. ascending deep waters

have been proven. Those are likely to exhibit a higher pressure potential than the aquifer water they penetrate. The complexity is enlarged by the heterogeneous DSG sediments and its

5. dense pore waters,

including occurring potential(s). A solitary topography-driven potential in a system of freshwater density would result in decreasing heads towards the DS. Considering the increasing salinity towards the DS, potential lines favor inverse flow in the direction of the DSG sediment. In fact, the salinity of the DSG sediment pore water is similar to that of the DS brine. Thus, the for-

mation of a distinctive fresh-salt water interface is questionable. The potential of the brine saturated DSG sediment is driven by vertical and horizontal pressure differences that occur from aquitard intercalation and developed preferential freshwater flow paths, respectively. Confined aquifers produce artesian groundwater that has been observed near to the DS shoreline. Confined salt layers below freshwater dominated layers enhance this behavior. Water will diffuse through the aquitard until concentrations are equalized (osmosis). However, inflowing freshwater from the Judean Mountains may result in reverse osmosis. Freshwater passes existing conduits in the DSG sediment and increases the pressure in confined salt layers. Only water molecules are able to escape upwards. The salinity (and the mean residence time) of the remaining brine will increase and is likely to be even higher than the DS salinity. Due to increasing pressure differences this phenomenon should be more effective in the deep (restricted by existing voids) than in the shallow terrestrial. Similar mechanisms have been observed by Kushnir (2008). Subsequent processes that occur in the DSG sediment may be healing up of karstified tubes and reverse local penetration towards the DS. To summarize, especially in highly variable sediment compositions with salty-clastic interbedding groundwater movement may show inverse effects compared to those that have only been expected from the simple DS saltwater intrusion.

4.2.4 Discrete element network

The existing double continuum in the DSG sediment requires different parameterization of the matrix system and the conduit network. In the modeling approach discrete elements help to simulate such conduit networks. The aquifer is assumed to have only a limited number of 2D fracture sets serving as effective flow paths, whereas the surrounding rock matrix will be considered as nearly impermeable. For an acceptable model it is necessary to obtain information about the structure and geometry of the fractures, such as their roughness or heterogeneity, to translate them into sensible parameters for the model. Otherwise, the assessment of storage capacities and velocities will become erroneous, because natural fractures are of quite irregular shape. Therefore, rather extensive field explorations are compulsory, which is also the most severe disadvantage. Moreover, probably a lack of information referring to the fracture widths will become a problem because of their difficult determination in the depth. Additionally, computational capacity mostly does not allow considering small-sized fractures. Although, the information about the shape of the conduits is sparse, the usefulness and applicability of a discrete element network within FEFLOW was examined in the study.

4.3 Model code and problem settings

The applied numerical model was developed by using the FEFLOW code (DHI-WASY Software 2012). The FEFLOW 6.1 software package (Finite Element Subsurface Flow & Transport Simulation System) facilitates the modeling of fluid flow and transport of dissolved constituents and/or heat processes in the subsurface. In detail, the model provides "three-dimensional and two-dimensional, areal and cross-sectional (horizontal, vertical or axisymmetric), fluid density-coupled, also thermohaline, or uncoupled, variably saturated, transient or steady state, flow, mass and heat transport and reactive multi-species transport in subsurface water resources with or without one or multiple free surfaces" (DHI-WASY Software 2012). Groundwater movement in porous and fractured media can be modeled, which is essential when the contribution of salt cavities in the DSG sediment to groundwater will be modeled.

The numerical method of finite elements is used by FEFLOW to solve the non-linear partial differential equation of groundwater flow. By default, the Galerkin FEM is applied; optional the streamline upwind method with automatic time step control is used. The mathematical modeling principles of FEFLOW refer to the balance laws of mass conservation, momentum conservation and energy conservation. In problem settings with parameter zones of variable hydraulic conductivities Diersch (2010d) advised to use the algebraic multigrid equation solver (SAMG, by K. Stueben, FhG-SCAI) for flow and mass transport. Table 6 and Table 7 outline possible problem settings in FEFLOW. In the case of density-dependent flow, flow and transport simulation are always done simultaneously until attaining convergence with iteratively (for steady-state done once) calculating 1. Darcy-flow/transport, 2. state dependencies (steady-state, transient), 3. Darcy-flow/transport etc.

Table 6: Problem class definition within FEFLOW

1. State of saturation	
Saturated	**Unsaturated**
• Darcy equation • model not necessarily fully saturated/confined	• Richards equation • also variably saturated media
2. Time setting of flow/transport	
Flow	**Flow and mass transport**
• steady • transient	• steady flow and steady transport • steady flow and transient transport • transient flow and transient transport

Table 7: Projection within FEFLOW

2D	3D
• horizontal confined • horizontal unconfined (phreatic, also partially confined) • vertical (confined in saturated mode) • axisymmetric (radial symmetry)	• confined (default) • unconfined (also partially confined)

4.3.1 Parameter references

Spatially distributed parameters are used for the setup of the model and include boundary conditions (BC) and material properties.

BCs are applied on a nodal basis. Only one BC can be applied at a node. The applied BCs are subdivided into flow BCs and mass transport BCs (Table 8).

The relevant properties of the medium are defined as material properties and are applied on an elemental basis within FEFLOW. They are subdivided into flow and mass properties (Table 9).

Table 8: Flow and mass boundary conditions within FEFLOW

Flow Boundary Conditions	Mass Transport Boundary Conditions
time-constant or according to a time series	
Dirichlet	
Hydraulic-head BC *advanced:* • *Hydraulic-head BC (Pressure)* • *Hydraulic-head BC (Saltwater Head)* • *Hydraulic-head BC (Saturation)* • *Hydraulic-head BC (Moisture Content)*	Mass-concentration BC
Neumann	
Fluid-flux BC *advanced:* • *Fluid-flux BC (Gradient) – unsaturated models* • *Fluid-flux BC (Integral) – unconfined models with free and movable surface*	Mass-flux BC
Cauchy	
Fluid-transfer BC *advanced:* • *Fluid-transfer BC (Integral) – unconfined models with free and movable surface*	Mass-transfer BC
Source/sink	
Well BC (abstraction/infiltration, nodal or along screen)	Mass nodal sink/source BC

Constraints on Flow Boundary Conditions	Mass Transport Constraint Conditions
technically implemented in FEFLOW by converting the type of BC when the constraint is activated	
physical limits	
• hydraulic head/fluid transfer type limited by min/max flow rate • fluid flux/well type limited by min/max hydraulic head • fluid-transfer type limited by hydraulic-head	• mass-concentration/mass-transfer type limited by min/max mass flux • mass-flux/mass-nodal type limited by min/max concentration

Table 9: Flow and mass transport properties within FEFLOW

Flow properties	Mass transport properties
simulated on an elemental basis	
• Transmissivity (for 2D horizontal confined models, else hydraulic conductivity used for input) • Conductivity • Aquifer top/bottom elevation (2D) • In/Outflow on top/bottom GW recharge 2D and 3D!, inflow from underlying aquifer) • Density ratio (density-dependent models) • Drain-/Fillable Porosity [] = specific yield, for unconfined models • Specific storage (Compressibility) ([] for 2D confined, [1/L] for other 2D, 3D) • Source/sink (flow) [m/d] [1/d] (2D: GW recharge, 3D: not for GW recharge) • Transfer Rate (Flow) (only together with Transfer BC)	• Aquifer thickness (Mass) • Porosity (Mass) (effective porosity) • Molecular diffusion [m^2/s] • Sorption coefficient (Henry) • Dispersivity [m] (low ones need fine spatial discretization) • Decay-rate constant [1/s] (1st order decay for the simulated species) • Source/sink (Mass) [$g/m^2/d$] [$g/m^3/d$] (biological decay) • Transfer rate (Mass) (only together with Transfer BC) • Sorption coefficient 2 (Freundlich, Langmuir)

4.3.2 Discrete elements

Salt karst features in the DSG sediment of the study area can be realized in FEFLOW by discrete elements. Water pathways, which result from salt karstification, are assumed to occur mostly as small fissures, dissolution conduits or large tubes in the subsurface. Therefore, flow cannot be described by the conventional Darcy equation in continuous media.

The standard numerical approach in porous media can be combined with interconnected 1D (bar elements) and 2D (areal elements) features to simulate free-fluid movement. Non-linear fluid motion equations are applied for the 1D or 2D discrete elements, i.e. Hagen-Poiseuille and Manning-Strickler (Table 10). Hagen-Poiseuille and Manning-Strickler both can only describe laminar flow behavior and are eventually converted to Darcy flux velocities within FEFLOW. For 1D and

2D plane and axisymmetrical (cylindrical) parallel flow Hagen-Poiseuille is applied, describing a linear relationship with respect to the pressure gradient and gravity. The fluid motion for channel flow is described by the vertical integrated Navier-Stokes equation resulting in a reduced momentum equation. A friction law like Manning-Strickler can express the shear effect at the bottom. For the 3D porous matrix the Darcy approach still holds (Diersch 2010c).

Table 10: 1D and 2D discrete feature elements that can be applied within FEFLOW (Diersch 2010c)

Type	Fluid motion law	Application
1D, plane (phreatic, non-phreatic)	Darcy or Hagen-Poiseuille or Manning-Strickler	Channels, mine stopes
1D, axisymmetric (phreatic, non-phreatic)		Pumping wells, abandoned wells, boreholes
2D, plane (non-phreatic)		Fractures, faults
2D, plane (phreatic)		Runoff, overland flow

There are three geometries available in 2D models: 1D discrete feature selected along an arbitrary node path and 1D discrete feature selected along a slice edge. In 2D models, faces cannot be utilized for discrete elements. For adaptation of the discrete elements, the following characteristic flow parameters need to be considered: Cross-section area A [L²] (1D feature type) and hydraulic aperture b [L] (governing the flow velocity according to the law of Hagen-Poiseuille). The cross-section area is defined perpendicular to the flow direction and is calculated from the product of hydraulic aperture b and width B (Figure 23). The hydraulic aperture b denotes the perpendicular distance between the adjacent walls of a conduit and is similar to the hydraulic diameter. Regarding the hydraulic radius for that application (submerged slit plane) it is defined as quotient of cross-section area and wetted perimeter (Equation 3). The average flow velocity $\overline{u}$ depends on the hydraulic aperture. The water flux Q is the product of flow velocity, depending on the hydraulic aperture of Hagen-Poiseuille, and hydraulic aperture (b) (Equation 4 and Equation 5).

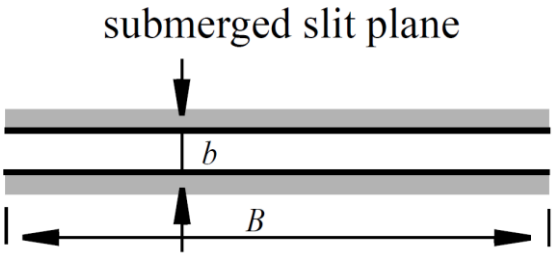

Figure 23: 1D geometry type which is applied for discrete element modeling

$$r_{hydr} = \frac{cross - sectional\ area}{wetted\ perimeter} = \frac{bB}{2B} = \frac{b}{2}$$ **Equation 3**

where

b	hydraulic aperture [m]
B	width [m]

$$\bar{u} = -\frac{b^2}{12\mu}\left(\frac{dp}{dx} - \rho g_x\right)$$ **Equation 4**

where

b	hydraulic aperture [m]
μ	kinematic viscosity [m²/s]
dp/dx	pressure gradient [Pa]
ρ	fluid density [kg/m³]
g	gravity [9.81 m/s²]

$$Q = \bar{u}b = -\frac{b^3}{12\mu}\left(\frac{dp}{dx} - \rho g_x\right) = -\frac{r_{hydr}^2}{3\mu}\left(\frac{dp}{dx} - \rho g_x\right)$$ **Equation 5**

where

$\bar{u}$	average flow velocity [m/s]
b	hydraulic aperture [m]
μ	kinematic viscosity [m²/s]
dp/dx	pressure gradient [Pa]
ρ	fluid density [kg/m³]
g	gravity [9.81 m/s²]
r_{hydr}	hydraulic radius [m]

In terms of geometric variations, discrete features are added to the matrix permeability to realize higher flow velocities, i.e. the previously defined hydraulic conductivity of the area is maintained and additional pathways have been created. A typical workflow of applying discrete features from a slice-edge selection in 2D sections is displayed in Table 11.

Table 11: Workflow for the application of discrete elements in 2D sections

Discrete Element Workflow	
Interface component	***Step***
Selection Toolbar	Select slice edges or nodes
Maps Panel	Choose respective supermesh as selection map
Selection Toolbar	Select respective map polygon
Spatial Units Panel	Slice-Edge Selections: Store current selection
Data Panel	Discrete Features: Add slice-edge feature element and choose flow law

4.4 Model discretization

The conceptual model was converted to a numerical model within FEFLOW. In this procedure, a supermesh was created and a triangle mesh was assigned to the vertical slice – as preparation for the following simulation. The stereographic x-z coordinate system, defined in ArcGIS, was used as local coordinate system in FEFLOW.

The existing transect from the conceptual model was cut at the base of -620 m msl. The decision was based on the minor knowledge of the Tertiary sediments where no specific geological layers according to drillings can be resolved. By this geometrical assumption, the Kurnub sandstone is excluded in the model.

The 2D finite element mesh was created by the triangle mesh generator (Figure 24) with a certain number of total elements (e.g. 1,000 elements). The hydraulic conditions of the model were defined within the FEFLOW *Problem Settings* (Figure 24). The 2D-slice is regarded as vertical, planar projection. To improve the quality of the mesh, angles of finite elements can be reduced during post-processing (max. interior angle of triangles). The applied initial meshing density is displayed in Figure 25. A relative density of 2 was applied to the Cretaceous units *Cu*, *Kuey* and *Klhh* next to the DSG, to the debris (*Qli/Nqef/Q0*) and to the undifferentiated DSG sediment, a relative density 30 times the default density was applied to the differentiated DSG sediment. The increase of the meshing density should avoid numerical instabilities due to inadequate triangle size. The initial model in total consists of 15,956 mesh elements and 8,176 mesh nodes.

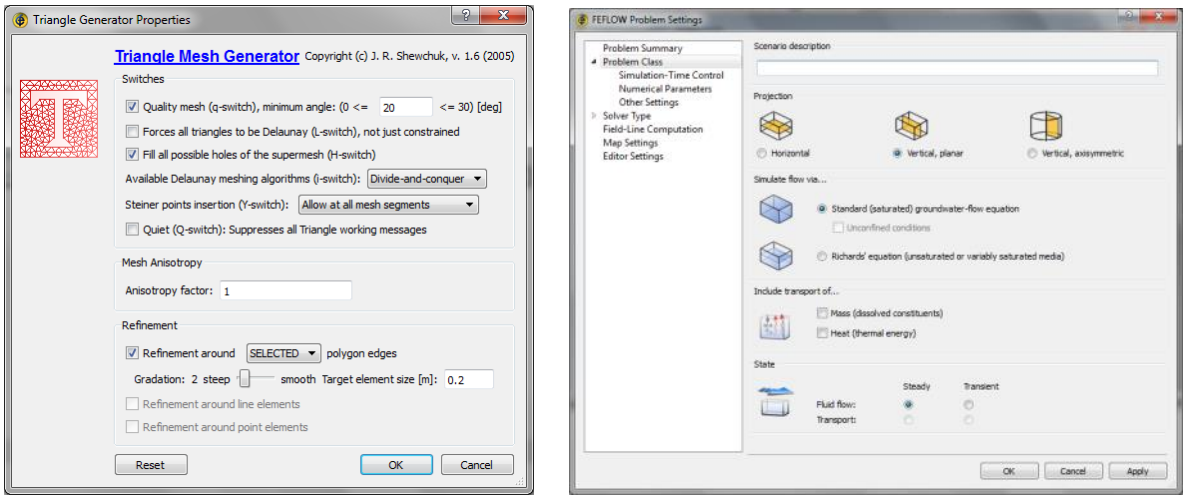

Figure 24: Triangle mesh generator and scenario description of a steady-state model

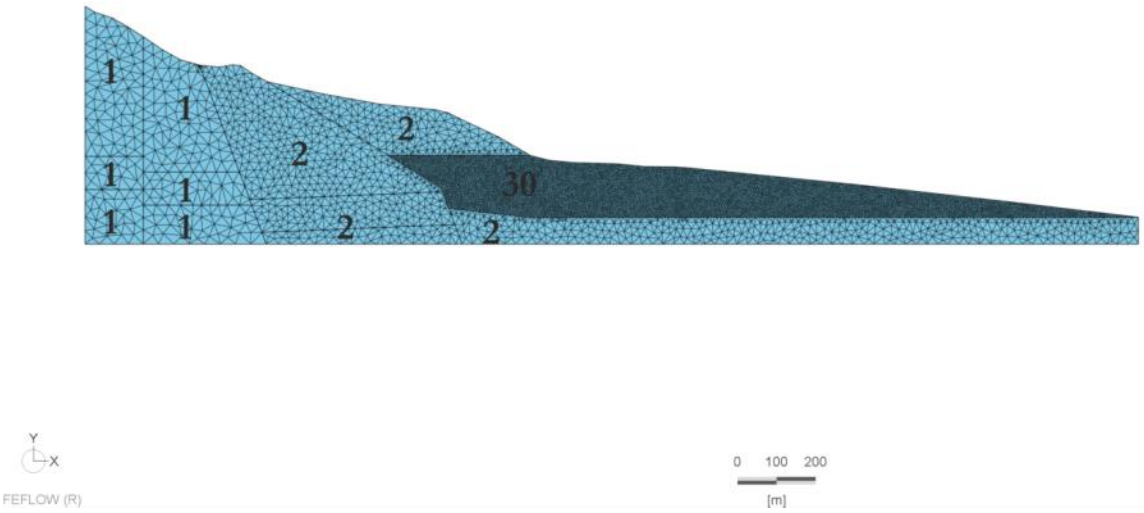

Figure 25: Applied initial meshing density

4.5 Boundaries

Pressure heads on the western boundary of the model have been applied according to the known confined and unconfined aquifers of the Judean Mountains. The Lower Judea Group is assumed to exhibit a higher potential than the upper Judea Group and is therefore regarded as confined (based on Figure 18). The Lower Judea Group was assigned a hydraulic head of -300 m msl and the Upper Judea Group (aquitard and aquifer, unconfined) was assigned a hydraulic head of -320 m msl (both Dirichlet BCs). A hydraulic head BC (saltwater head) with a constant value of -425 m msl (equal to the pressure head as combination of elevation and water column pressure) was set for the DS bottom and for the eastern BC. No flow on the remaining top, no flow for the bottom. Groundwater recharge is not considered for the DSG sediment. Mass concentration BCs (equals TDS) were applied for the DS bottom and the eastern domain boundary (350 g/L) and for the western boundary (800 mg/L). Subsequently, the density ratio has been calculated to 0.24. Variations in boundary conditions are listed in Table 16.

4.6 Model execution and calibration

The input models for the numerical modeling are the conceptual models which are displayed in Figure 20, Figure 21 and Figure 22. The numerical modeling faces the hydraulic heads within the system Cretaceous aquifer – DSG – DS and the lateral density variability including saltwater intrusion. The scenarios eventually aim for a possible discharge of inflowing water from the Judean Mountains to the DS, i.e. surface and subsurface discharge locations along the Wadi Darga outlet provide the constraint to calibrate the model. The time frame of streamlines was generally set to a maximum of 5,000 d according to realistic residence times indicated by hydrochemical findings. The algebraic multigrid SAMG solver was used for the flow and mass transport modeling.

- ✓ A summary of the model properties is provided at the end of the sensitivity analysis in Table 16. A synopsis of every applied model property is compiled in appendix B and covers supermesh characteristics, problem class, FEM mesh geometry, boundary conditions, parameter assignment, flow and mass budgets. The link to the tables is provided by the form *[No. x]* within the continuous text.

The development of the models and scenarios obeyed the sequence in Table 12. Due to the lack of observation heads and temporal continuity of literature data, groundwater heads were sensitively calibrated according to a realistic variance of hydraulic material settings, residence times indicated by hydrochemical findings and the spatial distribution of spring outlets. By the methods of sediment refinement, sediment resolution and discrete elements, the model calibration should also reveal spring contributing layers of the DSG with lateral and depth dependency.

The conducted sensitivity analysis is based on the calibrated model and serves for the layer specific variation of hydraulic conductivities and the variation of DE inside the DSG.

The uncertainty analysis faces the variation of parameters and settings with expected none-dominant impact on the established models or serves for the numerical improvement of the models. These variations have been assigned to the entire model domain.

The models/scenarios were evaluated according to a constraint index (cf. chapter *Constraint Index CI*).

Table 12: Flowchart for the development of the models and scenarios

Model calibration
↓
Sensitivity analysis
↓
Uncertainty analysis

4.6.1 From initial to standard model

The first concept of the numerical model setup and the corresponding parameterization of the hydrological settings of the study area are shown in Figure 26 and Table 13. Applied flow properties are hydraulic conductivity and density ratio. Applied mass transport properties are molecular diffusion and dispersivity. Due to applied confined conditions the influence of the porosity (mass transport property) is negligible. Due to applied steady-state conditions the influence of the specific storage (fluid flow material parameter) is negligible. The influence of the anisotropy of conductivity, molecular diffusion and dispersivity was tested during the uncertainty analysis.

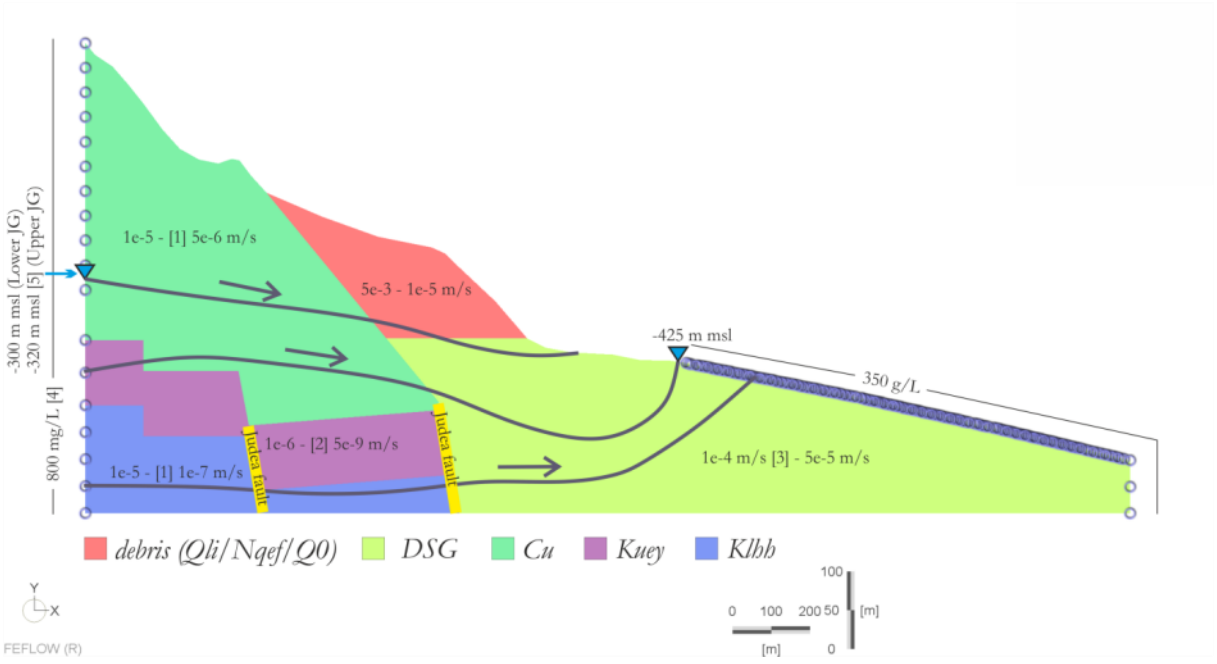

Figure 26: Hydrogeological properties for the numerical modeling. Assumed hydraulic conductivities and mass concentrations are based on literature values or the conceptual approach. Flow potentials and expected flow lines are denoted. *1* Gvirtzman et al. (1997), *2* Gräbe et al. (2013), *3* Wollman et al. (2003), *4* Möller et al. (2009b), *5* Ben-Itzhak and Gvirtzman (2005). JG *Judea Group*

Table 13: Other used material properties of fluid flow and mass transport for the simulations

Parameter	Symbol	Value	Unit	Reference
anisotropy of conductivity	Φ	1	1	-
anisotropy angle	Ξ_{aniso}	0	deg	-
specific storage	S_S	$1*10^{-4}$	1/m	Kiro (2007)
porosity	ε	0.3	1	Freeze and Cherry (1979)
molecular diffusion	D_d	$1*10^{-9}$	m^2/s	Freeze and Cherry (1979)
longitudinal dispersivity	β_L	5	m	Yechieli et al. (2001)
transverse dispersivity	β_T	0.5	m	Yechieli et al. (2001)

Figure 26 contains ranges of hydraulic conductivities and boundary conditions for the calibration models. For details refer to Table 16 and appendix B, respectively. The modeling process started with the simplest available model solution *[No. 006]*. The mass concentration influence was examined *[No. 012]*. Different head BCs on the western boundary were tested *[No. 013, 021]*. Streamline upwinding was applied *[No. 014]*. After successful calibration the model was compli-

cated by the implementation of an additionally permeable layer within the DSG *[No. 017, 018]*. Hydraulic conductivity values for the DSG have been varied from $1*10^{-2}$ to $1*10^{-7}$ m/s *[No. 020]*. The standard model *[No. 029]* was finally established after the application of the following features:

- increasing the hydraulic conductivity of the Upper Judea Group aquitard (*Kuey*) and the Lower Judea Group by two orders of magnitude ($1*10^{-6}$ m/s and $1*10^{-5}$ m/s, respectively) and increasing the hydraulic conductivity of the Upper Judea Group aquifer by one order of magnitude to $1*10^{-5}$ m/s (according to pers. communication to A. Gräbe, UFZ Leipzig, the upper range of permeabilities within the Cretaceous hard rock, cf. Gräbe et al. 2013)
- decreasing the hydraulic conductivity of the debris (*Qli/Nqef/Q0*) by one order of magnitude ($1*10^{-5}$ m/s)
- assuming the lumped hydraulic conductivity of the DSG sediment to $5*10^{-5}$ m/s
- imitating the Judean fault system as two water pathways to divert water amounts to the DS by the application of two discrete features (Hagen-Poiseuille, 1D, Arbitrary, source: 0/d) (Figure 26)

To check the sensitivity of the adapted model with respect to the DSG hydraulic conductivity, this parameter was again varied in a broad range. The kf-value for the entire sediment in front of the mountain range (*Qli/Nqef/Q0*, DSG sediment differentiated and undifferentiated) was adapted and varied in the range of $1*10^{-7}$ m/s to $1*10^{-2}$ m/s. The intention was to recognize any kind of spring in the transition zone from the Judean Mountains to the DSG sediment, in particular if the expected low hydraulic conductivity of the sediment is applied *[No. 039 to 043]*.

4.6.2 DSG layering

After the estimation of the impact of certain layers of the DSG on the transport model *[No. 030]* (Figure 27), all geological layers of the drilling ML-4 with their respective kf-values (Table 5) have been implemented in the DSG sediment of the model domain. The result should provide indications of preferred flow paths and areas of preferred discharge to the DS *[No. 035]*.

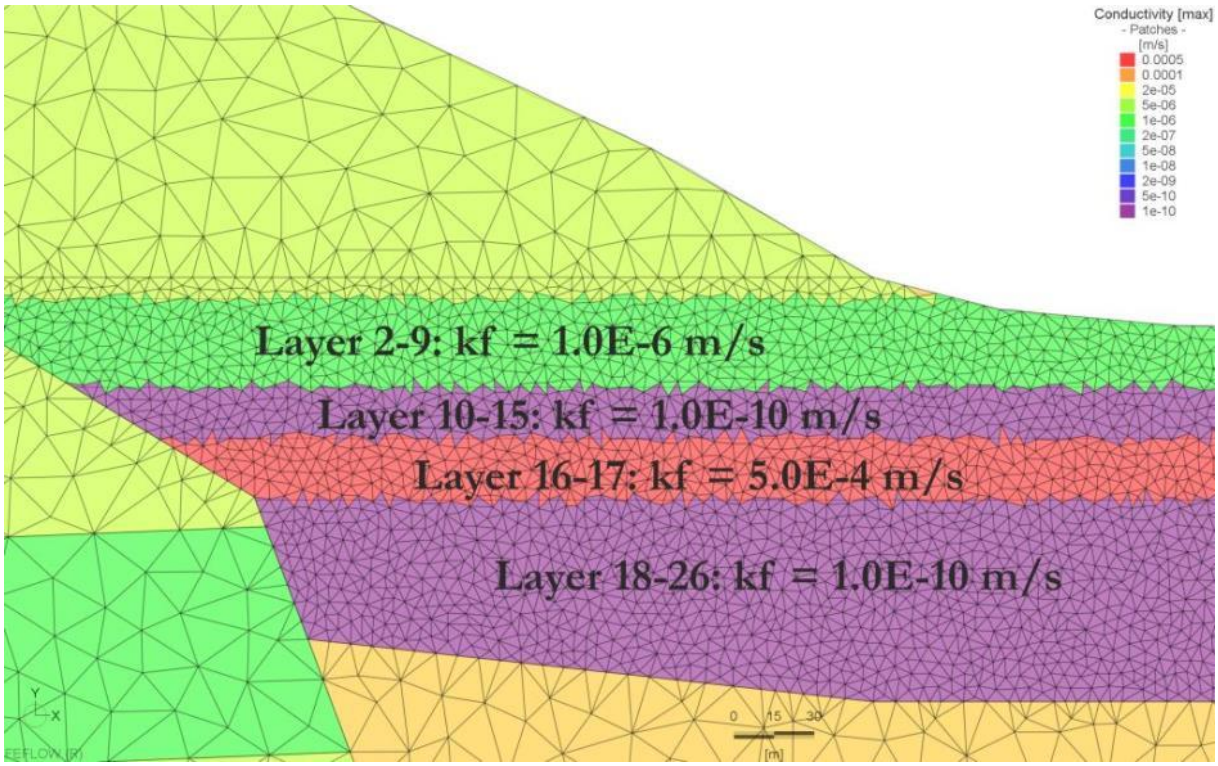

Figure 27: Assigned hydraulic conductivities for the 4-layer DSG sediment

4.6.3 Deduction of a DE network

In order to deduce a DE network, DE were selectively applied on the DSG layers. Initially, the existing cavity in the stratigraphic log of ML-4 was utilized (meter 47 to 49, Table 3) and subjected to discrete elements. Finite elements of layer 18 to 23 with their small total thickness have been refined once. As far as the beginning of the fresh-salt water interface, discrete elements have been applied to the cavity (Hagen-Poiseuille, Slice-Edge, cross-section area: 1 m², aperture width: 0.001 m). The mentioned limitation to the fresh-salt water interface rises from the conception that the dissolution of rock salt by inflowing fresh water is prevented in front of the interface *[No. 031]*.

Not only the cavity is supposed to be object of dissolution but also the crystalline evaporates within the DSG. Therefore, a network of discrete features (Hagen-Poiseuille, Slice-Edge, cross-section area: 1 m²) was created on clay and salt layers. According to Figure 21 the layers of interest are

- gypsum/clay: layer 11, 13, 16, 17, 25, 26, 28, 29, 30, 31, 32, 33, 34
- halite: layer 18, 19, 20, 21, 23
- cavity: layer 22

Different hydraulic apertures have been applied:

- gypsum/clay: 0.001 m
- halite: 0.01 m
- cavity: 0.5 m

The discrete features have been applied on these layers and assigned with the aforementioned hydraulic aperture. The spatial distribution is illustrated in Figure 28 *[No. 038]*.

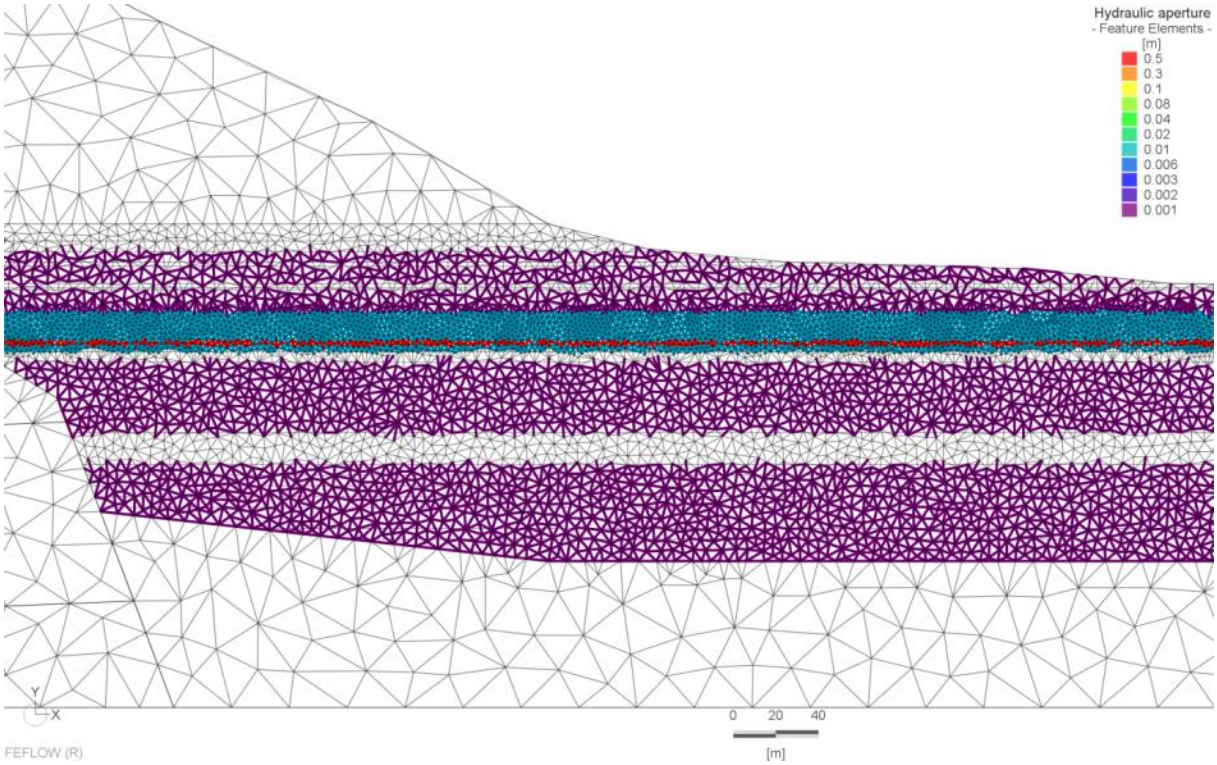

Figure 28: Discrete element network

Two other cases have been investigated to prove the hydraulic aperture influence:

- The hydraulic aperture of gypsum/clay and halite was increased to 0.01 m *[No. 045]*.
- The hydraulic aperture of gypsum/clay and halite was increased to 0.1 m *[No. 046]*.

How does the time-dependent behavior of streamlines within the DSG sediment look like? What are typical flow velocities (1) in the Judea aquifer, (2) in the transition zone from the Judean Mountains to the DSG sediment, (3) within the DSG sediment and (4) near to the outlet to the DS? To investigate these differences, the Darcy flux distribution in the domain of the network model with increased DE hydraulic aperture (045) was analyzed.

4.7 Sensitivity analysis

4.7.1 Scenario: Matrix flow threshold

To investigate the sensitivity of the multilayer model (035) a scenario has been conducted that aim uniform changes in hydraulic conductivities of the DSG, adjusting to the DS discharge constraint.

The objective of the matrix flow threshold scenario was to determine the hydraulic conductivity threshold value for realizing the matrix flow through the DSG sediment to the DS by overcoming the fresh-salt water interface (with t = 5,000 d). Only the primary porosity of the sediment should influence the water flow, DE were not considered in that setup. The hydraulic conductivi-

ty of each DSG sediment layer (differentiated and undifferentiated DSG) was continuously diminished by 10% of the original kf-value (Table 5). If the streamline to the DS broke off, the scenario would be closed (abort criterion).

- *No. 047*: 1.0*kf
- *No. 048*: 0.9*kf
- *No. 049*: 0.8*kf
- *No. 050*: 0.7*kf
- *No. 051*: 0.6*kf
- *No. 052*: 0.5*kf

4.7.2 Scenario: Hydraulic aperture vs. depth

To investigate the sensitivity of the discrete element network, several scenarios have been conducted that aim spatial variations and variations of discrete element input parameters.

The described changes during this scenario were conducted on the matrix flow threshold model that was realized with 50% of the original hydraulic conductivity (052). For the applied DE a constant cross-section area of 1 m² was used. To investigate the correlation between hydraulic aperture and depth, the hydraulic aperture was increased with depth to investigate if an conduit opening would result in the overcoming of the impacting DS pressure potential. As reference, a model with homogeneous hydraulic aperture of the clay layers was created at first *[No. 054]*:

- clay: layer 11, 13, 16, 17, 20, 25, 27, 28, 30, 31, 33 (according to Figure 21)
- homogeneous hydraulic aperture: 0.001 m

The increase of the value of the hydraulic aperture with depth was realized for two cases:

1. linear increase of two magnitudes within 100 m from 0.001 m to 0.1 m (starting with layer 11 of depth 0 m) *[No. 055]*
2. linear increase of three magnitudes within 100 m from 0.001 m to 1 m (starting with layer 11 of depth 0 m) *[No. 056]*

The specific values for each layer have been assigned according to this law and are displayed in Table 14 and Figure 29.

Table 14: Hydraulic aperture increase with depth

layer	depth [m]	hydraulic aperture [m]	
		case 1	*case 2*
11	0	0.001	0.001
13	7	0.007	0.070
16	18	0.018	0.180
17	25	0.025	0.250
20	33	0.033	0.330
25	52	0.051	0.519
27	85	0.084	0.849
28	100	0.100	1.000
30	110	0.109	1.099
31	115	0.114	1.149
33	130	0.129	1.299

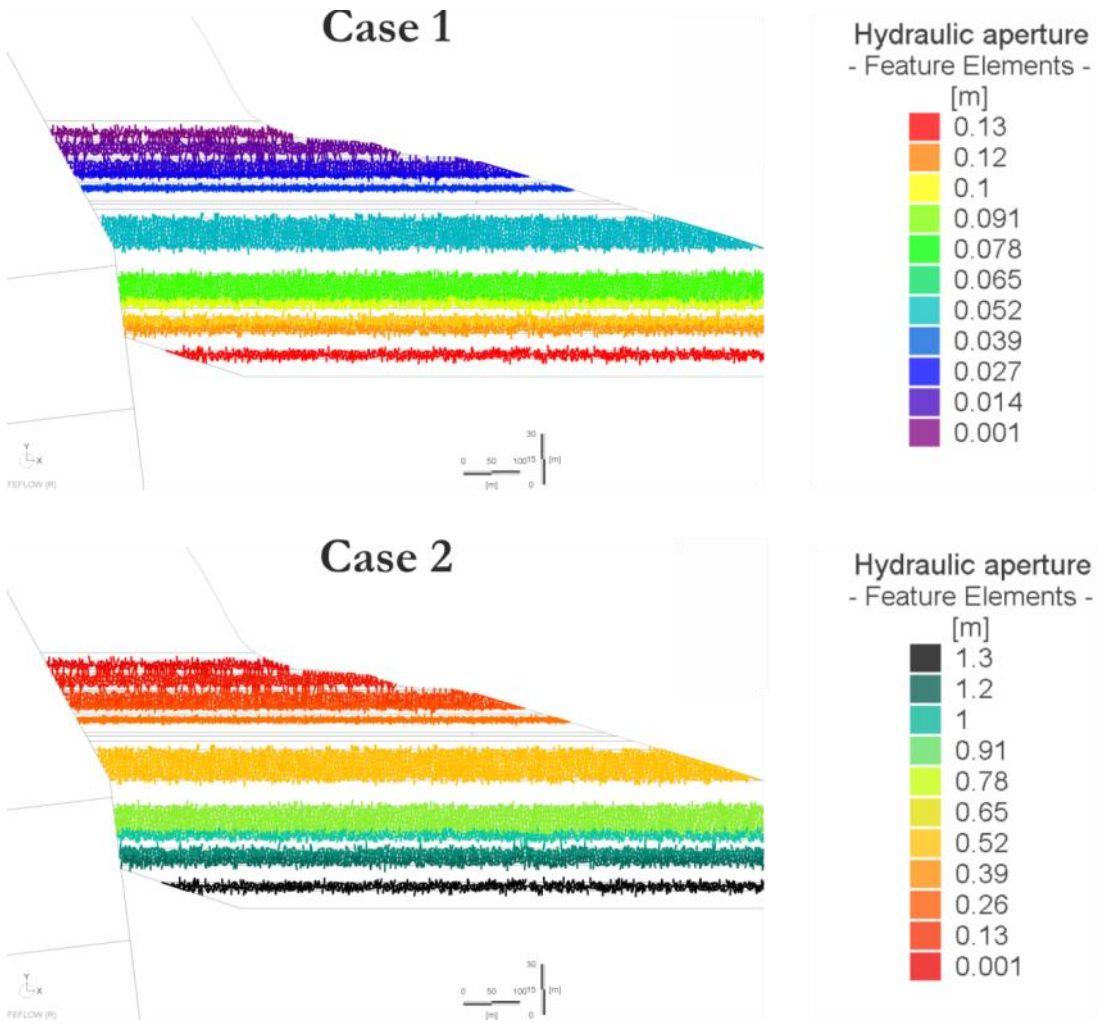

Figure 29: Hydraulic aperture distribution for case 1 and case 2

4.7.3 Scenario: Cross-section area threshold

The hydraulic aperture was tested for its impact on hydraulic conductivity distribution in the DSG sediment. The second important parameter of the DE is the cross-section area which was varied during the following two scenarios.

The aim was to determine the minimum value for the cross-section area (similar to the matrix flow threshold scenario) for realizing the discharge through the DSG sediment to the DS by overcoming the fresh-salt water interface (with t = 3,000 d). The scenario was applied to the network model (038) with constant hydraulic aperture in the clay layers of 0.001 m (discrete features: Hagen-Poiseuille, Slice-Edge). During the process of trial and error the value for the cross-section area was continuously enlarged starting with $1*10^{-4}$ m² till reaching the threshold value *[No. 057]*.

4.7.4 Scenario: Cross-section area vs. depth

The dependency between increasing DE cross-section area with depth and hydraulic conductivity was examined (analogously to the hydraulic aperture vs. depth scenario). The depth-depending cross-section area was applied on the previous model (057).

The increasing cross-section area with depth was realized for two cases:

1. linear increase of two magnitudes within 100 m from 0.005 m² to 0.5 m² (starting with layer 11 of depth 0 m) *[No. 058]*
2. linear increase of three magnitudes within 100 m from 0.005 m² to 5 m² (starting with layer 11 of depth 0 m) *[No. 059]*

The specific values of each layer have been assigned according to this law and are displayed in Table 15 and Figure 30.

Table 15: Cross-section area increase with depth

layer	depth [m]	cross-section area [m²]	
		case 1	*case 2*
11	0	0.005	0.005
13	7	0.035	0.350
16	18	0.089	0.899
17	25	0.124	1.249
20	33	0.163	1.648
25	52	0.257	2.597
27	85	0.421	4.246
28	100	0.500	5.000
30	110	0.545	5.495
31	115	0.569	5.744
33	130	0.644	6.494

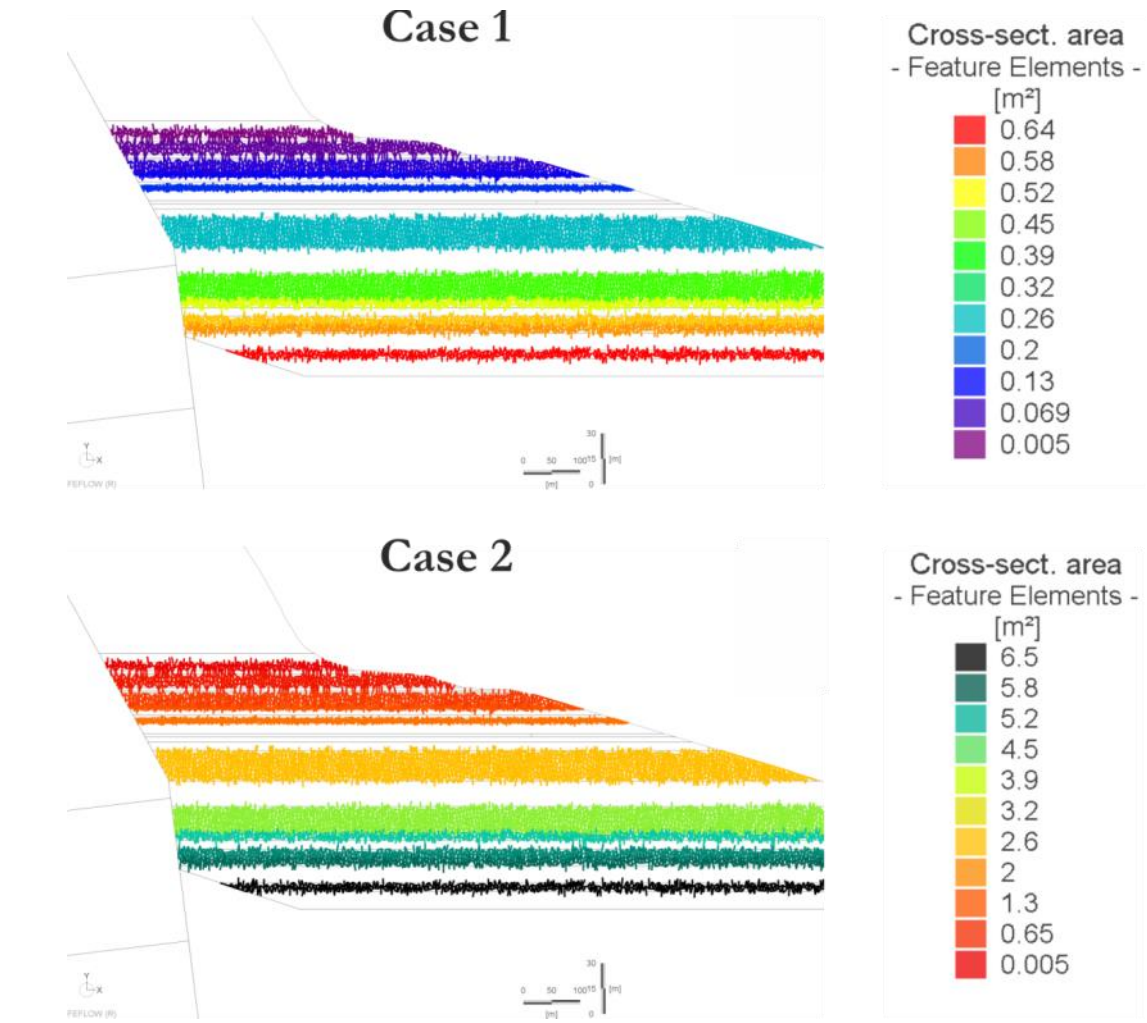

Figure 30: Cross-section area distribution for case 1 and case 2

4.7.5 Scenario: Discrete element frequency

A reduction of the tube occurrence towards the DS is expected. Therefore, the number of DE was continuously reduced according to a shrinking maze structure to examine the effects on the resulting discharge patterns.

Firstly, the model with constant cross-section area (057) was tested without DE *[No. 061]*. Secondly, different DE schemes were applied (Figure 31). The scenarios were applied on the constant cross-section model (057) with a DE cross-section area of $5*10^{-3}$ m² and a DE hydraulic aperture of $1*10^{-3}$ m *[No. 062, 063, 064, 068, 070, 071]*. For the scenario where 50% of the clay layers were assigned with DE, elements on the left side of the median were selected (DS averted side). The median is the axis that divides the DSG sediment in two equal areas. To realize this scenario, a polygonal region was selected which comprises all clay layers and is limited by the median. To remove all the layers which are not clay layers, the existing clay layers were intersected with the polygonal selection.

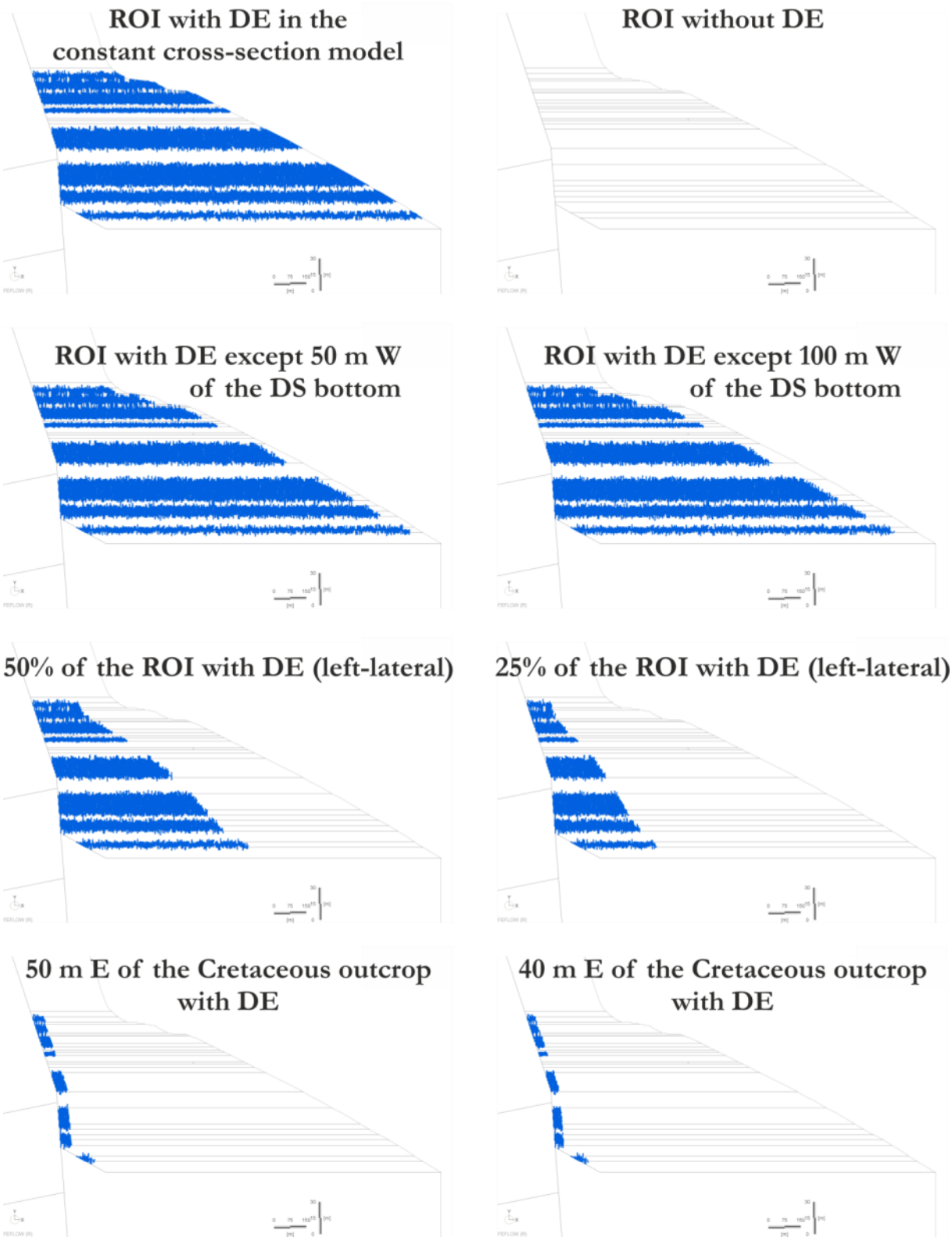

Figure 31: Applied DE frequency schemes The distribution of DE (blue) was varied within the clay layers of the DSG (ROI). DE exhibit a cross-section area of $5*10^{-3}$ m² and a hydraulic aperture of $1*10^{-3}$ m

4.7.6 Scenario: Discrete element inclination

To investigate impacts on the flow behavior that are induced by the inclination of discrete features, some of the DE from the constant cross-section model (057) have been oriented vertical with horizontally connecting tubes. In the frame of DS level fluctuations, vertical connecting tubes would be plausible if the lake level was deeper than the current one (cf. Waldmann et al. 2007). Vertical discrete elements (2 m selection width) have been arbitrarily assigned along the cross-section with an equidistance of 50 m within the clay layers. Horizontal tubes are likely along layer boundaries. Thus, they have been applied on the top and bottom of each clay layer bundle with a polygonal selection (2 m selection height). For the horizontal applied DE, the DSG selection was intersected with the horizontal polygonal selection. For the vertical applied DE, the clay layer selection was intersected with the vertical polygonal selection. Layers 11, 13, 16 and 17 have been refined due their small thickness. After refinement the model in total consists of 25,167 elements and 12,826 nodes. The applied schemes are depicted in Figure 32 *[No. 075 – only refinement, No. 076 – only horizontal tubes, No. 077 – only vertical tubes, No. 078 – DE mesh]*.

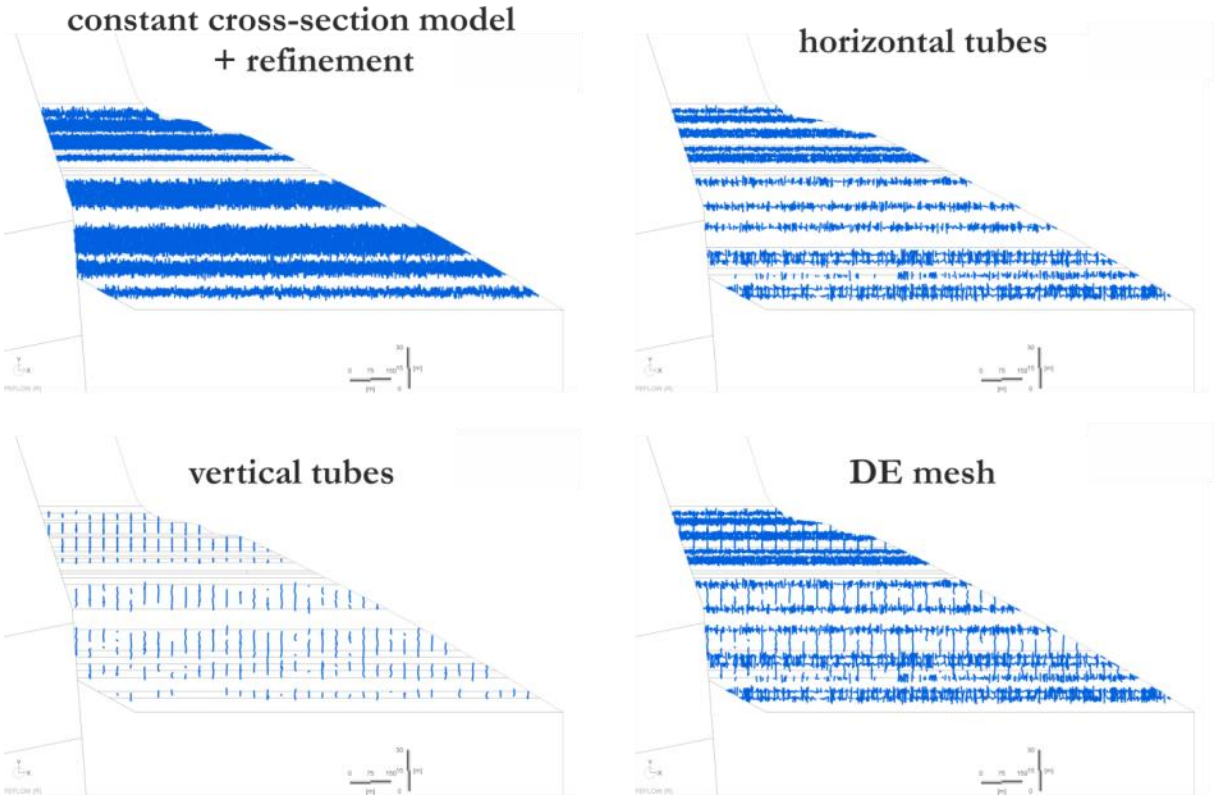

Figure 32: Applied DE inclination schemes DE exhibit a cross-section area of $5*10^{-3}$ m² and a hydraulic aperture of $1*10^{-3}$ m

4.7.7 Scenario: Salinity pool for ascending deep waters

For the investigation of uprising brines along faults, an additional mass-concentration BC with the concentration of a brine water was assigned to the two 1D node paths of the conceptual Judean fault system (cf. Figure 26, start with 100 g/L, increment 50 g/L) *[No. 079 to 084]*. The scenario was applied on the constant cross-section model (057).

4.7.8 Scenario: Debris removal

Although the geological map (Mor and Burg 2000) clearly indicates coarse-grained debris (designated as *Qli*, *Nqef*) above the differentiated DSG by its morphology, the geological continuation in depth is not as clear. Both outcropping Cretaceous rocks and DSG sediment are interacting in that area. Subsequently, the hydraulic conditions are blurred as well. To examine the impact of the debris on the streamlines, it has been excluded from numerical modeling. As consequence, either additional surface springs or a compression of the streamlines towards the DSG are expected. The scenario was applied on model 070 *[No. 090]*.

Table 16: Synopsis of the developed models. The multilayer DSG reflects the fact that all layers of the drilling have been incorporated. DE on faults are consistently applied with CS = 1 m² and HA = 0.001 m. FBW *flow boundary condition on the western boundary, Dirichlet type*, FBE *flow boundary condition on the eastern boundary, Dirichlet type*, MBW *mass boundary condition on the western boundary, Dirichlet type*, MBE *mass boundary condition on the eastern boundary, Dirichlet type*, DE *discrete elements*, CS *cross-section area*, HA *hydraulic aperture*, JG *Judea Group*.

Model No.	Name	Applied on	FBW [msl], FBE [msl], MBW [mg/L], MBE [g/L]	DSG Layering	kf DSG [m/s]	DE on DSG	DE on faults	Remarks
STEP 1: Model calibration								
006	initial model	-	-320, -425, 800, 350	1-layer DSG	1E-4	no DE	no DE	-
012	model without mass transport	006	-320, -425	1-layer DSG	1E-4	no DE	no DE	only flow modeling
013	model with partly applied western BC	006	-320, -425, 800, 350	1-layer DSG	1E-4	no DE	no DE	no flow BC above -330 m msl
014	model with upwinding	006	-320, -425, 800, 350	1-layer DSG	1E-4	no DE	no DE	streamline upwinding applied
017	model with permeable layer	006	-320, -425, 800, 350	2-layer DSG	1E-4	no DE	no DE	spatially limited kf increase (-454 to -468 m msl)
018	model with discrete feature	017	-320, -425, 800, 350	2-layer DSG	1E-4	DE applied	no DE	DE (DSG) on permeable layer (CS: 1 m², HA: 1 m): first DE test
020	model with varying kf-value for the DSG	014	-320, -425, 800, 350	1-layer DSG	variable	no DE	no DE	DSG kf sensitivity test
021	model with splitted western BC	014	-320/-300, -425, 800, 350	1-layer DSG	1E-4	no DE	no DE	Upper JG: -320 m msl (uncnf.), Lower JG.: -300 m msl (cnf.)
029	standard model	021	-320/-300, -425, 800, 350	1-layer DSG	5E-5	no DE	DE applied	kf values of Cretaceous, DSG and debris adapted; DE (faults)
043	models with kf contrast from standard	029	-320/-300, -425, 800, 350	1-layer DSG	variable	no DE	DE applied	DSG kf sensitivity test
030	4 layer model	029	-320/-300, -425, 800, 350	4-layer DSG	variable	no DE	DE applied	high-low conductivity zone test
035	multilayer model	029	-320/-300, -425, 800, 350	multilayer DSG	variable	no DE	DE applied	all drilling layers included
031	cavity model	030	-320/-300, -425, 800, 350	4-layer DSG	variable	DE applied	DE applied	DE (DSG) (CS: 1 m², HA: 0.001 m) on cavity: influence of cavity tested
038	network model	035	-320/-300, -425, 800, 350	multilayer DSG	variable	DE applied	DE applied	DE (DSG) on clay + salt layers (CS: 1 m², HA: variable): selective conduit influence test
045	network model with increased aperture	038	-320/-300, -425, 800, 350	multilayer DSG	variable	DE applied	DE applied	DE (DSG) on clay + salt layers (CS: 1 m², HA: variable): DE hydraulic aperture change
STEP 2: Sensitivity analysis								
047 to 052	matrix flow threshold model	035	-320/-300, -425, 800, 350	multilayer DSG	variable	no DE	DE applied	100→50% (047→052) of the original kf value (DSG)
054	constant hydraulic aperture	052	-320/-300, -425, 800, 350	multilayer DSG	variable	DE applied	DE applied	DE (DSG) only on clay layers: constant CS (1 m²), constant HA (0.001 m)
055	hydraulic aperture vs. depth (low gradient)	052	-320/-300, -425, 800, 350	multilayer DSG	variable	DE applied	DE applied	DE (DSG) only on clay layers: constant CS (1 m²), variable HA
056	hydraulic aperture vs. depth (high gradient)	052	-320/-300, -425, 800, 350	multilayer DSG	variable	DE applied	DE applied	DE (DSG) only on clay layers: constant CS (1 m²), variable HA
057	constant cross-section	038	-320/-300, -425, 800, 350	multilayer DSG	variable	DE applied	DE applied	DE (DSG) only on clay layers: CS adapted to 0.005 m², constant HA (0.001 m)
058	cross-section vs. depth (low gradient)	057	-320/-300, -425, 800, 350	multilayer DSG	variable	DE applied	DE applied	DE (DSG) only on clay layers: variable CS, constant HA (0.001 m)
059	cross-section vs. depth (high gradient)	057	-320/-300, -425, 800, 350	multilayer DSG	variable	DE applied	DE applied	DE (DSG) only on clay layers: variable CS, constant HA (0.001 m)
061	discrete element frequency (without DE)	057	-320/-300, -425, 800, 350	multilayer DSG	variable	no DE	DE applied	DE (DSG) removal
062	discrete element frequency 50%	057	-320/-300, -425, 800, 350	multilayer DSG	variable	DE applied	DE applied	DE (DSG) only on clay layers, reduced amount: constant CS (0.005 m²), constant HA (0.001 m)
063	discrete element frequency 25%	057	-320/-300, -425, 800, 350	multilayer DSG	variable	DE applied	DE applied	DE (DSG) only on clay layers, reduced amount: constant CS (0.005 m²), constant HA (0.001 m)
064	discrete element frequency 50 m E	057	-320/-300, -425, 800, 350	multilayer DSG	variable	DE applied	DE applied	DE (DSG) only on clay layers, reduced amount: constant CS (0.005 m²), constant HA (0.001 m)
068	discrete element frequency 40 m E	057	-320/-300, -425, 800, 350	multilayer DSG	variable	DE applied	DE applied	DE (DSG) only on clay layers, reduced amount: constant CS (0.005 m²), constant HA (0.001 m)
070	discrete element frequency 50 m W	057	-320/-300, -425, 800, 350	multilayer DSG	variable	DE applied	DE applied	DE (DSG) only on clay layers, reduced amount: constant CS (0.005 m²), constant HA (0.001 m)
071	discrete element frequency 100 m W	057	-320/-300, -425, 800, 350	multilayer DSG	variable	DE applied	DE applied	DE (DSG) only on clay layers, reduced amount: constant CS (0.005 m²), constant HA (0.001 m)
075	discrete element inclination (refinement)	057	-320/-300, -425, 800, 350	multilayer DSG	variable	DE applied	DE applied	DE (DSG) only on clay layers: constant CS (0.005 m²), constant HA (0.001 m)
076	discrete element inclination (horizontal)	057	-320/-300, -425, 800, 350	multilayer DSG	variable	DE applied	DE applied	DE (DSG) only on clay layers, only horizontal tubes: constant CS (0.005 m²), constant HA (0.001 m)
077	discrete element inclination (vertical)	057	-320/-300, -425, 800, 350	multilayer DSG	variable	DE applied	DE applied	DE (DSG) only on clay layers, only vertical tubes: constant CS (0.005 m²), constant HA (0.001 m)
078	discrete element inclination (mesh)	057	-320/-300, -425, 800, 350	multilayer DSG	variable	DE applied	DE applied	DE (DSG) only on clay layers, only horizontal + vertical tubes: constant CS (0.005 m²), constant HA (0.001 m)
079	salinity pool (100 g/L)	057	-320/-300, -425, 800, 350 MB faults: 100 g/L	multilayer DSG	variable	DE applied	DE applied	additional salinity pool on faults; DE (DSG) only on clay layers: constant CS (0.005 m²), constant HA (0.001 m)
083	salinity pool (300 g/L)	057	-320/-300, -425, 800, 350 MB faults: 300 g/L	multilayer DSG	variable	DE applied	DE applied	additional salinity pool on faults; DE (DSG) only on clay layers: constant CS (0.005 m²), constant HA (0.001 m)
090	debris removal	070	-320/-300, -425, 800, 350	multilayer DSG	variable	DE applied	DE applied	debris removed; DE (DSG) only on clay layers, reduced amount: constant CS (0.005 m²), constant HA (0.001 m)
STEP 3: Uncertainty analysis								
applied on 070								

4.8 Uncertainty analysis

The uncertainty analysis was imposed on the model with the optimal solution after the sensitivity analysis in order to evaluate the influence of model settings. For the evaluation, the obtained streamline and salinity pattern were compared to the reference streamline and salinity pattern.

4.8.1 Mesh quality

The mesh quality of the model domain was tested by smoothing the entire mesh once.

4.8.2 Reference concentration

The salt water concentration C_S of the DS was changed from 350 kg/m³ to 400 kg/m³ to examine the impact of the maximum concentration in the model domain on the streamline pattern and the advance of the fresh-salt water front.

4.8.3 Anisotropy of conductivity

The fraction K_{min}/K_{max} was chosen to 0.1 instead of 1 in order to reduce the conductivity in z-direction by one magnitude.

4.8.4 Dispersivity and molecular diffusion

Dispersivity and molecular diffusion are utilized as mass transport material parameter. Both are regarded as scale-dependent parameters. The default values for the longitudinal dispersivity $\beta_L = 5$ m and the transversal dispersivity $\beta_T = 0.5$ m ($\beta_T/\beta_L = 0.1$) were changed for the entire model domain according to certain ratios (cf. Yechieli et al. 2001, Kiro 2007), as follows:

1. $\beta_T/\beta_L = 1$ with $\beta_T = 5$
2. $\beta_T/\beta_L = 0.5$ with $\beta_T = 0.5$
3. $\beta_T/\beta_L = 0.01$ with $\beta_T = 0.01$
4. $\beta_T/\beta_L = 0.001$ with $\beta_T = 0.005$

Molecular diffusion was changed in the range of 10^{-7} to 10^{-11} m²/s for the entire model domain.

4.9 Constraint Index CI

The constraint index (Equation 6) is used for the evaluation of the model results and the accompanied uncertainties. The constraint is reflected by the surface and sublacustrine discharges to the DS (Figure 16). Impacting factors are

Z – Elevation difference between observed and simulated discharge points
B – Total flow and mass balance
F – Frequency of discharge points along the entire eastern boundary
D – Density of discharge points

$$Constraint\ Index\ CI = Z + B + F + D \qquad \textbf{Equation 6}$$

where

Z	1 = high: Σ(Z1+Z2) ≥ 59 m 2 = medium: 49 m ≤ Σ(Z1+Z2) < 59 m 3 = low: Σ(Z1+Z2) < 49 m
B	1 = high: fluid balance > 100 m³/d, mass balance > 100 g/s or not calculated 2 = medium: fluid balance < 100 m³/d 3 = low: fluid balance < 10 m³/d, mass balance < 100 g/s
F	3 = high: cluster frequency ≥ 4 2 = medium: 2 ≤ cluster frequency < 4 1 = low: cluster frequency < 2
D	0.5 = low surface discharge (higher than -424 m msl) 1.0 = medium surface discharge (higher than -424 m msl) 0.5 = high surface discharge (higher than -424 m msl) 0.5 = discharge at -425±1 m msl (transition zone) 0.5 = low shallow sublacustrine discharge (higher than -465 m msl) 1.0 = medium to high shallow sublacustrine discharge (higher than -465 m msl) 1.0 = sublacustrine discharge at greater depth (lower than -465 m msl)

The classification of Z values is expressed by the sum of Z1 and Z2. Z1 is the distance to the highest spring of -407 m msl. Z2 is the distance to the lowest spring of -475 m msl (Figure 16).

The total flow and mass balance B is calculated from the applied Dirichlet BC on the western and eastern side of the model (chapter *Rate budget*).

The frequency of discharge points F along the entire eastern boundary is regarded as the number of discharge clusters. A cluster comprises one or several discharge points that can be captured by a circle with a radius of 1 m.

The density of discharge points D assigns additional index points to the models and is related to the intensity of discharge points (cf. Figure 16).

- 1 point for models which exhibit similar discharge amounts compared to the observed discharge amounts (medium surface discharge and medium to high shallow sublacustrine discharge)
- 1 point for models with existing sublacustrine discharge in greater depth
- 0.5 points for models with low and high surface discharge, low shallow sublacustrine discharge and discharge at -425±1 m msl

The discharge amount (low, medium or high) has been evaluated according to the number of streamlines. Applicable to all models, one streamline contains 24 seeds per node with an initial radius at the western boundary of 5 m. In this context, a *feature* either denotes *surface discharge (higher than -424 m msl), discharge at -425±1 m msl, sublacustrine discharge (higher than -465 m msl)* or *sublacustrine discharge at greater depth*. The attributes for the discharge amount, which are low (1 streamline), medium (2 to 3 streamlines) and high (≥4 streamlines), are defined for the case if

1. one cluster belongs to the *feature*: Number of streamlines within that cluster
2. several clusters belong to the *feature*: Number of streamlines for the cluster with the highest number of streamlines

For instance, there might be two clusters belonging to the feature *surface discharge (higher than -424 m msl)* with a low number of streamlines for cluster 1 and with a medium number of streamlines for the other cluster 2. The highest streamline number, i.e. the number of streamlines for cluster 2, determines the assigned index points, which is 1 point for *medium surface discharge (higher than -424 m msl)*.

5 Results

Depending on the data scarcity the simulation of the flow processes in the study area are dominated by an array of uncertainties. Therefore, the simulation starts with the simplest hydrogeological conditions (Figure 26), which step by step are specified and adapted on the field observations. The model calibration ends with the creation of a standard model (029), which includes all major hydrogeological structures and their important material parameterization. The standard model represents the basis for further calibration models and scenarios with respect to the adaption of flow paths in the DSG sediments.

5.1 Model calibration

5.1.1 From initial to standard model

Table 17, Table 18 and Table 19 contain the development from the initial model (006) to the standard model (029). With respect to the setup of flow paths inside the DSG sediments a base assumption was set at the beginning of the model calibration. In general, the bulk sediment can be characterized by a kf-value of 10^{-7} m/s, which is a typical hydraulic conductivity for a mixed salt-clay layer with some embedded gravel layers (Domenico and Schwartz 1998). Also numerical simulations of Gräbe et al. (2013) reveal that the sediment controls the discharge from the Judean aquifer to the DS. However, applying a kf-value of 10^{-7} m/s water is not able to enter the DSG during the conducted steady-state simulations. Therefore, the hydraulic conductivity of the DSG was adapted to values between 10^{-4} to 10^{-5} m/s to produce realistic travel times and optimal results for the model without division of the DSG sediment, which are comparable to the field observation along the shoreline of the DS.

Table 17: Results for the initial to the standard model (hydraulic heads)

	Simulated hydraulic heads
Model 006 (initial model)	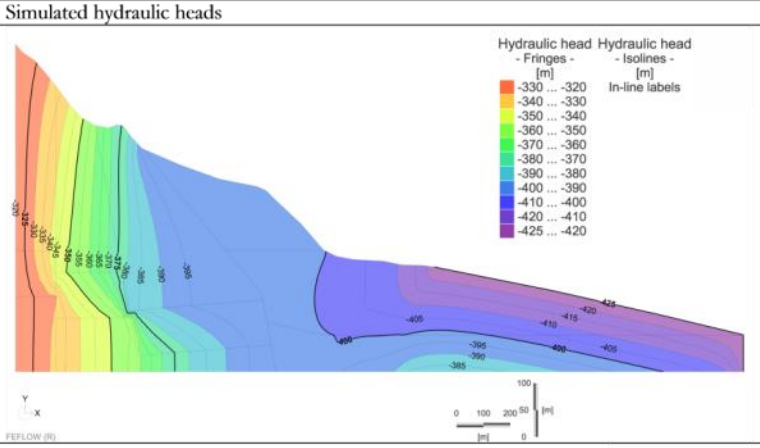
Model 014 (upwinding)	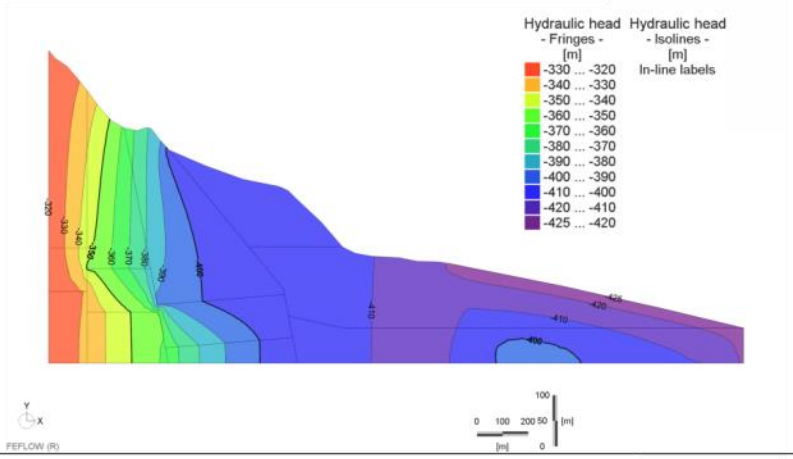
Model 021 (splitted western BC)	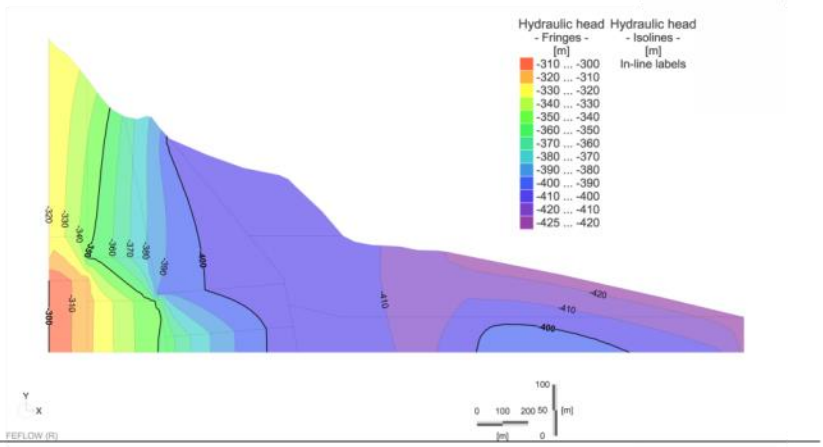
Model 029 (standard model)	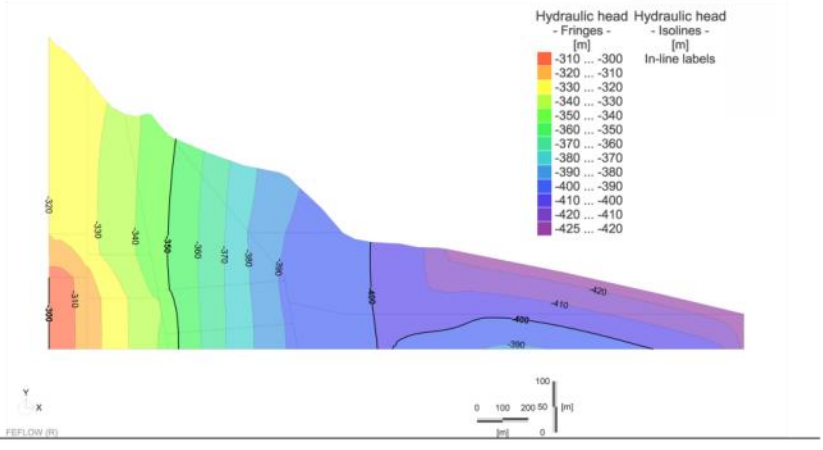

Table 18: Results for the initial to the standard model (streamlines)

	Shape of streamlines
Model 006 (initial model)	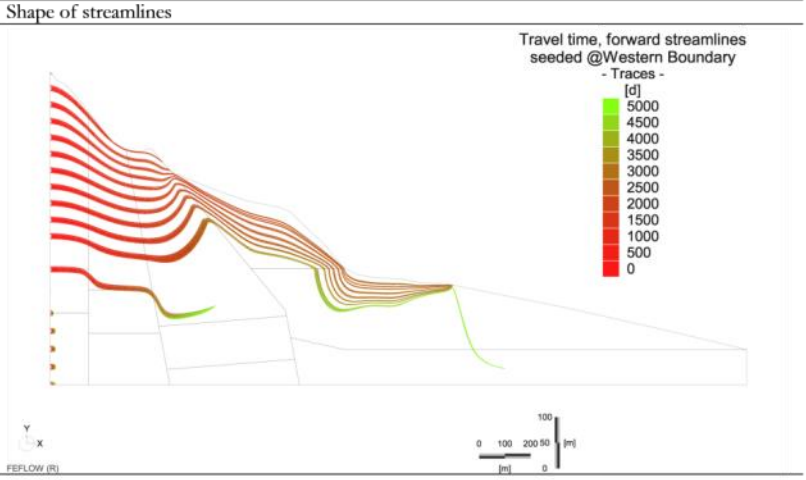
Model 014 (upwinding)	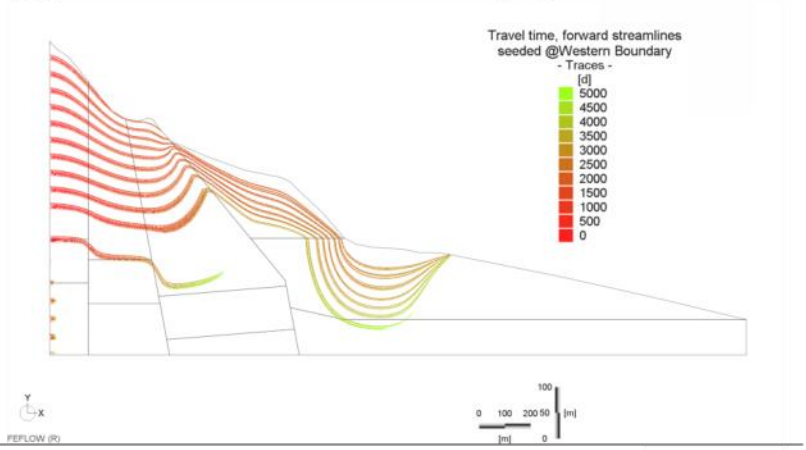
Model 021 (splitted western BC)	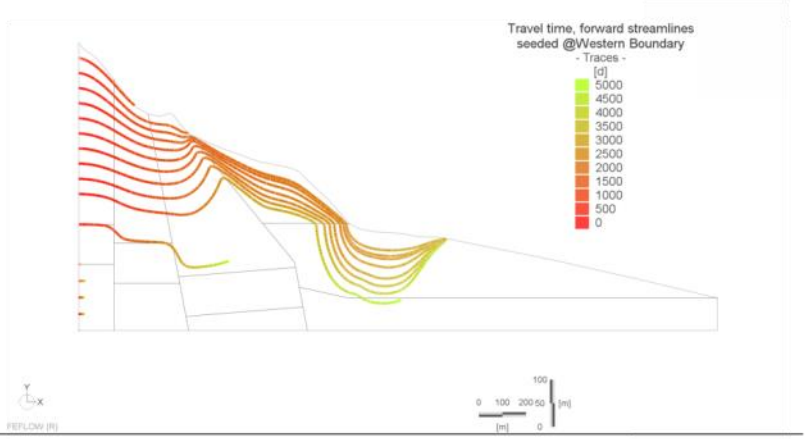
Model 029 (standard model)	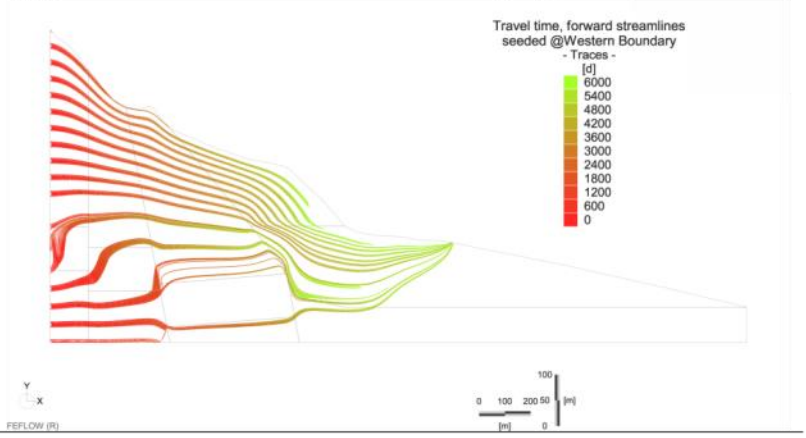

Table 19: Results for the initial to the standard model (mass concentration patterns)

	Shape of fresh-salt water interface
Model 006 (initial model)	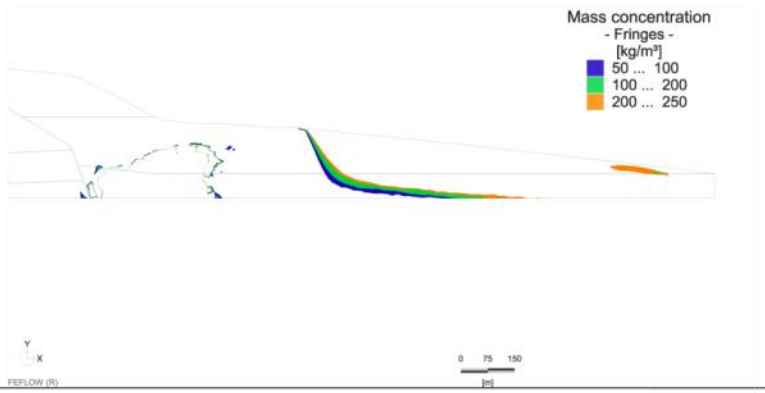
Model 014 (upwinding)	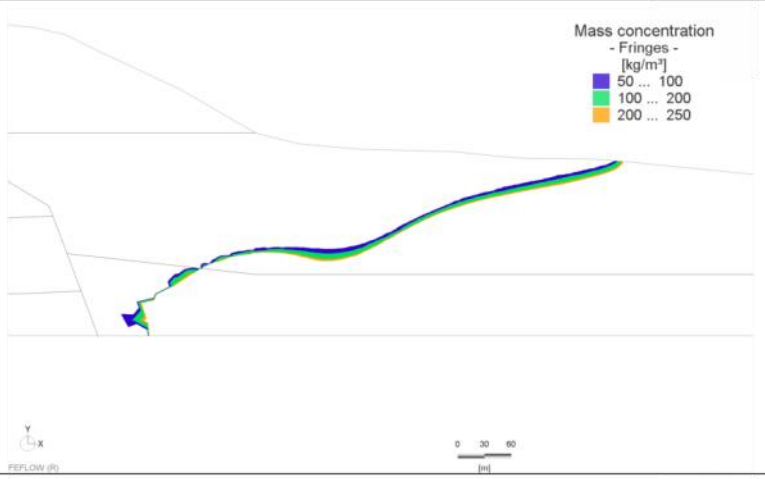
Model 021 (splitted western BC)	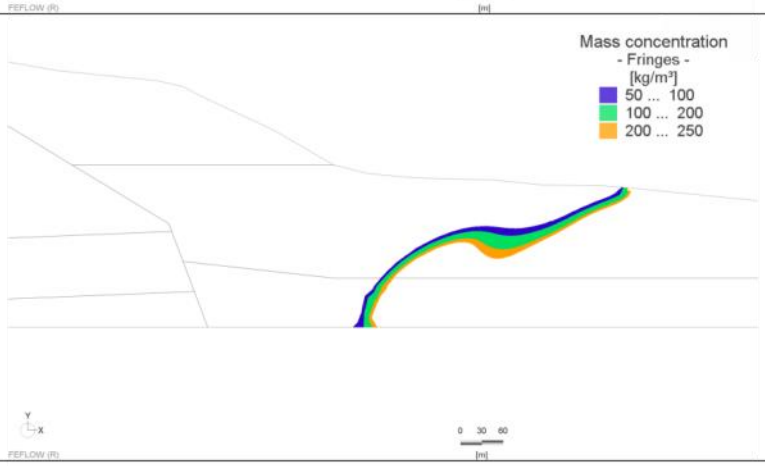
Model 029 (standard model)	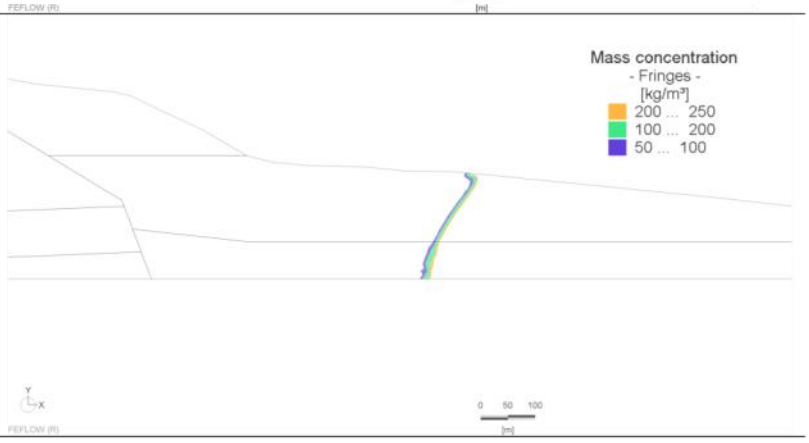

The modeling results exhibit the expected topography-driven groundwater flow from the Judean Mountains via the DSG sediment towards the DS. The potential heads of the Judea Group are nearly equidistant (Table 17). Closer to the DS, potential lines are sensitive to the layering of the DSG sediment reverting flow lines to the vertical. Subhorizontal heads below the DS increase with larger depth and yield uprising water flow towards the DS bottom. Based on the used BC of the mass concentration the formation of a fresh-salt water interface close to the DS is observable in all models.

The simulated models differ strongly in the development of streamlines (Table 18) and the fresh-salt water interface (Table 19). In the frame of the presented work it was reproducible that the shape of streamlines and the fresh-salt water interface was strongly related to the option of the western BC, to the parameterization of the DSG sediment and streamline upwinding. The latter presents a numerical option that smoothed the concentration gradient from the Judea Group towards the DS and results in an improved visualization of the fresh-salt water interface (014). The resulting fresh-salt water interface exhibits a wedge-like appearance with a larger advance in the deeper DSG and delineates a realistic distribution of mass concentrations in the non-differentiated Quaternary sediments according to Ghyben-Herzberg. The adjustment of streamline upwinding was used as standard method for the further models.

The modification of the western BC reveals the distribution of the streamlines inside the Judea Group. A water level lowering (013) results in the decrease of flow velocities within the hard rock aquifer and unrealistic long travel times. The separation of the BC in confined Lower Judea Group (BC from -480 m msl to model bottom) and unconfined Upper Judea Group (BC from -10 m msl to -480 m msl) in model 021 results in a plausible distribution of both, hydraulic heads and streamlines inside the Cretaceous aquifers. In model 021, the fresh-salt water front exhibits the wedge-like advance within the DSG. The adjustment of the western BC was used as standard method for the further models. A single permeable layer within the DSG group (017) does not channel the flow that is entering the DSG sediment from the Judean Mountains. The additional discrete feature on that layer (018) causes an extended but sharp wedge-like fresh-salt water interface. Eventually, the standard model (029) comprises all necessary features and fulfills the discharge to the DS.

The final variation of hydraulic conductivities of the DSG sediment was done prior to the separation of DSG layers (043), with the resulting streamline patterns displayed in Figure 33. Travel times of simulations with kf-values lower $1*10^{-6}$ m/s prevent inflow to the DSG sediment within the upper limit of 5,000 d. Hydraulic conductivity values larger than $1*10^{-4}$ m/s reveal a high flow and mass imbalance of the system, with outflow prevailing over inflow. The simulations with low kf-values of the DSG sediment could prove uprising water in the rear of the DSG sediment but could not prove any surface water spring. Though, no terrestrial discharge could be proven by that simulation, there is the possibility of that: High conductivity areas within the Judea Group would facilitate flow entrance to the sediment. These waters may rise from deep-seated aquifers as well. The increase of hydraulic conductivity of the sediment by one magnitude from $1*10^{-5}$ to $1*10^{-4}$ m/s completely changed the flow behavior. With $1*10^{-5}$ m/s, the pressure within the lower Judea Group aquifer is dominantly released to the upper Judea Group aquifer. But making the sediment slightly more conductive will release this pressure in the direction of the DS. It means

the opposite pressure from the DSG sediment is not large enough to counter the inflowing water volume. Therefore, sublacustrine and terrestrial (surface) discharge might occur in dependence of slight conductivity changes in the range of $1*10^{-4}$ to $1*10^{-5}$ m/s in the DSG sediment (only matrix flow, no DE in the DSG).

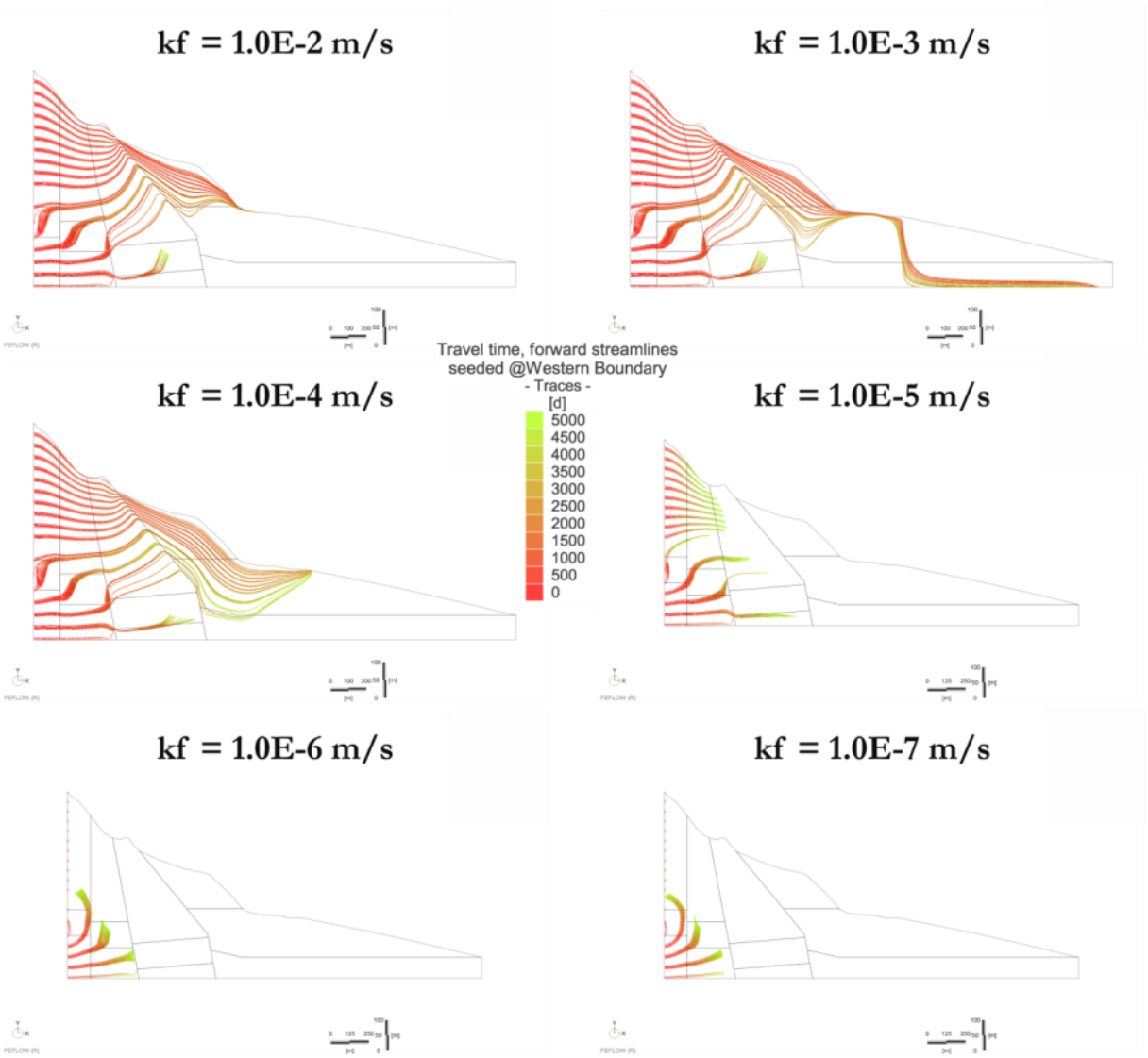

Figure 33: Streamlines (models with kf contrast from standard, x:z = 1:2)

The presented results reveal that the hydraulic properties of the DSG sediments have a very sensitive effect on the groundwater flow paths. Inside the DSG sediments unknown mineral distribution, unknown solution processes and resulting undefined dimensions of the conduit network demand for the separation of the sediments in a multilayer and discrete element model.

5.1.2 DSG layering

The well ML-4 (Figure 21) represents the standard profile for the DSG sediments in the study area. Therefore, the information about the hydraulic conductivity of ML-4 is implemented in model 030 according to Figure 27 and the standard model. The model exhibits that heterogeneities within the DSG sediment are easily triggered by strata of higher conductivity.

The simulation of the multilayered model (035) exhibits diffuse increments of hydraulic heads within the DSG sediment reflecting the heterogeneous media (Figure 34). Subhorizontal flow lines characterize layers of lower hydraulic conductivity where water tends to stagnate. Subvertical heads imply horizontal flow paths inside layers of higher hydraulic conductivity, facilitating discharge to the DS as well. However, not every high conductivity zone realizes flow to the DS. Single sublacustrine discharge to the DS is indicated for a depth of -451 m msl (Figure 35). In Figure 36 it is visible that the fresh-salt water interface is turned forwards (push mechanism) in areas with high conductive layers. The more impermeable layers preserve the subvertical interface and the intrusion of saline waters (pull mechanism). The mass concentration pattern reflects a push-pull salinity mechanism with subvertical interface sections along highly conductive layers and subhorizontal interface sections along almost impermeable layers (Figure 37). Obviously, the transition to subhorizontal shapes occurs within the more impermeable layer.

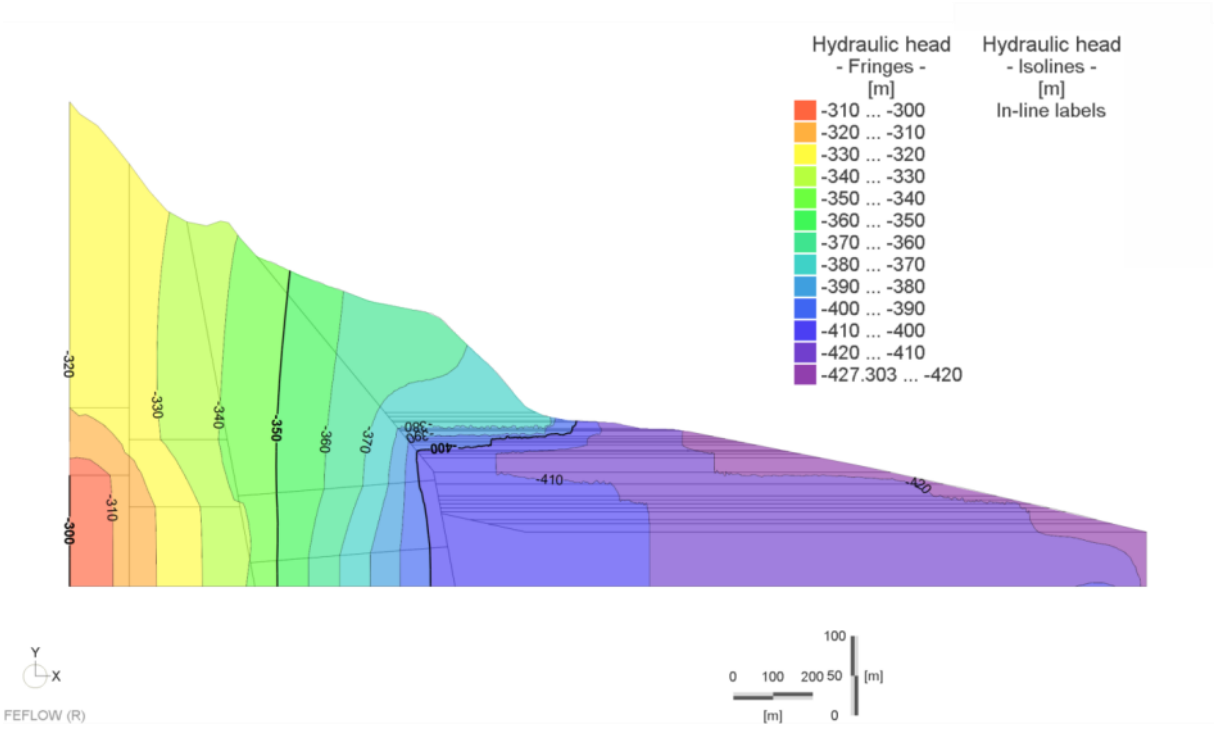

Figure 34: Hydraulic heads (multilayer model, x:z = 1:2)

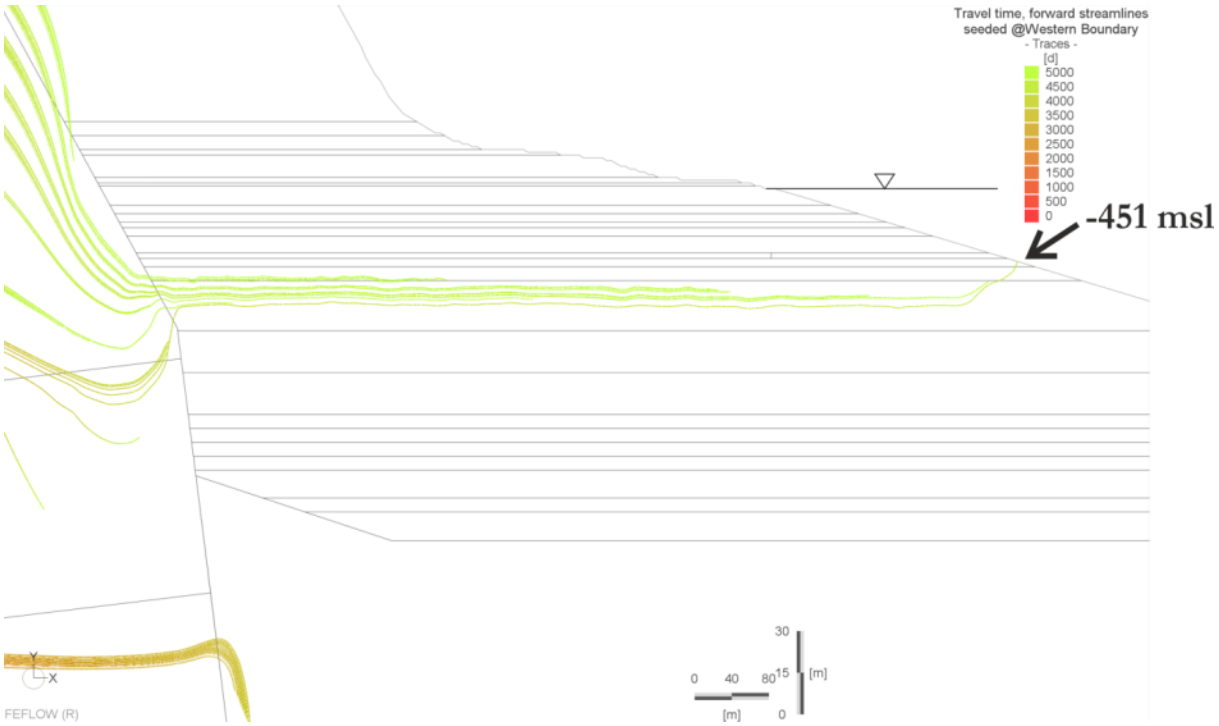

Figure 35: Streamlines (multilayer model, x:z = 1:2)

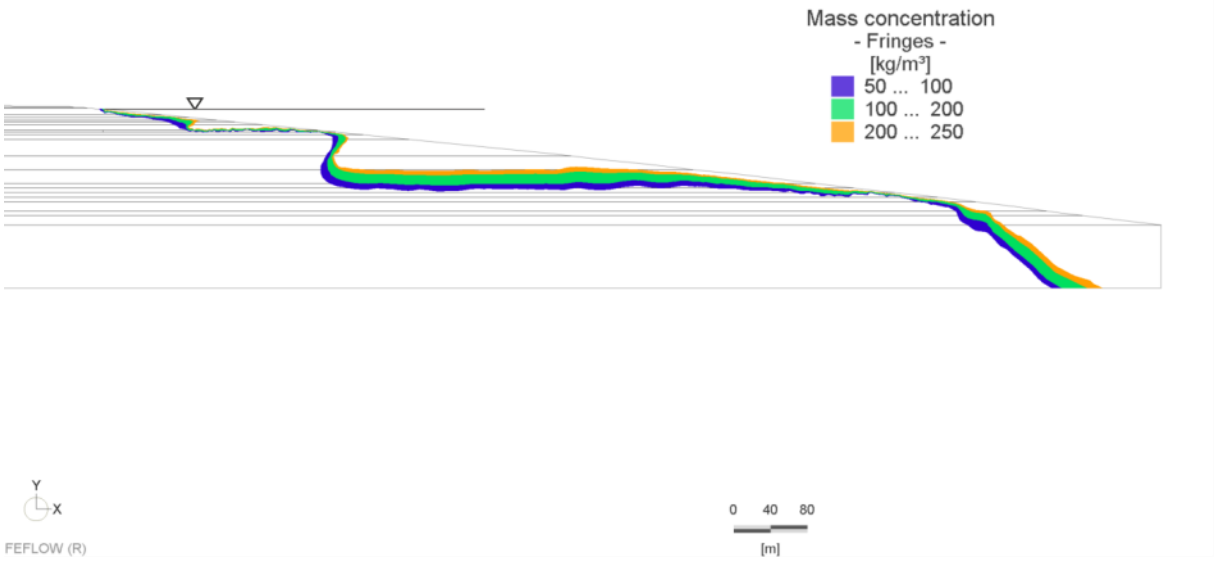

Figure 36: Mass concentration pattern (multilayer model, x:z = 1:1)

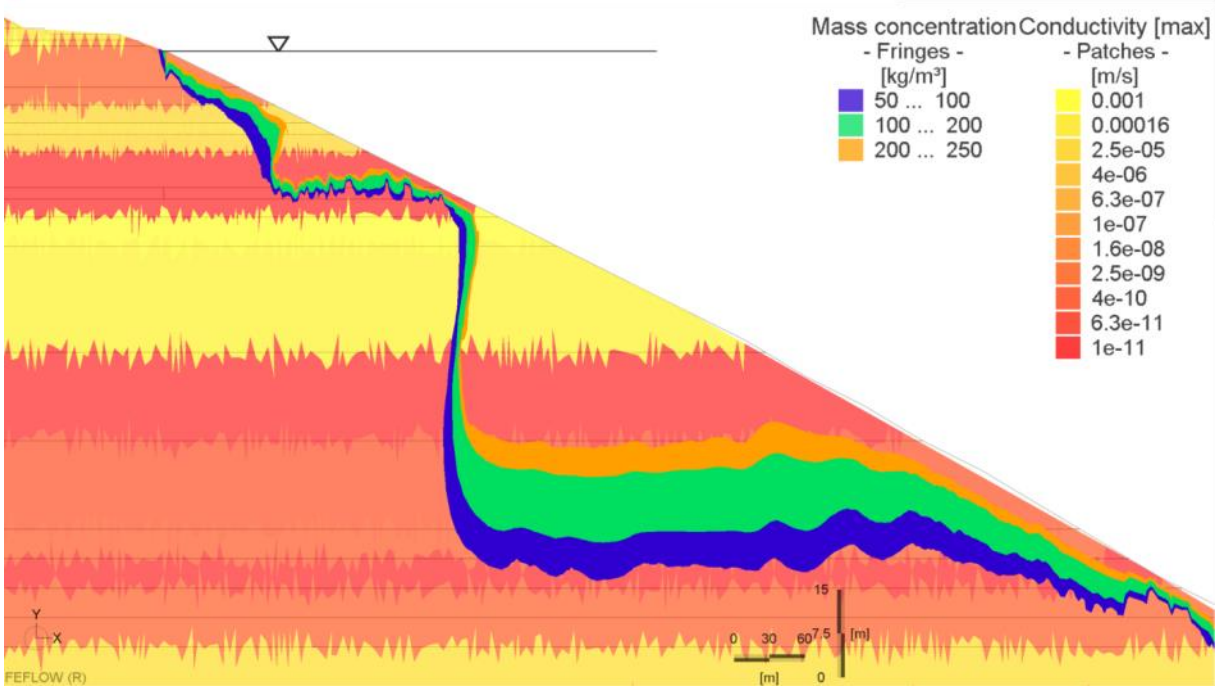

Figure 37: Push-pull-mechanism. Correlation of subvertical interface sections along highly conductive layers (push mechanism) and subhorizontal interface sections along almost impermeable layers (pull-mechanism)

5.1.3 Deduction of a DE network

Analog to Figure 28 a discrete element network was implemented in the multilayer model (035) for further specification of the models. The matrix of the DSG is defined by the hydraulic conductivities of the ML-4 layers. The adjustments of discrete elements in FEFLOW are used to reproduce heterogeneities of hydraulic conductivity inside the DSG sediment with respect conduits triggered by chemical solution processes.

The application of discrete elements (cross-section area: 1 m², hydraulic aperture: 0.001 m) on the existing cavity (031) resulted in a similar hydraulic head pattern compared to the multilayer model. The discrete element network (038) produced a very shallow hydraulic gradient pattern in the DSG sediment (Figure 38). Inside the DSG sediment the water flow to the DS is stopped. With larger travel times single discharge to the surface is indicated for a depth of -384 m msl (Figure 39). The highly conductive layers attract inflowing saltwater and distribute high salinity zones in the entire DSG sediment, even in the transition zone between Judean Mountains and DSG sediment (Figure 40).

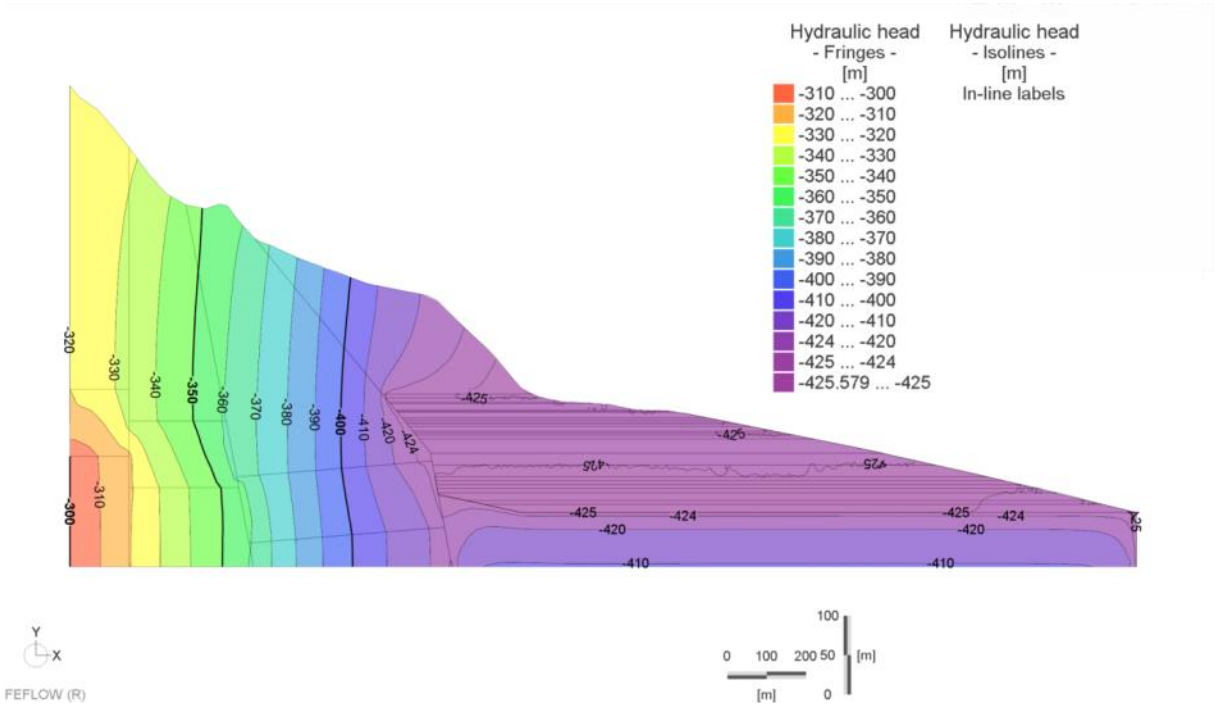

Figure 38: Hydraulic heads (network model, x:z = 1:2)

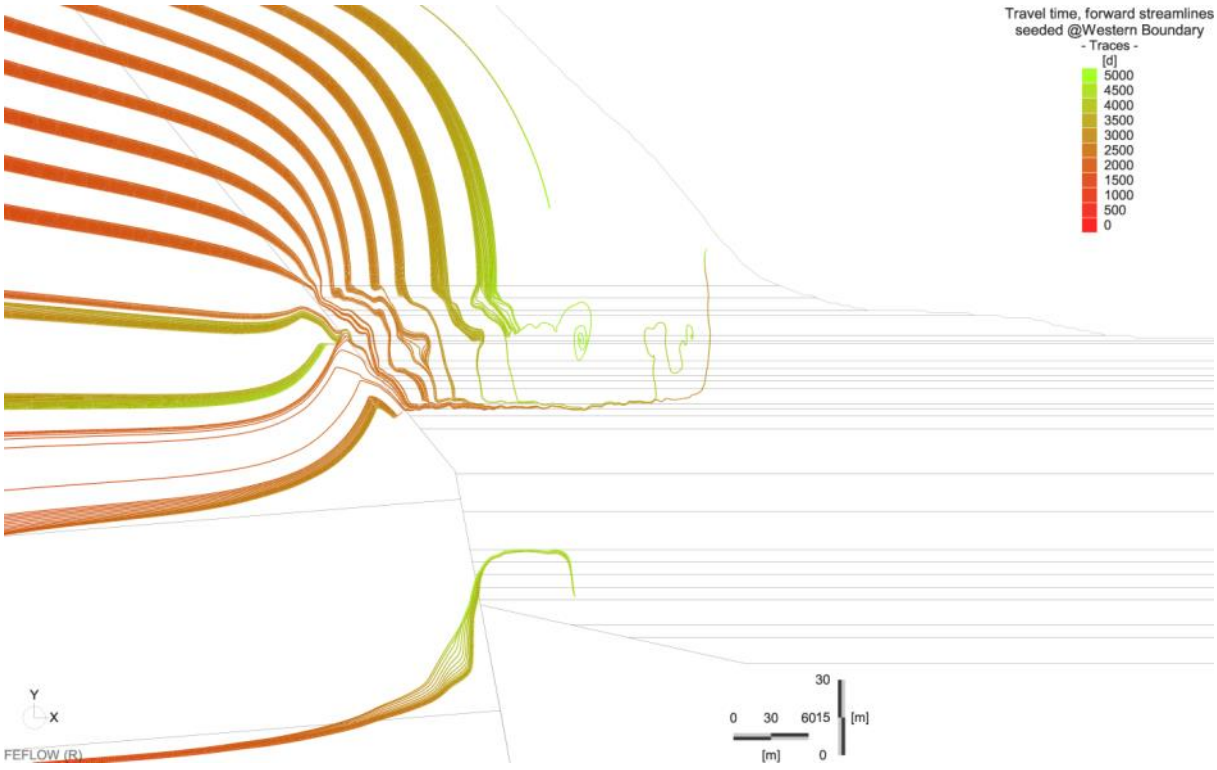

Figure 39: Streamlines (network model, x:z = 1:5)

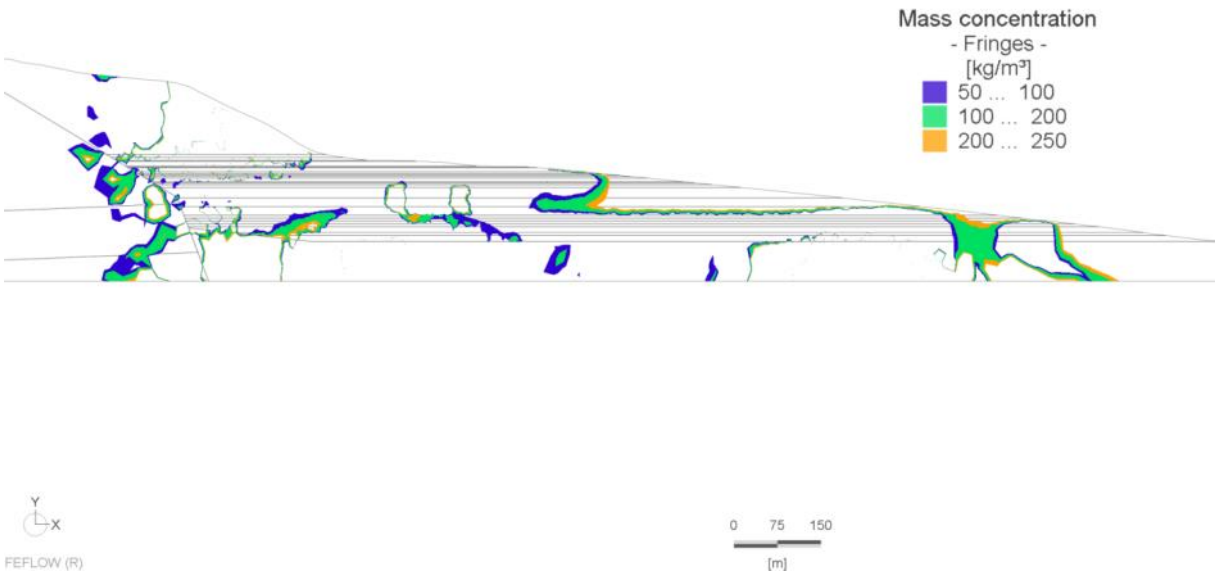

Figure 40: Mass concentration pattern (network model, x:z = 1:1)

In model 045 a tenfold increasing of the DE hydraulic aperture of the gypsum/clay layers from 0.001 m to 0.01 m produced discharge to the DS in a depth of -461 m msl after 2,500 d (Figure 41). The mass concentration pattern exhibits less splitting in large gradient concentration zones compared to the previous model and reveals a sharp interface at least for the upper part of the DSG sediment. The interface has no contact to the DS anymore and propagates more than 200 m away from the DS (Figure 42). The increase of the hydraulic aperture to a value of 0.1 m for gypsum/clay and halite resulted in numerical instability with unreasonable hydraulic heads.

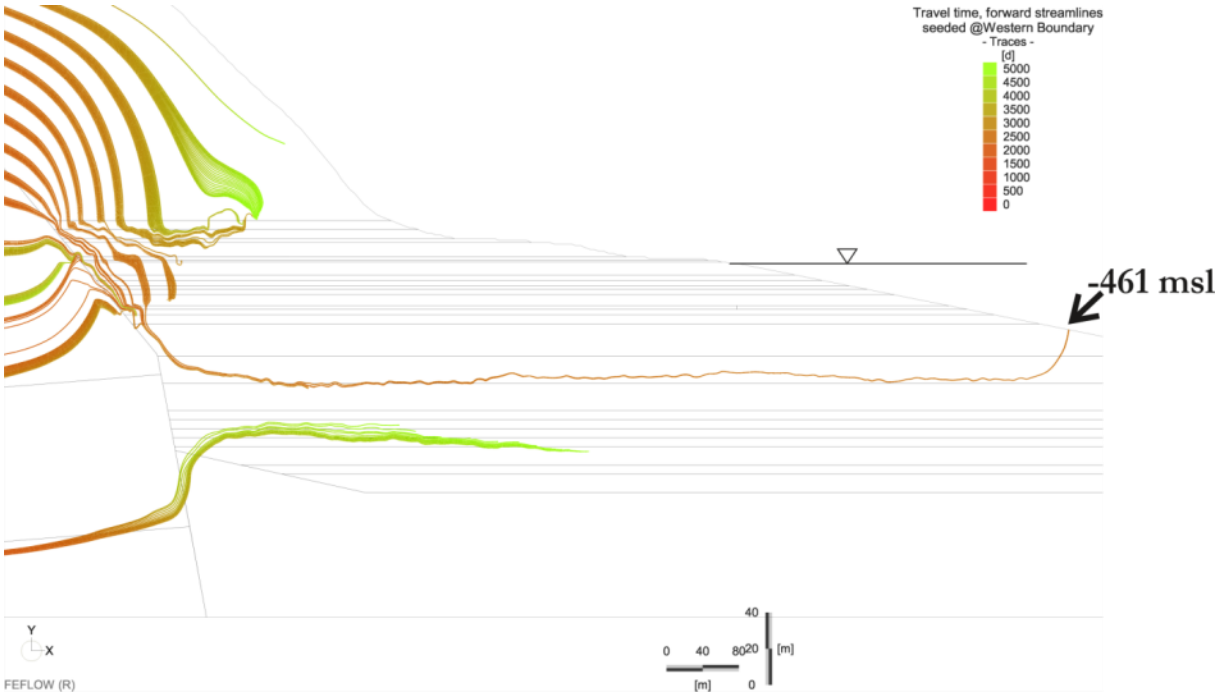

Figure 41: Streamlines (network model with increased aperture, x:z = 1:2)

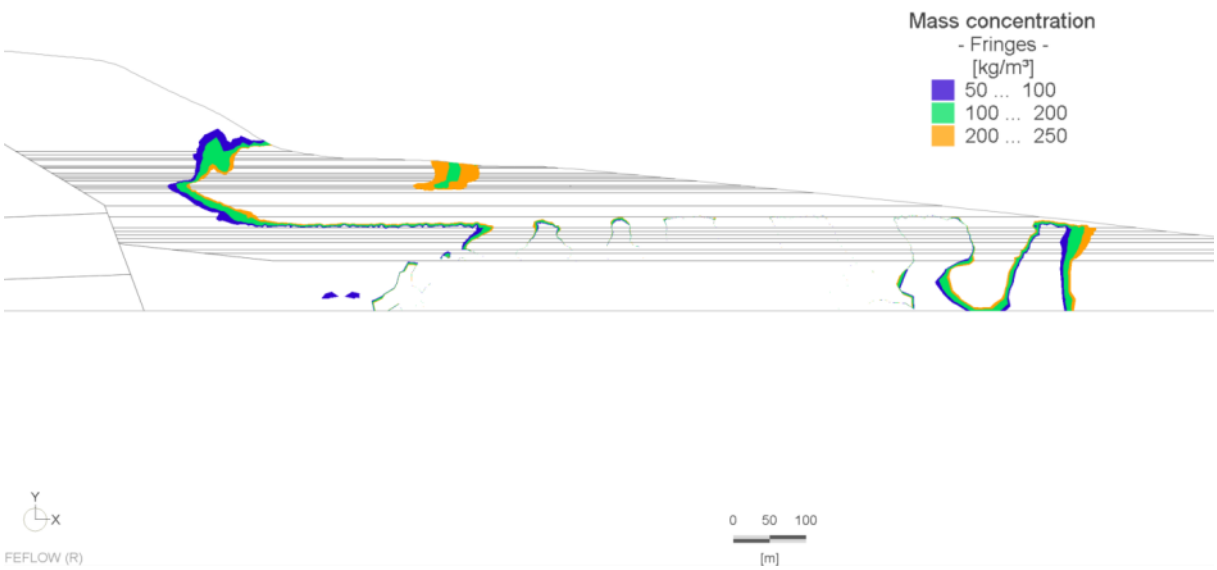

Figure 42: Mass concentration pattern (network model with increased aperture, x:z = 1:1)

Regarding the travel time distribution within the model domain, water needs the largest travel time through the Judean Mountains. Especially, due to the large residence times inside the Upper Judea Group aquitard *Kuey* groundwater movement is prone to dispersion and diffusion instead of convection. Residence times within the first 300 m of the DSG sediment are rather large, reducing considerably within the conduit/conduits and prolonging slightly to the outlet of the DSG sediment (Figure 43 – 045). These are typical simulated groundwater velocity ranges in the

1. Judea aquifer: $3*10^{-6}$ to $2*10^{-7}$ m/s (0.02 to 0.3 m/d)
2. transition zone: $3*10^{-4}$ to $3*10^{-6}$ m/s (0.3 to 30 m/d)
3. DSG sediment conduit: $4*10^{-2}$ to $4*10^{-3}$ m/s (350 to 3,500 m/d)
4. DSG sediment outlet: $4*10^{-3}$ to $3*10^{-4}$ m/s (30 to 350 m/d)

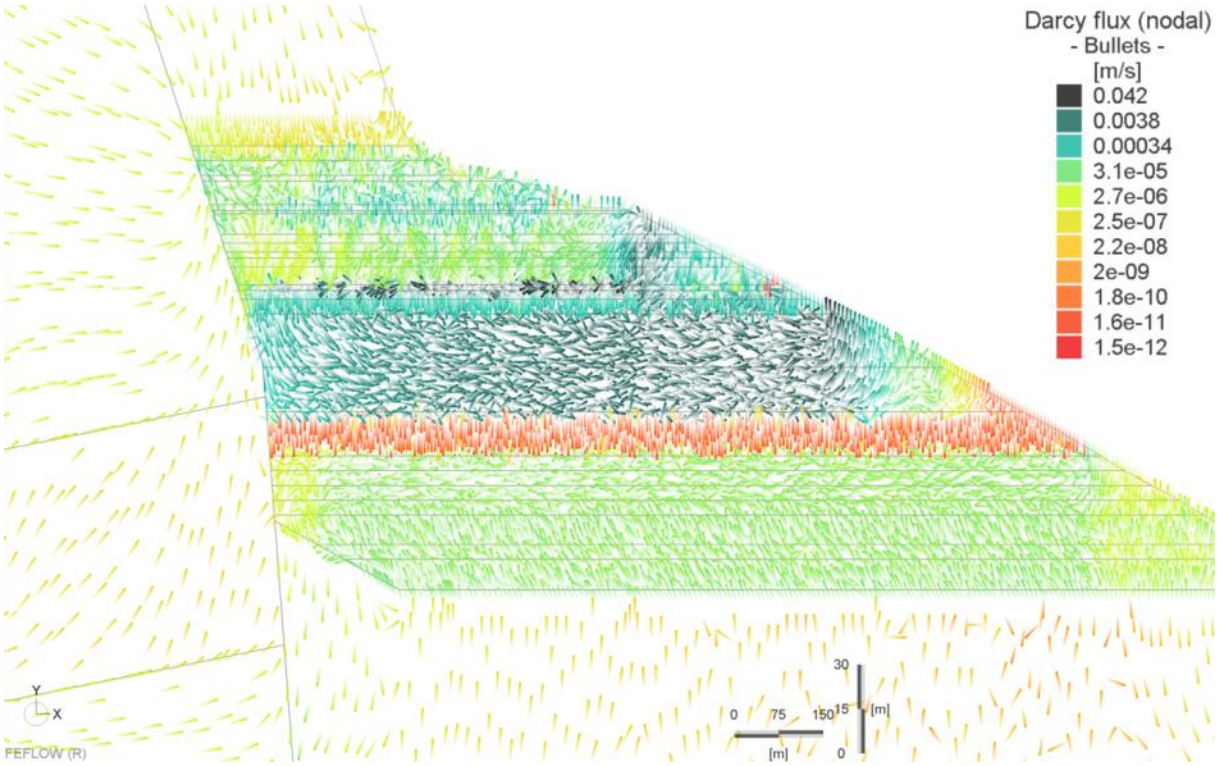

Figure 43: Darcy flux in the DSG (network model with increased aperture, x:z = 1:5)

5.2 Sensitivity analysis

The model calibration revealed that similar model results were simulated by the implementation of different subsurface structures in the DSG sediments. The presented scenarios of the sensitivity analysis are based on the multilayer model (035) where variations of hydraulic conductivities (based on the ML-4 borehole information) and different applied DE parameters (cross-section area, hydraulic conductivity) and DE network patterns in the DSG (based on the network model 038) were sensitively analyzed. Table 16 gives an overview of the developed scenarios.

5.2.1 Scenario: Matrix flow threshold

The hydraulic conductivity of the DSG sediment was tested with respect to spreading of flow paths. During the scenario analysis the hydraulic conductivity of the DSG sediments was stepwise reduced by 10%. A reduction to 50% of the initial hydraulic conductivity (model 052) results in the loss of contact between the streamlines and the DS. The streamline plots of the sequential hydraulic conductivity reduction are shown in Figure 44. The scientific findings confirm the results of the model calibration: At least certain layers (layer 16 and 17 in that case) need to exhibit hydraulic conductivities of 10^{-4} to 10^{-5} m/s (cf. Table 5) to enable a groundwater flow through the DSG sediments without the application of DE.

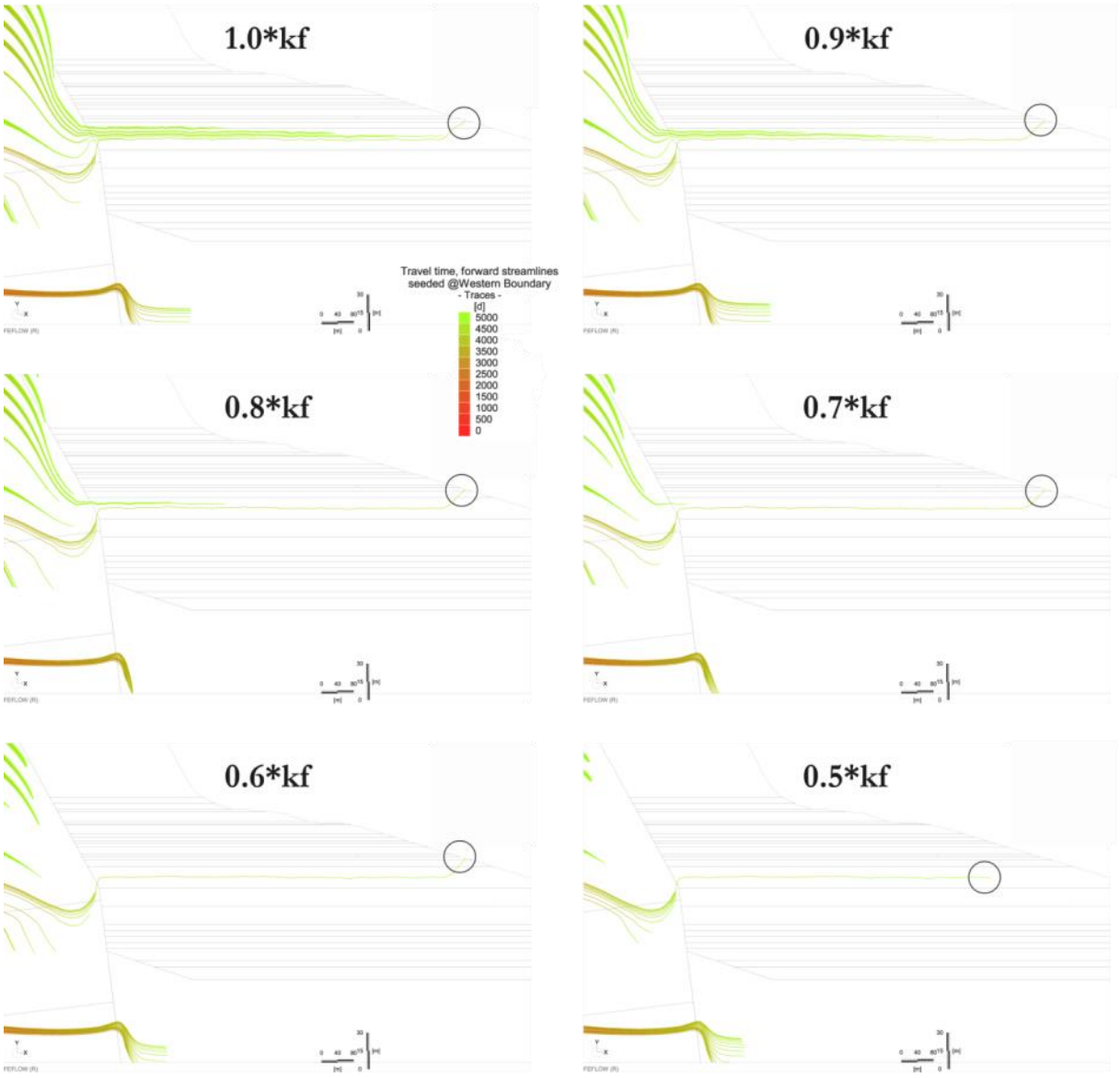

Figure 44: Streamlines (matrix flow threshold model, x:z = 1:5)

5.2.2 Scenario: Hydraulic aperture vs. depth

Applied on the model 052 the relation between hydraulic apertures of DE on the clay layers and depth was investigated. In the chapter *Model design* was described that a realistic range of hydraulic aperture values from minimum 1 mm to maximum 1.3 m were tested in case 1 (model 055) and case 2 (model 056). In both models the hydraulic aperture increases with the depth to investigate a possible compensation of the impacting DS pressure potential. The results of both models show that water flow is not sensitive to increasing apertures with increasing depth (Figure 45). Water flow in the deeper subsurface can therefore not be induced from increasing hydraulic aperture to the depth.

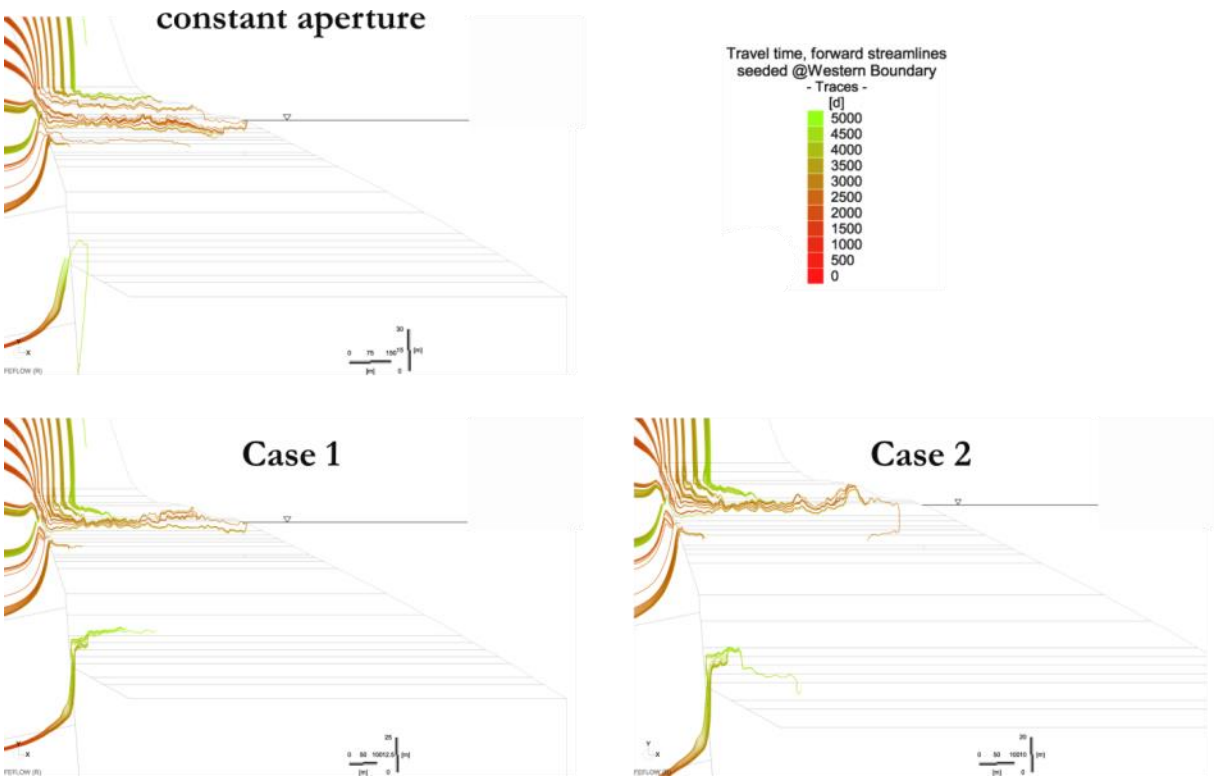

Figure 45: Streamlines (hydraulic aperture vs. depth, x:z = 1:5). Contrasted are case 1 (aperture value increased by 2 magnitudes) and case 2 (aperture value increased by 3 magnitudes) with the reference model of constant aperture

The model 054 with homogeneous distribution of the hydraulic aperture reveals preferred flow paths in the upper DSG sediment with several discharge points to the DS in a depth of -408 m msl, -411 m msl, -414 m msl and -425 to -426 m msl, respectively. The mass concentration pattern of the model with constant hydraulic aperture (054) exhibits saltwater intrusion in the lower DSG sediment with a sharp interface compared to the density distribution of the network model (Figure 46). In terms of the push-pull-mechanism this scenario offers a worst case with a complete freshwater breakthrough in the upper DSG sediment and saltwater flushing of the entire lower DSG sediment. The two case scenarios do not show a sharp fresh-salt water interface but an inhomogeneous distribution of large salinity gradients.

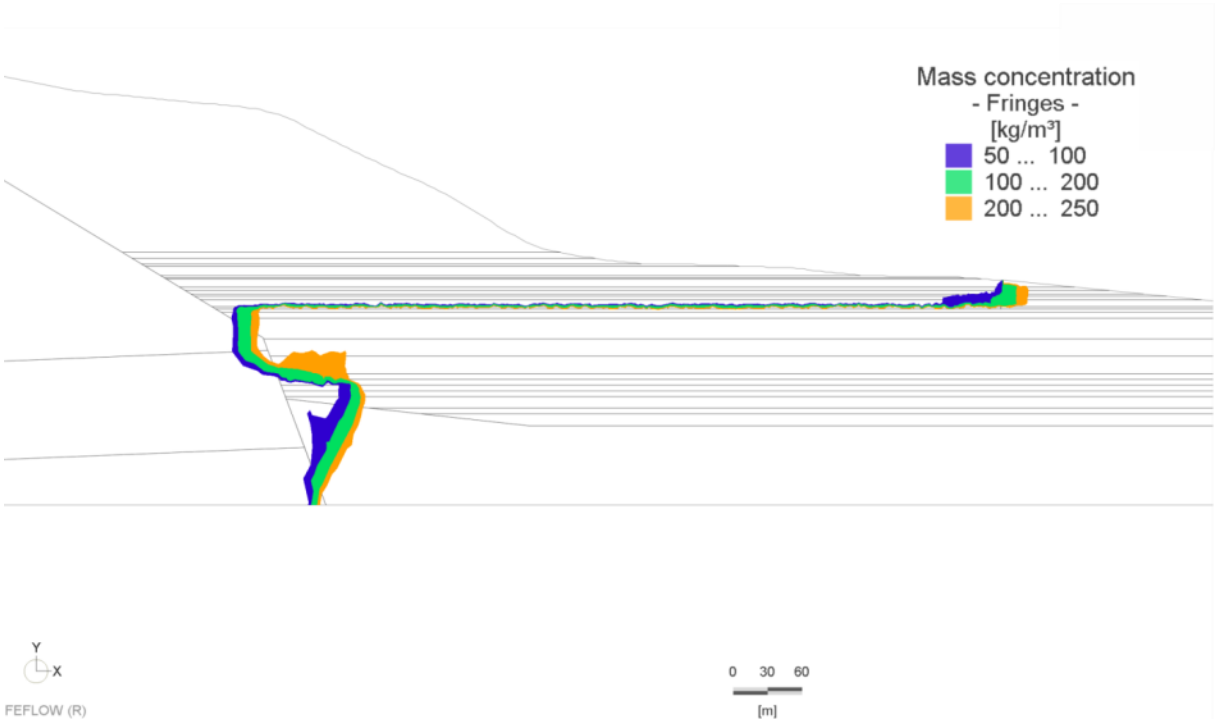

Figure 46: Mass concentration pattern (hydraulic aperture vs. depth, x:z = 1:1)

5.2.3 Scenario: Cross-section area threshold

Applied on the network model (038), in model 057 the relation between DE cross-section area and spreading of streamlines inside the DSG was tested. The minimum cross-section area for which discharge to the DS can be realized (threshold value) was determined to $5*10^{-3}$ m² for a given hydraulic aperture of 0.001 m in the clay layers and a time frame of 3,000 d (Figure 47). Smaller values of the cross-section area result in the loss of contact between the streamlines and the DS.

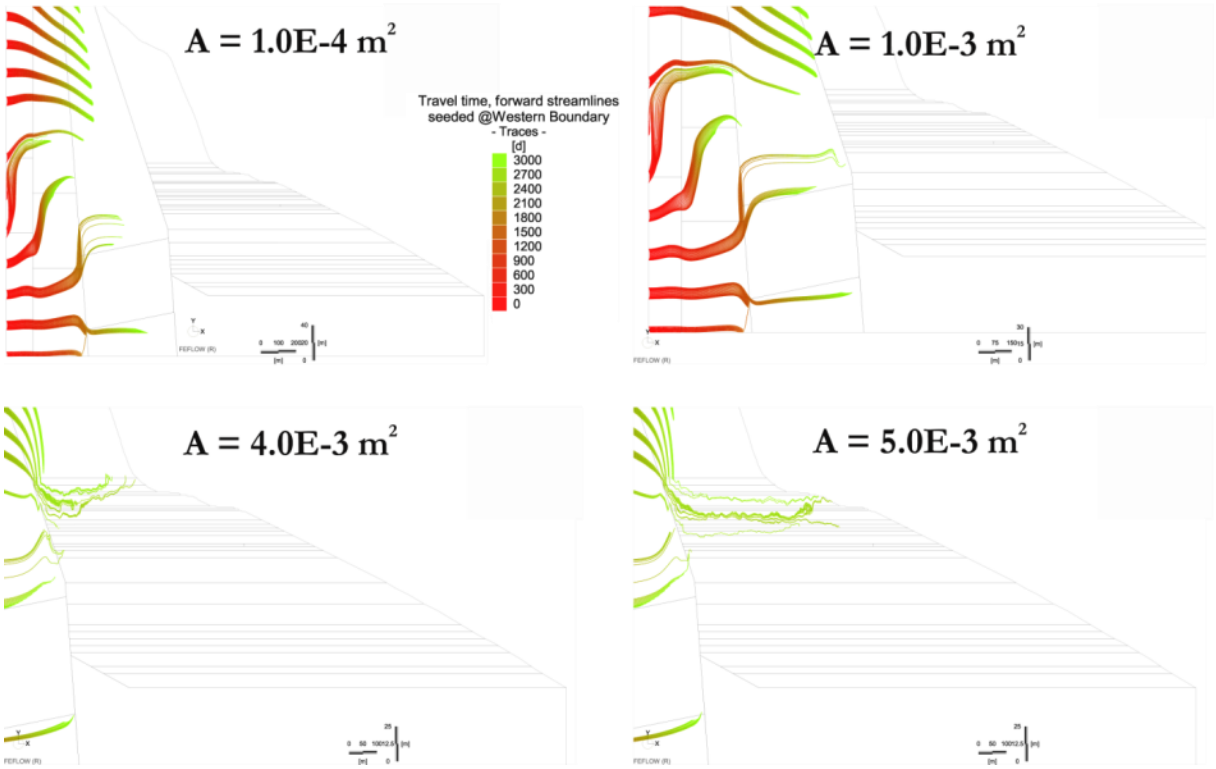

Figure 47: Streamlines (cross-section area threshold, 3,000 d). The minimum cross-section area of $5*10^{-3}$ m² for realizing discharge to the DS was determined by continuous increase of the cross-section area

In a second step, the travel time distribution for the streamlines was additionally modified to 5,000 d (Figure 48). For that case it was possible to simulate discharge to the DS in the lower DSG sediment as well. The smaller cross-section area in the lower DSG sediment compared to the previous model with 1 m² cross-section area allows freshwater pathways even in the deeper DSG and prevents the large-scale saltwater intrusion. Simulated discharge points can be located in a depth of -408 m msl, -411 m msl, -414 m msl, -425 m msl and -489 m msl, respectively. The mass concentration output for the threshold cross-section area shows irregular zones of high concentration gradients.

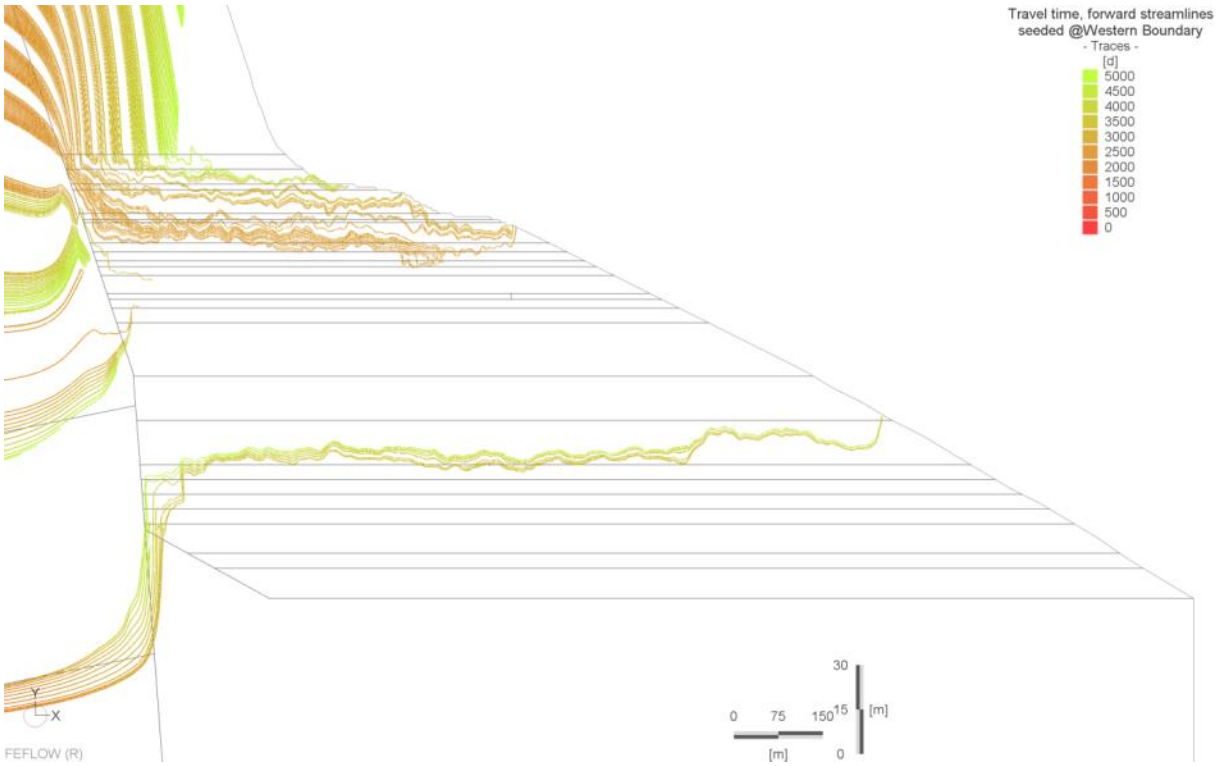

Figure 48: Streamlines (cross-section area threshold, 5,000 d)

5.2.4 Scenario: Cross-section area vs. depth

Applied on the constant cross-section model (057) the relation between DE cross-section area and depth was investigated. In the chapter *Model design* the dimension of the cross-section area was described for two gradients according to case 1 (058) and case 2 (059). Cross-section areas from 0.005 m² to 6.5 m² were used in the different models. The results of both models reveal that discharge to the DS occurs in the upper part of the DSG similar to the reference model with constant cross-section area (Figure 49). The simulations produced small fluid and mass imbalances and thus provided a reasonable result for water pathways according to expected openings in the DSG clay layers. Analog to the scenario hydraulic aperture vs. depth (055, 056), larger cross-section areas do not result in discharge in deeper layers of the DSG. On the contrary, streamlines are repressed and determined by the advance of the fresh-salt water front in the deeper DSG (Figure 50).

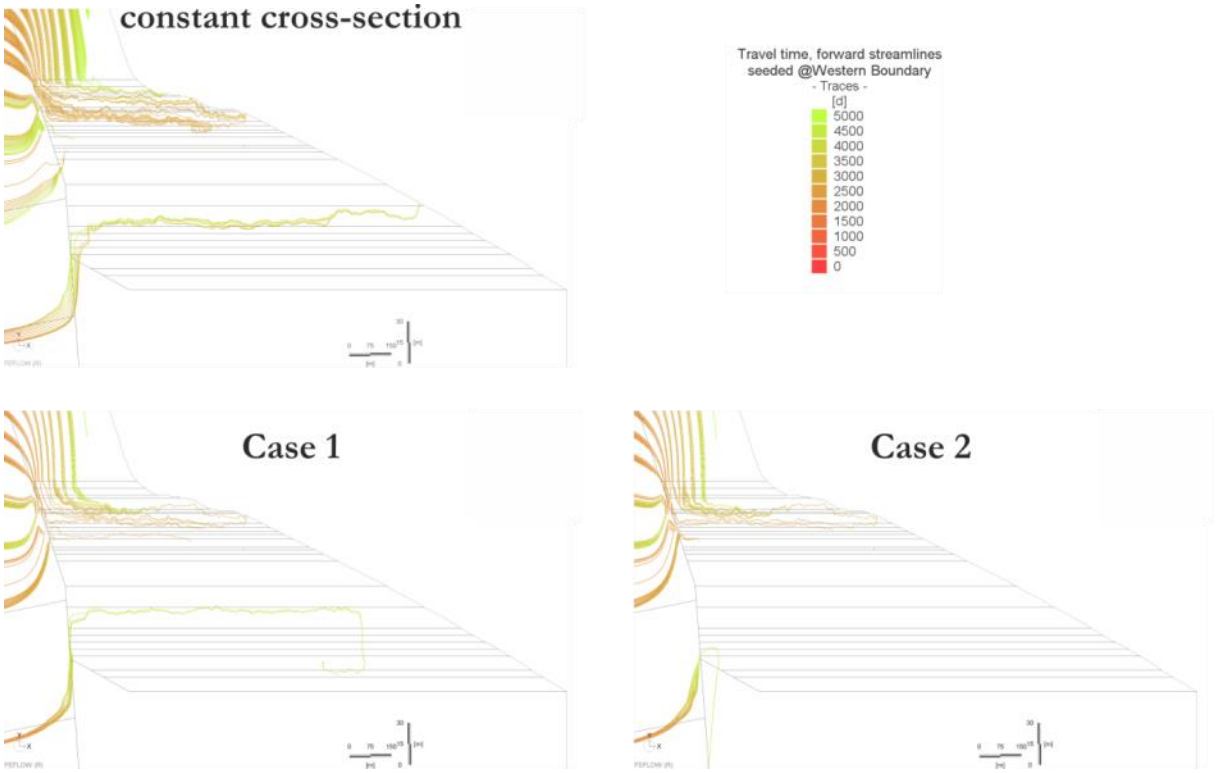

Figure 49: Streamlines (cross-section area vs. depth, x:z = 1:5). Contrasted are case 1 (cross-section area increased by 2 magnitudes, linear) and case 2 (cross-section area increased by 3 magnitudes, linear) with the reference model of constant cross-section area

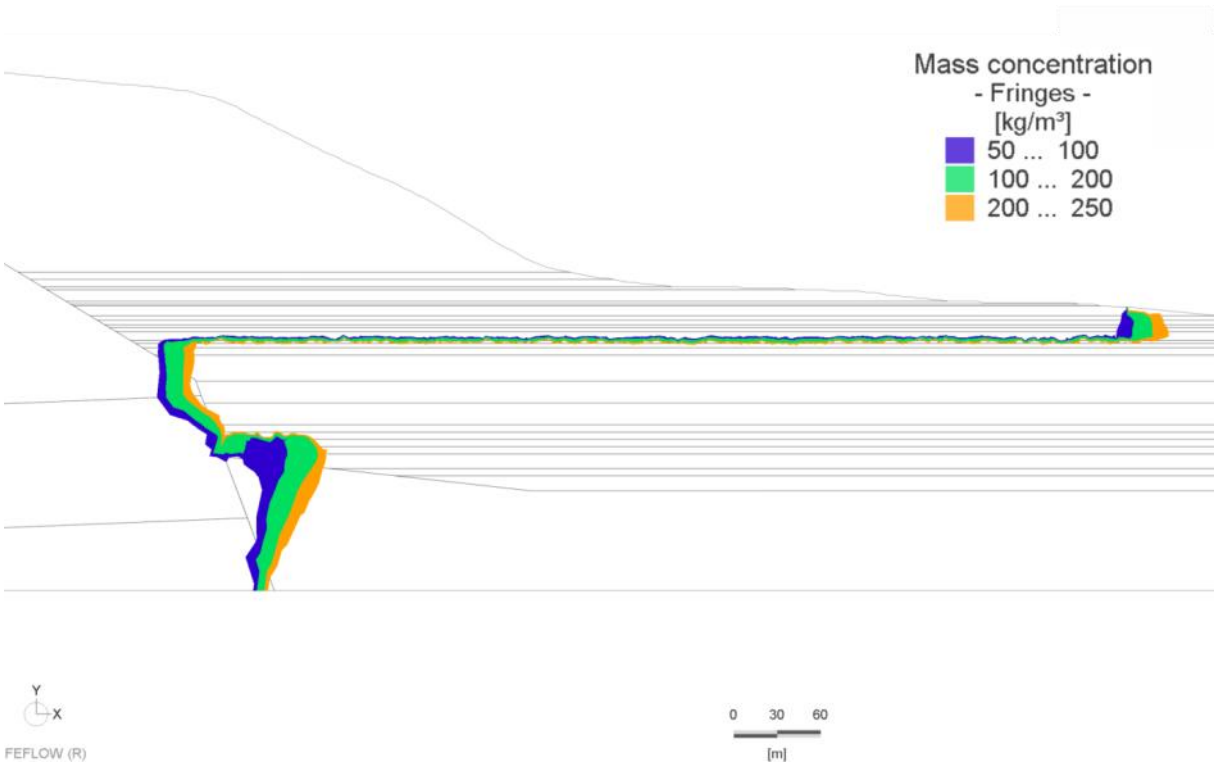

Figure 50: Mass concentration pattern (cross-section area vs. depth, case 2, x:z = 1:1)

5.2.5 Scenario: Discrete element frequency

Analog to Figure 31 in the chapter *Model design* the permeability of the DSG sediment was simulated according to different DE frequency schemes. The simulations reveal that DE have to be implemented in an area 50 m away from the outlet of the hard rock aquifer inside the DSG (model 064) to facilitate discharge to the DS at a depth of -451 m msl (Figure 51).

To simultaneously facilitate surface discharge, these discrete elements have to end not closer than 50 m away from the DS bottom (model 070, Figure 51). That means, a discrete element scheme that stops only 100 m behind the DS bottom (model 071) will not produce surface discharge. Springs for the model 070 occur in a depth of -419 m msl, -421 m msl, -428 m msl, -433 m msl, -451 m msl and -528 m msl, respectively. The most balanced flow and mass error is achieved for the 50 m W DE scheme (model 070).

The mass concentration pattern of the discharge producing scenario exhibits a sharp interface subparallel to the bottom of the DS. Freshwater output dominates saltwater intrusion (Figure 52).

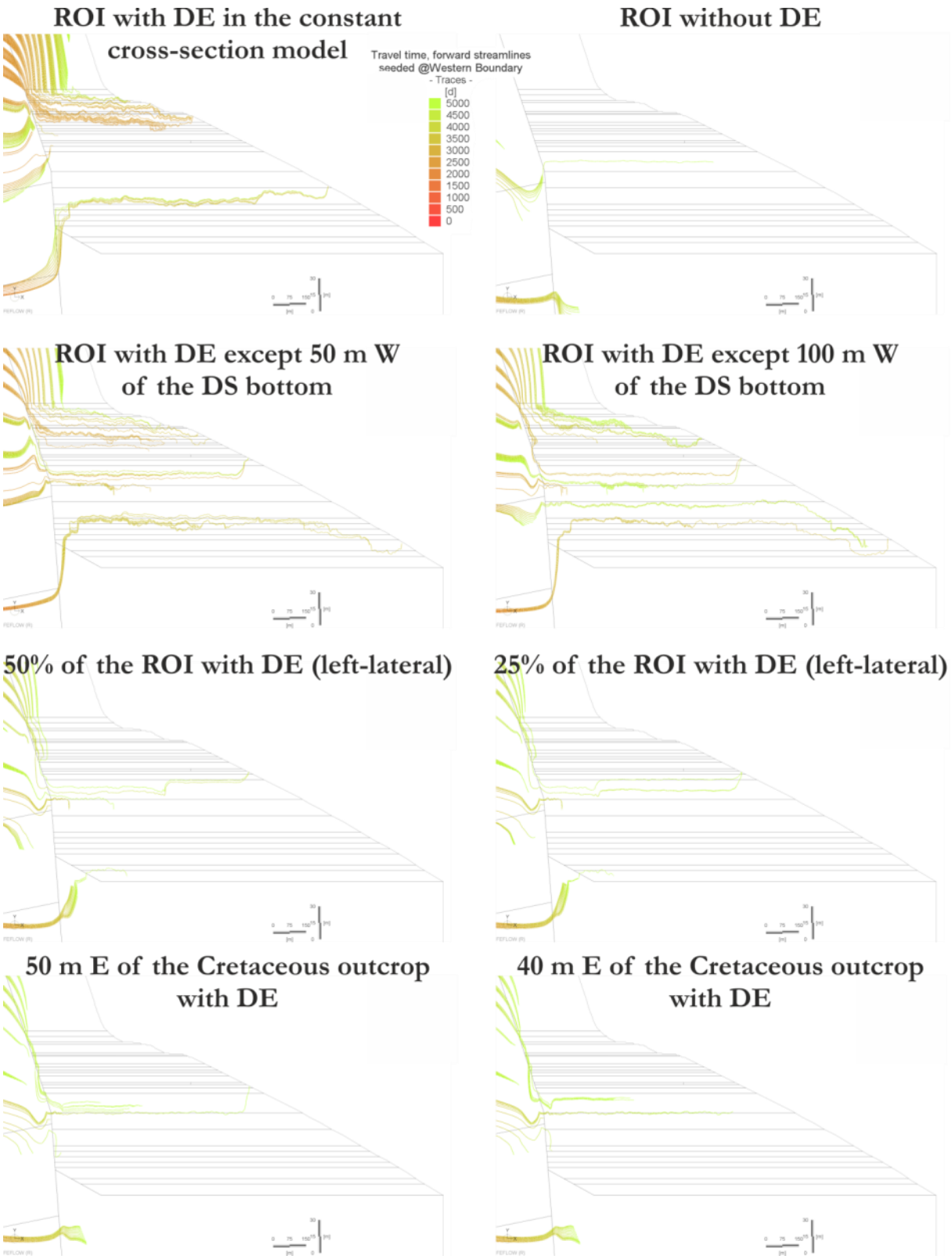

Figure 51: Streamlines (discrete element frequency, x:z = 1:5). Contrasted are the cases 50 m W, 100 m W, 50%, 25%, 50 m E, 40 m E. The models of the first row serve as worst-case models (constant cross-section model, without DE)

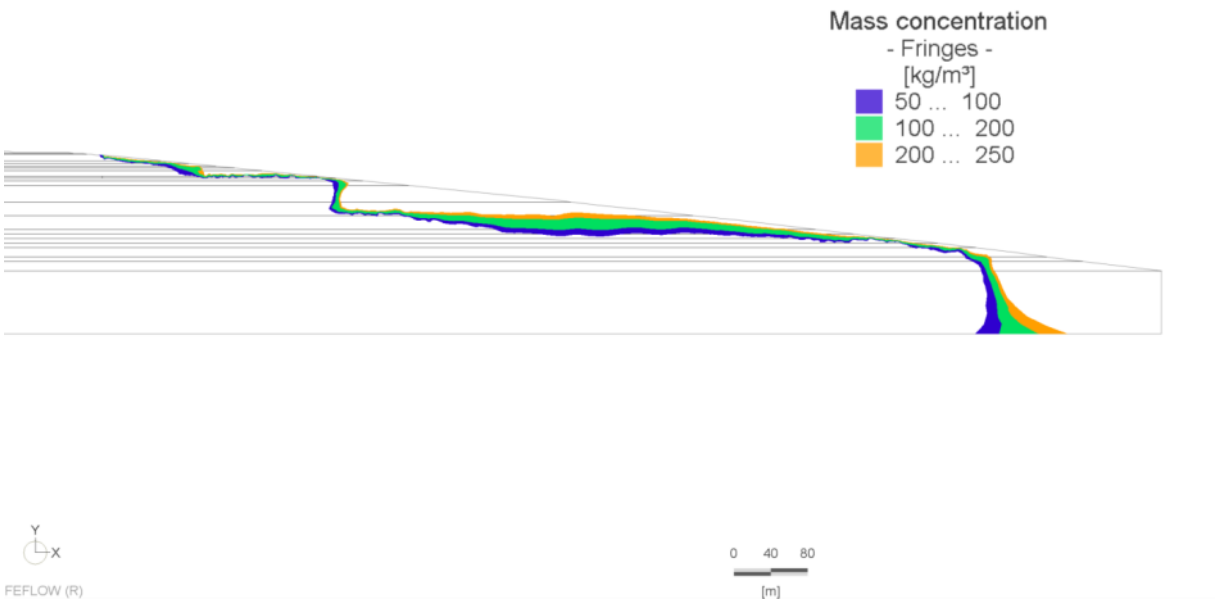

Figure 52: Mass concentration pattern (discrete element frequency, x:z = 1:1)

5.2.6 Scenario: Discrete element inclination

The refinement of the upper clay layers (075) does not significantly change the discharge pattern. The inclination scenarios could only prove single sublacustrine discharge, no surface springs (Figure 53). With respect to exclusively horizontal tubes (076) discharge to the DS was simulated in a depth of -433 m msl. With respect to exclusively vertical tubes (077) discharge to the DS was simulated in a depth of -451 m msl. With respect to the fully applied DE mesh (078) discharge to the DS was simulated in a depth of -432 m msl.

After the refinement the mass concentration pattern displays major saltwater intrusion in the lower part of the DSG sediment. The other models show a sharp interface subparallel to the bottom of the DS, similar to the previous DE frequency scenario.

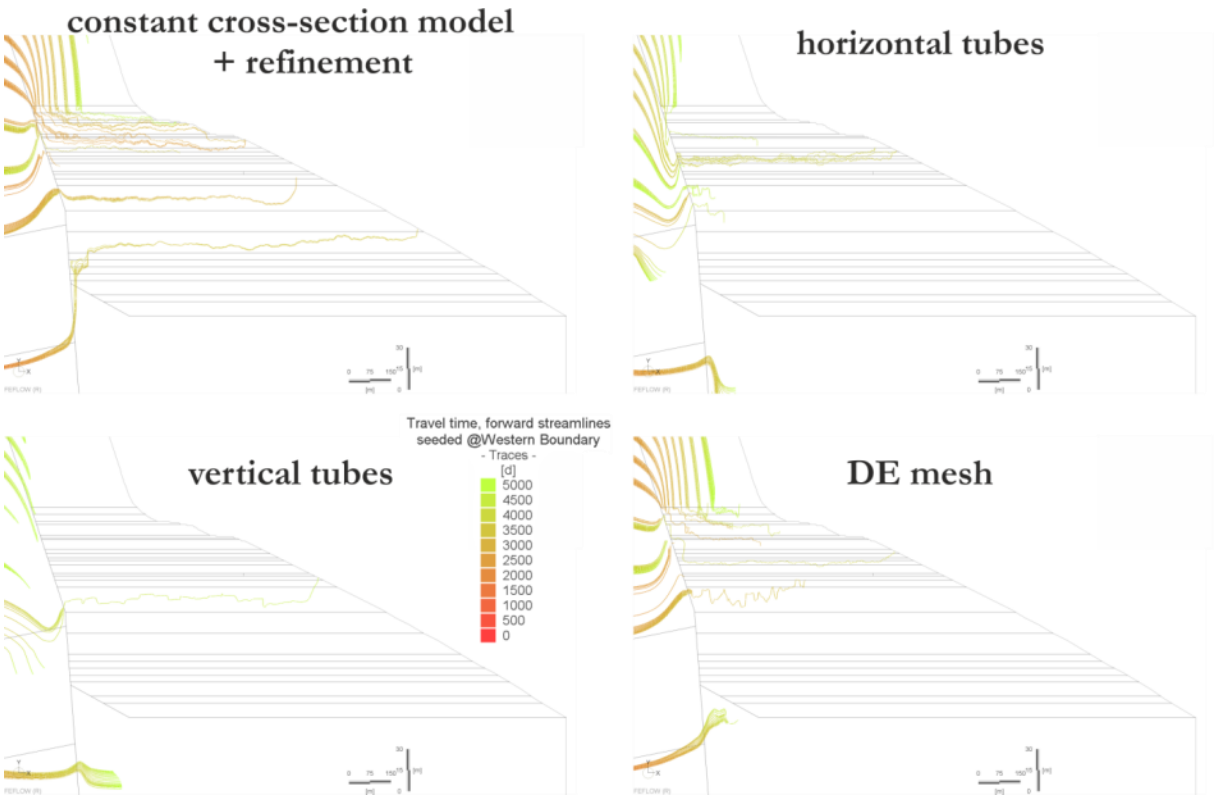

Figure 53: Streamlines (discrete element inclination, x:z = 1:5). Contrasted are the cases for realizing discharge to the DS by an DE inclination scheme (only horizontal tubes, only vertical tubes, horizontal and vertical tubes) and the constant cross-section reference model

5.2.7 Scenario: Salinity pool for ascending deep waters

The additional brine pool is located in a freshwater dominated area and results in the repressing of freshwater within the Lower Judea Group aquifer. The increasing saltwater pressure does not facilitate water from the Lower Judea Group aquifer to rise along the Judean fault (cf. Figure 26) and to enter the DSG sediment (Figure 54). On the contrary, lower streamlines remain in the Lower Judea Group. This distribution becomes even more distinctive with higher concentrations along the Judean faults (e.g. model 083). Discharge to the DS in the upper part of the DSG sediment is not considerably influenced by the additional salinity input due to the higher elevation level of the streamlines generating these discharges.

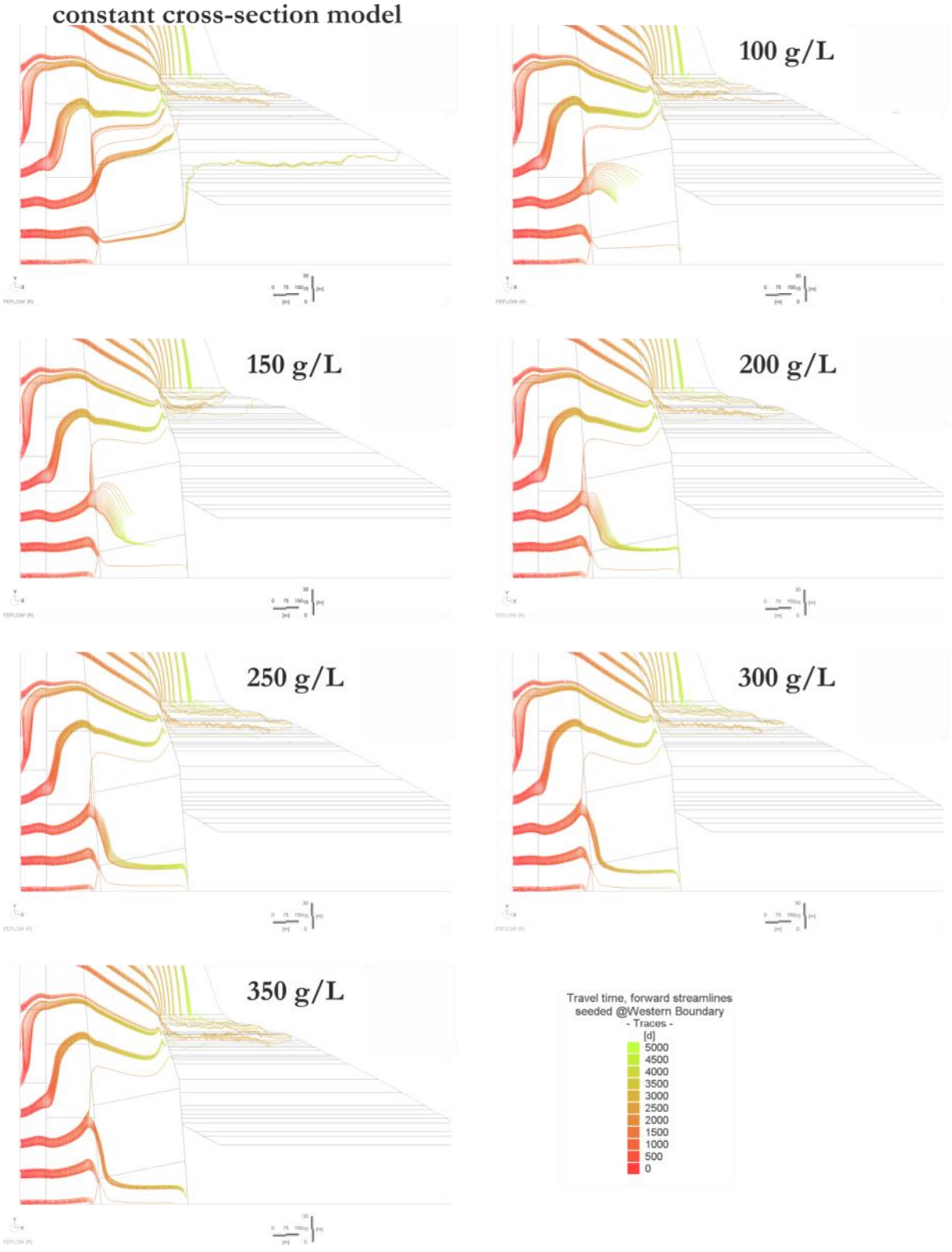

Figure 54: Streamlines (salinity pool, x:z = 1:5). Contrasted are the cases for varying concentrations of the salinity pool (100 to 350 g/L in 50 g/L steps) and the constant cross-section reference model

The mass concentration pattern was voided for the scenario with 100 and 150 g/L. With increasing concentration of the salinity pool the fresh-salt water interface sharpens along and above the Judean fault within the Cretaceous limestone (Figure 55).

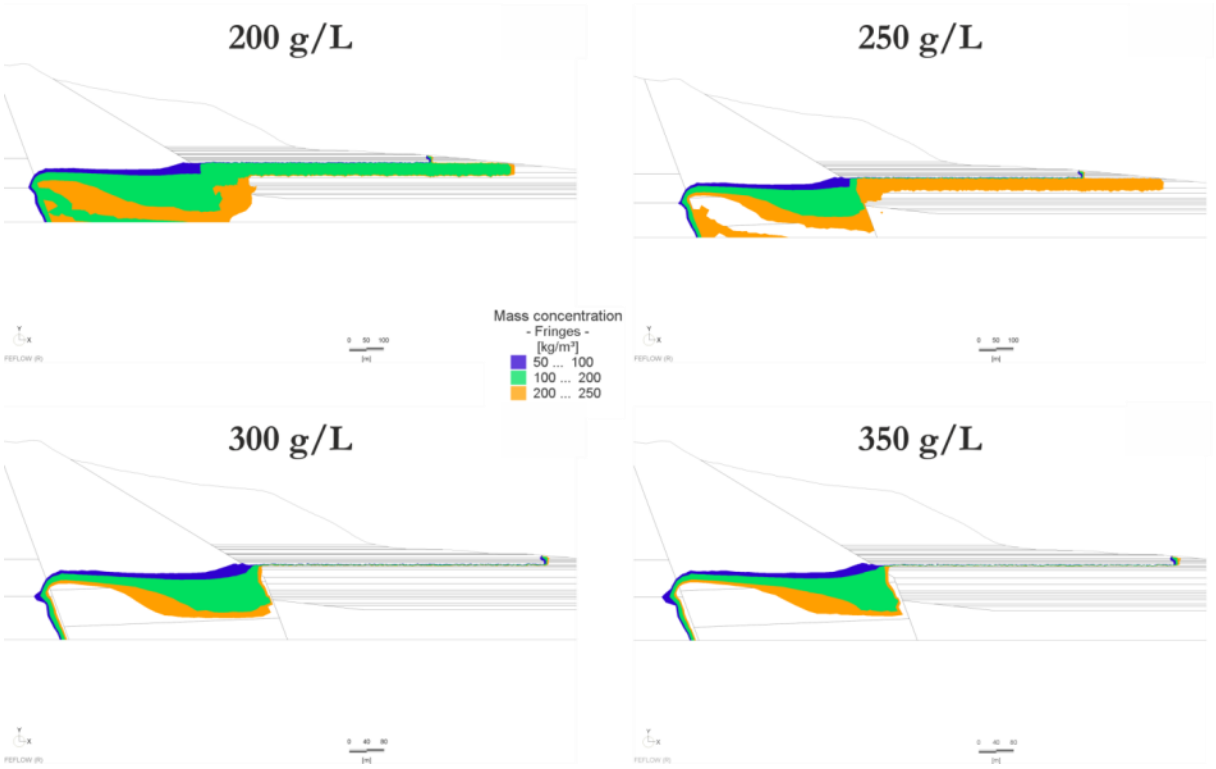

Figure 55: Mass concentration patterns (salinity pool, x:z = 1:1) Contrasted are the patterns for concentrations of 200 g/L, 250 g/L, 300 g/L and 350 g/L

5.2.8 Scenario: Debris removal

The removal of the debris above the differentiated DSG has no impact on the propagation of the fresh-salt water interface within the DSG. Compared to the *discrete element frequency 50 m W* model, the hydraulic heads exhibit no shift within the Cretaceous rocks or the DSG. Streamlines in the Upper Judea Group converge in the direction of the DSG and attain the differentiated DSG almost completely (Figure 56). The streamline pattern reveals an increase of the streamline density within the lower part of the differentiated DSG. However, it does not result in increasing discharge points to the DS. Contrary, the number of discharge points decreased due to lacking surface discharge: The contribution of inflowing water from the debris ceased. Simulated subsurface springs occur in a depth of -437 m, -451 m and -528 m msl, respectively. The rate budget is as balanced as the *discrete element frequency 50 m W* model.

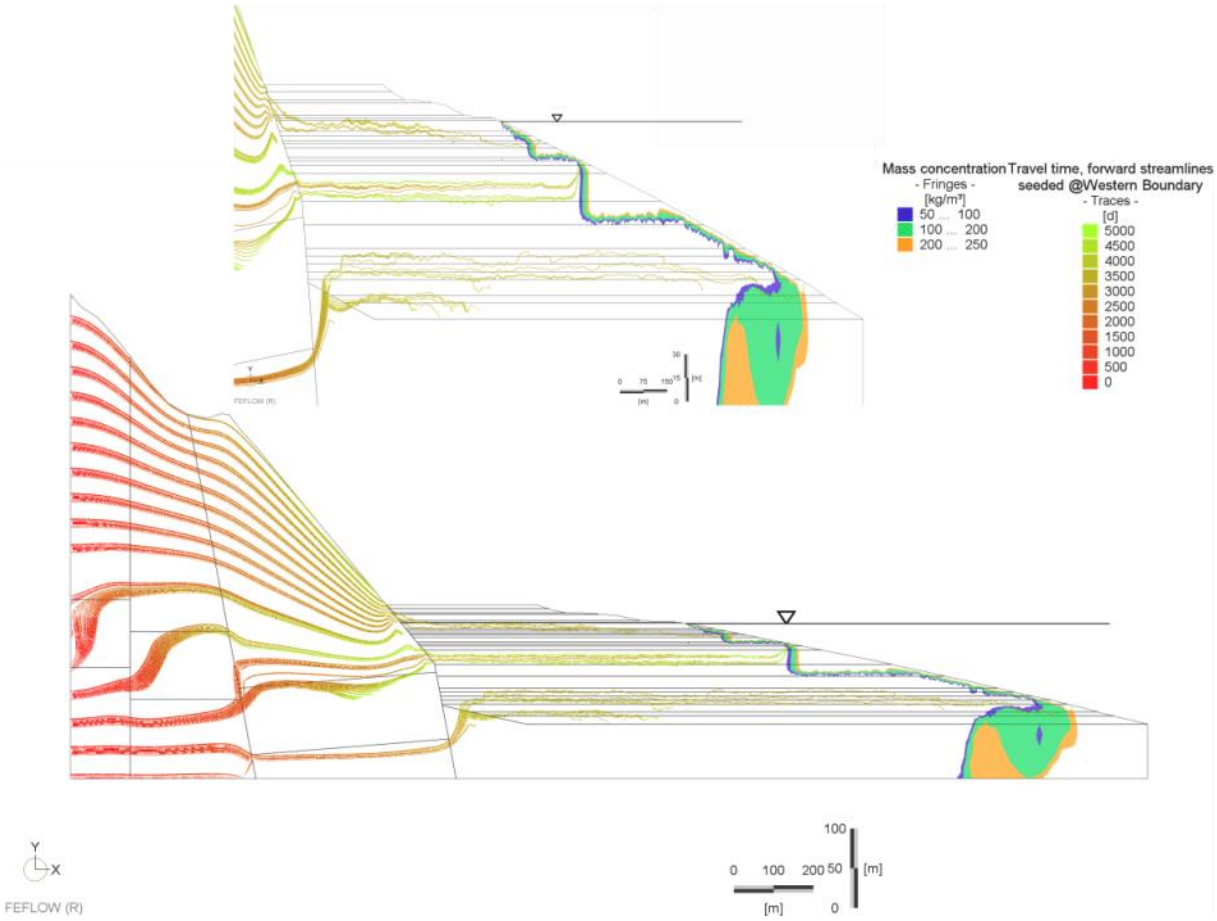

Figure 56: Streamline and mass concentration pattern (debris removal) for the entire model domain (x:z = 1:2) and the DSG close-up (x:z = 1:5)

5.3 Uncertainty analysis

The uncertainty analysis was imposed on the *discrete element frequency 50 m W* model (070). It was selected as reference model because it presents the optimal solution after the sensitivity analysis (cf. chapter *Constraint Index*).

5.3.1 Mesh quality

The mesh quality could be considerably improved by reducing the maximum interior angle of triangles (Figure 57). Regarding obtuse-angled triangles, 0.0% are larger than 120° and 4.1% larger than 90° (cf. reference model: 0.8% > 120°, 18.5% > 90°). Models based on that mesh deliver more stable results in areas with previously red triangles. The total flow balance could be slightly reduced to a value of -7 m³/d.

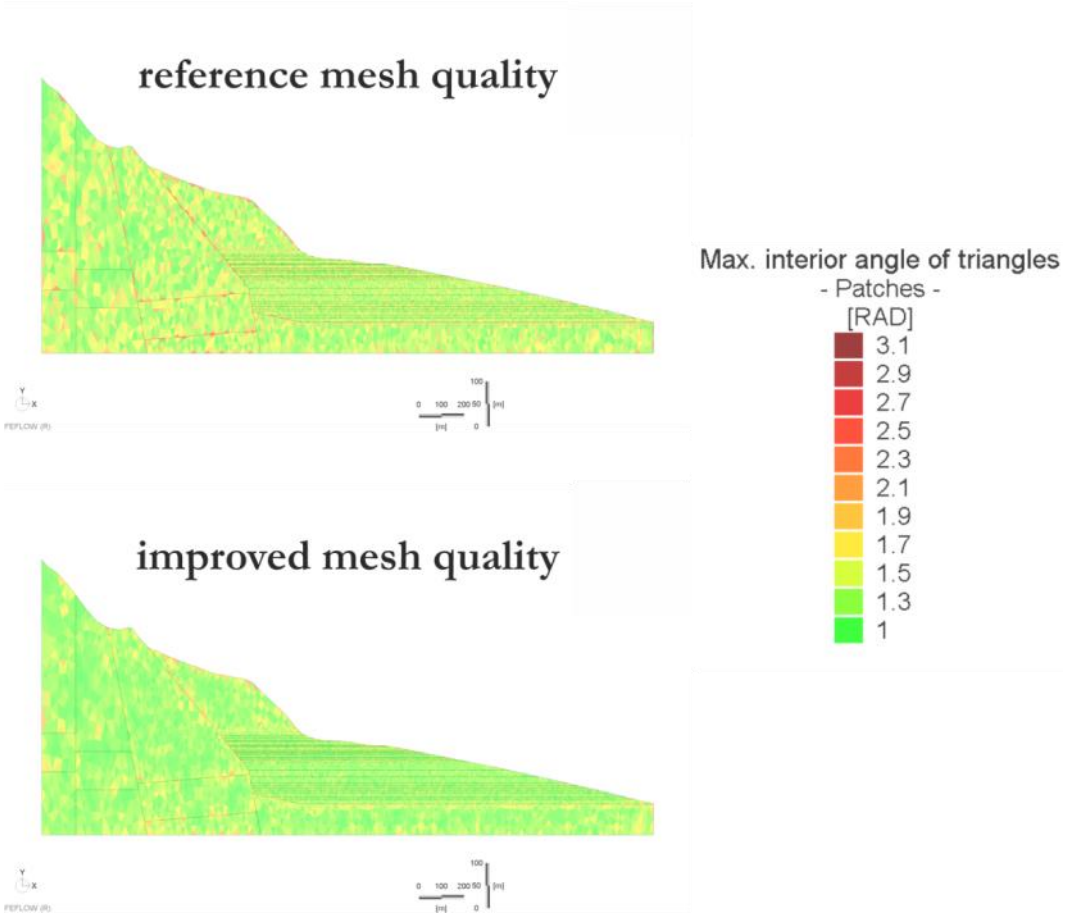

Figure 57: Reference and improved mesh quality

5.3.2 Reference concentration

The applied change in the reference concentration C_S (50 g/L increase) has no impact on the streamline pattern or the propagation of the fresh-salt water interface within the DSG (Figure 58). The rate budget equals the reference's one.

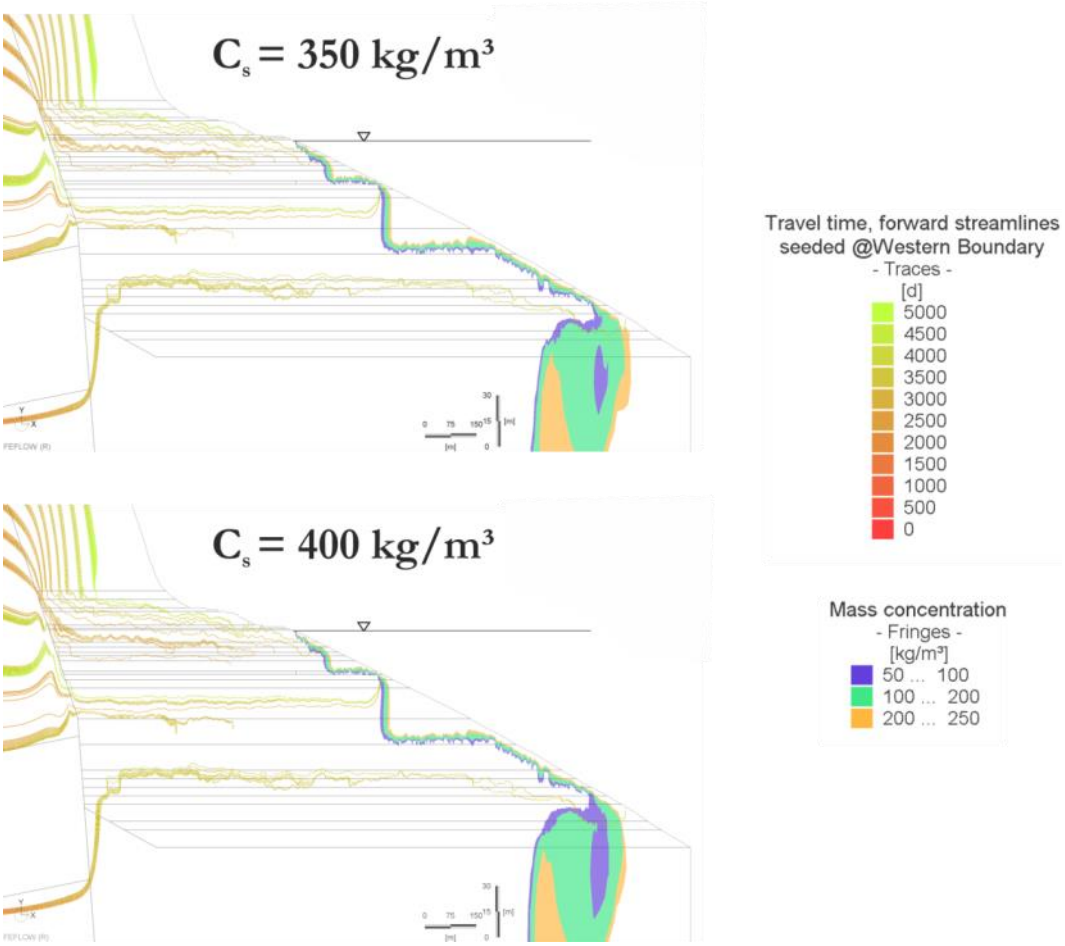

Figure 58: Streamline and mass concentration pattern for a minor change in C_S (x:z = 1:5)

5.3.3 Anisotropy of conductivity

The reduction of conductivity in vertical direction results in the decrease of the streamline density within the DSG (Figure 59). Streamlines in the upper part of the DSG does not attain the surface within 5,000 d. Subsurface discharge is discernible in shallow and large depth. The mass concentration pattern is distinguished from the reference pattern by a sharp interface in the lower part of the DSG (-538 m msl down to the model domain bottom). Flow and mass are slightly more balanced compared to the reference model.

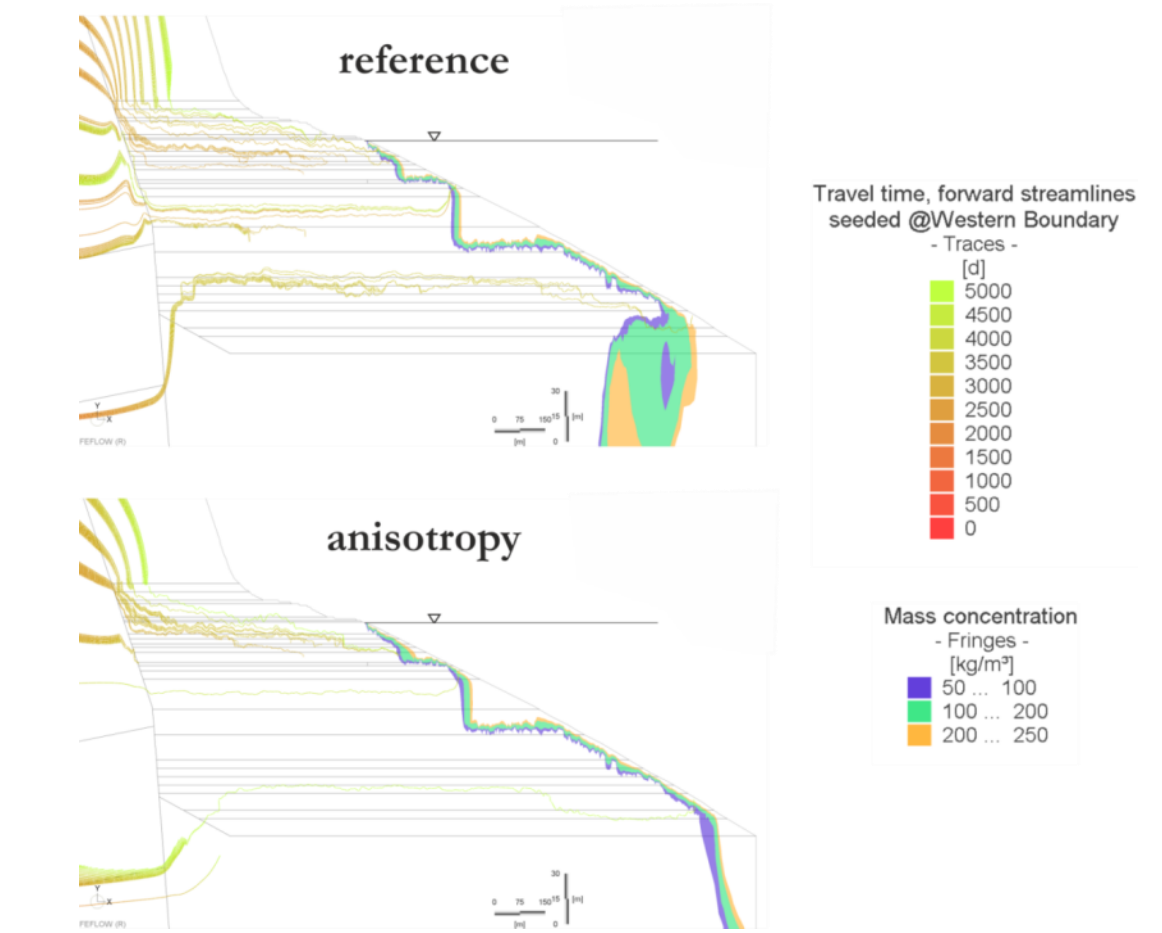

Figure 59: Streamline and mass concentration pattern for anisotropic conductivity (x:z = 1:5)

5.3.4 Dispersivity and molecular diffusion

The change in dispersivity and molecular diffusion has no impact on the streamline pattern but result in different salinity distributions in the lower part of the DSG, dominantly in the undifferentiated DSG (Figure 60). The fresh-salt water interface above the deepest discharge to the DS (-528 m msl) is not affected by changing transverse to longitudinal ratios. As trend, Figure 61 reveals that a decreasing β_T/β_L ratio results in an increasing fluid flow and mass flow imbalance. Larger values for molecular diffusion improve the inland propagation of the fresh-salt water interface to a minor extent (Figure 62). The solver did not converge for molecular diffusion values larger than 10^{-7} m²/s.

With respect to the DE, the solver did not converge for DE molecular diffusion values smaller than $D_d = 1*10^{-10}$ m²/s and larger than $D_d = 1*10^{-7}$ m²/s. Within this range the mass concentration pattern of the adapted model does not distinguish from that of the reference model. The solver does not converge for DE longitudinal dispersivities smaller than 1 m. Values between 5 m and 1 m do not result in obvious changes of the salinity pattern.

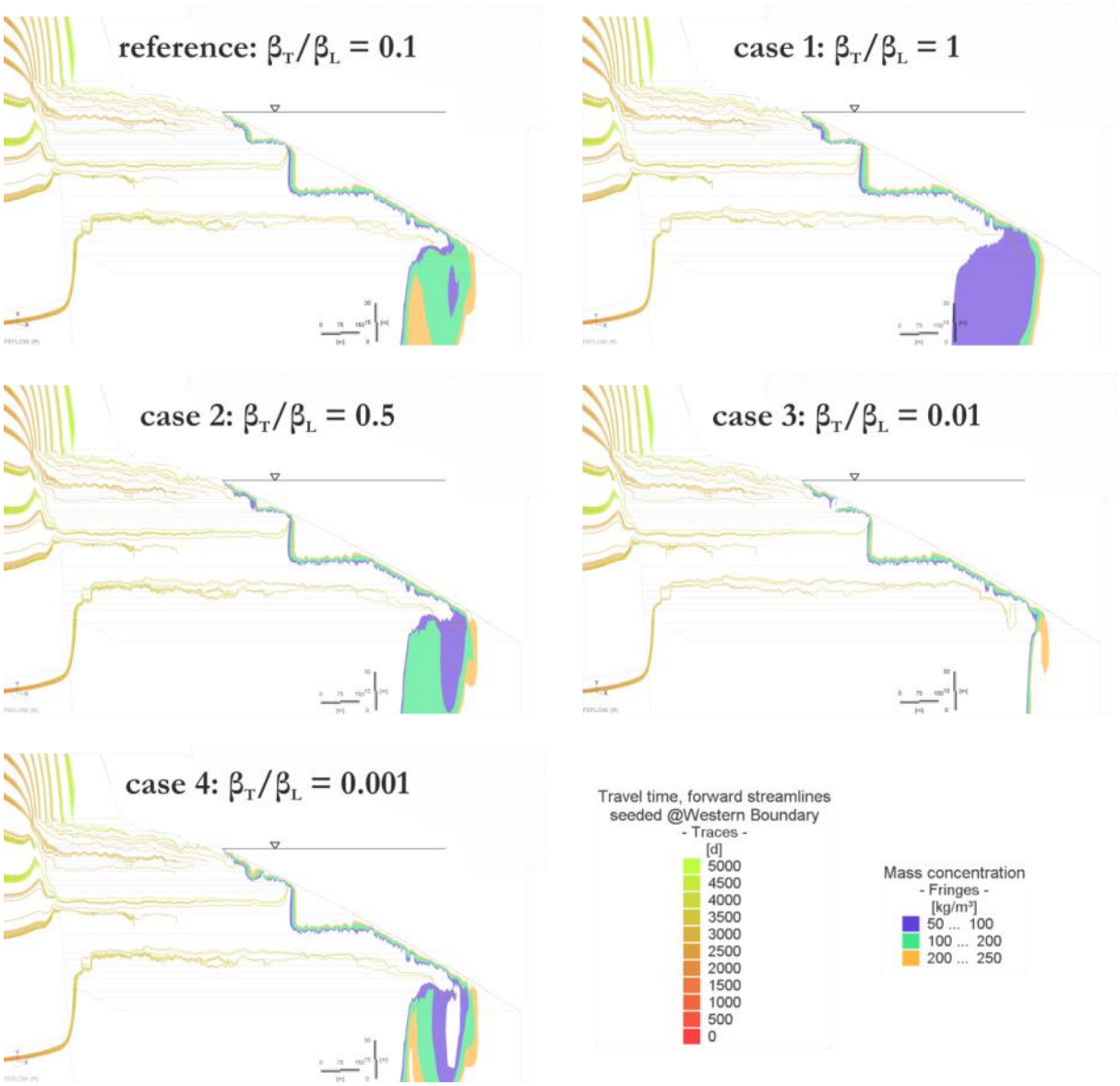

Figure 60: Streamline and mass concentration patterns for different dispersivity ratios (x:z = 1:5)

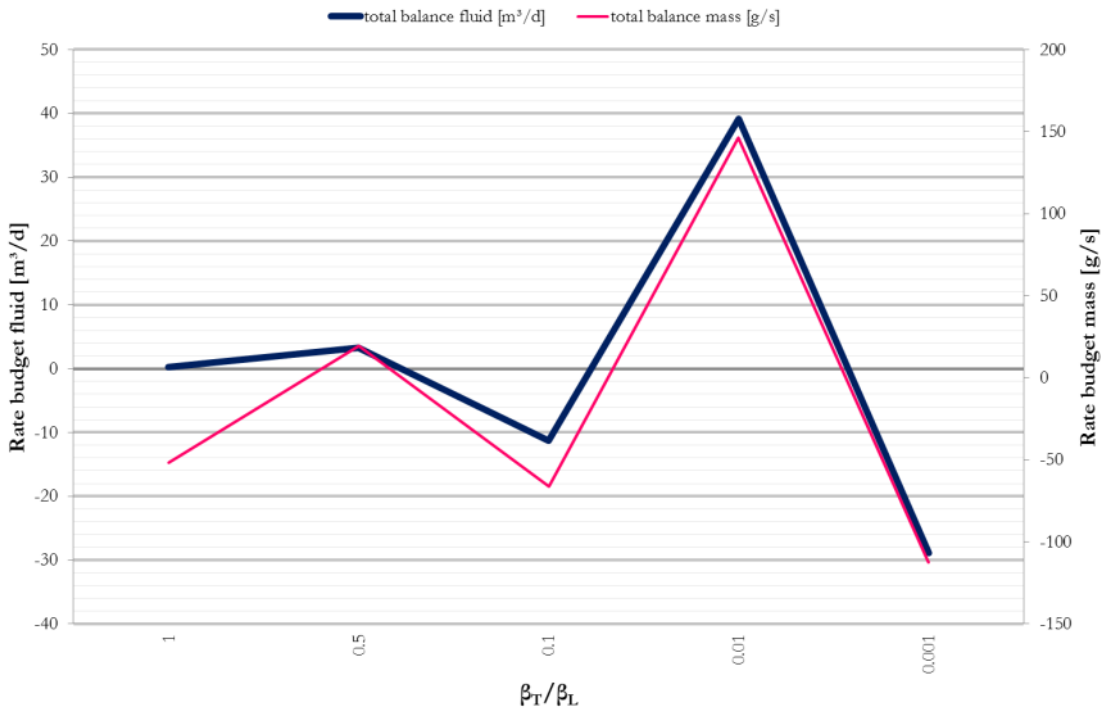

Figure 61: Rate budget of applied dispersivity ratio cases

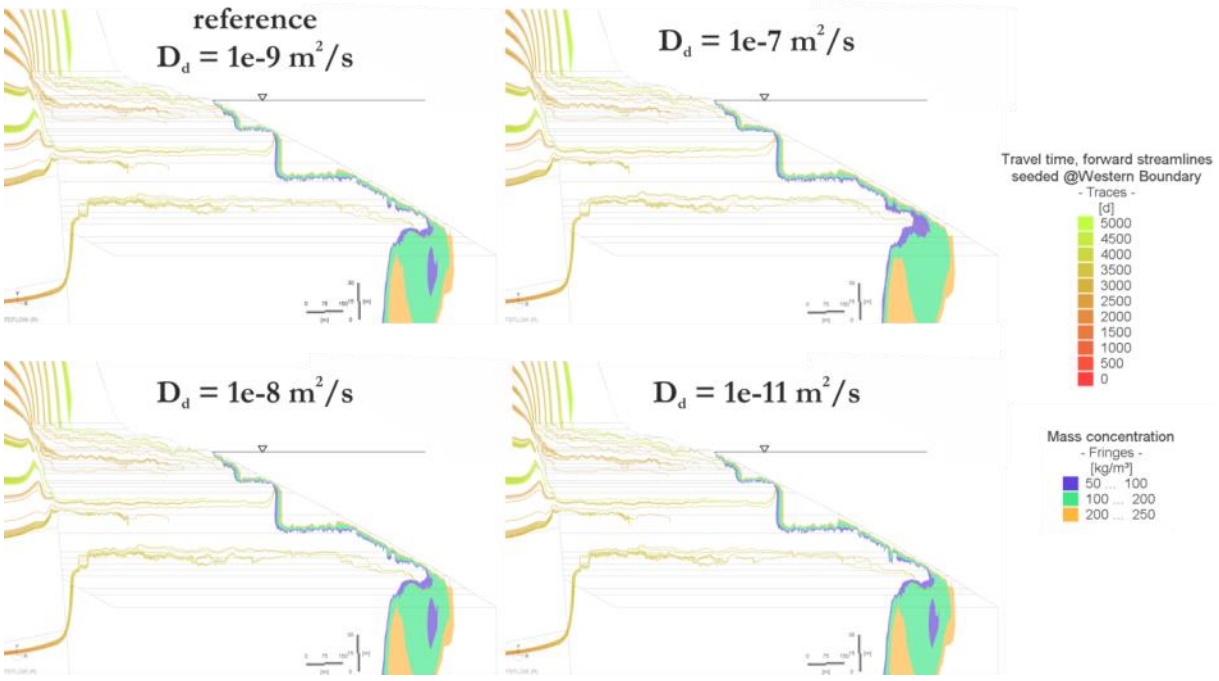

Figure 62: Streamline and mass concentration patterns for molecular diffusion ranges (x:z = 1:5)

5.4 Constraint Index CI

The constraint index is used for the evaluation of the model results and their uncertainties. The calculated constraint index for the different models is displayed in Figure 63. The composition of the constraint index for models with CI > 5 is compiled in Table 20.

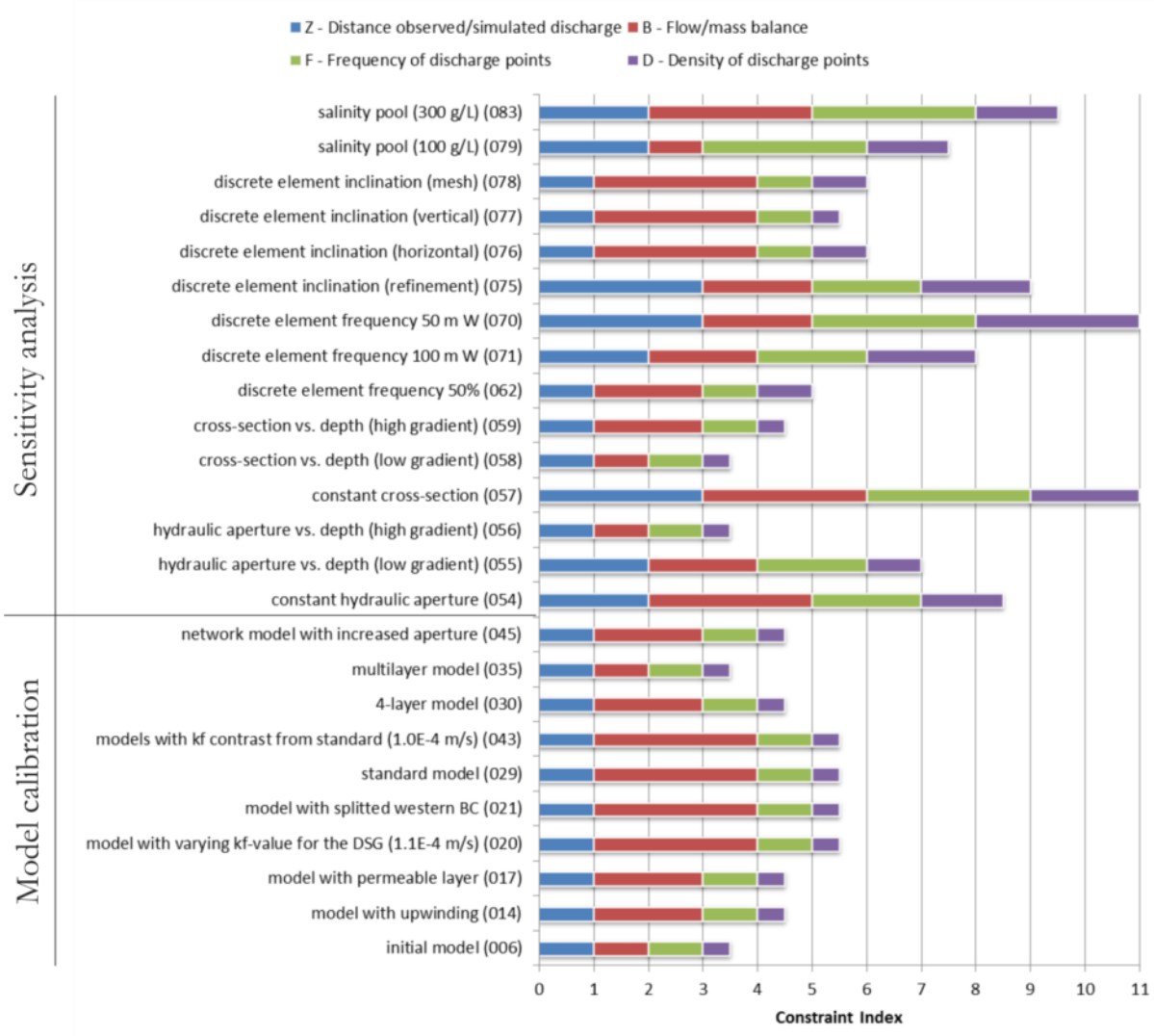

Figure 63: Bar diagram for the CI calculation including the distribution of the impacting factors for the different models

Table 20: Constraint Index CI. Z: Elevation difference between observed and simulated discharge points. B: Total flow and mass balance. F: Frequency of discharge points along the entire eastern boundary. D: Density of discharge points. Shown are the elevation of discharge for each model, the sum of the distances to the highest spring Z1 and the lowest spring Z2, the cluster frequency and the index points for the density specific features: a *low surface discharge*, b *medium surface discharge*, c *high surface discharge*, d *discharge at -425±1 m msl*, e *low shallow sublacustrine discharge*, f *medium to high shallow sublacustrine discharge* and g *sublacustrine discharge in greater depth*

	Model	Z	B	F	D	*CI*	Discharge [m msl]	Σ (Z1+Z2) [m]	Cluster frequ.	a	b	c	d	e	f	g
Model calibration	model with varying kf-value for the DSG (1.1E-4 m/s) (020)	1	3	1	0.5	*5.5*	-424 to -426	66	1	0	0	0	0.5	0	0	0
	model with splitted western BC (021)	1	3	1	0.5	*5.5*	-425	68	1	0	0	0	0.5	0	0	0
	standard model (029)	1	3	1	0.5	*5.5*	-425 to -426	67	1	0	0	0	0.5	0	0	0
	models with kf contrast from standard (1.0E-4 m/s) (043)	1	3	1	0.5	*5.5*	-424 to -426	66	1	0	0	0	0.5	0	0	0
Sensitivity analysis	constant hydraulic aperture (054)	2	3	2	1.5	*8.5*	-407 to -408; -414; -425 to -426	49	3	0	1	0	0.5	0	0	0
	hydraulic aperture vs. depth (low gradient) (055)	2	2	2	1.0	*7.0*	-414 to -415; -424 to -426	56	2	0	0	0.5	0.5	0	0	0
	constant cross-section (057)	3	3	3	2.0	*11.0*	-408; -411; -414; -425; -489	15	5	0.5	0	0	0.5	0	0	1
	discrete element frequency 100 m W (071)	2	2	2	2.0	*8.0*	-433; -451; -524	50	3	0	0	0	0	0	1	1
	discrete element frequency 50 m W (070)	3	2	3	3.0	*11.0*	-419; -421; -428; -433; -451; -528	36	5	0	1	0	0	0	1	1
	discrete element inclination (refinement) (075)	3	2	2	2.0	*9.0*	-412; -414; -425; -488	18	3	0	0	0.5	0.5	0	0	1
	discrete element inclination (horizontal) (076)	1	3	1	1.0	*6.0*	-433	68	1	0	0	0	0	0	1	0
	discrete element inclination (vertical) (077)	1	3	1	0.5	*5.5*	-451	68	1	0	0	0	0	0.5	0	0
	discrete element inclination (mesh) (078)	1	3	1	1.0	*6.0*	-432	68	1	0	0	0	0	0	1	0
	salinity pool (300 g/L) (083)	2	3	3	1.5	*9.5*	-408; -411; -414; -424 to -426	50	4	0	1	0	0.5	0	0	0

The optimum solution with the highest CI of 11 was developed during the sensitivity analysis and is represented by the models *constant cross-section* and *discrete element frequency 50 m W*. Both models contain the sophisticated discrete element approach. Applied DE within the DSG sediment exhibit a constant hydraulic aperture of 0.001 m and a constant cross-section area of 0.005 m². Springs for the *constant cross-section* model occur in a depth of -408, -411, -414, -425 and -489 m msl and for *the discrete element frequency 50 m W* model in a depth of -419, -421, -428, -433, -451 and -528 m msl, respectively. In the ranking the highest valued models are followed by the models *salinity pool (300 g/L)* and *discrete element inclination (refinement)* with 9.5 and 9.0 index points, respectively.

For the following models both surface and sublacustrine discharge were simulated:

- constant cross-section (057)
- DE frequency 50 m W (070)
- DE inclination (refinement) (075)

Exclusively sublacustrine discharge was simulated in the models:

- 4-layer model (030)
- multilayer model (035)
- network model with increased aperture (045)
- DE frequency 50% (062)
- DE frequency 100 m W (071)
- DE inclination (horizontal) (076)
- DE inclination (vertical) (077)
- DE inclination (mesh) (078)

The constraint index as simple evaluation algorithm helped to determine a numerical model with the lowest uncertainty that coincide best with the known boundary conditions and hydrogeological parameter settings of the DSG system.

5.5 Rate budget

The rate budget of fluid flow and mass flow is an analysis tool that reveals the quality of the simulated models. For the analysis every model with simulated discharge to the DS has been considered. Models with a balanced fluid and mass budget indicate a reliable model setup. Rate budgets with a CI > 5 are displayed in Figure 64. Fluid and mass inflow and outflow of these models are balanced. Except from the models *constant hydraulic aperture* (054) and *hydraulic aperture vs. depth* (055) with large cross-section areas of 1 m^2, the models exhibit a similar water budget. Statistical parameters of the model rate budgets are displayed in Table 21. Concerning the differentiated DSG, about 70% of the model domain inflow enters the differentiated DSG and about 70% of the model domain outflow escapes from the differentiated DSG (Table 21).

Large DE cross-section areas of 1 m^2 compared to 0.005 m^2 considerably increase the fluid and mass inflow and outflow. However, those models exhibit a medium constraint index and coincide less to the observed discharge patterns than models with lower values of the DE cross-section area (e.g. model 057: *constant cross-section* or model 070: *DE frequency 50 m W*). Therefore, the median instead of the average discharge value of the DSG (130 m^3/d) is likely to reflect the natural system, as a rough estimation indicates: Comparing the simulated discharge volume of 130 m^3/d to the simulated discharge volume of the Kane-Samar springs which is $11*10^6$ m^3/a (Gräbe et al. 2013), the latter discharge corresponds to the discharge of the studied Wadi Darga cross-section (1 m width), if the amount of 11*10 m^3/a is equally distributed along a distance of about 230 m.

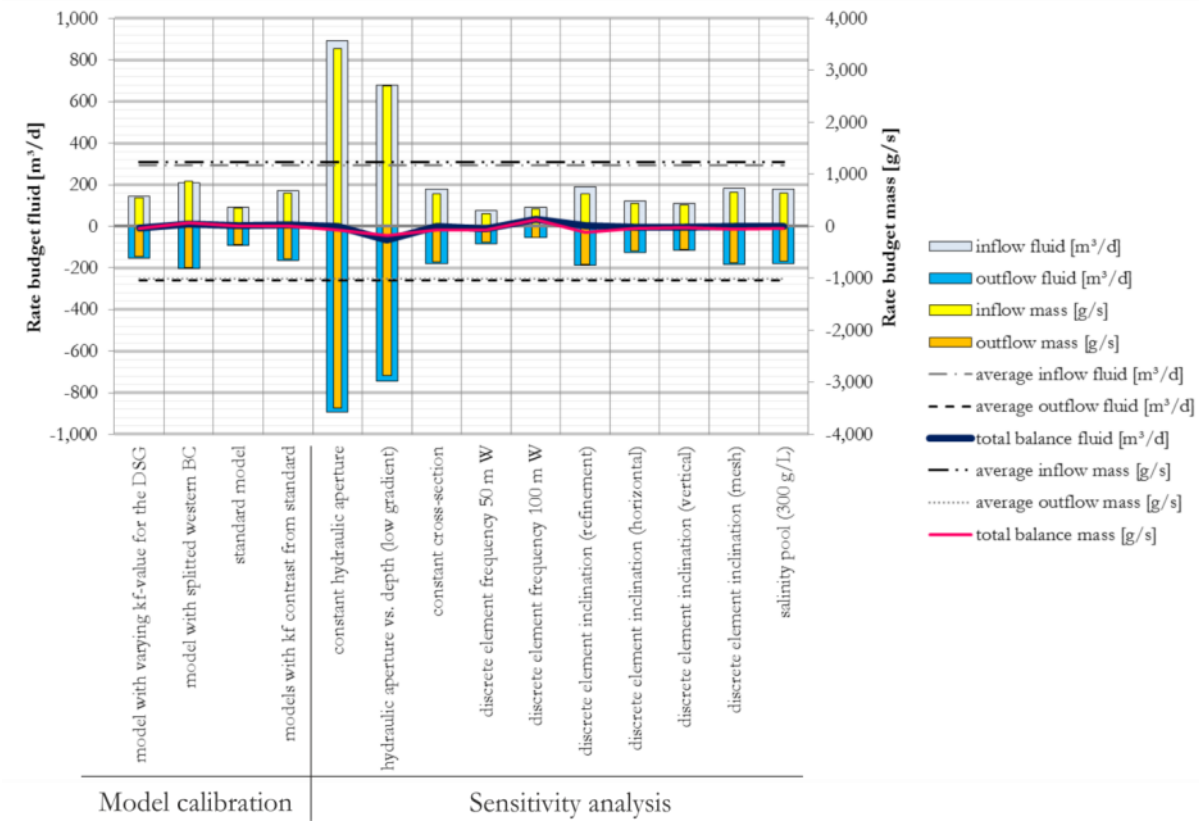

Figure 64: Rate budgets of fluid flow and mass flow. For the calculation of the average values the models displayed in Figure 63 were considered

Table 21: Statistical parameters of the model rate budgets. Balance (1) is related to the mean values. Balance (2) is related to the median values. Positive balance values indicate flow/mass excess, negative values indicate flow/mass deficit of the system

parameter	**fluid inflow [m³/d]**	**fluid outflow [m³/d]**	**mass inflow [g/s]**	**mass outflow [g/s]**
Model domain				
mean (1)	290	260	1,230	1,010
median (2)	180	180	630	680
minimum	70	40	240	180
maximum	1,260	1,270	4,870	4,960
balance (1)	30 (-10%)		220 (-18%)	
balance (2)	0		-50 (+8%)	
DSG (differentiated)				
median	130	130	440	480

6 Conclusions

The study covered the groundwater flow processes from the Judean Mountains via the DSG sediments into the DS, on- and offshore. A small coastal strip north of Wadi Darga was selected, where such groundwater discharge is observable in form of surface and sublacustrine springs. The displayed plots indicate the blocking function of the DSG sediment. Further, it could be shown that groundwater passes the sediments only via preferential flows (multilayered model and discrete elements). The groundwater flow in the overall impermeable sediment with a highly heterogeneous hydraulic conductivities distribution is governed by gravitational forces. The investigation results confirm the sensitivity for spatially and temporally dependent flow and transport parameter and imply the dynamics within the depositional system. The used software package FEFLOW 6.1 was successfully applied for finite element subsurface flow and density modeling in the DSG sediments of Wadi Darga. The applied scale of the model exhibits that the introduction of discrete features as conduit network is suitable for a regional multilayer aquifer with dissolution voids.

The sensitivity analysis of the conduit network revealed that small DE cross-section areas and low values of hydraulic aperture facilitate the supply of freshwater to the DS. Comparable to an aquitard, a considerable amount of freshwater flow from the Judean Mountains (Upper and Lower Judea Group) to the DS can only occur if saltwater intrusion is minimized by nearly impermeable DSG strata. Consequently, large conduits in the lower part of the DSG sediment will favor salinity intrusion (pull mechanism) due to the low opposing pressure on the freshwater supply side and cause high saline pore waters in the DSG sediment. A depth of -528 m msl is the deepest point for a subsurface spring (revealed by the DE frequency 50 m W model 070). Below, the dominance of seawater intrusion exacerbates freshwater outlets. The larger freshwater springs have been observed on the shoreline only a few meters below the DS surface till -433 m msl (cf. DE frequency 50 m W model 070). These outlets are governed by larger tubes, either in hydraulic aperture or cross-section area. However, they can only occur in shallow areas where saltwater pressure does not prevail over the inflowing freshwater pressure (push mechanism). Consequently, the discharge system is particularly susceptible if conduits are permanently developing in the upper part of the DSG sediment. There, dissolution processes may result in small increases of cross-section areas or breakthrough of strongly tortuous pathways and effectively change the amount and frequency of springs on the shoreline of the DS to higher values. Especially, cross-section areas and hydraulic apertures in the range of 5 mm to 5 cm result in surface and subsurface springs. Opposite, precipitation may effectively decrease the discharge to the DS. To summarize, the variability of discharge to the DS is larger in the upper DSG sediment.

In the proper meaning of the hydraulic aperture/cross-section area vs. depth scenario such distribution is not expected in the clay layers of the DSG sediment and deserves chiefly as mathematical manipulation of the model. In the case of different openings in the subsurface with depth (not strictly continuous), conclusions for fresh-salt water migration paths might still be drawn from that investigation.

Due to the (1) high freshwater potential resulting from the high-sloping Judean Mountains and (2) low permeable layers within the DSG, the fresh-salt water interface does not exhibit the typical inland wedge shape with depth as expected according to the Ghyben-Herzberg relation, with

DE (e.g. model 071) or without DE (e.g. model 035). In fact, the interface reveals a more subparallel arrangement immediate along the transition from the DSG to the DS. Only along layers of higher permeability in a depth of about 10 m and 40 to 70 m the potential of the high-dense DS water results in an initial wedging and lifting of freshwater, for models with DE (e.g. model 071) and without DE (e.g. model 035): Saltwater intrudes about 60 m inland in a depth of about 10 m and about 350 m inland (equals 1/3 of the horizontal DSG extension) in a depth of about 40 to 70 m. A decrease of the freshwater potential due to droughts or a possible additional abstraction in the catchment area of Wadi Darga may enhance the intrusion of saltwater.

As proven by the discrete element frequency approach, only a small area of the DSG sediment in the transition zone of Cretaceous limestone and DSG sediment need to exhibit pathways of additional permeability to allow discharge to the DS. Such dissolution voids can easily be created by inflowing freshwater which dissolves precipitated salt crystals or layers. By passing layers of higher matrix permeability, groundwater finally attains the DS (cf. DE frequency 50 m W model 070).

Simulated models without division of the DSG and without applied DE do not exhibit sublacustrine discharge and a dominantly escape in a depth of -424 m msl to -426 m msl. At least the division of the DSG is required to enable groundwater flow along better permeable layers. Simultaneous surface and sublacustrine discharge demands for the application of DE: DE are either applied on the clay layers (constant-cross-section model 057) or they are implemented in an relatively small area 50 m away from the outlet of the hard rock aquifer inside the DSG (DE frequency 50 m W model 070). Both cases require a constant DE cross-section area (0.005 m^2) and constant DE hydraulic aperture (0.001 m). Preferred pathways and subsequent discharge to the DS are not sensitive for selected horizontal or vertical implemented DE (scenarios 076 to 078). These directions of additional permeability do not increase the discharge. On the contrary, the amount and arrangement of selected DE in those scenarios diminish discharge to the DS and do not approximate the natural system. This behavior results from the assumed confined aquifer that is not influenced by the spatial direction of tubes if the number and opening parameters of tubes in different direction scenarios are the same.

Additionally to the advance of the DS saltwater front, the lack of sublacustrine freshwater discharge may coincide with a salinity input to the DSG system along the Judean faults. The scenario of the salinity pool provides an equal discharge pattern compared to the constant cross-section model (057) except the discharge in greater depth (-489 m msl for the constant cross-section model). Thus, deep ascending brines might play a major role in the contribution to the local drainage network, as proposed by Gvirtzman (2006), and cannot be excluded according to the conducted salinity pool scenarios.

Model layers with applied discrete features are comparable to the hydrogeological compartment 1 in Figure 19. Conduits allow accelerated water migration through the DSG sediment. Areas adjacent to the Cretaceous rock/DSG sediment transition zone exhibit conditions (environment 2 in Figure 19) where large dissolution voids favor higher flow velocities.

In fact, freshwater passes the DSG sediments, which have a minimum thickness of 150 m and a low bulk hydraulic conductivity. Observed terrestrial and sublacustrine discharges to the DS seem not to reflect the amount of water that is recharged in the Judean Mountains and discharged to

the Quaternary DSG. However, model results prove that flow and mass balance is attained in a time frame of 5,000 d, i.e. the inflowing equals the outflowing water and mass (cf. chapter *Rate budget*). To fulfill the rate budget balance water does not necessarily need to escape from the sediment and occur as spring in the given time frame.

The advection-dominated groundwater movement within the model domain is influenced by the choice of the longitudinal and transverse dispersivity, as shown in the uncertainty analysis. In the range of applied literature values, these changes did not considerably influence the resulting flow and mass pattern. With respect to the anisotropy of conductivity, it will decelerate discharge to the DS and has to be appreciated for hydraulic sediment studies in order to improve the model, eventually. In general, the model delivered more stable results for a onetime smoothing of mesh elements and is highly recommended to utilize.

The implementation of complex discrete feature configurations mostly prevents the output of the demanded mass concentration pattern within FEFLOW (voided output, e.g. models 079, 080). The reason is the impossibility of solving the mathematical equations during the steady-state transport modeling (convergence failed). In the frame of density-dependent modeling this behavior implies the tendency for a self-perturbing system and does not reveal any steady-state solution. With respect to the prediction of the fresh-salt water interface position, a quasi-steady-state model (transient model with large simulation time) is recommended to examine the behavior of the fresh-salt water interface position. The required back coupling of flow and transport solution in an iterative way is fulfilled in the transient case and would provide reasonable results and mass concentration outputs of certain time steps (e.g. for 5,000 d). Even very large time frames will provide a dynamic system with significant changes in the position of the interface. This behavior needs to be considered when discrete feature and transport processes (e.g. transport of contaminants) are combined. Regarding the calculated flow and mass balance, the simulated models demand for a balanced distributed sources/sinks term. However, due to the applied intrinsic fluid density a buoyancy term appears in the flow rate budget calculation as well, which is listed as distributed sources and sinks. Although, no sources or sinks have been manually applied, processes triggered by the density are considered as a kind of internal BC within the FEFLOW rate budget calculation.

With respect to the kinetics of mass transport, a major challenge is the estimation of the exchange coefficient between matrix and conduit and the corresponding kinetics of sediment erosion. In FEFLOW, mass transfer rates can only be indirectly applied by mass concentration differences in matrix and conduits (time-dependent mass exchange possible via source-code embedding module). Complex geometry and turbulent flow exacerbate the evaluation of the lumped exchange coefficient. The determination of an optimum exchange coefficient was presented by Chen et al. (2012) within a pipe-flow Stokes-Darcy simulation model.

The constraint index helped to explain the determination of the system inherent singularity by exposing an optimal scenario with the governing conditions for its possibility. Varying parameters and increased data density for sure will change the system but can then easily be weaved into the result interpretation. Only then, water decision makers have the required scientific insurance for the practical utilization of the resource.

7 Discussion

The study emphasizes the necessity of high-quality calibration data. Only the accessibility of geological logs and spring location constraints provided the substratum for the systematic approach of discrete element zones and facilitated the qualitative evaluation of possible model scenarios.

With respect to water saturation, the recorded streamline situations would only be true if the entire transect is water saturated. It appeared to be useful to apply the western hydraulic-head BC only for the saturated part. Unsaturated parts of the model demand for an unsaturated flow mode. The subsequent default no-flow BC above would then only produce flow lines for the part of the applied hydraulic-head BC. The reasons why the application of this method failed are (1) models with underlying unsaturated mode crashed due to unknown reasons and (2) a complex combined flow and mass transport model in unsaturated mode with the coupling of Richards and Darcy equation was regarded as non-viable procedure for this study and is therefore recommended for further research. The important ROI for the study, the DSG sediment, is considered to be water saturated. Therefore, the confined saturated approach holds.

Another modeling result for the Judea Group aquifer produces a hydraulic-head at the western boundary of the study area with a value of -380 m msl (A. Gräbe, pers. communication, refers to the modeling in Gräbe et al. 2013). However, due to OpenGeoSys modeling instabilities this value is not taken as hard fact and neglected as value for the western BC.

As matter of discussion, the sediment fill of the transition zone between the Cretaceous aquifers and the alluvial fan at elevations higher than -400 m msl cannot be resolved in terms of the lake sediment contribution and subsequent diminished hydraulic conductivity. Impermeable lenses could conceivably act as hydraulic barriers. Contrary, the erosion of fine sediments could have totally blurred the former lake sediment deposition, which would favor the dewatering of the debris.

The geological logs represent a rough estimation of the grain size along a certain layer. However, these layers have not been determined by a hydraulic point of view. Thin permeable layers in a layer of overall impermeable material may channel the water flow and produce the discharge that has to be modeled. For instance, clay layers are always interrupted by separation layers as salt or gravel and cannot be represented as single clay layer unit.

The model setup was applied to one slice within the study area. Another slice would only be useful to display topography. Due to the transfer of the analogous sediment setup, the depth profile would have been created according to the chosen cross-section. At the most, there would be some geological variations of the Cretaceous aquifer and therefore of the hydraulic input behavior. In fact, information from another drilling in the north of the study area would have been useful, e.g. from the Kane-Samar drilling MH TURYAVAH T/2 AMOK with a depth of 56 m. As further composition of the DSG sediment it would complete the picture of the study area, in addition to the already known composition of the central and southern part of the Wadi Darga fan.

In visualization of groundwater flow, isohypses are helpful for the interpretation of groundwater flow. In FEFLOW, the isohypses are related to freshwater, not to saltwater. This technique has

some serious effects on the interpretation of the geometry of the flow network. Answers to the potentials of the groundwater demand for a recalculation of potential lines for saltwater. The modeled isohypses give no indication of the position of the fresh-salt water interface. For the latter issue the mass concentration distribution pattern needs to be utilized.

The modeled isohypses are freshwater isohypses per definition. Therefore, the position of potential lines may be shifted according to the density dependency. As conclusion, a precise localisation of the fresh-salt water interface is not possible to predict. According to a pressure distribution in the vertical z-direction under hydrostatic conditions and a linear increase of density with depth (Equation 7) the hydraulic head obeys Equation 8 (Diersch 2010a). Consequently, the saltwater head is lower compared to the same situation with freshwater.

$$\begin{cases} \dfrac{dp}{dz} = -\rho g \\ p = p(z) = -g \displaystyle\int_{z_1}^{z} \rho(\theta) d\theta \end{cases}$$

Equation 7

where

p	hydrostatic pressure [kbar]
g	gravity [9.81 m/s²]
ρ	fluid density [kg/m³]

$$h = h_0 + \frac{\bar{\alpha}}{2}\Delta z$$

Equation 8

where

h_0	head at location z = 0 [m]
$\bar{\alpha}$	fluid density difference ratio []
Δz	depth [m]

The fluid flow mechanisms in the transition zone of freshwater and saltwater are supposed to be driven by convection and density. However, mesoscale dispersion effects due to density equilibration need to be mentioned as well. Particularly, a passive hydrogeological system in the north of the delta with low amounts of inflowing freshwater facilitates dispersion to becoming the dominant process of water movement.

The applied density ratio α in FEFLOW is based on the calculation of the fresh-salt water interface according to the Ghyben-Herzberg equation. The advance of the saltwater front depends on this relation and demands for the formulation of some limitations. The sharp interface avoids mixing and evokes a static behavior. In terms of dispersion, the real-world shape of the interface is likely to be different, even not considered the transient behavior yet. For instance, Pool and Carrera (2011) applied a correction factor to account for mixing during seawater penetration. In fact, parameters of dispersivity and diffusivity are adaptable in FEFLOW and serve as corrective for a sharp interface in order to facilitate mixing of freshwater and saltwater.

Indeed, options as the statistical distribution of initial fracture diameters or the time-dependent shape of fractures with breakthrough curves are not designated within FEFLOW. However, regarding the time-dependent dissolution enlargements of conduits in the DSG sediment, a promising option in FEFLOW is the implementation of the IFMSetFrac module within the source code (IFM API). Specific fracture elements, fracture types, hydraulic apertures and cross-section areas can be iteratively defined during the simulation. Eventually, a time-dependent development of the cross-section areas might be applicable, however require additional effort in sensitivity analysis and ensuring numerical stability.

Discrete elements cannot be arbitrarily implemented in the finite element mesh but they are fixed to the position of the mesh element edges. By mesh refining the position of the discrete elements may be approximated sufficiently enough. It is worth to mention that not only the FEFLOW code is able to simulate discrete features in an existing matrix continuum, especially if turbulent flow is expected in conduits, which cannot be realized in FEFLOW so far. Shoemaker et al. (2008) developed a turbulent conduit flow process (CFP) in the USGS MODFLOW code. The conduits will be applied either by using a discrete pipe network, a high-conductivity flow layer with option for turbulent flow or a combination of both. The discrete pipe network is based on the CAVE model and demands for the definition of geometry and hydraulic characteristics of conduits. In practical this discrete conduit flow was for instance successfully applied on the Madison karst aquifer in South Dakota (USA) to amplify the existing EPM (equivalent porous media) model (Saller et al. 2013). The incorporation of the Colebrook-White law for turbulent flow (used for the Moody diagram) within FEFLOW as addition to the laminar Hagen-Poiseuille would be a promising option to enhance pipe flow modeling and to approximate flow even in larger conduits where turbulent flow is expected.

All conducted models have been operated in steady-state mode. However, the investigation of time-dependent groundwater heads and saltwater intrusion phenomena in the dynamic system of the DSG sediment demands for a transient representation in a future development. For instance, the seasonal change of water supply and the corresponding water feeding mechanism in the Wadi Darga outlet should be reflected in a transient response to the heads and discharge within the DSG sediments. When conducting a transient FEFLOW model, the implementation of Goode's method should be considered. It allows determining residence times of groundwater in the DSG sediment. Compared to conventional performed particle-tracking methods Goode's method considers physical processes of advection, diffusion and dispersion. Those processes can as well be applied for conclusions regarding transport through hydrological windows of leaky aquifers (Diersch 2010c). For successful application within FEFLOW the required parameters need to be selected carefully.

The only existence of high conductive layers does not necessarily result transport connectivity. The network geometry is critical for transport dynamics as well: As numerically proven by Ronayne (2013) the more tortuous the network the greater is the degree of conduit-matrix mixing and reduced transport connectivity. Such complex conduit geometry could result in much higher residence times within the DSG sediment. FEFLOW facilitates to implement more complex geometries of discrete features (Diersch 2010b).

Do the simulated Darcy velocities correlate to the turbidity observations in the spring area of the DSG sediments (chapter *Hydrogeology*)? Indeed, the larger simulated discharges with a larger amount of suspended clayey material are fed by higher hydraulic conductivity zones with larger flow velocities within a range of 10^{-3} to 10^{-2} m/s. Even the maximum simulated flow velocity does not exceed the critical velocity of 0.2 m/s for the erosion of unconsolidated dry clay (Hjulström 1935). To explain the transport of suspended material to the DS other factors have to be taken into consideration as high tortuosity within the conduits. This phenomenon would cause velocity peaks that facilitate small-scale but efficient clay mineral erosion. A further explanation is that the large pore water content within the DSG sediment may reduce intra-crystalline bonding forces of clay minerals due to enhanced H_2O-inclusion into the layer structure. This may effect easier erosion at lower velocities. Smaller discharges with lower groundwater velocities in the delivering DSG layers are usually in the range of 10^{-4} to 10^{-6} m/s. These velocities are not effective for clay mineral erosion and produce more clear water without clay suspension.

In order to setup a model with a higher resolution in depth, at least drilling logs along a lateral section of some 100 m depth are required. The assignment of hydraulic conductivities is based on visual interpretation of borehole logs. In fact, field and laboratory tests on the respective layers would increase practical reliability. The degree and shape of salt karst in gypsum and aragonite units need to be updated from field evidence. The water transition from the Lower Judea Group aquifer towards the undifferentiated DSG is unresolved and demands for further investigation. What are the governing factors for water flow in deeper parts of the DSG section? Future studies need as well focus on the observation of hydraulic heads and on methods to track the existing water pathways in the DSG sediment, as geophysical surface penetration or tracer studies.

8 References

Abelson, M et al. 2002, Development of the Dead Sea sinkholes - Detection from aerial photographs up to 2001. Report GSI/30/2002. In Hebrew, Israel, 30 p.

Abelson, M et al. 2006, 'Evolution of the Dead Sea sinkholes' in New frontiers in Dead Sea paleoenvironmental research, eds Y Enzel, A Agnon & M Stein, The Geological Society of America, Boulder, Colo, p. 241–253.

Aeschbach-Hertig, W and Gleeson, T 2012, 'Regional strategies for the accelerating global problem of groundwater depletion', Nature Geoscience, 5, 12, p. 853–861.

Agnon, A et al. 2006, Geological Map of Israel, 1:50,000. Sedom, Sheet 20-I, II. Isr. Geol. Surv., Jerusalem.

Agnon, A and Sagy, A 2011, Geological Map of Israel, 1:50,000. Newe Zohar, Sheet 16-III, IV. Isr. Geol. Surv., Jerusalem.

Arad, A and Michaeli, A 1967, 'Hydrogeological investigations in the western catchment of the Dead Sea', Israel Journal of Earth Sciences, 16, p. 181–186.

Bartov, Y et al. 2006, 'Current depositional environments at the Dead Sea margins as indicators of past lake levels' in New frontiers in Dead Sea paleoenvironmental research, eds Y Enzel, A Agnon & M Stein, The Geological Society of America, Boulder, Colo, p. 127–140.

Begin, ZB 1974, 'Lake Lisan - the Pleistocene precursor of the Dead Sea', Geological Society of America Bulletin, 63, p. 1–38.

Belitzky, S and Mimran, Y 1996, 'Active salt diapirism at the Zahrat El-Qurein dome, lower Jordan Valley, Jordan', Israel Journal of Earth Sciences, 45, 1, p. 11–18.

Ben-Avraham, Z and Brink, U ten 1989, 'Transverse faults and segmentation of basins within the Dead Sea Rift', Journal of African Earth Sciences (and the Middle East), 8, 2–4, p. 603–616.

Bender, F 1968, Geological Map of Jordan, 1:250,000. Sheet Amman. Geological Survey of the Fed. Rep. of Germany, Hannover.

Ben-Gai, Y and Ben-Avraham, Z 1995, 'Tectonic processes in offshore northern Israel and the evolution of the Carmel structure', Marine and Petroleum Geology, 12, 5, p. 533–548.

Ben-Itzhak, L and Gvirtzman, H 2005, 'Groundwater flow along and across structural folding: an example from the Judean Desert, Israel', Journal of Hydrology, 312, 1, p. 51-69.

Blake, G and Goldschmidt, J 1947, Geology and water resources of Palestine. Dept. of Land Settlement; Water Commissioner, Govt. Printer, Palestine.

Bookman, R et al. 2004, 'Late Holocene lake levels of the Dead Sea', Geological Society of America Bulletin, 116, p. 555–571.

Buchbinder, B et al. 2000, 'Sequence development of Late Cenomanian–Turonian carbonate ramps, platforms and basins in Israel', Cretaceous Research, 21, 6, p. 813–843.

Chen, C et al. 2009, 'A GIS based hydrosystem model for the jericho Plain, Palestine' in The water of the Jordan Valley. Scarcity and deterioration of groundwater and its impact on the regional development, eds H Hötzl, P Möller & E Rosenthal, Springer, Berlin, p. 349–360.

Chen, N et al. 2012, 'Calibrating the exchange coefficient in the modified coupled continuum pipe-flow model for flows in karst aquifers', Journal of Hydrology, 414–415, 0, p. 294–301.

DHI-WASY Software 2012, FEFLOW 6.1. Finite Element Subsurface Flow & Transport Simulation System - User Manual. Firstly introduced package by Diersch, H.-J. G. in 1979, Berlin, 116 p.

Diersch, HG 2010a, 'About the formulation of hydraulic head boundary (potential) conditions for fluid density-dependent groundwater problems' in FEFLOW White Papers Volume 1, ed DHI-WASY Software, p. 135–140.

Diersch, HG 2010b, 'Appendix D' in FEFLOW White Papers Volume 1, ed DHI-WASY Software, p. 194–198.

Diersch, HG 2010c, 'Discrete feature modeling of flow, mass and heat transport processes by using FEFLOW' in FEFLOW White Papers Volume 3, ed DHI-WASY Software, p. 151–198.

Diersch, HG 2010d, 'Using and testing the algebraic multigrid equation solver SAMG in FEFLOW' in FEFLOW White Papers Volume 3, ed DHI-WASY Software.

DIN EN ISO 14688-1, 2011-06-00, Geotechnical investigation and testing - Identification and classification of soil - Part 1: Identification and description.

Domenico, PA and Schwartz, FW 1998, Physical and chemical hydrogeology, Wiley, New York, xiii, 506 p.

Druckman, Y and Kashai, E 1981, The Helez Deep and Devora 1A boreholes and their implication to oil prospects in Pre-Jurassic strata in Israel. Rep. OD/1/81, Geol. Surv. Israel, Jerusalem, 23 p.

Dweik, H & Shuval, HI (eds.) 2007, Water resources in the Middle East. Israel-Palestinian water issues - from conflict to cooperation, Springer, Berlin [u.a.], xiv, 454 p.

Enzel, Y et al. 2000, 'Holocene Earthquakes inferred from a Fan-Delta Sequence in the Dead Sea Graben', Quaternary Research, 53, 1, p. 34–48.

Eyal, Y et al. 2002, 'High-resolution seismic study of the Nahal Darga fan-delta, Dead Sea, Israel, with the aim to relate the surface and subsurface tectonic structures', Stephan Mueller Special Publication Series, Volume 2, p. 21–33.

Ezersky, M et al. 2011, 'TEM study of the geoelectrical structure and groundwater salinity of the Nahal Hever sinkhole site, Dead Sea shore, Israel', Journal of Applied Geophysics, 75, 1, p. 99–112.

Flexer, A et al. 2000, 'A Neogene salt body as the primary source of salinity in Lake Kinneret', Arch. Hydrobiol., 55, p. 1–17.

Flexer, A 2001, 'The Pre-Neogene Geology of the Near East' in The Jordan Rift Valley, ed A Horowitz, A.A. Balkema Publishers, Lisse, Exton, PA.

Flexer, A et al. 2009, 'Regional setting' in The water of the Jordan Valley. Scarcity and deterioration of groundwater and its impact on the regional development, eds H Hötzl, P Möller & E Rosenthal, Springer, Berlin, p. 3–13.

Freeze, RA and Cherry, JA 1979, Groundwater, Prentice-Hall, Englewood Cliffs, N.J, xvi, 604 p.

Frumkin, A et al. 2011, 'The Dead Sea sinkhole hazard: Geophysical assessment of salt dissolution and collapse', Geomorphology and Natural Hazards in Karst Areas, 134, 1–2, p. 102–117.

Galeati, G et al. 1992, 'Coupled and partially coupled Eulerian-Lagrangian model of freshwater-seawater mixing', Water Resources Research, 28, 1, p. 149–165.

Gardosh, M et al. 1990, 'Holocene tectonic deformation along the western margins of the Dead Sea', Geologic and Tectonic Processes of the Dead Sea Rift Zone, 180, 1, p. 123–137.

Garfunkel, Z 1989, 'Tectonic setting of Phanerozoic magmatism in Israel', Israel Journal of Earth Sciences, 38, 3-4, p. 51–74.

Garfunkel, Z and Ben-Avraham, Z 1996, 'The structure of the Dead Sea basin', Tectonophysics, 266, 1/4, p. 155–176.

Gavrieli, I and Stein, M 2006, 'On the origin and fate of the brines in the Dead Sea basin' in New frontiers in Dead Sea paleoenvironmental research, eds Y Enzel, A Agnon & M Stein, The Geological Society of America, Boulder, Colo, p. 183–194.

Gilbert, GK 1914, The transportation of debris by running water. U.S. Geological Survey Professional Paper, 86, 263 p.

Gräbe, A et al. 2013, 'Numerical analysis of the groundwater regime in the western Dead Sea escarpment, Israel + West Bank', Environmental Earth Sciences, 69, 2, p. 571–585.

Guttman, J et al. 2000, Hydrogeology of the Eastern Aquifer in the Judea Hills and Jordan Valley. German- Israeli-Palestinian Joint Research. Mekorot Report 468. Project 02WT9719.

Guttman, J 2000, Hydrogeology of the eastern aquifer in the Judea Hills and Jordan Valley. Multi-Lateral Project, Project 02WT9719 within the framework of the German-Israeli-Jordanian-Palestinian Joint Research Program for the sustainable utilization of aquifer systems. Mekorot.

Guttman, J 2009, 'Hydrogeology' in The water of the Jordan Valley. Scarcity and deterioration of groundwater and its impact on the regional development, eds H Hötzl, P Möller & E Rosenthal, Springer, Berlin, p. 55–74.

Gvirtzman, H et al. 1997, 'Hydrogeological modeling of the saline hot springs at the Sea of Galilee, Israel', Water Resources Research, 33, 5, p. 913–926.

Gvirtzman, H 2006, 'Groundwater hydrology and paleohydrology of the Dead Sea rift valley' in New frontiers in Dead Sea paleoenvironmental research, eds Y Enzel, A Agnon & M Stein, The Geological Society of America, Boulder, Colo, p. 95–111.

Haliva-Cohen, A et al. 2012, 'Sources and transport routes of fine detritus material to the Late Quaternary Dead Sea basin', Quaternary Science Reviews, 50, 0, p. 55–70.

Hall, JK 2000, Orthographic satellite imagery coverage, Israel and adjacent areas. Sheet 13: Dead Sea Bathymetry. 1:100,000. Isr. Geol. Surv. Rep. GSI/16/2000.

Hall, JK & Krasheninnikov, VA (eds.) 2005, Geological framework of the Levant, Volume II: the Levantine Basin and Israel. Plate IV, Historical Productions-Hall, Jerusalem, 826 p.

Henry, HR 1964, 'Effects of dispersion on salt enrichment in coastal aquifers', U.S. Geological Survey Water Supply Paper, 1613-C, Sea water in coastal aquifers, p. C70-C84.

Hjulström, F 1935, Studies of the morphological activity of rivers as illustrated by the River Fyris. Inaugural dissertation, 527 p.

Horowitz, A (ed.) 2001, The Jordan Rift Valley, A.A. Balkema Publishers, Lisse, Exton, PA, 730 p.

Hurwitz, S et al. 2000, 'Transient groundwater-lake interactions in a continental rift: Sea of Galilee, Israel', Geological Society of America Bulletin, 112, p. 1694–1702.

I.O.C 1982, Seismic cross-sections from En Gedi. Time migration sections and index map. The Israel National Oil Co. Ltd. Mezada Permit.

Ionescu, D et al. 2012, 'Microbial and Chemical Characterization of Underwater Fresh Water Springs in the Dead Sea', PLoS ONE, 7, 6, e38319.

Katz, A et al. 1977, 'The geochemical evolution of the Pleistocene Lake Lisan-Dead Sea system', Geochimica et Cosmochimica Acta, 41, 11, p. 1609–1626.

Kiro, Y 2007, The effect of the Dead Sea level drop on the groundwater system in the alluvial aquifer in its vicinity. In Hebrew. Report GSI/05/2007, Jerusalem, 108 p.

Kiro, Y et al. 2008, 'Time response of the water table and saltwater transition zone to a base level drop', Water Resources Research, 44, 12, p. W12442.

Kushnir, S 2008, 'Mechanisms of spontaneous concentration of underground waters and their role in the formation of vertical hydrogeochemical zonality in a zone of hypergenesis (physical-chemical analysis)', Geologiya i Geokhimiya Goryuchikh Kopalin3, p. 78–87.

Lensky, NG et al. 2005, 'Water, salt, and energy balances of the Dead Sea', Water Resources Research, 41, 12, p. W12418.

Mallast, U et al. 2011, 'Derivation of groundwater flow-paths based on semi-automatic extraction of lineaments from remote sensing data', Hydrology and Earth System Sciences, 15, 8, p. 2665–2678.

Mallast, U et al. 2013, 'Localisation and temporal variability of groundwater discharge into the Dead Sea using thermal satellite data', Environmental Earth Sciences, 69, 2, p. 587–603.

Massari, F and Colella, A 1988, 'Evolution and types of fan-delta systems in some major tectonic settings' in Fan deltas : sedimentology and tectonic settings, ed W Nemec, Blackie, Glasgow, p. 103–122.

Michelson, H 1978, 'Stratigraphy of the lake area' in Lake Kinneret, ed C Serruya, W. Junk, The Hague, Boston.

Migowski, C et al. 2006, 'Holocene climate variability and cultural evolution in the Near East from the Dead Sea sedimentary record', Holocene Climate and Cultural Evolution in Late Prehistoric-Early Historic West Asia, 66, 3, p. 421–431.

Möller, P et al. 2007, 'Hydrochemical processes in the lower Jordan valley and in the Dead Sea area', Chemical Geology, 239, 1-2, p. 27–49.

Möller, P et al. 2009a, 'Characterization of recharge areas by rare earth elements and stable isotopes of H2O' in The water of the Jordan Valley. Scarcity and deterioration of groundwater and its impact on the regional development, eds H Hötzl, P Möller & E Rosenthal, Springer, Berlin, p. 123–148.

Möller, P et al. 2009b, 'Hydrochemical aspects - Characterization of aquifer environments by major and minor elements and stable isotopes of sulfate' in The water of the Jordan Valley. Scarcity and deterioration of groundwater and its impact on the regional development, eds H Hötzl, P Möller & E Rosenthal, Springer, Berlin, p. 83–121.

Mor, U and Burg, A 2000, Geological Map of Israel, 1:50,000. Mizpe Shalem, Sheet 12-III. Isr. Geol. Surv., Jerusalem.

NASA 2010, Dead Sea border. Deduced from a Landsat image.

NASA and METI 2011, ASTER GDEM Version 2. Dead Sea region with a resolution of 30 m.

Nativ, R 1997, 'Saline springs near/in Lake Kinneret, their origin and the mechanisms controlling their discharge', Terra Nostra, 4/97,

Pickrill, RA and Irwin, J 1982, 'Predominant headwater inflow and its control of lake-river interactions in Lake Wakatipu', New Zealand Journal of Marine and Freshwater Research, 16, 2, p. 201–213.

Pool, M and Carrera, J 2011, 'A correction factor to account for mixing in Ghyben-Herzberg and critical pumping rate approximations of seawater intrusion in coastal aquifers', Water Resources Research, 47, 5, p. 1–9.

PWA 2005, Master Data of Palestinian Wells In West Bank. Palestinian Water Authority. Available from: http://www.pwa.ps/ [25 September 2013].

Raz, E 1986, Geological Map 1:50,000. Sheet En-Gedi. Section 3. Geological Survey of Israel.

Raz, E 2000, Formation of sinkholes in the Dead Sea area - a surface survey. Report GSI/31/2000. In Hebrew, Israel, 67 p.

Ronayne, MJ 2013, 'Influence of conduit network geometry on solute transport in karst aquifers with a permeable matrix', Advances in Water Resources, 56, 0, p. 27–34.
Rosenthal, E et al. 2006, 'The paleoenvironment and the evolution of brines in the Jordan-Dead Sea transform and in adjoining areas', International Journal of Earth Sciences, 95, 4, p. 725–740.
Rosenthal, E et al. 2009, 'The hydrochemical history of the Rift' in The water of the Jordan Valley. Scarcity and deterioration of groundwater and its impact on the regional development, eds H Hötzl, P Möller & E Rosenthal, Springer, Berlin, p. 75–82.
Salameh, E 2001, 'The potential of groundwater artificial recharge in the Jordan valley area / Jordan' in Selected contributions to applied geology in the Jordan Rift Valley, eds B Merkel, R Azzam & Z Qannam, Technische Universität Bergakademie, Freiberg, p. 63–81.
Salameh, E 2002, 'Sources of water salinities in the Jordan Valley area/Jordan', Acta hydrochimica et hydrobiologica, 29, 6/7, p. 329–362.
Saller, SP et al. 2013, 'Comparison of a karst groundwater model with and without discrete conduit flow', Hydrogeology Journal, 21, 7, p. 1555–1566.
Schäfer, A 2005, Klastische Sedimente. Fazies und Sequenzstratigraphie, Elsevier, Spektrum Akad. Verl., München, Heidelberg, x, 414 p.
Scholz, CA et al. 1993, 'Deltaic sedimentation in a rift valley lake: New seismic reflection data from Lake Malawi (Nyasa), East Africa', Geology, 21, p. 395–399.
Shoemaker, WB et al. 2008, Documentation of a conduit flow process (CFP) for MODFLOW-2005. US Geological Survey Techniques and Methods, book 6, chap A24, USGS, Reston, VA, 50 p.
Siebert, C 2013, 'Sediment composition along the western Dead Sea in relation to its contribution to groundwater chemistry.' in Conceptual cross-section through the sedimentary body along the western shore. Verbundprojekt: IWRM Helmholtz Dead Sea, Israel (ISR), Jordanien (JOR), Palästina (PLA): TP4: SUMAR. Förderkennzeichen: 02WM0848. Final report, eds S Geyer, C Siebert, T Rödiger & U Mallast, p. 245–250.
Siivola, J & Schmid, R 2007, List of Mineral Abbreviations. Recommendations by the IUGS Subcommission on the Systematics of Metamorphic Rocks: Web Version 01.02.07. Available from: http://www.bgs.ac.uk/scmr/docs/papers/paper_12.pdf.
Stein, M 2001, 'The sedimentary and geochemical record of Neogene-Quaternary water bodies in the Dead Sea Basin - inferences for the regional paleoclimatic history', Journal of Paleolimnology, 26, 3, p. 271–282.
Stein, M et al. 2010, 'Abrupt aridities and salt deposition in the post-glacial Dead Sea and their North Atlantic connection', Quaternary Science Reviews, 29, 3–4, p. 567–575.
Torfstein, A et al. 2008, 'Gypsum as a monitor of the paleo-limnological–hydrological conditions in Lake Lisan and the Dead Sea', Geochimica et Cosmochimica Acta, 72, 10, p. 2491–2509.
Torfstein, A et al. 2013, 'Integrated multi-site U–Th chronology of the last glacial Lake Lisan', Geochimica et Cosmochimica Acta, 104, 0, p. 210–231.
UFZ 2011, DEM from the Dead Sea region generated from airborne photos. Resolution of 5 m. Recorded by Christian Siebert within the SUMAR project.
Voss, CI 1984, A finite-element simulation model for saturated-unsaturated, fluid-density-dependent ground-water flow with energy transport or chemically-reactive single-species solute transport, U. S. Geological Survey, Reston, VA, United States (USA), 49 p.
Voss, CI and Souza, WR 1987, 'Variable density flow and solute transport simulation of regional aquifers containing a narrow freshwater-saltwater transition zone', Water Resources Research, 23, 10, p. 1851–1866.
Waldmann, N 2002, The geology of the Samra Formation in the Dead Sea basin. M.Sc. Thesis, The Hebrew University of Jerusalem, Jerusalem, Israel, 175 p.
Waldmann, N et al. 2007, 'Primary carbonates and Ca-chloride brines as monitors of a paleo-hydrological regime in the Dead Sea basin', Quaternary Science Reviews, 26, 17–18, p. 2219–2228.
Wernicke, J 2010, Sinkholes as an indicator for groundwater flow: A remote sensing supported sedimentological study from the West Coast of the Dead Sea. Diploma Thesis at University Leipzig, 113 p.
Wollman, S et al. 2003, Summary of results for the test pumping in Nahal Arugot, Dead Sea sinkholes project: Stage B. Report GSI/42/2003. In Hebrew, Jerusalem, 10 p.
Yechieli, Y et al. 1990, Chemical processes at the interface between the Dead Sea and groundwater. ES-48/90, Rehovat, Israel, 19 p.
Yechieli, Y et al. 1993, 'Late Quaternary Geological History of the Dead Sea Area, Israel', Quaternary Research, 39, 1, p. 59–67.

Yechieli, Y et al. 1995, 'Aquifer Characteristics Derived From the Interaction Between Water Levels of a Terminal Lake (Dead Sea) and an Adjacent Aquifer', Water Resources Research, 31, 4, p. 893–902.
Yechieli, Y 2000, 'Fresh-Saline Ground Water Interface in the Western Dead Sea Area', Ground Water, 38, 4, p. 615–623.
Yechieli, Y et al. 2001, 'Factors controlling the configuration of the fresh-saline water interface in the Dead Sea coastal aquifers: synthesis of TDEM surveys and numerical groundwater modeling', Hydrogeology Journal, 9, 4, p. 367–377.
Yechieli, Y 2005, Geological and hydrological findings from wells near the Dead Sea. Sinkhole Project - Phase Two. In Hebrew. TR-GSI/06/2005, Jerusalem.
Yechieli, Y 2006, 'Response of the groundwater system to changes in the Dead Sea level' in New frontiers in Dead Sea paleoenvironmental research, eds Y Enzel, A Agnon & M Stein, The Geological Society of America, Boulder, Colo, p. 113–126.
Yechieli, Y et al. 2006, 'Sinkhole "swarms" along the Dead Sea coast: Reflection of disturbance of lake and adjacent groundwater systems', Geological Society of America Bulletin, 118, 9-10, p. 1075–1087.
Yechieli, Y et al. 2009, 'The effect of base level changes and geological structures on the location of the groundwater divide, as exhibited in the hydrological system between the Dead Sea and the Mediterranean Sea', Journal of Hydrology, 378, 3–4, p. 218–229.
Yechieli, Y et al. 2010, 'Response of the Mediterranean and Dead Sea coastal aquifers to sea level variations', Water Resources Research, 46, 12, p. 1–11.
Yechieli, Y and Gat, J 1997, 'Geochemical and hydrological processes in the coastal environment of the Dead Sea' in The Dead Sea. The lake and its setting, eds TM Niemi, Z Ben-Avraham & J Gat, Oxford University Press, New York, p. 252–264.
Yechieli, Y and Ronen, D 1997, 'Early diagenesis of highly saline lake sediments after exposure', Chemical Geology, 138, 1–2, p. 93–106.

9 Appendix

Attached are the

- Explanation of common FEFLOW 6.1 features which were faced during the development of the models, among these are helpful remarks to settings and model adaptations (appendix A)
- Synopsis of the model properties (appendix B): The hydraulic conductivity parameterization (Flow Properties – DSG sediment – according to kf parameterization) is displayed in Table 5. Concerning the total balance of the rate budget, positive values indicate flow/mass excess (italic), negative values indicate flow/mass deficit of the system. Total balance values < 10 are denoted in *green*, between 10 and 100 in *orange* and > 100 in *red*. Important changes during the model development are denoted in *blue*.

Appendix A: FEFLOW 6.1 features

Budget with Slice and 3D view

- budget quantities can also be visualized in the FE-Slice View and 3D View windows by adding the Budget component from the Data panel to the View Components panel

Constraints on Flow Boundary Conditions

- physical limits (hydraulic head/fluid transfer type limited by min/max flow rate, fluid flux/well type limited by min/max hydraulic head, fluid-transfer type limited by hydraulic-head)
- technically implemented in FEFLOW by converting the type of BC when the constraint is activated

Mass Transport **C**onstraint Conditions

- physical limits (mass-concentration/mass-transfer type limited by min/max mass flux, mass-flux/mass-nodal type limited by min/max concentration)
- technically implemented in FEFLOW by converting the type of BC when the constraint is activated

Convergence failure

- solver failed to converge with the log output: "Math: Argument domain error in function sqrt!" or output: "Unknown error"

Save as **D**AC-file

- click record next to start simulation
- save before simulation, otherwise no streamlines can be created

Density/concentration settings for water

- material property density ratio
- problem settings - problem class - transport settings - reference values – C_0 as BC for fresh water, C_S as BC for salt water (C_S appears when the Hydraulic-head (Saltwater head is applied)

Density plot

- via mass concentration visualization
- use "user data" in the data panel - add nodal expression - define density as function of concentration

Density ratio

- after applying the density ratio alpha, C_S automatically appears in the transport settings of the problem settings (e.g. C_S = 340,000 mg/L, C_0 = 800 mg/L)

Workflow for the application of **D**iscrete features in 2D sections

- select slice edges or select nodes

- select by map polygon after choosing the supermesh as selection map
- within the slice-edge selections in the spatial units: store current selection
- within discrete features in the data panel: add slice-edge feature element - choose the flow law
- rename the new feature

Elevation as process variable in 2D

- Elevation is the current elevation (z-coordinate) for each mesh node. In case of a model with moving mesh technique for handling the phreatic surface, the elevation may change during the simulation. Elevation exists only for 3D models.
- Reference elevation is the original elevation (z-coordinate) for each mesh node in case of a model with moving mesh technique for handling the phreatic surface. Reference elevation only exists for 3D models with a moving mesh property.

Flow Boundary Conditions (time-constant or according to a time series):

- Hydraulic-head BC = Dirichlet
  - advanced:
    - Hydraulic-head BC (Pressure)
    - Hydraulic-head BC (Saltwater Head)
    - Hydraulic-head BC (Saturation)
    - Hydraulic-head BC (Moisture Content)
- Fluid-flux BC = Neumann
  - advanced:
    - Fluid-flux BC (Gradient) - unsaturated models
    - Fluid-flux BC (Integral) - unconfined models with free and movable surface
- Fluid-transfer BC = Cauchy
  - advanced:
    - Fluid-transfer BC (Integral) - unconfined models with free and movable surface
- Well BC (abstraction/infiltration, nodal or along screen)

Geometry adaptation

- within the Maps panel an existing map (e.g. ESRI Shape File) can be replaced by a map with new geometry information that may be created by ArcGIS
- set as selection map
- select by map polygon, select all polygons except the ones which should be removed
- invert selection
- delete elements in the mesh geometry toolbar

Apply **H**ydraulic conductivities manually within FEFLOW

- within the fem-file
- via map in the data panel: select the shp-file and "set as selection map"
- select conductivity via the data panel

- select by map polygon
- assign kf value for the respective polygon
- "clear as selection map"

Assignment of **H**ydraulic conductivities

- export supermesh as shp (all elements)
- ArcGIS- kf zuweisen in neues shp file
- import new shp file as map in FEFLOW
- problem settings - snap distance 0 to select only the elements in the respective polygon
- the imported shp file: set as selection map to assign polygons as conductivities - select by map polygon

Transfer **H**ydraulic conductivities from ArcGIS to FEFLOW

- within ArcGIS attribute the kf to the corresponding layer
- after importing the new supermesh-file, link the kf attribute field to conductivity [max]
- click on "links attributes" - kf
- click on select all
- click on assign

Initial heads (default is 0 m)

- define any hydraulic head as start parameter which lies above the saturated part of the model

Mass Transport Boundary Conditions (time-constant or according to a time series)

- Mass-concentration BC = Dirichlet
- Mass-flux BC = Neumann
- Mass-transfer BC = Cauchy
- Mass nodal sink/source BC

Material Properties (simulated on an elemental basis)

- flow
  - Transmissivity (2D horizontal confined, else kf)
  - Conductivity
  - Aquifer top/bottom elevation (2D)
  - In/Outflow on top/bottom GW recharge 2D and 3D!, e.g. inflow from underlying aquifer
  - Density ratio (density-dependent models)
  - Drain-/Fillable Porosity [] = specific yield, for unconfined models
  - Specific storage (Compressibility) ([] with 2D confined, [1/L] with other 2D, 3D)
  - Source/sink (flow) [m/d] [1/d] (2D: GW recharge, 3D: not for GW recharge)
  - Transfer Rate (Flow) (only together with Transfer BC)
- mass transport
  - Aquifer thickness (Mass)
  - Porosity (Mass) (effective porosity)

- Molecular diffusion [m²/s]
- Sorption coefficient (Henry)
- Dispersivity [m] (low ones need fine spatial discretization)
- Decay [1/s] (1st order)
- Source/sink (Mass) [g/m²/d] [g/m³/d] (biological decay)
- Transfer rate (Mass) (only together with Transfer BC)
- Sorption coefficient 2 (Freundlich, Langmuir)

Mesh quality check

- data panel - auxiliary data - stream function - best is to use "Max. interior angle of triangles" - select nodes to choose the erroneous triangles - smooth mesh

Numerical parameters

- stop simulation before changing
- Error tolerance: default is 1*10e-3, use e.g. 100 instead of 1, Absolute L1 integral error norm results in most reliable results of groundwater heads
- Max. number of iterations: e.g. 400
- upwinding option: to smoothen deep concentration gradients

To **P**in the coordinates

- pin coordinates toolbar with F2

Import a **P**olygon geometry from ArcGIS to FEFLOW

- within the maps panel: add the shp-files created in ArcGIS with the attributed kf values or replace the existing map by the new one created with new polygons in ArcGIS as well together
- avoid enclave polygons in ArcGIS

Preparation of folder

- folder fem, input, results and smh to create before each new project

Refinement of discretization

- node or element selection
- refine elements

Salting-up

- via the transport model - assign as concentration property

Saltwater-head boundary condition

- problem settings - include transport of mass
- h = phi + z = p/(rho+g) + z
- The conversion to an equivalent fresh water head hfw is based on: hfw = hsw + alpha (hsw - z) with hsw: saltwater head, alpha: density ratio, z: nodal elevation (z coordinate in 3D, y coordinate in 2D cross-sectional/axisymmetric models)

- salt-water head automatically calculated when C_S is added

Export/Import **S**ettings

- slice views with (e.g. with custom color properties) can be saved as *xml*-file

Triangle generator

- triangle *dll*-file necessary for triangle mesh because a large number of polygons could not be implemented otherwise
- http://www.cs.cmu.edu/~quake/triangle.html (retrieved October 2013)

Visualization

- Hydraulic head as continuous or isolines
- Pressure as continuous or isolines
- Nodal fluid-flux vector field: bullets, vectors, arrows
- Streamlines: after selection of the boundary, create forward and backward streamlines, activate traces in the view components panel (e.g. change the maximum travel time, change radius, e.g. 5 m)
- use import/export settings (saved as *xml*-files) for easy transfer of the personal visualization settings from one model to next model

Appendix B: Synopsis of the model properties

Table B1: Properties of model 006 to 021

ID		006	012	013	014	017	018	020	021
Slice		for all drillings	for all drillings	for all drillings	for all drillings	Drapot 4	Drapot 4	for all drillings	for all drillings
Supermesh	Number of Elements		12	12	12	12	12	12	12
	Number of Nodes		115	115	115	115	115	115	115
	Number of Polygons		12	12	12	12	12	12	12
Problem Class	Description	Combined flow and mass transport	Separate flow process	Combined flow and mass transport	Combined flow and mass transport	Combined flow and mass transport	Combined flow and mass transport	Combined flow and mass transport	Combined flow and mass transport
	Type	Saturated	Saturated	Saturated	Saturated	Saturated	Saturated	Saturated	Saturated
	Projection	Vertical confined 2D aquifer	Vertical unsaturated 2D aquifer	Vertical confined 2D aquifer	Vertical confined 2D aquifer	Vertical confined 2D aquifer	Vertical confined 2D aquifer	Vertical confined 2D aquifer	Vertical confined 2D aquifer
	Free surface	no	no	no	no	no	no	no	no
	Time Class	Steady flow + Steady transport	Steady flow	Steady flow + Steady transport	Steady flow + Steady transport	Steady flow + Steady transport	Steady flow + Steady transport	Steady flow + Steady transport	Steady flow + Steady transport
	Time Stepping	Constant time steps	Constant time steps	Constant time steps	Constant time steps	Constant time steps	Constant time steps	Constant time steps	Constant time steps
	Error tolerance								
	Norm	Absolute L1 integral error norm	Absolute L1 integral error norm	Absolute L1 integral error norm	Absolute L1 integral error norm	Absolute L1 integral error norm	Absolute L1 integral error norm	Absolute L1 integral error norm	Absolute L1 integral error norm
	Value [10^{-3}]	10	10	10	10	10	10	10	10
	Maximum number of iterations	400	400	400	400	400	400	400	400
	Solver Type	Algebraic multigrid SAMG	Algebraic multigrid SAMG	Algebraic multigrid SAMG	Algebraic multigrid SAMG	Algebraic multigrid SAMG	Algebraic multigrid SAMG	Algebraic multigrid SAMG	Algebraic multigrid SAMG
	Upwinding	No upwinding	No upwinding	No upwinding	Streamline upwinding	No upwinding	Streamline upwinding	Streamline upwinding	Streamline upwinding
	Number of Species	1	1	1	1	1	1	1	1
	Transport settings								
	Reference values		none						
	C_0 [mg/L]								
	C_1 [mg/L]	800	800	800	800	800	800	800	800
		350000	350000	350000	350000	350000	350000	350000	350000
FEM-Mesh	Meshi elements	15956	15956	15956	15956	15956	15956	15956	15956
	Applied total elements	10000	10000	10000	10000	10000	10000	10000	10000
	Meshing density [not listed units not refined]								
	Qll/QetFQ0	2	2	2	2	2	2	2	2
	DSG sediment differentiated	50	50	50	50	50	50	50	50
	DSG sediment undifferentiated	2	2	2	2	2	2	2	2
	Cu next to DSG	2	2	2	2	2	2	2	2
	Kuey next to DSG	2	2	2	2	2	2	2	2
	Klih next to DSG	2	2	2	2	2	2	2	2
	Mesh nodes	8176	8176	8176	8176	8176	8176	8176	8176
	Problem Geometry								
	X [m]	0	0	0	0	0	0	0	0
	Y [masl]	-620	-620	-620	-620	-620	-620	-620	-620
	Width [m]	2711	2711	2711	2711	2711	2711	2711	2711
	Height [m]	610	610	610	610	610	610	610	610
	Triangle quality	0.8% > 120°, 17.9% > 90°	0.8% > 120°, 17.9% > 90°	0.8% > 120°, 17.9% > 90°	0.8% > 120°, 17.9% > 90°	0.8% > 120°, 17.9% > 90°	0.8% > 120°, 17.9% > 90°	0.8% > 120°, 17.9% > 90°	0.8% > 120°, 17.9% > 90°
BCs	Fluid flow			W BC applied from -330.5 to bottom:					
	Hydraulic-head BC								
	Western Boundary [value in masl]	-320	-320	-320	-320	-320	-320	-320	-320 - 320 (up_Judea), -300 (low_Judea)
	Hydraulic-head BC (Saltwater head)		Hydraulic-head BC:						
	Eastern Boundary and DS [value in masl]	-425	-425	-425	-425	-425	-425	-425	-425
	Fluid-flux BC								
	Western Boundary [m/d]								
	Mass transport	no	no						
	Mass-concentration BC								
	Western Boundary [value in mg/L]	800	800	800	800	800	800	800	800
	Eastern Boundary and DS [value in mg/L]	350000	350000	350000	350000	350000	350000	350000	350000
Flow Properties	Conductivity [m/s]								
	Qll/QetFQ0	5.0E-05	5.0E-05	5.0E-05	5.0E-05	5.0E-05	5.0E-05	5.0E-05	5.0E-05
	DSG sediment	1.1E-04	1.1E-04	1.1E-04	1.1E-04	1.1E-04	1.1E-04	1.1E-04	1.1E-04
	Model 003017: Permeable layer						1.0E-02		
	Model 003030, 003031: ML-4: 2-9								
	Model 003030, 003031: ML-4: 10-15								
	Model 003030, 003031: ML-4: 16-17								
	Model 003030, 003031: ML-4: 18-26								
	DSG undifferentiated	1.1E-04	1.1E-04	1.1E-04	1.1E-04	1.1E-04	1.1E-04	1.1E-04	1.1E-04
	Cu	6.3E-06	6.3E-06	6.3E-06	6.3E-06	6.3E-06	6.3E-06	6.3E-06	6.3E-06
	Kuey	5.0E-09	5.0E-09	5.0E-09	5.0E-09	5.0E-09	5.0E-09	5.0E-09	5.0E-09
	Klih	1.6E-07	1.6E-07	1.6E-07	1.6E-07	1.6E-07	1.6E-07	1.6E-07	1.6E-07
	Density ratio [] automat. calculated	0.24	0.00	0.24	0.24	0.24	0.24	0.24	0.24
Discrete features		no	no	no	no	no	yes (DSG)	no	no
Refinement		no	no	no	no	no	no	no	no
Rate budget	inflow Dirichlet-BCs fluid [m³/d]	6.6E+02	2.8E+01	2.7E+02	2.1E+02	2.5E+02	7.0E+03	1.4E+02	2.1E+02
	outflow Dirichlet-BCs fluid [m³/d]	-1.8E+02	-2.8E+01	-5.2E+02	-1.9E+02	-3.1E+02	-4.9E+03	-1.5E+02	-2.0E+02
	inflow Dirichlet-BCs mass [g/s]	4.6E+03		1.3E+03	7.8E+02	1.3E+03	2.8E+04	5.4E+02	8.7E+02
	outflow Dirichlet-BCs mass [g/s]	-8.3E+02		-1.7E+03	-8.0E+02	-1.1E+03	-2.0E+04	-5.8E+02	-8.0E+02
	total balance fluid [m³/d]	*4.8E-02*	*1.0E-04*	*2.3E+03*	*1.3E-01*	*-5.4E+01*	*2.1E-03*	*9.4E+00*	*9.3E-00*
	total balance mass [g/s]	*3.7E-03*		*3.5E+03*	*-1.6E+01*	*-2.4E+02*	*8.5E-02*	*-3.4E+01*	*6.8E+01*

Table B2: Properties of model 029 to 041

ID		029	030	031	035	038	039	040	041
Slice		for all drillings	ML-4	ML-4	ML-4	ML-4	for all drillings	for all drillings	for all drillings
Supermesh	Number of Elements	12	12	12	12	12	12	12	12
	Number of Nodes	115	115	115	115	115	115	115	115
	Number of Polygons	12	12	12	12	12	12	12	12
Problem Class	Description	Combined flow and mass transport	Combined flow and mass transport	Combined flow and mass transport	Combined flow and mass transport	Combined flow and mass transport	Combined flow and mass transport	Combined flow and mass transport	Combined flow and mass transport
	Type	Saturated	Saturated	Saturated	Saturated	Saturated	Saturated	Saturated	Saturated
	Projection	Vertical confined 2D aquifer	Vertical confined 2D aquifer	Vertical confined 2D aquifer	Vertical confined 2D aquifer	Vertical confined 2D aquifer	Vertical confined 2D aquifer	Vertical confined 2D aquifer	Vertical confined 2D aquifer
	Free surface	no	no	no	no	no	no	no	no
	Time Class	Steady flow + Steady transport	Steady flow + Steady transport	Steady flow + Steady transport	Steady flow + Steady transport	Steady flow + Steady transport	Steady flow + Steady transport	Steady flow + Steady transport	Steady flow + Steady transport
	Time Stepping	Constant time steps	Constant time steps	Constant time steps	Constant time steps	Constant time steps	Constant time steps	Constant time steps	Constant time steps
	Error tolerance								
	Norm	Absolute L1 integral error norm	Absolute L1 integral error norm	Absolute L1 integral error norm	Absolute L1 integral error norm	Absolute L1 integral error norm	Absolute L1 integral error norm	Absolute L1 integral error norm	Absolute L1 integral error norm
	Value [10^{-2}]	10	10	10	10	10	10	10	10
	Maximum number of iterations	400	400	400	400	400	400	400	400
	Solver Type	Algebraic multigrid SAMG	Algebraic multigrid SAMG	Algebraic multigrid SAMG	Algebraic multigrid SAMG	Algebraic multigrid SAMG	Algebraic multigrid SAMG	Algebraic multigrid SAMG	Algebraic multigrid SAMG
	Upwinding	Streamline upwinding	Streamline upwinding	Streamline upwinding	Streamline upwinding	Streamline upwinding	Streamline upwinding	Streamline upwinding	Streamline upwinding
	Number of Species	1	1	1	1	1	1	1	1
	Transport settings								
	Reference values								
	C_0 [mg/L]	800	800	800	800	800	800	800	800
	C_S [mg/L]	350000	350000	350000	350000	350000	350000	350000	350000
FEM-Mesh	Mesh elements	15956	15956	20366	20366	20366	20366	20366	20366
	Applied total elements	10000	10000	10000	10000	10000	10000	10000	10000
	Meshing density [not listed units not refined]								
	Qli/Nqef/Q0	2	2	2	2	2	2	2	2
	DSG sediment differentiated	30	30	30	30	30	30	30	30
	DSG sediment undifferentiated	2	2	2	2	2	2	2	2
	Cu next to DSG	2	2	2	2	2	2	2	2
	Kuey next to DSG	2	2	2	2	2	2	2	2
	Klhh next to DSG	2	2	2	2	2	2	2	2
	Mesh nodes	8176	8176	10394	10394	10394	10394	10394	10394
	Problem Geometry								
	X [m]	0	0	0	0	0	0	0	0
	Y [masl]	-620	-620	-620	-620	-620	-620	-620	-620
	Width [m]	2711	2711	2711	2711	2711	2711	2711	2711
	Height [m]	610	610	610	610	610	610	610	610
	Triangle quality	0.8% > 120°, 17.9% > 90°	0.8% > 120°, 17.9% > 90°	0.8% > 120°, 18.5% > 90°	0.8% > 120°, 18.5% > 90°	0.8% > 120°, 18.5% > 90°	0.8% > 120°, 18.5% > 90°	0.8% > 120°, 18.5% > 90°	0.8% > 120°, 18.5% > 90°
BCs	Fluid flow								
	Hydraulic-head BC								
	Western Boundary [value in masl]	-320 (up. Judea), -300 (low. Judea)	-320 (up. Judea), -300 (low. Judea)	-320 (up. Judea), -300 (low. Judea)	-320 (up. Judea), -300 (low. Judea)	-320 (up. Judea), -300 (low. Judea)	-320 (up. Judea), -300 (low. Judea)	-320 (up. Judea), -300 (low. Judea)	-320 (up. Judea), -300 (low. Judea)
	Hydraulic-head BC (Saltwater head)								
	Eastern Boundary and DS [value in masl]	-425	-425	-425	-425	-425	-425	-425	-425
	Fluid-flux BC								
	Western Boundary [m/d]								
	Mass transport								
	Mass-concentration BC								
	Western Boundary [value in mg/L]	800	800	800	800	800	800	800	800
	Eastern Boundary and DS [value in mg/L]	350000	350000	350000	350000	340000	340000	340000	340000
Flow Properties	Conductivity [m/s]								
	Qli/Nqef/Q0	1.0E-05	1.0E-05	1.0E-05	1.0E-05	1.0E-05	1.0E-09	1.0E-08	1.0E-07
	DSG sediment	5.0E-05			according to kf parameterization	according to kf parameterization	1.0E-09	1.0E-08	1.0E-07
	Model 003017: Permeable layer								
	Model 003030, 003031: ML-4: 2-9		1.0E-06	1.0E-06					
	Model 003030, 003031: ML-4: 10-15		1.0E-10	1.0E-10					
	Model 003030, 003031: ML-4: 16-17		5.0E-04	5.0E-04					
	Model 003030, 003031: ML-4: 18-26		1.0E-10	1.0E-10					
	DSG undifferentiated	5.0E-05	5.0E-05	5.0E-05	5.0E-05	5.0E-05	1.0E-09	1.0E-08	1.0E-07
	Cu	1.0E-05	1.0E-05	1.0E-05	1.0E-05	1.0E-05	1.0E-05	1.0E-05	1.0E-05
	Kuey	1.0E-06	1.0E-06	1.0E-06	1.0E-06	1.0E-06	1.0E-06	1.0E-06	1.0E-06
	Klhh	1.0E-05	1.0E-05	1.0E-05	1.0E-05	1.0E-05	1.0E-05	1.0E-05	1.0E-05
	Density ratio [], automat. calculated	0.24	0.24	0.24	0.24	0.24	0.24	0.24	0.24
Discrete features		yes (Judea fault)	yes (Judea fault)	yes (DSG, Judea fault)	yes (Judea fault)	yes (DSG, Judea fault)	yes (Judea fault)	yes (Judea fault)	yes (Judea fault)
Refinement		no	no	layer 10-15	no	no	no	no	no
Rate budget	**inflow Dirichlet-BCs fluid [m³/d]**	9.3E+01	1.3E+02		2.5E+02	2.7E+03	6.1E+00	6.2E+00	6.3E+00
	outflow Dirichlet-BCs fluid [m³/d]	-9.0E+01	-3.7E+01		-6.5E+01	-2.7E+03	-6.1E+00	-6.2E+00	-6.3E+00
	inflow Dirichlet-BCs mass [g/s]	3.5E+02	4.9E+02		9.8E+02	1.2E+04	7.2E-02	2.1E-01	1.6E+00
	outflow Dirichlet-BCs mass [g/s]	-3.5E+02	-1.8E+02		-2.5E+02	-1.0E+04	-7.2E-02	-2.1E-01	-1.6E+00
	total balance fluid [m³/d]	*2.5E+00*	*9.3E+01*	voided output	*1.8E+02*	-1.0E+01	*2.0E-05*	*5.4E-04*	-5.5E-03
	total balance mass [g/s]	*1.7E+00*	*3.1E+02*	voided output	*7.3E+02*	*1.6E+03*	*1.8E-04*	*3.4E-03*	*8.2E-03*

Table B3: Properties of model 042 to 047

ID		042	043-1E-5	043-1E-4	043-1E-3	043-1E-2	045	046	047
Slice		for all drillings	for all drillings	for all drillings	for all drillings	for all drillings	ML-4	ML-4	ML-4
Supermesh	Number of Elements	12	12	12	12	12	12	12	12
	Number of Nodes	115	115	115	115	115	115	115	115
	Number of Polygons	12	12	12	12	12	12	12	12
Problem Class	Description	Combined flow and mass transport	Combined flow and mass transport	Combined flow and mass transport	Combined flow and mass transport	Combined flow and mass transport	Combined flow and mass transport	Combined flow and mass transport	Combined flow and mass transport
	Type	Saturated	Saturated	Saturated	Saturated	Saturated	Saturated	Saturated	Saturated
	Projection	Vertical confined 2D aquifer	Vertical confined 2D aquifer	Vertical confined 2D aquifer	Vertical confined 2D aquifer	Vertical confined 2D aquifer	Vertical confined 2D aquifer	Vertical confined 2D aquifer	Vertical confined 2D aquifer
	Free surface	no	no	no	no	no	no	no	no
	Time Class	Steady flow + Steady transport	Steady flow + Steady transport	Steady flow + Steady transport	Steady flow + Steady transport	Steady flow + Steady transport	Steady flow + Steady transport	Steady flow + Steady transport	Steady flow + Steady transport
	Time Stepping	Constant time steps	Constant time steps	Constant time steps	Constant time steps	Constant time steps	Constant time steps	Constant time steps	Constant time steps
	Error tolerance								
	Norm	Absolute L1 integral error norm	Absolute L1 integral error norm	Absolute L1 integral error norm	Absolute L1 integral error norm	Absolute L1 integral error norm	Absolute L1 integral error norm	Absolute L1 integral error norm	Absolute L1 integral error norm
	Value [10^{-3}]	10	10	10	10	10	10	10	10
	Maximum number of iterations	400	400	400	400	400	400	400	400
	Solver Type	Algebraic multigrid SAMG	Algebraic multigrid SAMG	Algebraic multigrid SAMG	Algebraic multigrid SAMG	Algebraic multigrid SAMG	Algebraic multigrid SAMG	Algebraic multigrid SAMG	Algebraic multigrid SAMG
	Upwinding	Streamline upwinding	Streamline upwinding	Streamline upwinding	Streamline upwinding	Streamline upwinding	Streamline upwinding	Streamline upwinding	Streamline upwinding
	Number of Species	1	1	1	1	1	1	1	1
	Transport settings								
	Reference values								
	C_0 [mg/L]	800	800	800	800	800	800	800	800
	C_S [mg/L]	350000	350000	350000	350000	350000	350000	350000	350000
FEM-Mesh	Mesh elements	20366	20366	20366	20366	20366	20366	20366	20366
	Applied total elements	10000	10000	10000	10000	10000	10000	10000	10000
	Meshing density [not listed units not refined]								
	Qli/Nqef/Q0	2	2	2	2	2	2	2	2
	DSG sediment differentiated	30	30	30	30	30	30	30	30
	DSG sediment undifferentiated	2	2	2	2	2	2	2	2
	Cu next to DSG	2	2	2	2	2	2	2	2
	Kuey next to DSG	2	2	2	2	2	2	2	2
	Klhh next to DSG	2	2	2	2	2	2	2	2
	Mesh nodes	10394	10394	10394	10394	10394	10394	10394	10394
	Problem Geometry								
	X [m]	0	0	0	0	0	0	0	0
	Y [masl]	-620	-620	-620	-620	-620	-620	-620	-620
	Width [m]	2711	2711	2711	2711	2711	2711	2711	2711
	Height [m]	610	610	610	610	610	610	610	610
	Triangle quality	0.8% > 120°, 18.5% > 90°	0.8% > 120°, 18.5% > 90°	0.8% > 120°, 18.5% > 90°	0.8% > 120°, 18.5% > 90°	0.8% > 120°, 18.5% > 90°	0.8% > 120°, 18.5% > 90°	0.8% > 120°, 18.5% > 90°	0.8% > 120°, 18.5% > 90°
BCs	Fluid flow								
	Hydraulic-head BC								
	Western Boundary [value in masl]	-320 (up. Judea), -300 (low. Judea)	-320 (up. Judea), -300 (low. Judea)	-320 (up. Judea), -300 (low. Judea)	-320 (up. Judea), -300 (low. Judea)	-320 (up. Judea), -300 (low. Judea)	-320 (up. Judea), -300 (low. Judea)	-320 (up. Judea), -300 (low. Judea)	-320 (up. Judea), -300 (low. Judea)
	Hydraulic-head BC (Saltwater head)								
	Eastern Boundary and DS [value in masl]	-425	-425	-425	-425	-425	-425	-425	-425
	Fluid-flux BC								
	Western Boundary [m/d]								
	Mass transport								
	Mass-concentration BC								
	Western Boundary [value in mg/L]	800	800	800	800	800	800	800	800
	Eastern Boundary and DS [value in mg/L]	340000	340000	340000	340000	340000	340000	340000	340000
Flow Properties	Conductivity [m/s]								
	Qli/Nqef/Q0	1.0E-06	1.0E-05	1.0E-04	1.0E-03	1.0E-02	1.0E-05	1.0E-05	1.0E-05
	DSG sediment	1.0E-06	1.0E-05	1.0E-04	1.0E-03	1.0E-02	according to kf parameterization	according to kf parameterization	according to kf parameterization
	Model 003017: Permeable layer								
	Model 003030, 003031: ML-4: 2-9								
	Model 003030, 003031: ML-4: 10-15								
	Model 003030, 003031: ML-4: 16-17								
	Model 003030, 003031: ML-4: 18-26								
	DSG undifferentiated	1.0E-06	1.0E-05	1.0E-04	1.0E-03	1.0E-02	5.0E-05	5.0E-05	5.0E-05
	Cu	1.0E-05	1.0E-05	1.0E-05	1.0E-05	1.0E-05	1.0E-05	1.0E-05	1.0E-05
	Kuey	1.0E-06	1.0E-06	1.0E-06	1.0E-06	1.0E-06	1.0E-06	1.0E-06	1.0E-06
	Klhh	1.0E-05	1.0E-05	1.0E-05	1.0E-05	1.0E-05	1.0E-05	1.0E-05	1.0E-05
	Density ratio [], automat. calculated	0.24	0.24	0.24	0.24	0.24	0.24	0.24	0.24
Discrete features		yes (Judea fault)	yes (Judea fault)	yes (Judea fault)	yes (Judea fault)	yes (Judea fault)	yes (DSG, Judea fault)	yes (DSG, Judea fault)	yes (Judea fault)
Refinement		no	no	no	no	no	no	no	no
Rate budget	**inflow Dirichlet-BCs fluid [m³/d]**	8.2E+00	2.8E+01	1.7E+02	1.0E+03	9.5E+03	1.6E+04	1.8E+03	8.2E+01
	outflow Dirichlet-BCs fluid [m³/d]	-8.1E+00	-2.8E+01	-1.6E+02	-1.4E+03	-5.4E+04	-1.6E+04	-1.1E+03	-1.5E+02
	inflow Dirichlet-BCs mass [g/s]	1.5E+01	1.0E+02	6.3E+02	4.2E+03	6.2E+04	6.3E+04	7.1E+03	3.4E+02
	outflow Dirichlet-BCs mass [g/s]	-1.4E+01	-1.0E+02	-6.2E+02	-5.3E+03	-1.0E+05	-6.4E+04	-4.1E+03	-4.8E+02
	total balance fluid [m³/d]	*9.1E-02*	*5.8E-01*	*7.0E+00*	-3.7E+02	-4.5E+04	*1.6E+01*	*7.5E+02*	-7.1E+01
	total balance mass [g/s]	*4.7E-01*	*2.8E+00*	*1.0E+01*	-1.1E+03	-4.2E+04	-1.4E+03	*3.1E+03*	-1.5E+02

Table B4: Properties of model 048 to 056

ID		048	049	050	051	052	054	055	056
Slice		ML-4	ML-4	ML-4	ML-4	ML-4	ML-4	ML-4	ML-4
Supermesh	Number of Elements	12	12	12	12	12	12	12	12
	Number of Nodes	115	115	115	115	115	115	115	115
	Number of Polygons	12	12	12	12	12	12	12	12
Problem Class	Description	Combined flow and mass transport	Combined flow and mass transport	Combined flow and mass transport	Combined flow and mass transport	Combined flow and mass transport	Combined flow and mass transport	Combined flow and mass transport	Combined flow and mass transport
	Type	Saturated	Saturated	Saturated	Saturated	Saturated	Saturated	Saturated	Saturated
	Projection	Vertical confined 2D aquifer	Vertical confined 2D aquifer	Vertical confined 2D aquifer	Vertical confined 2D aquifer	Vertical confined 2D aquifer	Vertical confined 2D aquifer	Vertical confined 2D aquifer	Vertical confined 2D aquifer
	Free surface	no	no	no	no	no	no	no	no
	Time Class	Steady flow + Steady transport	Steady flow + Steady transport	Steady flow + Steady transport	Steady flow + Steady transport	Steady flow + Steady transport	Steady flow + Steady transport	Steady flow + Steady transport	Steady flow + Steady transport
	Time Stepping	Constant time steps	Constant time steps	Constant time steps	Constant time steps	Constant time steps	Constant time steps	Constant time steps	Constant time steps
	Error tolerance								
	Norm	Absolute L1 integral error norm	Absolute L1 integral error norm	Absolute L1 integral error norm	Absolute L1 integral error norm	Absolute L1 integral error norm	Absolute L1 integral error norm	Absolute L1 integral error norm	Absolute L1 integral error norm
	Value [10^{-3}]	10	10	10	10	10	10	10	10
	Maximum number of iterations	400	400	400	400	400	400	400	400
	Solver Type	Algebraic multigrid SAMG	Algebraic multigrid SAMG	Algebraic multigrid SAMG	Algebraic multigrid SAMG	Algebraic multigrid SAMG	Algebraic multigrid SAMG	Algebraic multigrid SAMG	Algebraic multigrid SAMG
	Upwinding	Streamline upwinding	Streamline upwinding	Streamline upwinding	Streamline upwinding	Streamline upwinding	Streamline upwinding	Streamline upwinding	Streamline upwinding
	Number of Species	1	1	1	1	1	1	1	1
	Transport settings								
	Reference values								
	C_0 [mg/L]	800	800	800	800	800	800	800	800
	C_S [mg/L]	350000	350000	350000	350000	350000	350000	350000	350000
FEM-Mesh	Mesh elements	20366	20366	20366	20366	20366	20366	20366	20366
	Applied total elements	10000	10000	10000	10000	10000	10000	10000	10000
	Meshing density [not listed units not refined]								
	Qli/Nqef/Q0	2	2	2	2	2	2	2	2
	DSG sediment differentiated	30	30	30	30	30	30	30	30
	DSG sediment undifferentiated	2	2	2	2	2	2	2	2
	Cu next to DSG	2	2	2	2	2	2	2	2
	Kuey next to DSG	2	2	2	2	2	2	2	2
	Klhh next to DSG	2	2	2	2	2	2	2	2
	Mesh nodes	10394	10394	10394	10394	10394	10394	10394	10394
	Problem Geometry								
	X [m]	0	0	0	0	0	0	0	0
	Y [masl]	-620	-620	-620	-620	-620	-620	-620	-620
	Width [m]	2711	2711	2711	2711	2711	2711	2711	2711
	Height [m]	610	610	610	610	610	610	610	610
	Triangle quality	0.8% > 120°, 18.5% > 90°	0.8% > 120°, 18.5% > 90°	0.8% > 120°, 18.5% > 90°	0.8% > 120°, 18.5% > 90°	0.8% > 120°, 18.5% > 90°	0.8% > 120°, 18.5% > 90°	0.8% > 120°, 18.5% > 90°	0.8% > 120°, 18.5% > 90°
BCs	Fluid flow								
	Hydraulic-head BC								
	Western Boundary [value in masl]	-320 (up. Judea), -300 (low. Judea)	-320 (up. Judea), -300 (low. Judea)	-320 (up. Judea), -300 (low. Judea)	-320 (up. Judea), -300 (low. Judea)	-320 (up. Judea), -300 (low. Judea)	-320 (up. Judea), -300 (low. Judea)	-320 (up. Judea), -300 (low. Judea)	-320 (up. Judea), -300 (low. Judea)
	Hydraulic-head BC (Saltwater head)								
	Eastern Boundary and DS [value in masl]	-425	-425	-425	-425	-425	-425	-425	-425
	Fluid-flux BC								
	Western Boundary [m/d]								
	Mass transport								
	Mass-concentration BC								
	Western Boundary [value in mg/L]	800	800	800	800	800	800	800	800
	Eastern Boundary and DS [value in mg/L]	340000	340000	340000	340000	340000	340000	340000	340000
Flow Properties	Conductivity [m/s]								
	Qli/Nqef/Q0	1.0E-05	1.0E-05	1.0E-05	1.0E-05	1.0E-05	1.0E-05	1.0E-05	1.0E-05
	DSG sediment	according to kf parameterization	according to kf parameterization	according to kf parameterization	according to kf parameterization	according to kf parameterization	according to kf parameterization	according to kf parameterization	according to kf parameterization
	Model 003017: Permeable layer								
	Model 003030, 003031: ML-4: 2-9								
	Model 003030, 003031: ML-4: 10-15								
	Model 003030, 003031: ML-4: 16-17								
	Model 003030, 003031: ML-4: 18-26								
	DSG undifferentiated	4.5E-05	4.0E-05	3.5E-05	3.0E-05	2.5E-05	2.5E-05	2.5E-05	2.5E-05
	Cu	1.0E-05	1.0E-05	1.0E-05	1.0E-05	1.0E-05	1.0E-05	1.0E-05	1.0E-05
	Kuey	1.0E-06	1.0E-06	1.0E-06	1.0E-06	1.0E-06	1.0E-06	1.0E-06	1.0E-06
	Klhh	1.0E-05	1.0E-05	1.0E-05	1.0E-05	1.0E-05	1.0E-05	1.0E-05	1.0E-05
	Density ratio [], automat. calculated	0.24	0.24	0.24	0.24	0.24	0.24	0.24	0.24
Discrete features		yes (Judea fault)	yes (Judea fault)	yes (Judea fault)	yes (Judea fault)	yes (Judea fault)	yes (DSG, Judea fault)	yes (DSG, Judea fault)	yes (DSG, Judea fault)
Refinement		no	no	no	no	no	no	no	no
Rate budget	**inflow Dirichlet-BCs fluid [m³/d]**	9.6E+01	6.7E+01	6.5E+01	6.5E+01	6.5E+01	8.9E+02	6.8E+02	5.0E+03
	outflow Dirichlet-BCs fluid [m³/d]	-8.3E+01	-8.4E+01	-7.1E+01	-5.9E+01	-5.3E+01	-8.9E+02	-7.4E+02	-4.6E+04
	inflow Dirichlet-BCs mass [g/s]	3.7E+02	2.6E+02	2.5E+02	2.4E+02	2.5E+02	3.4E+03	2.7E+03	1.0E+05
	outflow Dirichlet-BCs mass [g/s]	-3.2E+02	-3.1E+02	-2.7E+02	-2.3E+02	-2.0E+02	-3.5E+03	-2.9E+03	-1.6E+05
	total balance fluid [m³/d]	*1.2E+01*	-1.7E+01	-6.4E+00	*6.0E+00*	*1.2E+01*	-3.7E-02	-6.6E+01	-4.1E+04
	total balance mass [g/s]	*5.0E+01*	-5.3E+01	-1.9E+01	*1.7E+01*	*4.8E+01*	-7.7E+01	-1.8E+02	-5.8E+04

Table B5: Properties of model 057 to 068

ID		057	058	059	061	062	063	064	068
Slice		ML-4	ML-4	ML-4	ML-4	ML-4	ML-4	ML-4	ML-4
Supermesh	Number of Elements	12	12	12	12	12	12	12	12
	Number of Nodes	115	115	115	115	115	115	115	115
	Number of Polygons	12	12	12	12	12	12	12	12
Problem Class	Description	Combined flow and mass transport	Combined flow and mass transport	Combined flow and mass transport	Combined flow and mass transport	Combined flow and mass transport	Combined flow and mass transport	Combined flow and mass transport	Combined flow and mass transport
	Type	Saturated	Saturated	Saturated	Saturated	Saturated	Saturated	Saturated	Saturated
	Projection	Vertical confined 2D aquifer	Vertical confined 2D aquifer	Vertical confined 2D aquifer	Vertical confined 2D aquifer	Vertical confined 2D aquifer	Vertical confined 2D aquifer	Vertical confined 2D aquifer	Vertical confined 2D aquifer
	Free surface	no	no	no	no	no	no	no	no
	Time Class	Steady flow + Steady transport	Steady flow + Steady transport	Steady flow + Steady transport	Steady flow + Steady transport	Steady flow + Steady transport	Steady flow + Steady transport	Steady flow + Steady transport	Steady flow + Steady transport
	Time Stepping	Constant time steps	Constant time steps	Constant time steps	Constant time steps	Constant time steps	Constant time steps	Constant time steps	Constant time steps
	Error tolerance								
	Norm	Absolute L1 integral error norm	Absolute L1 integral error norm	Absolute L1 integral error norm	Absolute L1 integral error norm	Absolute L1 integral error norm	Absolute L1 integral error norm	Absolute L1 integral error norm	Absolute L1 integral error norm
	Value [10^{-3}]	10	10	10	10	10	10	10	10
	Maximum number of iterations	400	400	400	400	400	400	400	400
	Solver Type	Algebraic multigrid SAMG	Algebraic multigrid SAMG	Algebraic multigrid SAMG	Algebraic multigrid SAMG	Algebraic multigrid SAMG	Algebraic multigrid SAMG	Algebraic multigrid SAMG	Algebraic multigrid SAMG
	Upwinding	Streamline upwinding	Streamline upwinding	Streamline upwinding	Streamline upwinding	Streamline upwinding	Streamline upwinding	Streamline upwinding	Streamline upwinding
	Number of Species	1	1	1	1	1	1	1	1
	Transport settings								
	Reference values								
	C_0 [mg/L]	800	800	800	800	800	800	800	800
	C_S [mg/L]	350000	350000	350000	350000	350000	350000	350000	350000
FEM-Mesh	Mesh elements	20366	20366	20366	20366	20366	20366	20366	20366
	Applied total elements	10000	10000	10000	10000	10000	10000	10000	10000
	Meshing density [not listed units not refined]								
	Qli/Nqef/Q0	2	2	2	2	2	2	2	2
	DSG sediment differentiated	30	30	30	30	30	30	30	30
	DSG sediment undifferentiated	2	2	2	2	2	2	2	2
	Cu next to DSG	2	2	2	2	2	2	2	2
	Kuey next to DSG	2	2	2	2	2	2	2	2
	Klhh next to DSG	2	2	2	2	2	2	2	2
	Mesh nodes	10394	10394	10394	10394	10394	10394	10394	10394
	Problem Geometry								
	X [m]	0	0	0	0	0	0	0	0
	Y [masl]	-620	-620	-620	-620	-620	-620	-620	-620
	Width [m]	2711	2711	2711	2711	2711	2711	2711	2711
	Height [m]	610	610	610	610	610	610	610	610
	Triangle quality	0.8% > 120°, 18.5% > 90°	0.8% > 120°, 18.5% > 90°	0.8% > 120°, 18.5% > 90°	0.8% > 120°, 18.5% > 90°	0.8% > 120°, 18.5% > 90°	0.8% > 120°, 18.5% > 90°	0.8% > 120°, 18.5% > 90°	0.8% > 120°, 18.5% > 90°
BCs	Fluid flow								
	Hydraulic-head BC								
	Western Boundary [value in masl]	-320 (up. Judea), -300 (low. Judea)	-320 (up. Judea), -300 (low. Judea)	-320 (up. Judea), -300 (low. Judea)	-320 (up. Judea), -300 (low. Judea)	-320 (up. Judea), -300 (low. Judea)	-320 (up. Judea), -300 (low. Judea)	-320 (up. Judea), -300 (low. Judea)	-320 (up. Judea), -300 (low. Judea)
	Hydraulic-head BC (Saltwater head)								
	Eastern Boundary and DS [value in masl]	-425	-425	-425	-425	-425	-425	-425	-425
	Fluid-flux BC								
	Western Boundary [m/d]								
	Mass transport								
	Mass-concentration BC								
	Western Boundary [value in mg/L]	800	800	800	800	800	800	800	800
	Eastern Boundary and DS [value in mg/L]	340000	340000	340000	340000	340000	340000	340000	340000
Flow Properties	Conductivity [m/s]								
	Qli/Nqef/Q0	1.0E-05	1.0E-05	1.0E-05	1.0E-05	1.0E-05	1.0E-05	1.0E-05	1.0E-05
	DSG sediment	according to kf parameterization	according to kf parameterization	according to kf parameterization	according to kf parameterization	according to kf parameterization	according to kf parameterization	according to kf parameterization	according to kf parameterization
	Model 003017: Permeable layer								
	Model 003030, 003031: ML-4: 2-9								
	Model 003030, 003031: ML-4: 10-15								
	Model 003030, 003031: ML-4: 16-17								
	Model 003030, 003031: ML-4: 18-26								
	DSG undifferentiated	2.5E-05	2.5E-05	2.5E-05	2.5E-05	2.5E-05	2.5E-05	2.5E-05	2.5E-05
	Cu	1.0E-05	1.0E-05	1.0E-05	1.0E-05	1.0E-05	1.0E-05	1.0E-05	1.0E-05
	Kuey	1.0E-06	1.0E-06	1.0E-06	1.0E-06	1.0E-06	1.0E-06	1.0E-06	1.0E-06
	Klhh	1.0E-05	1.0E-05	1.0E-05	1.0E-05	1.0E-05	1.0E-05	1.0E-05	1.0E-05
	Density ratio [], automat. calculated	0.24	0.24	0.24	0.24	0.24	0.24	0.24	0.24
Discrete features		yes (DSG, Judea fault)	yes (DSG, Judea fault)	yes (DSG, Judea fault)	yes (Judea fault)	yes (DSG, Judea fault)	yes (DSG, Judea fault)	yes (DSG, Judea fault)	yes (DSG, Judea fault)
Refinement		no	no	no	no	no	no	no	no
Rate budget	**inflow Dirichlet-BCs fluid [m³/d]**	1.8E+02		1.3E+03	6.5E+01	7.7E+01	7.4E+01	7.2E+01	7.1E+01
	outflow Dirichlet-BCs fluid [m³/d]	-1.8E+02		-1.3E+03	-5.3E+01	-5.9E+01	-5.7E+01	-5.6E+01	-5.6E+01
	inflow Dirichlet-BCs mass [g/s]	6.3E+02		4.9E+03	2.5E+02	2.9E+02	2.8E+02	2.7E+02	2.7E+02
	outflow Dirichlet-BCs mass [g/s]	-6.9E+02		-5.0E+03	-2.0E+02	-2.1E+02	-2.1E+02	-2.0E+02	-2.0E+02
	total balance fluid [m³/d]	-1.6E+00	voided output	-7.1E-01	*1.2E+01*	*1.8E+01*	*1.7E+01*	*1.6E+01*	*1.5E+01*
	total balance mass [g/s]	-6.2E+01	voided output	-8.1E+01	*4.8E+01*	*8.0E+01*	*7.4E+01*	*6.7E+01*	*6.6E+01*

Table B6: Properties of model 070 to 080

ID		070	071	075	076	077	078	079	080
Slice		ML-4	ML-4	ML-4	ML-4	ML-4	ML-4	ML-4	ML-4
Supermesh	Number of Elements	12	12	12	12	12	12	12	12
	Number of Nodes	115	115	115	115	115	115	115	115
	Number of Polygons	12	12	12	12	12	12	12	12
Problem Class	Description	Combined flow and mass transport	Combined flow and mass transport	Combined flow and mass transport	Combined flow and mass transport	Combined flow and mass transport	Combined flow and mass transport	Combined flow and mass transport	Combined flow and mass transport
	Type	Saturated	Saturated	Saturated	Saturated	Saturated	Saturated	Saturated	Saturated
	Projection	Vertical confined 2D aquifer	Vertical confined 2D aquifer	Vertical confined 2D aquifer	Vertical confined 2D aquifer	Vertical confined 2D aquifer	Vertical confined 2D aquifer	Vertical confined 2D aquifer	Vertical confined 2D aquifer
	Free surface	no	no	no	no	no	no	no	no
	Time Class	Steady flow + Steady transport	Steady flow + Steady transport	Steady flow + Steady transport	Steady flow + Steady transport	Steady flow + Steady transport	Steady flow + Steady transport	Steady flow + Steady transport	Steady flow + Steady transport
	Time Stepping	Constant time steps	Constant time steps	Constant time steps	Constant time steps	Constant time steps	Constant time steps	Constant time steps	Constant time steps
	Error tolerance								
	Norm	Absolute L1 integral error norm	Absolute L1 integral error norm	Absolute L1 integral error norm	Absolute L1 integral error norm	Absolute L1 integral error norm	Absolute L1 integral error norm	Absolute L1 integral error norm	Absolute L1 integral error norm
	Value [10^{-3}]	10	10	10	10	10	10	10	10
	Maximum number of iterations	400	400	400	400	400	400	400	400
	Solver Type	Algebraic multigrid SAMG	Algebraic multigrid SAMG	Algebraic multigrid SAMG	Algebraic multigrid SAMG	Algebraic multigrid SAMG	Algebraic multigrid SAMG	Algebraic multigrid SAMG	Algebraic multigrid SAMG
	Upwinding	Streamline upwinding	Streamline upwinding	Streamline upwinding	Streamline upwinding	Streamline upwinding	Streamline upwinding	Streamline upwinding	Streamline upwinding
	Number of Species	1	1	1	1	1	1	1	1
	Transport settings								
	Reference values								
	C_0 [mg/L]	800	800	800	800	800	800	800	800
	C_S [mg/L]	350000	350000	350000	350000	350000	350000	350000	350000
FEM-Mesh	Mesh elements	20366	20366	25167	25167	25167	25167	25167	25167
	Applied total elements	10000	10000	10000	10000	10000	10000	10000	10000
	Meshing density [not listed units not refined]								
	Qli/Nqef/Q0	2	2	2	2	2	2	2	2
	DSG sediment differentiated	30	30	30	30	30	30	30	30
	DSG sediment undifferentiated	2	2	2	2	2	2	2	2
	Cu next to DSG	2	2	2	2	2	2	2	2
	Kuey next to DSG	2	2	2	2	2	2	2	2
	Klhh next to DSG	2	2	2	2	2	2	2	2
	Mesh nodes	10394	10394	12826	12826	12826	12826	12826	12826
	Problem Geometry								
	X [m]	0	0	0	0	0	0	0	0
	Y [masl]	-620	-620	-620	-620	-620	-620	-620	-620
	Width [m]	2711	2711	2711	2711	2711	2711	2711	2711
	Height [m]	610	610	610	610	610	610	610	610
	Triangle quality	0.8% > 120°, 18.5% > 90°	0.8% > 120°, 18.5% > 90°	0.9% > 120°, 19% > 90°	0.9% > 120°, 19% > 90°	0.9% > 120°, 19% > 90°	0.9% > 120°, 19% > 90°	0.9% > 120°, 19% > 90°	0.9% > 120°, 19% > 90°
BCs	Fluid flow								
	Hydraulic-head BC								
	Western Boundary [value in masl]	-320 (up. Judea), -300 (low. Judea)	-320 (up. Judea), -300 (low. Judea)	-320 (up. Judea), -300 (low. Judea)	-320 (up. Judea), -300 (low. Judea)	-320 (up. Judea), -300 (low. Judea)	-320 (up. Judea), -300 (low. Judea)	-320 (up. Judea), -300 (low. Judea)	-320 (up. Judea), -300 (low. Judea)
	Hydraulic-head BC (Saltwater head)								
	Eastern Boundary and DS [value in masl]	-425	-425	-425	-425	-425	-425	-425	-425
	Fluid-flux BC								
	Western Boundary [m/d]								
	Mass transport								
	Mass-concentration BC							additional 100 mg/L on the Judea fault	additional 150 mg/L on the Judea fault
	Western Boundary [value in mg/L]	800	800	800	800	800	800	800	800
	Eastern Boundary and DS [value in mg/L]	340000	340000	340000	340000	340000	340000	340000	340000
Flow Properties	Conductivity [m/s]								
	Qli/Nqef/Q0	1.0E-05	1.0E-05	1.0E-05	1.0E-05	1.0E-05	1.0E-05	1.0E-05	1.0E-05
	DSG sediment	according to kf parameterization	according to kf parameterization	according to kf parameterization	according to kf parameterization	according to kf parameterization	according to kf parameterization	according to kf parameterization	according to kf parameterization
	Model 003017: Permeable layer								
	Model 003030, 003031: ML-4: 2-9								
	Model 003030, 003031: ML-4: 10-15								
	Model 003030, 003031: ML-4: 16-17								
	Model 003030, 003031: ML-4: 18-26								
	DSG undifferentiated	2.5E-05	2.5E-05	2.5E-05	2.5E-05	2.5E-05	2.5E-05	2.5E-05	2.5E-05
	Cu	1.0E-05	1.0E-05	1.0E-05	1.0E-05	1.0E-05	1.0E-05	1.0E-05	1.0E-05
	Kuey	1.0E-06	1.0E-06	1.0E-06	1.0E-06	1.0E-06	1.0E-06	1.0E-06	1.0E-06
	Klhh	1.0E-05	1.0E-05	1.0E-05	1.0E-05	1.0E-05	1.0E-05	1.0E-05	1.0E-05
	Density ratio [], automat. calculated	0.24	0.24	0.24	0.24	0.24	0.24	0.24	0.24
Discrete features		yes (DSG, Judea fault)	yes (DSG, Judea fault)	yes (DSG, Judea fault)	yes (DSG, Judea fault)	yes (DSG, Judea fault)	yes (DSG, Judea fault)	yes (DSG, Judea fault)	yes (DSG, Judea fault)
Refinement		no	no	yes	no	no	no	no	no
Rate budget	**inflow Dirichlet-BCs fluid [m³/d]**	7.4E+01	9.0E+01	1.9E+02	1.2E+02	1.1E+02	1.8E+02		
	outflow Dirichlet-BCs fluid [m³/d]	-8.6E+01	-5.5E+01	-1.9E+02	-1.3E+02	-1.1E+02	-1.8E+02		
	inflow Dirichlet-BCs mass [g/s]	2.4E+02	3.4E+02	6.3E+02	4.4E+02	4.2E+02	6.5E+02		
	outflow Dirichlet-BCs mass [g/s]	-3.1E+02	-2.1E+02	-7.4E+02	-4.8E+02	-4.4E+02	-7.1E+02		
	total balance fluid [m³/d]	-1.1E+01	*3.5E+01*	*3.4E+00*	-2.8E+00	-5.8E+00	-4.8E-01	voided output	voided output
	total balance mass [g/s]	-6.6E+01	*1.3E+02*	-1.1E+02	-4.2E+01	-1.9E+01	-5.6E+01	voided output	voided output

Table B7: Properties of model 081 to 090

ID		081	082	083	084	090
Slice		ML-4	ML-4	ML-4	ML-4	ML-4
Supermesh	Number of Elements	12	12	12	12	12
	Number of Nodes	115	115	115	115	115
	Number of Polygons	12	12	12	12	12
Problem Class	Description	Combined flow and mass transport	Combined flow and mass transport	Combined flow and mass transport	Combined flow and mass transport	Combined flow and mass transport
	Type	Saturated	Saturated	Saturated	Saturated	Saturated
	Projection	Vertical confined 2D aquifer	Vertical confined 2D aquifer	Vertical confined 2D aquifer	Vertical confined 2D aquifer	Vertical confined 2D aquifer
	Free surface	no	no	no	no	no
	Time Class	Steady flow + Steady transport	Steady flow + Steady transport	Steady flow + Steady transport	Steady flow + Steady transport	Steady flow + Steady transport
	Time Stepping	Constant time steps	Constant time steps	Constant time steps	Constant time steps	Constant time steps
	Error tolerance					
	Norm	Absolute L1 integral error norm	Absolute L1 integral error norm	Absolute L1 integral error norm	Absolute L1 integral error norm	Absolute L1 integral error norm
	Value [10^{-3}]	10	10	10	10	10
	Maximum number of iterations	400	400	400	400	400
	Solver Type	Algebraic multigrid SAMG	Algebraic multigrid SAMG	Algebraic multigrid SAMG	Algebraic multigrid SAMG	Algebraic multigrid SAMG
	Upwinding	Streamline upwinding	Streamline upwinding	Streamline upwinding	Streamline upwinding	Streamline upwinding
	Number of Species	1	1	1	1	1
	Transport settings					
	Reference values					
	C_0 [mg/L]	800	800	800	800	800
	C_S [mg/L]	350000	350000	350000	350000	350000
FEM Mesh	Mesh elements	25167	25167	25167	25167	20566
	Applied toral elements	10000	10000	10000	10000	10000
	Meshing density [not listed units not refined]					
	QkNgeFQ0	2	2	2	2	2
	DSG sediment differentiated	30	30	30	30	30
	DSG sediment undifferentiated	2	2	2	2	2
	Cu next to DSG	2	2	2	2	2
	Kuey next to DSG	2	2	2	2	2
	Klth next to DSG	2	2	2	2	2
	Mesh nodes	12826	12826	12826	12826	10394
	Problem Geometry					
	X [m]	0	0	0	0	0
	Y [mas]	-620	-620	-620	-620	-620
	Width [m]	2711	2711	2711	2711	2711
	Height [m]	610	610	610	610	610
	Triangle quality	0.5% > 120°, 19% > 90°	0.5% > 120°, 19% > 90°	0.5% > 120°, 19% > 90°	0.5% > 120°, 19% > 90°	0.8% > 120°, 18.5% > 90°
BCs	Fluid flow					
	Hydraulic-head BC					
	Western Boundary [value in masl]	-320 (sp. Judea), -300 (low. Judea)	-320 (sp. Judea), -300 (low. Judea)	-320 (sp. Judea), -300 (low. Judea)	-320 (sp. Judea), -300 (low. Judea)	-320 (sp. Judea), -300 (low. Judea)
	Hydraulic-head BC (Saltwater head)					
	Eastern Boundary and DS [value in masl]	425	425	425	425	425
	Fluid-flux BC					
	Western Boundary [m/d]					
	Mass transport					
	Mass-concentration BC	additional 200 mg/L on the Judea fault	additional 350 mg/L on the Judea fault	additional 300 mg/L on the Judea fault	additional 350 mg/L on the Judea fault	
	Western Boundary [value in mg/L]	800	800	800	800	800
	Eastern Boundary and DS [value in mg/L]	340000	340000	340000	340000	340000
Flow Properties	Conductivity [m/s]	1.0E-05	1.0E-05	1.0E-05	1.0E-05	1.0E-05 removed
	QkNgeFQ0					
	DSG sediment	according to kf parameterization	according to kf parameterization	according to kf parameterization	according to kf parameterization	according to kf parameterization
	Model 003017: Permeable layer					
	Model 003030, 003031: ML-4: 2-9					
	Model 003030, 003031: ML-4: 10-15					
	Model 003030, 003031: ML-4: 16-17					
	Model 003030, 003031: ML-4: 18-26					
	DSG undifferentiated	2.5E-05	2.5E-05	2.5E-05	2.5E-05	2.5E-05
	Cu	1.0E-05	1.0E-05	1.0E-05	1.0E-05	1.0E-05
	Kuey	1.0E-06	1.0E-06	1.0E-06	1.0E-06	1.0E-06
	Klth	1.0E-05	1.0E-05	1.0E-05	1.0E-05	1.0E-05
	Density ratio [], automat. calculated	0.24	0.24	0.24	0.24	0.24
Discrete features		yes (DSG, Judea fault)	yes (DSG, Judea fault)	yes (DSG, Judea fault)	yes (DSG, Judea fault)	yes (DSG, Judea fault)
Refinement		no	no	no	no	no
Rate budget	inflow Dirichlet-BCs fluid [m³/d]	1.8E+02	1.8E+02	1.8E+02	1.8E+02	6.9E+01
	outflow Dirichlet-BCs fluid [m³/d]	-1.8E+02	-1.8E+02	-1.8E+02	-1.8E+02	-7.0E+01
	inflow Dirichlet-BCs mass [g/s]	6.2E+02	6.3E+02	6.3E+02	6.4E+02	2.3E+02
	outflow Dirichlet-BCs mass [g/s]	-6.0E+02	-6.0E+02	-6.0E+02	-6.0E+02	-2.0E+02
	total balance fluid [m³/d]	4.0E-02	3.7E-01	2.3E-01	-1.2E-01	-9.1E+00
	total balance mass [g/s]	-5.3E+01	-5.0E+01	-4.7E+01	-4.3E+01	-5.4E+01